THE UNIVERSITY *of* EDINBURGH

Reducing Unbalanced Magnetic Pull in Induction Machines

Haw Wooi Chuan

Doctor of Philosophy

The University of Edinburgh

2018

Abstract

Induction machines are the most widely used type of electrical machines because of their robustness, simplicity, and relatively low cost. However, the small airgap in the induction machine makes them more susceptible to Unbalanced Magnetic Pull (UMP). This is because the magnitude of the UMP is a function of the degree of eccentricity, which is the ratio between the length of misalignment and the mean airgap length. The bearing-related failure accounts for approximately 41% of the total failures of induction machines; the percentages of bearing-related failure would be higher for applications in a harsher environment. In this thesis, the UMP caused by rotor eccentricity is investigated, because a small degree of rotor eccentricity is unavoidable due to the manufacturing tolerance and 80% of the mechanical faults could cause rotor eccentricity in electrical machines.

When the rotor is not at the centre of the stator, the eccentric rotor causes an uneven airgap around the rotor, in which the magnetic permeance with the higher harmonics content will be created. The magnetomotive force (MMF) produces additional pole-pair ± 1 magnetic flux around the airgap. The interaction between each magnetic flux with its pole pair ± 1 magnetic flux produces UMP. As only the magnetic flux that crosses the airgap causes UMP, the magnetic flux is categorised into magnetising flux and airgap leakage flux, because both types of flux possess different characteristics at a different rotor slip. As the airgap leakage flux is difficult to calculate analytically, an empirical method is proposed to estimate the UMP caused by the airgap leakage flux. Then, the UMP caused by the magnetising flux can also be estimated by using the empirical method. The parameters for the empirical method can be found by using either the FEA or the experimental results.

The damping effect of the magnetising flux in a parallel connected rotor bar is discussed and a damping coefficient is introduced to explain this scenario. The damping coefficient can also be used to calculate the UMP in a steady state analysis. UMP comparisons between the cage rotor and wound rotor induction machines are made. The wound rotor has a much higher UMP because the pole-specific wound rotor could not damp the additional pole pair ± 1 magnetic flux. Therefore, a damper winding at the stator slot is also proposed in order to damp the UMP by producing a counteracting flux. In addition, analytical equations have also been derived for

different scenarios, such as static eccentricity, dynamic eccentricity, axial-varying eccentricity, and skew rotor bars. Finite Element Analysis (FEA) and experimental work are used to demonstrate the derived analytical equation. Furthermore, the power losses caused by the rotor eccentricity are investigated. Iron losses, copper losses, and frictional loss are discussed and compared with both the analytical equation and the FEA results.

In order to reduce the UMP in the induction machines, the two proposed methods are the slip control method and damper windings topology. The slip control method utilises the non-linearity characteristic of the UMP at different rotor slip. To find the optimum operating slip with the lowest UMP, the UMP/Torque ratio is introduced. The characteristics of the UMP/Torque ratio varies with the type and design of the induction machines. However, this method is only applicable when the machine is lightly loaded, because the magnetising flux is limited by the capped terminal voltage and the core saturation of the machine. For the damper winding topology, a circulating current flowing in the damper winding could produce a counteracting flux to damp the UMP. The proposed damper windings configuration is only suitable for the induction machine with an even pole pair number. Finally, comparisons between both UMP reduction methods are made.

Acknowledgement

First and foremost, I would like to express my sincere gratitude to my supervisor, Dr. Jonathan Ssek, who provided me with an opportunity to work under him. His guidance and constant faith in my work have helped me in all the time of research and writing of this thesis. Furthermore, I would like to thank Prof. David Dorrell for giving me advice on my works whenever I am stuck in my research. In addition, I would like to thank Sasa Djokic for valuable comments and suggestions to widen my perspective in thesis writing. I gratefully acknowledge the funding sources from the University of Edinburgh that made my PhD work possible.

I would like to extend my gratitude to my colleagues from the Institute for Energy Systems at the University of Edinburgh have helped me and ensured that my research life was not a lonely process. Particularly, they include Leong Kit Gan, Juan Pablo Echenique Subiabre, Ozan Keysan, Marios Sousounis, Renaldi, Yew Chuan Chong, Xiao Yun Rong, Faheem Akhter, Okechukwu Ubani, Serguey Maximov, Gunel Aghabayli, and Nisaar Ahmed.

In addition to the above, I would like to thank my family for all their love and encouragement. For my parents who raised me with a love of engineering and supported me in all my pursuits. I was very much privileged to learn from my father who is also an electrical engineer and consistently inspired me and gave me the confidence to go further. For my adorable sister who has always taken good care of the family while I am abroad. For my loving and understanding wife, father-in-law and mother-in-law, whose faithful support especially during the final stages of this PhD is so appreciated.

My research was made less stressful, because of the presence of Arsenal Football Club. I would extend my gratitude to the club and Arsene Wenger for filling up my life with football. I would like to acknowledge EUSA The Shop for selling the falafel wrap, which is the food for my lunch and dinner in the past four years.

Above all, I owe it all to Jiddu Krishnamurti for granting me wisdom and strength to undertake this research work and enabling me to its completion.

Declaration

I declare that this thesis was composed by myself, that the work contained herein is my own except where explicitly stated otherwise in the text.

Haw Wooi Chuan

Table of Contents

List of Tables

List of Figures

Abbreviations

2D	Two-dimensional
EMF	Electromotive Force
DFIG	Doubly Fed Induction Generator
DTC	Direct Torque Control
FEA	Finite Element Analysis
FFT	Fast Fourier Transform
FOC	Field Oriented Control
MMF	Magnetomotive Force
MWFA	Modified Winding Function Analysis
UMP	Unbalanced Magnetic Pull

Symbols

$\boldsymbol{A}$	Magnetic Potential
$\boldsymbol{b}$	Slot width
$\boldsymbol{B}$	Magnetic flux density
$\boldsymbol{e}$	Distance of eccentricity
$\boldsymbol{e_0}$	Permittivity of free space
$\boldsymbol{E}$	Electric field
$\boldsymbol{f}$	Frequency
$\boldsymbol{F_{eq}}$	Total force acting on the bearing
$\boldsymbol{g}$	Airgap length
$\boldsymbol{h}$	Horizontal
$\boldsymbol{I}$	Current
$\boldsymbol{I_M}$	Magnetising current
$\boldsymbol{I_R}$	Rotor current
$\boldsymbol{I_S}$	Stator current
$\boldsymbol{J}$	Current density
$\boldsymbol{k_c}$	Correction factor
$\boldsymbol{k_d}$	Distribution factor
$\boldsymbol{k_p}$	Pitch factor
$\boldsymbol{k_{sat}}$	Saturation factor

k_{sk}	Skew factor
k_w	Winding factor
k_σ	Leakage factor
l	Machine length
l_m	Magnetic flux length
l_t	Material thickness
L_{ag}	Airgap leakage inductance
L_m	Magnetising inductance
L_R	Rotor Inductance
L_S	Stator inductance
L_δ	Leakage inductance
n	Harmonics number
n_s	Synchronous rotating speed
N	Number of turn
N_r	Rotor slot number
N_s	Stator slot number
p	Pole pair number
P	Active Power
q	Number of slot per pole
r	Radius
R	Resistance
s	Rotor slip
S_a	Surface of conducting current
t	Time
T	Torque
μ_e	Effective permeability

$\boldsymbol{\mu_r}$	Relative permeability
$\boldsymbol{\mu_0}$	Permeability of free space
$\boldsymbol{U}$	Internal Voltage
$\boldsymbol{UMP}$	Unbalance Magnetic Pull
$\boldsymbol{V}$	Voltage
$\boldsymbol{W_r}$	Rotor weight
$\boldsymbol{X_m}$	Magnetising reactance
$\boldsymbol{\alpha}$	Angle at t = 0
$\boldsymbol{\beta}$	UMP damping coefficient
$\boldsymbol{\varepsilon}$	Degree of eccentricity
$\boldsymbol{\varepsilon_d}$	Degree of dynamic eccentricity
$\boldsymbol{\varepsilon_s}$	Degree of static eccentricity
$\boldsymbol{\Lambda}$	Magnetic permeance
$\boldsymbol{\rho}$	Charge density
$\boldsymbol{\tau}$	Pole pitch
$\boldsymbol{\omega_m}$	Rotor rotational frequency
$\boldsymbol{\omega}$	Angular frequency
$\boldsymbol{\sigma_E}$	Eddy current loss coefficient
$\boldsymbol{\sigma_{fric}}$	Friction loss coefficient
$\boldsymbol{\sigma_H}$	Hysteresis loss coefficient
$\boldsymbol{\gamma}$	UMP/torque Ratio
$\boldsymbol{\Phi}$, $\boldsymbol{\lambda}$	Magnetic flux
$\boldsymbol{\theta}$	Angle
$\boldsymbol{\varsigma}$	Skewing angle

1 Introduction

1.1 Background

In industrial applications, 35%-40% of the generated electrical energy is consumed by electrical motors [1]. Electrical motors are used in different types of applications, including pumps fans, mills, grinders, compressors, conveyors, and elevators. Within the industrial electrical motor applications, more than 90% of the motors are three-phase induction motors [2]. The popularity of induction machines is due to their robustness, high efficiency, and low cost. Despite the robustness of these induction machines, they are subjected to various types of failure, of which bearing failure is the most common failure [3]. The downtime of a machine could result in the loss of production and income [4]. Therefore, the importance of improving the induction machine reliability is highlighted.

A survey from the Institute of Electrical and Electronics Engineers (IEEE) had shown that the bearing failure accounted for 41% of all failures (see Figure 1-1) [5]. However, the percentage range of bearing failure can vary from 40% to 90%, depending on the type and size of the induction machine [3]. In the petrochemical industry, the bearing faults constitute 52% of the induction machine faults [6]. Bearing failure in the field survey for the US wind industry is 58%-70% for wind turbine generators with a power rating over 1 MW [7]; induction machines are the dominant type of technology used in medium and large wind turbines [8]. For the induction

machines used in military purposes, which are installed in warships, the bearing failures can go as high as 95% of the total failures because of high shock loading and harsh environments [9].

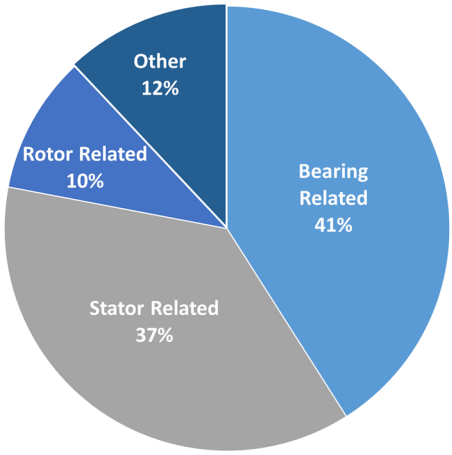

Figure 1-1: Failure distribution of the induction machine [5].

The causes of bearing failure can be distributed into: inappropriate lubrication of the bearing rolling element (80%), inadequate bearing selection (10%), improper mounting (5%), indirect failure (4%), and manufacturing error (1%) [10]. The inadequate bearing selection, improper mounting and manufacturing error can be categorised as human error which is not discussed in this thesis. Meanwhile, the indirect failure is caused by overloading, vibration, electric discharge, and temperature [11], in which UMP could be one of the contributing factors in the indirect failure.

As the inappropriate lubrication stands the largest percentage of bearing failures, the bearing lifetime would generally be affected by the minimum lubrication thickness and the lubrication regime would affect the bearing lifetime [12]. The fault tree analysis of the lubrication thickness and regime is shown in Figure 1-2, which shows the bearing load is one of the factors.

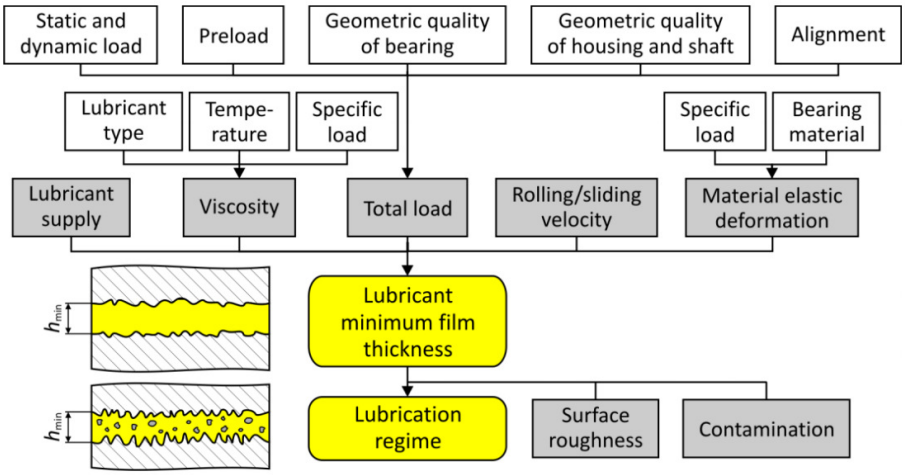

Figure 1-2: Factors that affect the lubrication film thickness and lubrication regime [12].

Although the machine can still be operated when its bearing is inappropriately lubricated, any additional loading could reduce the lubrication film thickness and lubrication regime, which reduces the bearing lifetime. It has been pointed out in [13] that 80% of mechanical faults lead to the rotor eccentricity in electrical machines. Any eccentricity in the machine will create excessive mechanical stress and cause more fatigue in the bearings [14]. In addition, the uneven magnetic flux distribution around the airgap of an eccentric rotor causes UMP, thus creating greater mechanical stress on the bearing. Subsequently, the UMP from the rotor shaft might accelerate wear on the bearing and cause greater rotor misalignment. Increasing misalignment could then further increase the UMP. This cycle continues until the bearing eventually fails. When a bearing fails, permanent damage to the machine may occur when the rotor bars collide with the stator.

1.1.1 Unbalanced Magnetic Pull

UMP is caused by the uneven distribution of the magnetic flux in the airgap which could be caused by winding faults, unbalanced three-phase supply, broken bars, etc. The focus of the thesis is on the UMP caused by rotor eccentricity. When the axial variation is not taken into consideration, there are two main types of rotor eccentricity which are the static and dynamic eccentricity.

In Figure 1-3(a), static eccentricity exists when the rotor rotates on its own axis, but not at the centre of the stator bore. The UMP caused by static eccentricity is a

constant force and a 2-times supply frequency force acting toward the direction of the narrowest airgap. The 2-times supply frequency force component is relatively small if compared to the constant force component, when the backward rotating flux is negligible [15]. In Figure 1-3 (b), dynamic eccentricity exists when the rotor rotates at the centre of the stator bore axis but not on its own axis. The minimum airgap rotates with the rotor rotating frequency. So, the UMP caused by dynamic eccentricity has the frequency of the rotor rotating frequency. Both of the static and dynamic eccentricity can exist together, which is referred to as, mixed eccentricity.

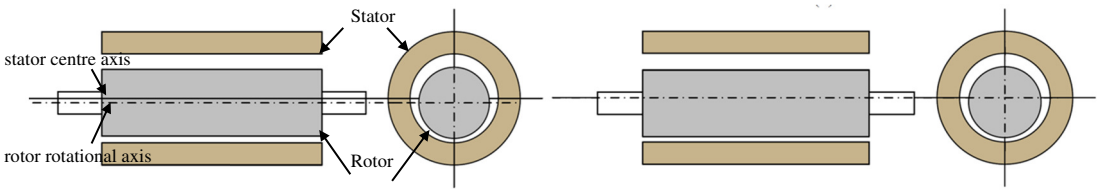

(a) (b)

Figure 1-3: The two main types of eccentricity: (a) static (b) dynamic.

While the constant UMP of static eccentricity acting in the same direction as the rotor weight, additional radial force is exerted on the bearing. That additional radial force would cause fatigue in the bearing and reduce the bearing lifetime. The greater radial force will also accelerate the severity of other mechanical faults. Furthermore, the efficiency of the machine is also reduced because of the additional bearing friction loss [16]. If the machines are coupled with other mechanical components, such as a gearbox, the UMP also affects the bearing lifetime of the gearbox, where the UMP amplifies the vibration of the gearbox. This is because the UMP reduces the overall system stiffness [17], [18].

With the constant UMP acting in the opposite direction, the load of the bearing will be reduced as there is a minimum load requirement for each bearing to ensure that the rolling element is tracked properly. Insufficient loading may lead to the skidding of the rolling element, which could then cause bearing failure [19].

Subsequently, for the dynamic UMP, whereby the minimum airgap changes the direction of the rotor position, it causes additional vibration in the machine. The

vibration of the machine depends on the natural frequency of the machine, in which the relationship between the rotational frequency and the vibration amplitude is non-linear [20].

1.1.2 Types of induction machines

Induction machines generally possess a relatively small airgap in order to minimise the magnetising current. The small airgap in the induction machines make them more susceptible to the UMP. This is because the magnitude of the UMP is a function of the degree of eccentricity, which is the ratio between the length of misalignment and the mean airgap length.

Categorising the type of induction machines based on the rotor configuration, the two types of induction machines are the cage rotor and the wound rotor induction machine. Although both types of induction machines work with the same concept, the cage rotor induction machine is more widely used. This is because the wound rotor induction machine has few significant disadvantages, namely: 1) frequent maintenance is required for the brushes and the collector rings of the wound rotor induction machine, 2) the insulation of the wound rotor is highly stressed by the heat dissipated and the centrifugal force, and 3) the external rotor resistance is hard to maintain [21].

However, wound rotor induction machines are popular in certain applications such as mills and cranes [22], in which a high starting torque is needed when there is no use of variable frequency drive (VFD). High starting torque can be achieved using higher external rotor resistance. In addition, speed control with a range of 0-10% below the synchronous speed can be achieved by varying the external resistance of the wound rotor induction machine, but this method is not very efficient, as more heat loss is caused by the external resistor [23].

The other advantage of the wound rotor induction machine is that the external component can be added to the rotor circuit, in which an additional voltage source can be connected to the wound rotor. This type of configuration is referred to as the doubly fed induction machine. Doubly Fed Induction Generator (DFIG) is widely used as the generator for a wind turbine, in which 48% of the overall offshore wind turbine is

accounted for [24]. The variation of speed depends on the power rating of the voltage supply of the rotor, in which the power rating of the converter is around 25% of the rated power [25].

1.1.3 Reducing UMP

As UMP causes an excessive bearing loading, this reduces the bearing lifetime. In addition, excessive loading also causes premature fatigue. Moreover, a weak plane inevitably exists in the material even if the material is 100% inclusion free and homogeneous [26]. For machines that are not heavily used, the bearing fatigue problem can be solved by choosing a stronger bearing to increase its lifetime. However, for heavily used machines, such as a renewable energy generator, which runs most of the year, the UMP will have a significant impact on the bearing lifetime. Many new types of enhanced bearing are designed for the harsh offshore environment and the high fatigue load, in which those bearings have a longer lifespan than the conventional one. Moreover, it is difficult to find the suitable bearing for those cases where the UMP is a few times the rotor weight.

In addition to enhancing the material of the bearing, reducing the UMP is key to prolonging the lifetime of the bearing. The most direct method to minimise bearing wear is to levitate the rotor shaft through magnetic bearing topology. Magnetic bearing topology is often used in high speed machines. The magnetic bearing could negate the radial force from the rotor. This might not only prevent bearing failure, but it may also reduce the bearing friction loss. However, the magnetic bearing requires additional windings and a control system which may be prone to failure and a whole new costly design is needed.

Due to the complexity of the magnetic bearing topology especially in a large machine where negating the UMP will be costly, the main suggestion proposed by this thesis is that instead of fully negating the UMP, the bearing lifetime can be prolonged through reducing the UMP. Therefore, the methods to reduce the UMP by using active control and the installation of damper windings are proposed in this thesis.

1.2 Research Methodology

The analyses of UMP were done by using analytical modelling, FEA modelling, empirical method, and experimental work. The modelling work is based on calculation of magnetic flux distribution in the machine to find the forces acting on the rotor. Time and space harmonics need to be considered in the analysis because the rotor MMF of the induction machine is induced by the stator flux. Also, rotor eccentricity causes the change of magnetic permeance, which produces additional magnetic flux space harmonics. Then, the forces exerted on the rotor at any instant of time can be calculated from the magnetic flux space harmonics distribution through the Maxwell Stress Tensor, in which the derivation had shown that UMP is produced by the interaction between each magnetic flux harmonics with its pole pair ± 1 magnetic flux.

The electromagnetic problems can be solved by analytical methods or numerical methods; the numerical method used in this thesis is the FEA. The main advantages of analytical methods are that they can be solved faster than the numerical methods. In addition, the analytical equation can aid clarity in the UMP analysis. Meanwhile, although solving machine geometry of induction machines with a small airgap is time consuming, the FEA method can model the complex physical geometry, so the magnetic saturation effect can also be taken into account.

Instead of solving the electromagnetic problems through theoretical models, empirical method is used to find the solutions based on statistical formulas, such as regression analysis, support vector machine method, chi-square analysis, random forest method and etc., in which the empirical model is developed based on the collected data. As some of the parameters used in the UMP analytical model are hard to be obtained, an empirical method is proposed in the thesis to calculate the UMP; the empirical model is built based on the theoretical study of UMP.

Although modelling of electrical machine is based on a physical system, works need to be done to verify the reliability of the model. In this thesis, experimental works were performed to validate both the FEA and the analytical model. During the experiment, static eccentricity was created after disassembling the stator and the rotor

of the induction machine. Instead of measuring the magnetic flux distribution to calculate UMP, the UMP is directly measured from the force plate, which is placed under the stator. As the experimental work is prone to various errors, preventive steps need to be taken to improve the accuracy of the experimental results.

1.3 Aims and Objectives

This project has several distinct objectives:

1. To investigate the cause of the UMP and to simplify the UMP calculation method.
2. To find the UMP for different type of rotor eccentricity.
3. To apply a control methodology on induction machines to reduce the UMP.
4. To develop a new set of winding configurations to reduce the UMP of a wound rotor induction machine.

To accomplish the above objectives, the work was divided into three key stages:

- Analysis of the magnetic flux caused by an eccentric rotor. This stage analyses the spatial harmonics flux around the airgap and its contribution towards the UMP. UMP from the static, dynamic and axial-varying static eccentricity are investigated on a cage rotor induction machine.
- Analysis of the optimum operating rotor slip. The simplified mathematical equation is developed to generalise the UMP of the induction machine. From this, the optimum rotor operating slip is investigated.
- Experimental evaluation. An induction motor using the proposed control strategy was tested. Conclusions are drawn regarding the effectiveness of the proposed methodology.

1.4 Thesis Outline

Chapter 2 reviews the work done by other researchers. The factors that affect the UMP are discussed. Comparisons between different methods of UMP analysis are done.

Chapter 3 presents the airgap magnetic flux of an eccentric rotor. The airgap magnetic flux information is essential in calculating the UMP. The UMP calculation is derived from the Maxwell Tensor Stress. Then, the FEA and experimental setup are shown.

Chapter 4 analyses the damping effect from the parallel circuit connection of the cage rotor bar. A damping coefficient is introduced for the UMP calculation. This has been verified by the FEA and the experimental model. Skewed rotor and axial-varying eccentricity are discussed and are simulated by using a multi-slice, 2-dimension FEA method. Then, power losses due to rotor eccentricity are discussed.

Chapter 5 presents the empirical method in order to estimate the UMP of both static and dynamic eccentricity. An UMP/Torque ratio is introduced to find the operating slip with the lowest UMP.

Chapter 6 shows the slip control method that reduces the UMP. The Matlab/Simulink model is used and is verified with the experimental results. Then, a new damper windings configuration for the wound rotor induction machine is also proposed.

An overview of the theoretical and experimental work is presented in Chapter 7. The main conclusions are drawn and discussed. Finally, future work and proposals are suggested.

1.5 Contribution to Knowledge

This thesis can be divided into two main parts, which are the calculation of UMP and the methods to reduce UMP.

During the first part of the thesis, the main challenges of UMP calculation in induction machines are the estimation of the higher harmonics flux that crosses the airgap and the calculation of the counteracting flux produced by the circulating current

in the rotor bars. The numerical methods have often been used by other researchers to solve the problems in the UMP calculation. However, solving the numerical problem is time-consuming; high computational power is needed. Therefore, a UMP Damping Coefficient is proposed to calculate the damping of UMP caused by the counteracting flux. In addition, an empirical method is proposed to estimate the higher harmonics flux for the UMP calculation. The empirical method is based on the proposed UMP Damping Coefficient and the categorisation of the magnetic flux across the airgap. With the proposed empirical method, a real-time UMP estimation may be feasible.

During the second part of the thesis, a damper winding configuration and slip control method are proposed to reduce UMP. The damper winding method has been previously proposed by other researchers in order to reduce the UMP of electrical machines. However, the winding configuration is rather complex and it could only damp the magnetic flux from a specific space harmonics. Hence, a simplified configuration is proposed for the machine with an even pole-pair number. Meanwhile, the slip control method can be achieved by varying the magnetising flux so that the machine could operate at the slip with the lowest UMP. The lowest UMP will exist at a particular slip, because of the nonlinear UMP-slip characteristic of induction machines.

My research project is funded by the Institute of Energy System (IES) at the University of Edinburgh. As one of the main research directions of IES is on tidal and wave renewable energy, works had been done to reduce the bearing failure in generators [27]. This is because bearing failure is one of the major issues when the generators operate in a harsh environment. The researches that had been done in the IES related to bearing failure include, the selection of bearing for wave and tidal application [28], minimising the bearing loading [29], and fatigue lifetime prediction [30]. Most of the work done in IES is on the linear generator and permanent magnet machine [31], [32], [33]. Therefore, my research's project is mainly focused on the induction machines to fill the knowledge gap in the group. Additionally, the proposed UMP calculation through empirical methods and the UMP reduction methods can also be used on the other types of generators.

1.6 List of Publications

I. H. Chuan and J. K. H. Shek, "Reducing Unbalanced Magnetic Pull of an induction machine through active control," *IET International Conference on Power Electronics, Machines and Drives*, Glasgow, 2016, pp. 1-6.

II. H. Chuan, J. K. H. Shek, "Minimising Unbalanced Magnetic Pull in Doubly Fed Induction Generators," *IET conference on Power Electronics, Machines and Drives*, Liverpool, 2018, pp. 1-6.

III. H. Chuan, J. K. H. Shek, "Calculation of unbalanced magnetic pull in induction machines through empirical method," *IET Electric Power Application*, 2018 [early-accessed].

IV. H. Chuan, J. K. H. Shek, "Unbalanced Magnetic Pull Damping Effect in Squirrel Cage Induction Machines," submitted to IEEE Energy Conversion

2 Literature Review

2.1 Rotor Eccentricity

Rotor eccentricity may occur in most electrical machines, even in newly manufactured machines [34], in which the small degree of eccentricity might be caused by the manufacturing tolerance. Typically, static eccentricity is caused by the stator core ovality or incorrect positioning of the rotor and the stator at the assembling stage [35]. Meanwhile, dynamic eccentricity is caused by a bent shaft, mechanical resonances at critical speed and bearing wear [36].

A small degree of static eccentricity occurs in the assembly stage and does not change with time if the rotor shaft assembly is sufficiently stiff [35]. In [37], the author states that the high UMP from static eccentricity could cause shaft flexing and dynamic eccentricity. Therefore, mixed eccentricity often co-exists in reality. The UMP has a snowball effect that will worsen over time. It may further end up causing rubbing of the stator and rotor that could damage the whole machine.

In addition, a non-constant eccentricity along the axial direction has been discussed in several papers [38], [39], [40]. Inclined eccentricity or axial-varying eccentricity assumes that the rotor does not bend and that the eccentricity changes linearly along the axial direction (see Figure 2-1(a)). For axial-varying eccentricity, an average eccentricity value is used for the UMP calculation. In [41], the author

discusses the curved dynamic eccentricity where axial direction changes are not linear due to bending of the rotor shaft, which is shown in Figure 2-1(b). In solving the axial-varying cases, a multi-slice 2D-FEA is used by most researchers.

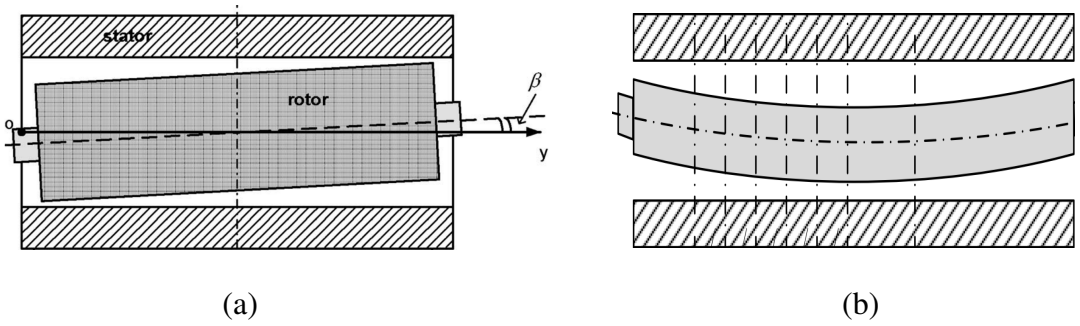

(a) (b)

Figure 2-1: (a) Axial-varying eccentricity of a straight rotor [38]. (b) Curve dynamic eccentricity [41].

In a three-phase supply with unbalanced voltage, the negative sequence voltage in the system produces a backward rotating flux that causes a torque pulsation at twice the supply frequency [42]. With the occurrence of rotor eccentricity, the backward rotating flux creates an additional 2-times supply frequency UMP [40]. In addition, the current unbalance is 6 to 10 times larger than the voltage unbalance [43]. A higher current will also produce higher airgap leakage flux, which in turn produces a higher UMP.

2.2 Slot Harmonics

Magnetic flux spatial harmonics caused by the stator and rotor slots produce unwanted effects such as crawling, locking, magnetic noise, vibration, and ripple [44]. In addition, the presence of the stator and rotor slots also causes additional UMP. In [45], the authors states that the rotor differential flux harmonics are mainly produced by the slot magnetomotive force (MMF). The slot permeance variation has little effect on the slot harmonics flux. However, the variation of slot permeance creates additional UMP. The vibration frequency is a function of the number of rotor and stator slots, and the rotating speed [46]. The vibration force produced by the slotting effect has a higher frequency. Resonance will occur when the vibration frequency approaches the

magnitude of either the stator core or stator tooth, which could amplify the vibration [47]. As FEA is commonly used to calculate the magnetic flux from the slotting harmonics, comparison of airgap flux calculated by the analytical model and FEA is made in [48], which is shown in Figure 2-2.

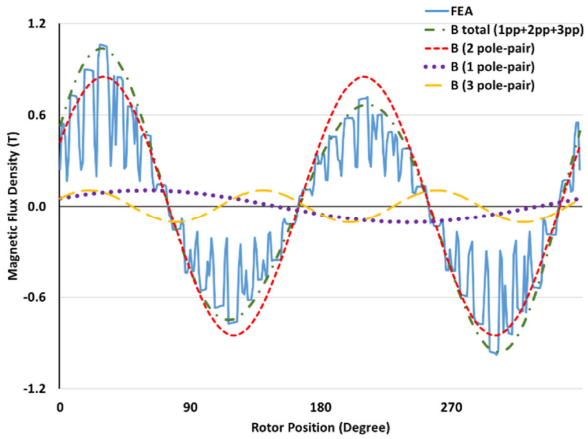

Figure 2-2: Magnetic flux in the airgap [48].

However, Dorrell pointed out that the vibration caused by the slotting effect can be neglected in the UMP analytical calculation for induction machines, since the slotting does not generate a substantial UMP [40]. Although the vibration caused by the slotting effect can be neglected, Dorrell demonstrated that the higher order space harmonics flux is caused by the stator and rotor slots harmonics, which are dominant in the high slip region [49]. In [50], the author demonstrated that the UMP difference with and without slotting effects is 4% for the 2-pole induction machine. The contribution of the slot harmonics of an eccentric rotor on the UMP is also discussed in [51]. By using FEA, the authors demonstrated that closing the rotor or stator slots could not reduce the UMP of an eccentric rotor. A further attempt at increasing the rotor slot number resulted in a 12% reduction in the UMP. Furthermore, a 2-pole induction machine is more vulnerable to the UMP oscillation because the sideband of the slot harmonics is separated by only two spatial harmonics, where the interaction might happen between the additional pole-pair flux of each sideband [52].

According to [53], a skewed rotor design was implemented to reduce the vibration of the machine. The best skewing factor to reduce the stator slot flux harmonics is one stator slot pitch. When the rotor slots are skewed, the rotating

magnetic flux from the stator can evenly distribute around the rotor regardless of the stator slots. However, the downside of rotor skewing is that the skewed rotor will produce larger UMP when eccentricity occurs in the rotor. In [54], the author shows that the parallel rotor bar can damp most of the UMP from the stator flux for a cage rotor without skewing. For a skewed cage rotor, the coupling between the stator and the rotor is reduced. Therefore, a skewed rotor amplifies the machine UMP because the stator flux cannot be completely damped by the cage rotor.

2.2.1 Knowledge gap in calculating the airgap magnetic flux

As the UMP is caused by the uneven distribution of magnetic flux around the airgap, understanding the magnetic flux that crosses the airgap is key in calculating the UMP in induction machines. Other than the magnetic flux with fundamental pole pair harmonics, the magnetic flux with belt and slot harmonics are the two main harmonics groups that contribute to the magnetic flux in the airgap. Both types of harmonics are a function of the number of slots.

Most literature has pointed out that the magnetic flux with higher space harmonics contributes to the UMP. However, the UMP caused by the higher harmonics flux is not comprehensively discussed. One of the reasons is the higher harmonics flux that crosses the airgap is highly dependent on the parameters and the design of the machine. Therefore, the higher harmonics flux that crosses the airgap is difficult to calculate using analytical model.

As the purpose of finding the higher harmonics flux is to calculate and to understand the UMP in the machine, instead of specifically finding the higher harmonics inductance, an empirical method is proposed to acquire the UMP caused by the higher harmonics flux. By using the FEA or experimental results, the parameters for the UMP calculation can be found with the proposed empirical method [48].

2.3 Method to Calculate the UMP

The uneven distribution of the magnetic flux can be caused by an eccentric rotor, stator and rotor slots, unbalanced supply voltage, stator or rotor ovality, or

winding fault. Different methods have been used to calculate the magnetic flux distribution, which can be further extended to calculate the UMP. The focus of this thesis is on the UMP caused by the rotor eccentricity.

2.3.1 Analytical modelling

UMP has been investigated for many years. The first paper that addresses this issue dates back to 1918 [55], where the unbalanced magnetic flux density is used to calculate the force exerted on the rotor. Then, a set of linear UMP equations were introduced by Robinson for low degrees of eccentricity [56]. Robinson further pointed out that the vibration caused by rotor eccentricity is twice the line voltage frequency. The UMP calculation using the rotating magnetic flux theory is then discussed in [57]. The author found that a vibration of twice the supply frequency is caused by the different rotating components in the machine. His work is further investigated by [58], [59], [60]. Finally, the damping effect from the parallel circuit of the cage rotor was observed in [61].

The magnetic permeance harmonic analysis is presented in [62]. The airgap permeance is expressed as a Fourier Series, which is used to modulate the MMF around the airgap. The generalised harmonic analysis was introduced by Williamson [63] and was used to find the coupling impedance of each circuit. Current information can be found after the voltage information is known. The conformal transformation was presented in [64], which involves transforming two eccentric circles into two concentric rotors, and, the symmetrical windings are transformed into an asymmetrical winding. Dorrell then combined both the generalised harmonic analysis and the conformal transformation [65] to calculate the UMP of the induction machine with parallel winding connections.

In addition to that method, the Modified Winding Function Analysis (MWFA) can be used to find the winding inductance of a machine with an eccentric rotor, where the magnetic characteristic is assumed linear [66], [67], [68]. The airgap flux can then be calculated with the inductance of both stator and rotor windings. Meanwhile, the saturation effect is considered in the MWFA by [69]. To improve the accuracy of

calculation, the saturation effect needs to be considered especially for a machine with a higher degree of rotor eccentricity because the stator teeth around the narrowest airgap are vulnerable to core saturation.

2.3.1 FEA modelling

FEA is a numerical method that subdivides the geometry of the problem into smaller parts to find a solution. FEA is used to calculate the magnetic flux distribution in the machine. Subsequently, the Maxwell Stress Tensor method is used to calculate the radial force exerted on the rotor [70]. The finite element is first brought up to be used to simulate an induction motor with an eccentric rotor [71], in which equalising current in the parallel windings caused by the additional pole pair ± 1 flux can be simulated by the FEA. DeBortoli further compared the airgap flux between the eccentric rotor and the concentric rotor by using the Fast Fourier Transform to examine the harmonics component of the airgap flux.

Most small and medium sized induction machines have a skewed rotor. The change in axial direction could not be assumed constant for a skewed rotor. 2D skewed rotor simulation is conducted in [72] by splitting an induction machine into several slices; the rotor of each slice is shifted with an angle. Then, the winding of each slice is linked with series circuit connections, resulting in the current in each slice is the same.

The frequency response function analysis was introduced in [73] to analyse the UMP caused by rotor whirling motion. A rotor whirling motion can be defined as the rotor that remains at the centre of the stator bore, but the centre axis of the rotor travels around the centre of the stator in a circular orbit with a certain frequency, which is illustrated in Figure 2-3. Therefore, the rotor whirling frequency is the rotational frequency of the rotor centre axis. Since the time-stepping FEA is time-consuming for simulating the UMP at each whirling frequency, an impulse method is introduced to shorten the computational time [74]. When using the impulse method in FEA, the rotor is moved away from its centre position for a short period of time. This rotor movement produces UMP, which representing the UMP due to the rotor whirling motion.

Analysing the rotor whirling motion through the impulse method could reduce the simulation time by 95%.

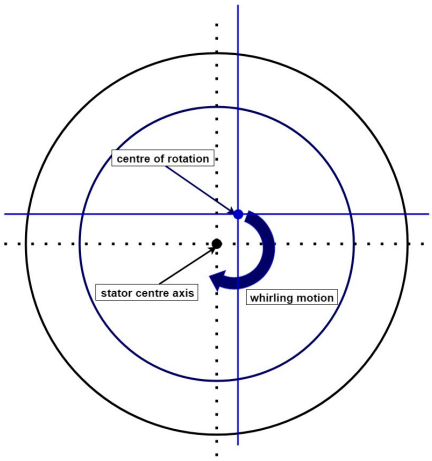

Figure 2-3: Illustration of the rotor whirling motion.

2.4 Homopolar Flux

The homopolar flux issue was first brought up in [75]. The homopolar flux is the flux that crosses the airgap once, and the return path of the flux will then pass through the end cap of the machine back to the stator or rotor. The flux path of the homopolar flux is illustrated in Figure 2-4. The homopolar flux exists in most eccentric rotors, especially in the 2-pole machine, where the homopolar flux is caused by the first permeance harmonics of the asymmetric airgap. As the pole pair number increases, the homopolar flux becomes negligible [65]. The homopolar flux is also negligible in a 2D analysis because the homopolar flux relies on the flux path between the stator and rotor.

A homopolar flux experiment was conducted in [76]. The author explained that the homopolar flux causes the 2 times supply frequency UMP oscillation. The 2 times supply frequency is caused by the interaction between the forward and backward rotating flux with a pole pair number difference of 1 in the airgap due to an oscillating uneven magnetic flux. In the case of the presence of the homopolar flux, the interaction with the 2-pole flux also causes an oscillation in the airgap. Furthermore, in [77], the author experimentally demonstrated that the 2 times supply frequency oscillation

could be reduced by removing the end cap. This can further prove that the homopolar flux causes the 2 times supply frequency.

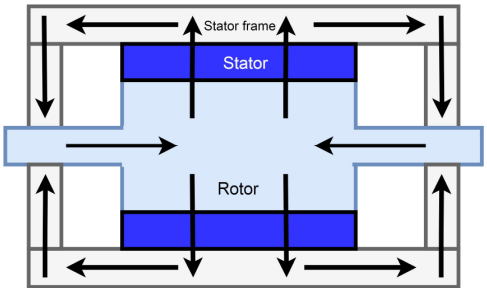

Figure 2-4: Homopolar flux path.

2.5 Bearing Failure

After presenting the concept of UMP in the previous sub-chapters, the impact of UMP on the bearing is discussed here. The main causes of bearing failure include: lubrication failures, misalignment, overheating, excessive load, normal fatigue failure, tight and lose fit, true and false brinelling, contamination, and corrosion [78]. Bearing discharge current is also another cause of bearing failure in electrical machines [79]; inverter-fed electrical machines are more likely to suffer as a result of bearing currents [80]. The bearing failures are categorised into single point defects and generalised roughness fault [81]. A single point defect is a localised defect on a surface. A common cause for this type of defect is the existence of pit or spall. For a generalised roughness fault, the condition of the bearing is degraded over a large area and becomes rough or deformed. This type of fault is usually caused by a lack of lubricant, or the existence of contamination.

Although there are many causes that lead to bearing failure, 80% of mechanical faults will cause an eccentric rotor to occur [13], hence, UMP will occur due to most mechanical faults in electrical machines. When the bearing is overloaded, this increases the probability of premature failure. Premature failure is due to the contact pressure between the rolling element and the bearing raceway, which is higher than the material yields strength [82]. As UMP causes additional radial load on the bearing, UMP will cause excessive bearing wear [83]. The authors in [84] had also

pointed out that the rotor eccentricity causes additional mechanical stress, which leads to more rubbing and fatigue on the ball bearing.

Even at normal operating condition in a healthy machine, fatigue failures may also occur [85]. It was noted in [86] that a rotating bearing has a limited lifetime because of the probability of subsurface initiated fatigue spall. In [87], the authors pointed that the rolling contact fatigue of rolling element bearing is a statistical phenomenon which is influenced by the material microstructure that possesses a heterogeneous nature. The fatigue spall may occur on the balls, the inner ring or the outer ring. Although rolling contact fatigue causes fatigue spall, the spall does not always stop the bearing from running. The fatigue failure progression is illustrated in Figure 2-5. In the continued operation of a bearing with fatigue spall, the dynamic loading caused by the contact with the rough spall surface is the main contributing factor that limits the remaining useful life [88].

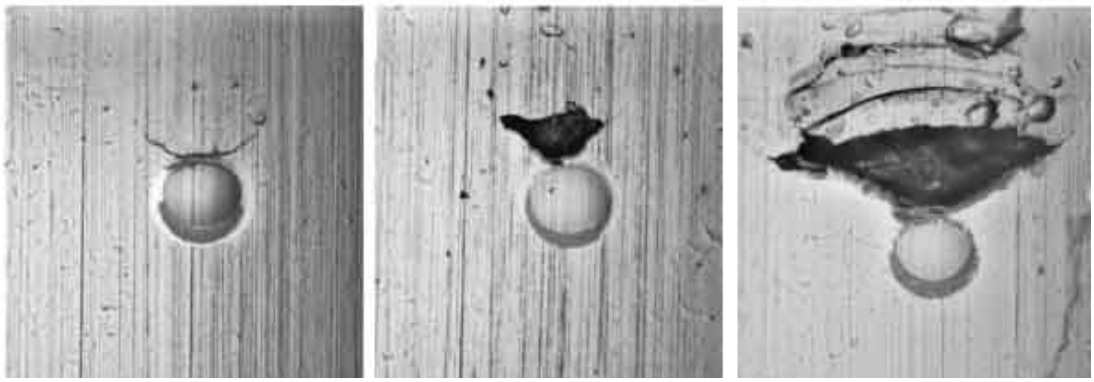

(a) (b) (c)

Figure 2-5: Progression of the surface fatigue in ball bearings (a) begins with a v-shaped spall (b) the spall grows in the rolling direction (c) material started to flake away from the surface [89].

2.6 Methods of Reducing UMP

UMP can be reduced to prolong the bearing lifetime in induction machines. The eccentric rotor produces additional magnetic permeance that causes the unsymmetrical distribution of the magnetic field around the airgap. As the UMP is caused by the uneven distribution of the airgap flux, the reduction of the UMP can be achieved by evening out the airgap flux distribution. The methods to achieve a more

even distribution of the airgap flux can be divided into two main categories, namely passive methods and active control.

2.6.1 Passive methods

Passive methods are used to reduce the UMP without any detection and input control signals. Different passive methods have previously been investigated. The main concept of passive methods is to introduce a parallel path connection in the machine in order to induce an equalising current that produces a counteracting flux to reduce the UMP by evenly distributing the flux. However, the downside of having a parallel winding connection is that the backwards rotating flux may exist due to the induced voltage being unbalanced. This backwards rotating flux could create a vibrating component at twice the supply frequency.

A parallel connection can occur in either the stator windings or rotor windings. For the rotor winding parallel connection configuration, the cage rotor bar is naturally parallel connected, and the wound rotor is series connected. Therefore, Bradford has shown that the cage rotor motor has 80% lesser UMP than the wound rotor induction motor [90]. Moreover, when the whirling frequency of the rotor rotates near the pole pair ± 1 flux frequency, the UMP of the machine will be higher because the flux could not be damped by the rotor [91].

For the cage rotor induction machine, the damping effect is only significant for the fundamental pole pair ± 1. The damping effect from the rotor MMF is negligible at start-up because the rotor could not damp the higher order space harmonics airgap flux [49]. In addition, in [92], the author mentioned that the UMP can be significantly damped when the number of parallel circuits is higher. Furthermore, the increment of the rotor slots number could also reduce the magnitude of the rotor differential flux because the average current flowing in each bar is reduced. The FEA results to prove this statement are shown in [51].

As the cage rotor already has many parallel circuits, the stator windings parallel connection is more effective in damping the UMP in a wound rotor induction machine because most of the pole pair ± 1 flux frequency is not damped. Therefore, the

additional parallel path in the stator can help damp the UMP [93]. In [94], the parallel path connection in the stator winding could damp the cage rotor induction machine at every whirling frequency including the pole pair ± 1 flux frequency. The damping of the higher space harmonic is also shown in this paper, but the damping effect is not as significant as the damping of the fundamental pole pair ± 1 flux.

Installing an extra damper winding is another method to reduce the UMP. The auxiliary windings can be installed at the stator, to solve the wound rotor UMP problem. The damper windings are often placed in a synchronous machine to help the machine start and reduce oscillations [95]. Dorrell has compared both cage rotor and wound rotor induction machines with an extra damper winding of pole pair ± 1 towards the main winding [96]. The results show a significant UMP decrease in the wound rotor induction machine because the wound rotor does not have a parallel path to damp the UMP. Dorrell also stated that damper winding would not have a significant effect on torque production in the case of the low degree of eccentricity. An external 4-pole winding has also been installed on a 2-pole machine in [97]. The author shows that 90% of the UMP can be damped, which was experimentally verified. However, the damping effect for both cases are pole specific, meaning that the uneven higher space harmonics flux could not be damped by the damper winding.

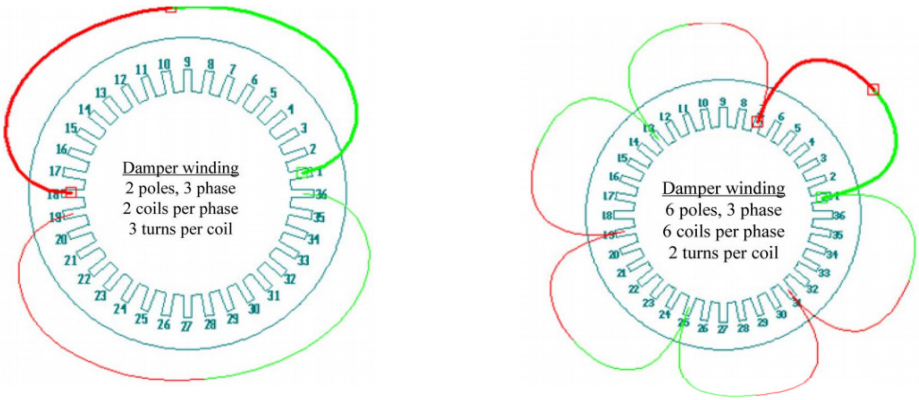

(a) (b)

Figure 2-6: (a) 1 pole pair (b) 3 pole pair damper winding in a 2 pole pair induction machine [96].

2.6.2 Active control

The UMP is described as the net radial force exerted on the rotor. In order to reduce the UMP, the key is to control the radial force exerted on the machine. Although not specifically designed to control the UMP, magnetic bearing topologies can be used to control the radial force. The machine with magnetic bearing is not only used to produce a force to levitate the rotor weight, but it is also used to control the rotor to be at the centre and rotating at the centre of the stator axis, in which no UMP is produced.

The dual windings scheme for magnetic bearings is more commonly discussed. For this scheme, an additional winding is installed to create a radial force. The installed windings need to be either pole pair $+1$ or pole pair -1. The magnetic bearing can be used in both the salient pole rotor and the cylindrical rotor [98], [99]. The key to controlling the rotor to be at the centre of the stator bore is knowing the permeance function of the machine and the flux distribution in the airgap. By using this information, the current required to levitate the rotor can be calculated. In [100], an additional 2 pole winding was wounded on a 4 pole machine. When the fundamental flux interacts with the pole pair flux of difference by 1, a radial force is produced which can offset the rotor weight and achieve magnetic bearing application. In [101], the author has designed the magnetic bearing configuration the other way round, where the 2 pole winding is the main winding, and the 4 pole pair winding produces the levitation force.

In conclusion, if the main goal is to completely eliminate the UMP, additional windings with a control topology are needed in order to produce the pole pair ± 1 flux, which generates a force to negate the UMP. This is because the pole pair ± 1 flux could not be generated through the original machine windings. Furthermore, the magnetic bearing can reduce the friction loss of the induction machine. The friction loss caused by the additional UMP can also be reduced when the UMP is reduced. However, additional losses from the levitation current are produced [101].

2.6.3 Knowledge gap in reducing the UMP

For reducing UMP through passive methods, although the damping of the parallel windings had been discussed and used by many researchers, the damping effect is not explicitly investigated. In this thesis, the UMP analytical model is developed to show the UMP damping effect. In addition, a UMP Damping Coefficient is introduced to simplify the UMP calculation for steady state operation [48]. The understanding of the damping effect can help in reducing the UMP or designing the induction machines.

Meanwhile, Dorrell had proposed installing the damper winding in wound rotor induction machines which could significantly reduce the UMP of the machines. However, the two sets of damper windings with different pole pair number are needed to be installed, which increases the complexity of in the machine windings. Therefore, by using the same concept proposed by Dorrell, a new set of damper windings configuration is proposed [102].

For reducing UMP through active control methods, additional sets of windings are required to produce the pole pair ± 1 flux to reduce UMP. In this case, the induction machine needs to be redesigned to accommodate the additional windings. For example, 10% of the original stator slot is used to wind the auxiliary windings, which reduces the power density of the machine [103]. Furthermore, an additional control is needed for the auxiliary windings to produce the counteracting flux. Therefore, instead of completely negating the UMP, a slip control method is proposed in this thesis to reduce the UMP [104]. The minimum UMP will exist at a certain slip due to the non-linear UMP-slip characteristic in induction machines. Hence, the induction machines can be controlled to operate at the optimum slip to reduce the UMP.

2.6.4 Reducing the UMP by using slip control method

To control the rotor slip, a variable frequency drive is needed. Although only around 20% of the induction machines are supplied with a variable frequency drive [105], nearly 90% of the electric motor drive systems in industrial application is the cage rotor induction machines. Previous research and development has improved the

efficiency of induction machines through slip optimisation [106], [107]. The increase in efficiency is achieved by changing the magnetising flux of the machine, so that the copper losses and the iron losses can be balanced. Also, the low power factor problem of a lightly-loaded induction machine can be solved by using the slip control method [108], in which reactive power is varied with the changing of active power.

Slip control not only improves the efficiency of the induction, but can also be used to reduce the UMP. Reducing UMP through the slip control method can be achieved by balancing the UMP caused by the magnetising flux and the UMP caused by the higher space harmonics flux. The UMP reduction percentage of a machine is based on the machine's optimum operating slip and the load of the machine. Each machine has its own optimum operating slip in minimising the UMP, which is machine-parameters dependent.

The UMP caused by the magnetising flux is much larger than the UMP caused by the higher harmonics flux when the machine operates close to its synchronous speed. Then, loading the machine would increase the UMP caused by the higher harmonics flux. Therefore, the freedom of balancing the UMP caused by both type of flux reduces as the slip increases, in which the percentage of UMP reduction decreases when the load increases. This method is more effective in reducing UMP when the induction machine is lightly loaded [48]. When implementing the slip control method on a specific application, the average load factor of the induction machines need to be evaluated. In the European Union, the average load factor of industrial and tertiary usage is around 57%; the average load factor of some industries can be as low as 25% [2]. Hence, reducing the UMP by using the slip control method could potentially be implemented in some of the industries.

2.7 Eccentricity Detection

Rotor eccentricity detection is important in calculating UMP, because UMP is a function of the airgap magnetic flux, rotor eccentricity, and the machine's dimensions. As the machine dimensions are fixed and the airgap magnetic flux can be

calculated from the voltage and current, knowing the rotor eccentricity will help to estimate the UMP in induction machines.

Traditionally, condition monitoring is achieved by using sensors and physical hardware to identify the fault [109]. For complex cases, the traditional approach has many limitations. It is difficult for the traditional approach to detect a fault in advance. One particular sensor used is the search coil, which consists of coils with a number of turns to measure the magnetic field variation passing through the coil. It can be used to detect the rotor slot number [110]. From the rotor slot frequency, the rotor speed can be estimated. The limitation in speed estimation by using the search coil is the lower speed limit, because the signal becomes insignificant when the rotor frequency drops.

In [111], the authors proposed a method to measure the eccentricity by using a search coil in PWM-inverter fed motors. The reason of using a search coil instead of the current detection method is because the high harmonic content produced by the inverter would affect the current waveform. Using a search coil to detect eccentricity is also shown in [112]. The authors conducted both experimental and simulation work with external search coils to detect static eccentricity.

Motor's current signature analysis (MSCA) was first implemented for rotor eccentricity detection in [35]. The purpose of condition monitoring through the electrical side is to implement a low cost detection method. The presence of static eccentricity can be estimated by checking the current frequency components caused by the eccentric rotor. For axial-varying eccentricity cases, the magnitude of the MCSA detection is the same as static eccentricity with constant axial eccentricity, where the average eccentricity of the axial-varying eccentricity equals the constant-axial static eccentricity [38].

In [113], the author shows that additional current frequency occurs when both static eccentricity and dynamic eccentricity exist. Static eccentricity and dynamic eccentricity have a cross coupling effect which can produce a current frequency to detect rotor eccentricity. The mixed eccentricity case is further analysed by using

MWFA in [67]. Experimental work and simulation work with different rotor bars has also been carried out by [114].

The limitations of MCSA include the eccentric airgap flux that needs to be the harmonics of the main pole-pair number in order to detect the frequency components of the current. Nandi has further suggested a new current detection method by changing the voltage spectra at switch-off [37]. This technique can be used on all numbers of cage rotor bars, but is only suitable for a moderate level of rotor eccentricity.

Furthermore, cases with low average static eccentricity are difficult to identify with traditional MCSA because there is other noise, such as the bearing vibration and additional stress on the bearing may affect the current waveform [38]. The offline eccentricity rotor monitoring method is discussed in [115]. The main concept is to use the inverter for exciting the motor with a small pulsating AC field superimposed on a DC field whenever the motor is at a standstill. The change in the pattern of differential inductance versus the DC-field level has been observed as an indicator of eccentricity.

2.8 Overview

As mentioned, rotor eccentricity may still occur even in a newly manufactured induction machine due to the mechanical tolerance. In addition, 80% of mechanical fault in induction machines lead to the occurrence of rotor eccentricity. The UMP causes additional mechanical loading on the bearing, which reduces the bearing fatigue life.

Permeance harmonics analysis and FEA are commonly used to investigate the airgap flux. Due to the complexity of machine geometry, FEA is good in finding the UMP caused by the higher harmonics flux. In addition, FEA can accurately calculate the effect of circulating current. However, FEA requires high computational power. Hence, new empirical method is proposed in this thesis to solve the problem.

Due to the parallel winding in the induction machines that produces counteracting flux to reduce the UMP, the cage rotor induction machine has a much lower UMP than the wound rotor induction machine. Therefore, the installation of damper windings has been proposed by Dorrell in order to reduce the UMP in wound rotor induction machines, in which the counteracting flux produced by the damper winding could damp the pole pair ± 1 magnetic flux. A new damper windings configuration based on this idea is also proposed in this thesis.

For reducing the UMP through active control, it has been shown in the magnetic bearing topology that either the pole pair $+1$ or -1 flux is produced by the auxiliary windings to create a radial force on the rotor. Therefore, a slip control method is proposed in the thesis to reduce the $+1$ or -1 flux of the fundamental magnetising flux, which will reduce the UMP.

3 Analytical Framework for UMP Evaluation

It is known that the uneven magnetic flux distribution around the airgap will cause UMP. Therefore, the information of the magnetic flux distribution is essential to calculate the UMP. For analytical modelling, the permeance harmonics method is commonly used to calculate the magnetic flux distribution around the airgap. Assumptions had been made to simplify the analytical calculations for the rotor with a low degree of rotor eccentricity. The Maxwell Stress Tensor is then applied on the magnetic flux harmonics to calculate the UMP. The airgap flux distribution is verified by using FEA. Next, the magnetic flux distribution for different rotor eccentricity is investigated by using a blank rotor where the flux distribution will not be influenced by the zigzag leakage flux. The percentages of the pole pair ± 1 magnetic flux is investigated and compared for different rotor eccentricity. Finally, UMP results from both FEA and experimental work are compared.

3.1 Magnetic Permeance

Permeance harmonics method is applied to calculate the magnetic flux distribution of a rotor with eccentricity, as it had been used by Dorrell [92]. The magnetic flux distribution around the airgap can be analysed by breaking down the magnetic flux into a series of space and time harmonics. Time harmonics are not the

primary concern for UMP calculation, because the changes of magnetic permeance does not affect the time harmonics of the magnetic flux. The calculation of UMP caused by dynamic eccentricity has the same derivation as the static eccentricity, in which it is modelled in the rotor rotating reference frame.

For a concentric rotor, the magnetic flux density around the airgap can be written as [104]:

$$B(\theta, t) = \sum_{p=-\infty}^{\infty} \boldsymbol{B} cos(\omega t + p\theta) d\theta \tag{3-1}$$

$$\boldsymbol{B} = \frac{\mu_e \mu_0 J}{l_m p} \tag{3-2}$$

where $\boldsymbol{B}$ is the magnetic flux density, θ is the rotor angle, t is the time, ω is the angular rotating frequency, p is the pole pair number, J is the current density, l_m is the magnetic path length, and μ_e is the effective permeability. The magnitude of the magnetic flux density is determined by the current density and the machine parameter, as shown in (3-2). The effective permeability of the magnetic flux line is shown:

$$\mu_e = \frac{\mu_r}{1 + \mu_r(\frac{g}{l_m})} \tag{3-3}$$

For the magnetic flux flowing in the iron core without saturation, the magnetic permeability of the iron core (μ_r) is assumed to be much higher than the permeability of the air. Therefore, the magnetic permeability from (3-3) can be simplified to:

$$\mu_e = \frac{l_m}{g} \tag{3-4}$$

Substituting (3-4) into (3-2), the magnetic flux path length is cancelled. The overall permeability becomes (3-4). This also shows that the magnetic permeability is inversely proportional to the airgap length.

3.1.1 Airgap length calculation

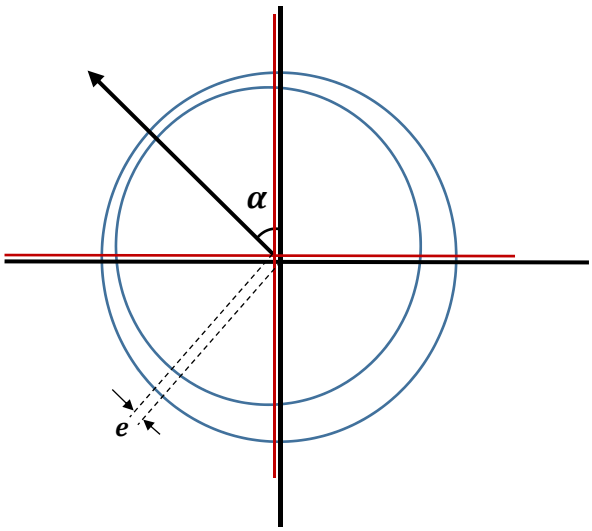

Figure 3-1: Cross section of an eccentric rotor.

Figure 3-1 shows the cross section of machine with rotor eccentricity. The angle α is the angle of the narrowest airgap. Assuming that rotor eccentricity is small if it is compared to the radius of the rotor, this means that the angle perpendicular to the eccentricity angle has the same airgap as an ideally positioned concentric rotor. The airgap length derivation is shown in Appendix C [15].

From Figure 3-1, the red axis is the centre axis of the rotor, the black axis is the centre axis of the stator, and e is the movement of the rotor that causes rotor eccentricity. The calculation of the airgap for an eccentric rotor, g', is:

$$g'(\theta, t) = g_0(1 - \varepsilon cos(\theta - \alpha)) \tag{3-5}$$

where g_0 is the mean airgap length and α is the angle of the eccentricity's direction. The degree of eccentricity, ε, is the ratio between the mean airgap length and the length of the eccentric rotor misalignment, e. The degree of eccentricity can be written as:

$$\varepsilon = \frac{e}{g_0} \tag{3-6}$$

The degree of eccentricity and the angle of the narrowest airgap from (3-5) is a function of both the static and dynamic eccentricity, which is shown in Figure 3-2.

The rotor eccentricity caused by the static and dynamic eccentricity are shown individually. In all the variables of the equations, the subscript "s" is for static eccentricity and "d" is for dynamic eccentricity. The airgap of the rotor with static eccentricity is:

$$g_s'(\theta,t) = g_0(1 - \overline{\varepsilon_s} cos(\theta - \alpha_s)) \tag{3-7}$$

The dynamic eccentricity is a function of the rotor rotating frequency, resulting the narrowest airgap to change in time and space. The airgap of a rotor with the dynamic eccentricity can be written as (3-8), where ω_r is the angular frequency of the rotor.

$$g_d'(\theta,t) = g_0(1 - \overline{\varepsilon_d}\, cos(\omega_r t + \theta - \alpha_d)) \tag{3-8}$$

To acquire the overall eccentricity, the vector of the static and dynamic eccentricity need to be added together. An example of the vector summation is shown in Figure 3-2, in which the direction of the dynamic eccentricity is a function of the rotational frequency, ω_r.

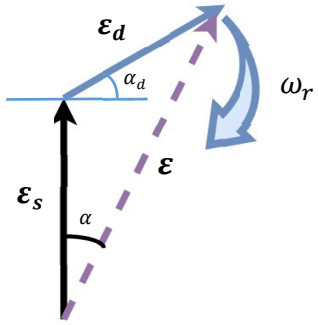

Figure 3-2: Vector summation of the degree of static and dynamic eccentricity.

Choosing the angle of the static eccentricity as the zero reference point:

$$\alpha_s = 0 \tag{3-9}$$

The overall degree of eccentricity can be written in (3-10), which is the vector summation of the degree of static and dynamic eccentricity. The α_d in (3-10) refers to the angle that is relative to the angle of static eccentricity at $t = 0$.

$$\varepsilon = \sqrt{(\overline{\varepsilon_s} + \overline{\varepsilon_d}\cos(\omega_r t - \alpha_d))^2 + \left(\overline{\varepsilon_d}\sin(\omega_r t - \alpha_d)\right)^2} \tag{3-10}$$

As the angle of the narrowest airgap is also a function of time and rotating frequency, the angle of the overall eccentricity will change if dynamic eccentricity exists. The angle of the narrowest airgap can be derived as:

$$\alpha = \tan^{-1}\frac{\overline{\varepsilon_s} + \overline{\varepsilon_d}\cos(\omega_r t - \alpha_d)}{\overline{\varepsilon_d}\sin(\omega_r t - \alpha_d)} \tag{3-11}$$

After applying trigonometry simplification on (3-11):

$$\alpha = \left(\tan^{-1}\frac{\overline{\varepsilon_s}}{\overline{\varepsilon_d}\sin(\omega_r t - \alpha_d)}\right) + \frac{1}{2}\pi - \omega_r t - \alpha_d \tag{3-12}$$

Referring to (3-12), the angle of the narrowest airgap for a mixed eccentricity case is a function of the rotational speed and the ratio between the static and the dynamic eccentricity. The angle of the narrowest airgap of the machine does not change linearly with time.

3.1.2 Magnetic permeance calculation

As the stator and rotor core are assumed to have infinite permeability, all the MMF of the magnetic circuit drops across the airgap. Therefore, the magnetic permeance of the machine is the inverse of airgap. Equation (3-13) shows the magnetic permeance, Λ, for an eccentric rotor case [15].

$$\Lambda = \frac{\mu_0}{g'(\theta, t)} = \frac{\mu_0}{g_0(1 - \varepsilon cos(\theta - \alpha))} \tag{3-13}$$

From [141], the Fourier Series expansion from (3-13) is shown in (3-14) and (3-15).

$$\Lambda_n = \frac{\mu_0}{g_0} \sum_{n=-\infty}^{\infty} \varepsilon^n cos^n(\theta - \alpha) \tag{3-14}$$

$$\Lambda_n = \frac{\mu_0}{g_0\sqrt{1-\varepsilon^2}} \left[1 + 2 \sum_{n=1}^{\infty} \left(\frac{1-\sqrt{1-\varepsilon^2}}{\varepsilon} \right)^n cos(n(\theta - \alpha)) \right] \tag{3-15}$$

where n is the permeance harmonics number. The normalised magnetic permeance magnitude of the constant to 4th harmonics are shown in Figure 3-3. The normalised magnitude of the magnetic permeance is found by dividing (3-15) with the magnetic permeance of a concentric rotor.

Figure 3-3 shows that the magnitude of all the magnetic permeance harmonics increases with the rotor eccentricity. For the degree of eccentricity below 0.2, the first permeance harmonic had shown the most significant increment as the degree of eccentricity increased. Hence, assumptions are made to simplify the analytical calculation for low degree of eccentricity, which is shown in Sub-section 3.1.3.

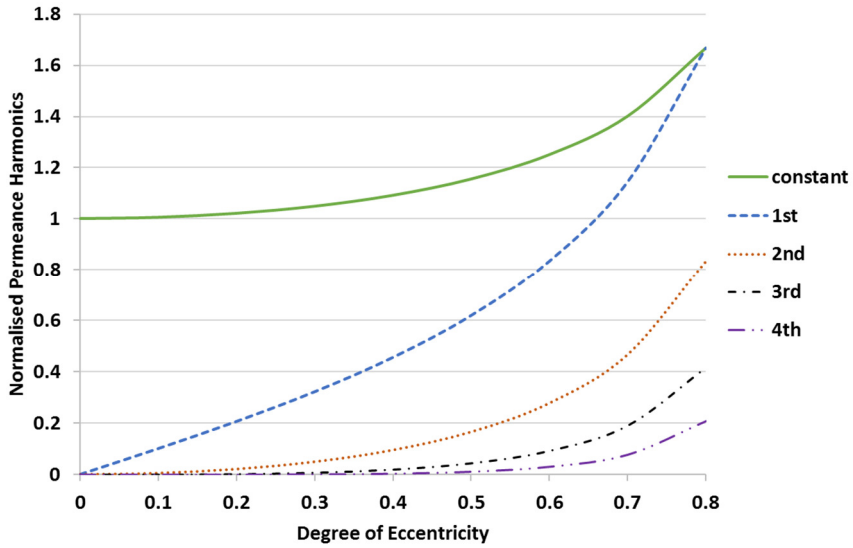

Figure 3-3: Normalised permeance harmonic versus degree of eccentricity.

The increment of the overall magnetic permeance harmonics means that less magnetising current is needed to produce the magnetic flux of the machine with the constant excitation voltage. However, the leakage inductance is also increased with the increment of eccentricity which is an unwanted scenario. Moreover, higher magnetic flux on the side with the narrowest airgap in the machine may cause magnetic

saturation in the iron core, especially at the tooth region. This magnetic saturation will reduce the iron core permeability. The iron core permeability cannot be neglected from the effective magnetic permeability formula in (3-3).

3.1.3 Assumptions

Two assumptions are made in this Sub-section to simplify the UMP analytical calculation for a low degree of eccentricity. The relationship between the magnetic permeance harmonics and the UMP is shown in (3-16), which is based on, 1) the magnitude of the magnetic permeance harmonics is linearly proportional to the magnetic flux, and 2) the UMP is proportional to the multiplication of each pole pair harmonics flux with its ± 1 sideband flux.

$$UMP \propto \sum_{n=1}^{\infty} \Lambda_n \Lambda_{n+1} \tag{3-16}$$

The results from the generalised calculation of UMP based on (3-16) is shown in Table 3-1. The contribution of the constant and the first normalised permeance harmonics toward the UMP calculation is compared with the contribution of all normalised permeance harmonics toward the UMP calculation.

Degree of Eccentricity	Contribution from all permeance harmonics	Contribution from constant and first permeance harmonic	Difference (%)
0	0.000	0.000	0.000
0.1	0.051	0.050	0.501
0.2	0.107	0.105	2.020
0.3	0.177	0.169	4.606
0.4	0.271	0.248	8.348
0.5	0.413	0.357	13.393
0.6	0.651	0.521	19.978
0.7	1.120	0.801	28.491
0.8	2.300	1.389	39.623

Table 3-1: Comparison of results with and without the assumption.

Table 3-1 shows that the difference between two cases is relatively small when the degree of eccentricity is below 0.2 (2%). In addition, the relationship of the first harmonics component and the degree of eccentricity is shown in Table 3-2.

Degree of Eccentricity	Magnitude of First Permeance Harmonic	Difference (%)
0	0	0
0.1	0.1007	0.7563
0.2	0.2062	3.1036
0.3	0.3218	7.2996
0.4	0.4554	13.861
0.5	0.6188	23.764
0.6	0.8333	38.889
0.7	1.1436	63.379
0.8	1.6667	108.33

Table 3-2: Assumption of the linear relationship between first permeance harmonic and degree of eccentricity.

Table 3-2 shows that the magnitude of the first permeance harmonic can be assumed to be equal to the degree of eccentricity for low degree of eccentricity UMP calculation; the error is 3% when the degree of eccentricity is 0.2. Combining both assumptions, the error is 6% when the degree of eccentricity is 0.2. From here, two assumptions can be made to simplify the model of low degree of eccentricity:

- Only the interaction between the constant component and the first permeance harmonic component is taken into account for the UMP calculation if the degree of eccentricity is lower than 0.2.
- The magnitude of the first magnitude permeance harmonic component is equal to the magnitude of the degree of eccentricity

These assumptions for low degrees of rotor eccentricity have also been used by many researchers to simplify the UMP calculation and to aid in the clarity of the analytical model [51], [116], [117].

3.1.4 Magnetic flux around the airgap

The magnetic flux around the airgap can be found by multiplying the magnetic permeance with the MMF around the airgap [15]:

$$B_p\ (\theta, t) = \Lambda_n \mathrm{J} \tag{3-17}$$

By applying the assumption in Sub-section 3.1.3, the magnetic flux distribution for static and dynamic eccentricity are analysed separately. Equation (3-18) shows the magnetic flux around the airgap for the static eccentricity.

$$\begin{aligned} B_{p,s}(\theta, t) &= \mathrm{J}\, cos(\omega t + p\theta) \times \Lambda_0\big(1 + \varepsilon_s cos(\theta - \alpha_s)\big) \\ &= B_p cos(\omega t + p\theta) + \frac{1}{2} B_p \varepsilon_s \cos(\omega t + (p-1)\theta - \alpha_s) \\ &\quad + \frac{1}{2} B_p \varepsilon_s \cos(\omega t + (p+1)\theta - \alpha_s) \end{aligned} \tag{3-18}$$

Equation (3-19) shows the magnetic flux around the airgap for the rotor with dynamic eccentricity, in which the rotating frequency is added into the equation, and α_d is the rotor position when $t = 0$.

$$\begin{aligned} B_{p,d}(\theta, t) &= \mathrm{J}\, cos(\omega t + p\theta) \times \Lambda_0\big(1 + \varepsilon_d cos(\theta - \alpha_d + \omega_r t)\big) \\ &= B_p cos(\omega t + p\theta) \\ &\quad + \frac{1}{2} B_p \varepsilon_d \cos((\omega - \omega_r)t + (p-1)\theta + \alpha_d) \\ &\quad + \frac{1}{2} B_p \varepsilon_d \cos((\omega + \omega_r)t + (p+1)\theta - \alpha_d) \end{aligned} \tag{3-19}$$

The formulas in (3-18) and (3-19) are applicable for all the magnetic flux space harmonics. Both equations show that the additional pole pair ± 1 flux exists in an eccentric rotor. The magnitude of the additional flux is half of the original flux multiplied with the degree of eccentricity.

3.2 Winding Harmonics

In an ideal case, the stator and rotor airgap MMF are assumed to be a pure sinusoidal waveform. However, in a real case scenario, the stator and rotor windings are discretised, which affects the MMF to be a step-sine wave. An example of the MMF distribution at an instant of time is shown in Figure 3-4.

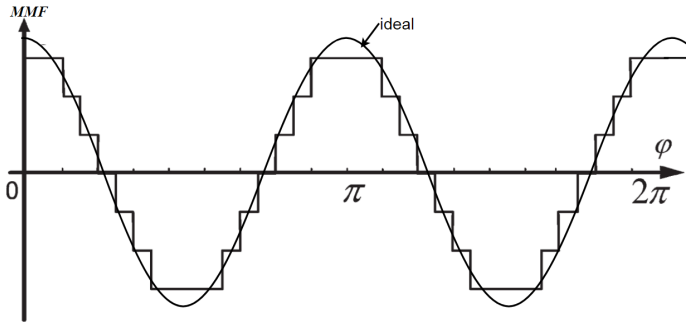

Figure 3-4: Comparison between ideal MMF and discretised MMF.

The MMF step waves can be analysed through Fourier series analysis, which divides the waves into a series of higher harmonics sine waves. For a machine with symmetrical geometry, the MMF with even space harmonics is zero. In addition, the summation of the three-phase MMF of a balanced three-phase voltage source will also nullify the magnetic from the 3rd harmonic group. The harmonics orders in the airgap are shown in (3-20).

$$n = 2mv \pm 1 \,, where\ v = 1, 2, 3 \ldots \tag{3-20}$$

Distributed windings are used in the induction motors. The harmonics of the airgap flux depends on the winding distribution. Single and double layers winding are commonly used in the stator winding design. The magnetic flux for each harmonic is [118]:

$$\Phi_n = \frac{2}{\pi} B_n \frac{\tau}{n} L \tag{3-21}$$

The induced EMF for each harmonic is:

$$\mathrm{E}_n = -\sqrt{2}\pi N_1 . k_{w,n}(nf)\Phi_n \tag{3-22}$$

The winding factor ($k_{w,n}$) is introduced as a ratio between the magnetic flux of the specific winding design with the single-layer full pitch non-skewed integer slot winding with the same number of turns and slots per pole per phase [119]. The winding factors are the product of the pitch factor (k_p), distribution factor (k_d), and the skewed factor (k_{sk}).

$$k_{w,n} = k_p . k_d . k_{sk} \tag{3-23}$$

The pitch factor is the vector sum of the induced EMF of two sides of the coil which is shown in Figure 3-5, where E is the EMF produced by one coil, E_R is the resultant EMF, n is the space harmonics number, and θ_c is the angle difference between the EMF of the calculated coil and the full-pitch coil. (3-24) shows the formula for the pitch factor. The maximum pitch coil factor is seen when the angle difference is 180^o where it is the full pitch coil.

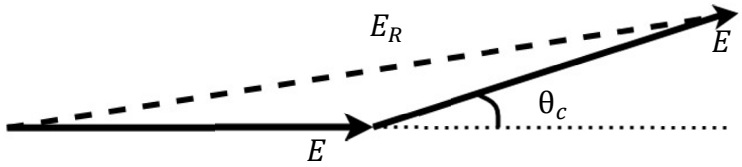

Figure 3-5: Resultant EMF of a short pitch coil.

$$k_p = \cos\left(\frac{n}{2}\theta_c\right) \tag{3-24}$$

The distribution factor is the ratio of the actual voltage obtained to the possible voltage of a concentrated coil in a single slot. The distribution factor is illustrated in Figure 3-6, where the magnitude and the direction of the arrows represent the vector of the EMF. The formula of the ratio can be written as (3-25), where m is the number of slots per pole per phase and q is the number of slots per pole. The maximum distribution factor could be achieved if a concentrated coil is used, where all the coils are bunched in one slot. However, the distribution of the coils needs to be placed in adjacent slots to achieve a smoother sinusoidal wave in the airgap.

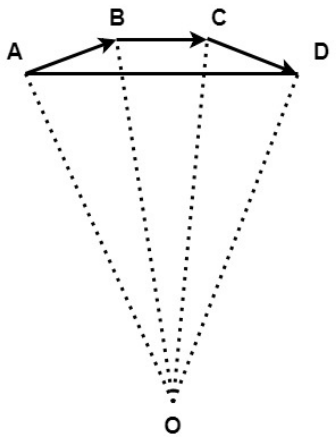

Figure 3-6: Phasor summation of the EMF in the distributed winding.

$$k_d = \frac{EMF\ induced\ in\ distributed\ winding}{EMF\ induced\ in\ the\ concentrated\ winding}$$

$$= \frac{Phasor\ summation\ of\ the\ EMF}{Arithmetic\ summation\ of\ the\ EMF}$$

$$= \frac{\overrightarrow{AB} + \overrightarrow{BC} + \overrightarrow{CD}}{\overrightarrow{AD}}$$

$$k_d = \frac{\sin\left(m\frac{\pi}{2q}\right)}{m\sin\left(\frac{\pi}{2q}\right)} \quad (3\text{-}25)$$

Then, the skew factor needs to be taken into account when an angular twist on the stator or rotor is applied. The skew factor is the ratio of the EMF induced in a skew conductor to the EMF induced in a non-skewed conductor. A skewed rotor is often used in a cage rotor induction machine. One of the purposes in skewing a rotor is to reduce the side effect from the stator slots harmonic flux, in which the angular shift in the rotor bar could reduce the induced EMF from the stator slot harmonics flux. To completely negate the effect from the stator slot flux harmonics, the rotor can be skewed by a stator slot pitch. The skew factor is shown in (3-26), where ς is the skewing in electrical angle.

$$k_{sk} = \frac{\sin\left(n\frac{\varsigma}{2}\right)}{n\frac{\varsigma}{2}} \quad (3\text{-}26)$$

For the 2D simulation, the skew factor is not under consideration. Therefore, it is assumed that the skew factor is 1. The winding factor for each machine in the thesis is shown in Table 3-3.

Harmonic / Machine	1st	5th	7th	11th	13th
1, 3	0.96	0.22	0.18	0.18	0.67
2	0.95	0.23	0.64	0.75	0.42
4	0.97	0.26	0.26	0.97	0.97

Table 3-3: Different harmonics of the winding factor for each induction machine.

3.3 Carter Factor

The airgap variation from the slot openings could not be neglected because the airgap in an induction machine is small. The slot opening causes the changes in the airgap magnetic permeance.

The stator slot opening can cause vibration but it has little influence on the UMP created by the rotor eccentricity [40]. Therefore, the vibration UMP caused by the stator slots opening is not considered in the thesis. However, the stator slot opening can cause the increment of the effective airgap [118]. To obtain the effective airgap length, the Carter Coefficient is applied on the original airgap, which is shown in (3-27). The Carter Coefficient is a simplified ratio of the effective airgap length and the original airgap length [120]. The increment of an effective airgap will affect the degree of eccentricity calculation from (3-6).

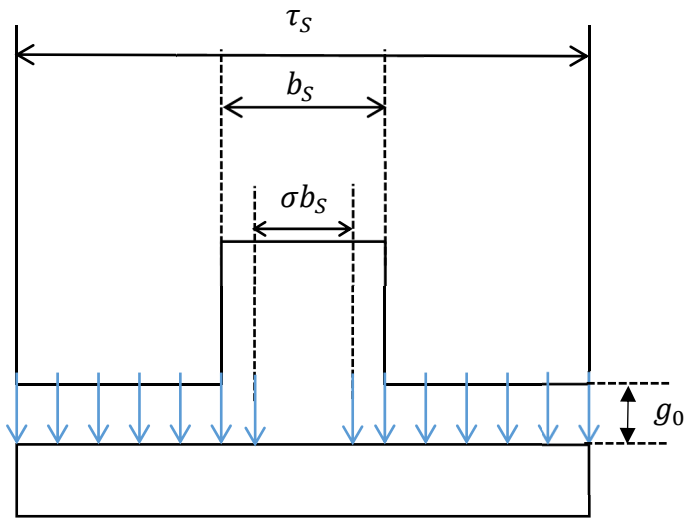

Figure 3-7: Distribution of airgap magnetic flux in a stator slot pitch span.

$$g_0{}^{eff} = k_C\, g_0 \tag{3-27}$$

$$k_C = \frac{\tau_S}{\tau_S - \sigma b_S} \tag{3-28}$$

Equation (3-28) shows the Carter Factor. As σb_S in (3-28) is a positive value, the Carter Factor is a number that is larger than one. From (3-27), the effective airgap length is the product of the Carter Factor with the mean airgap length. Therefore, slot opening will increase the effective airgap length. As the magnetic flux crossing from the stator slot is relatively smaller than the stator teeth, the variable σ is applied to the length of the slot opening length. The reduction ratio σ is derived as:

$$\sigma = \frac{\frac{b_S}{g_0}}{5 + \frac{b_S}{g_0}} \tag{3-29}$$

3.4 UMP Calculation

After understanding the magnetic flux density around the airgap, the UMP can be calculated by finding the force around the rotor or the stator with Maxwell Stress Tensor [92]. The Maxwell Stress Tensor expression for the normal force acting on the round surface is shown in (3-30), and the tangential force is shown in (3-31).

$$\sigma_n = \frac{{b_n}^2 - {b_t}^2}{2\mu_0} \tag{3-30}$$

$$\sigma_t = \frac{b_n b_t}{\mu_0} \tag{3-31}$$

The tangential component of the Maxwell Stress Tensor is used in torque calculation. When the machine is running at no load, the b_t is almost zero, so it is negligible [93]. Even when the machine runs at full load, b_t is also much lower than b_n. This is because the induction machine has a small airgap and the permeability of the stator and rotor iron core is higher than the airgap. So, most of the flux crosses the airgap normally. As the b_t and b_n in the normal stress component shown in (3-30) has a power of 2, the b_t can be neglected when $b_t << b_n$.

The UMP can be calculated by integrating the Maxwell Stress Tensor around the airgap [92]:

$$UMP = \int_0^{2\pi} \int_0^L \sigma_n \, r \, d\theta dL \tag{3-32}$$

Let the UMP component exerted on the rotor to be divided into X- and Y-axis components, the Y-axis component is:

$$UMP^y = \int_0^L \int_0^{2\pi} \sigma_n \, r \, cos\theta \, d\theta dL \tag{3-33}$$

The X-axis component is:

$$UMP^x = \int_0^L \int_0^{2\pi} \sigma_n \, r \, sin\theta \, d\theta dL \tag{3-34}$$

Equations (3-33) and (3-34) show the surface integration around the rotor surface. The $cos\ \theta$ and $sin\ \theta$ show the direction of the magnetic flux. The UMP for static eccentricity in the Y-axis direction derivation is shown in (3-35) to (3-38):

$$UMP_s{}^y = \frac{rL}{2\mu_0}\int_0^{2\pi}\Big(\boldsymbol{B}cos(\omega t + p\theta) + \frac{1}{2}\boldsymbol{B}\varepsilon\cos(\omega t + (p+1)\theta + \alpha_s) + \frac{1}{2}\boldsymbol{B}\varepsilon\cos(\omega t + (p-1)\theta + \alpha_s)\Big)^2\cos(\theta)\,d\theta \tag{3-35}$$

$$= \frac{rL}{2\mu_0}\int_0^{2\pi}\Big[\frac{1}{2}\boldsymbol{B}^2cos^2(\omega t + p\theta) + \frac{1}{2}\varepsilon^2\boldsymbol{B}^2cos^2(\omega t + (p+1)\theta + \alpha_s) + \frac{1}{2}\varepsilon^2\boldsymbol{B}^2cos^2(\omega t + (p-1)\theta + \alpha_s) + \varepsilon\boldsymbol{B}^2cos(\omega t + p\theta)cos(\omega t + (p+1)\theta + \alpha_s) + \varepsilon\boldsymbol{B}^2cos(\omega t + p\theta)cos(\omega t + (p-1)\theta + \alpha_s) + \frac{1}{4}\varepsilon^2\boldsymbol{B}^2cos(\omega t + (p+1)\theta)cos(\omega t + (p-1)\theta)\Big]\cos(\theta)\,d\theta \tag{3-36}$$

The 1st, 2nd, 3rd and 6th components in (3-36) are zero after integration:

$$UMP_s{}^y = \frac{rL}{2\mu_0}\int_0^{2\pi}\Big[\frac{1}{2}\varepsilon\boldsymbol{B}^2cos(2\omega t + (2p+1)\theta + \alpha_s) + \frac{1}{2}\varepsilon\boldsymbol{B}^2cos(-\theta - \alpha_s) + \frac{1}{2}\varepsilon\boldsymbol{B}^2cos(2\omega t + (2p-1)\theta + \alpha_s) + \frac{1}{2}\varepsilon\boldsymbol{B}^2cos(\theta + \alpha_s)\Big]\cos(\theta)\,d\theta \tag{3-37}$$

The 1st and 3rd components in (3-37) are zero after integration:

$$UMP_s{}^y = \frac{rL}{2\mu_0}\int_0^{2\pi}[\varepsilon\boldsymbol{B}^2cos(\theta + \alpha_s)]\cos(\theta)\,d\theta$$

$$= \frac{rL}{2\mu_0}\int_0^{2\pi}\frac{1}{2}[\varepsilon\boldsymbol{B}^2(\cos(\alpha_s) + \cos(2\theta + \alpha_s)]\,d\theta$$

$$= \frac{\pi rL}{2\mu_0}\varepsilon\boldsymbol{B}^2\cos(\alpha_s) \tag{3-38}$$

Derivations from (3-35)-(3-38) only consider the interaction between the magnetic flux with the same rotating direction. For the interaction between the opposite rotational flux, (3-37) becomes:

$$UMP_s{}^y = \frac{rL}{2\mu_0}\int_0^{2\pi}\Big[\frac{1}{2}\varepsilon \boldsymbol{B}^2 cos\big((2p+1)\theta+\alpha_s\big)+\frac{1}{2}\varepsilon \boldsymbol{B}^2 cos(2\omega t-\theta+\alpha_s) + \frac{1}{2}\varepsilon \boldsymbol{B}^2 cos\big((2p-1)\theta+\alpha_s\big)+\frac{1}{2}\varepsilon \boldsymbol{B}^2 cos(2\omega t+\theta+\alpha_s)\Big]\cos(\theta)\,d\theta$$

$$= \frac{\pi rL}{2\mu_0}\varepsilon \boldsymbol{B}^2\cos(2\omega t+\alpha_s) \tag{3-39}$$

The total UMP is contributed by the magnetic flux from each space harmonic, as shown in (3-40)-(3-43). The Y-axis UMP for static eccentricity:

$$UMP_s{}^y = \frac{\pi rL}{2\mu_0}\sum_{p=1}^{\infty}\varepsilon \boldsymbol{B_p}^2[\cos(\alpha_s)+\cos(2\omega t+\alpha_s)] \tag{3-40}$$

The X-axis UMP for static eccentricity:

$$UMP_s{}^x = \frac{\pi rL}{2\mu_0}\sum_{p=1}^{\infty}\varepsilon \boldsymbol{B_p}^2[\sin(\alpha_s)+\sin(2\omega t+\alpha_s)] \tag{3-41}$$

The Y-axis UMP for dynamic eccentricity:

$$UMP_d{}^y = \frac{\pi rL}{2\mu_0}\sum_{p=1}^{\infty}\varepsilon \boldsymbol{B_p}^2[cos(\omega_r \mathrm{t}+\alpha_r)+cos(2(\omega+\omega_r)\mathrm{t}+\alpha_d)] \tag{3-42}$$

The X-axis UMP for dynamic eccentricity:

$$UMP_d{}^x = \frac{\pi rL}{2\mu_0}\sum_{p=1}^{\infty}\varepsilon \boldsymbol{B_p}^2[sin(\omega_r \mathrm{t}+\alpha_r)+sin(2(\omega+\omega_r)\mathrm{t}+\alpha_d)] \tag{3-43}$$

The α_s and α_d are the summations of the angle between the narrowest airgap and the angle between the $B^{p\pm1}$ with B^p when $t=0$. If there is no interaction between the rotor and stator flux, the $B^{p\pm1}$ is always in-phase with B^p when $t=0$. The interaction between stator and rotor flux is discussed in the Sub-section 4.1.1.

From (3-40)-(3-43), the UMP can be divided into two parts: constant component and 2-times supply frequency component. The constant component of the UMP is caused by the interaction between two magnetic flux with the same rotational direction. The 2-times frequency component is produced by the interaction between two fluxes with the opposite rotational direction. If the entire magnetic circuit in the induction machine is series connected, the fundamental backwards rotational flux will be damped.

3.5 Finite Element Method

3.5.1 Introduction

FEA calculates electromagnetic problems through subdividing the geometry of the induction machine into smaller parts, which is called as finite elements. This process is time-consuming and requires significant computational power. An electrical machine involves interchanging electrical energy and mechanical energy. The relationship is explained by Maxwell's equation which is used in FEA to find the approximate solutions for the discretised finite elements. The set of four Maxwell's equations is shown in (3-44)-(3-47) [121].

Faraday's law of Induction:

$$\nabla \times \boldsymbol{E} = -\frac{\partial \boldsymbol{B}}{\partial t} \tag{3-44}$$

Ampere's Circuital Law:

$$\nabla \times \boldsymbol{B} = \mu_0 \left(\boldsymbol{J} - e_0 \frac{\partial \boldsymbol{E}}{\partial t} \right) \tag{3-45}$$

Gauss's Law:

$$\nabla \cdot \boldsymbol{E} = -\frac{\rho}{e_0} \tag{3-46}$$

Gauss's Law of Magnetism:

$$\nabla \cdot \boldsymbol{B} = \boldsymbol{0} \tag{3-47}$$

For Ampere's circuital law in (3-45), the displacement current is neglected for the electrical machine simulation, because the electromagnetic propagation is neglected where the electromagnetic field is quasi-static. From (3-47), the magnetic potential, $\boldsymbol{A}$, is introduced where the divergence of the curl of a vector becomes zero. This relationship can be written as [121]:

$$\boldsymbol{B} = \nabla \times \boldsymbol{A} \tag{3-48}$$

The electromagnetic quantities are related to the material properties. Equation (3-49) shows the magnetic properties and (3-50) shows the electrical properties.

$$\boldsymbol{B} = \mu\, \boldsymbol{H} \tag{3-49}$$

$$\boldsymbol{J} = \sigma\, .\boldsymbol{E} \tag{3-50}$$

Equation (3-49) and (3-50) are used to find the magnetic field intensity and the current density of the material. From (3-48), the Faraday's Law of Induction can be simplified into (3-51).

$$\boldsymbol{E} = -\frac{\partial \boldsymbol{A}}{\partial t} + \nabla\, \boldsymbol{U} \tag{3-51}$$

3.5.2 Simulation setup

For solving the induction machine problem, two types of conductors are used in the FEA modelling: 1) A solid conductor (the conductive material is in the computational domain, which is used for cage rotor bars), and 2) a stranded conductor (the current is assumed to be evenly distributed along the coil, which is used in the stator winding of both type of induction machine and also the rotor winding of wound rotor induction machine). The current density formula is based on the type of conductor, which is shown in (3-52) and (3-53) [122].

Stranded conductor: $\boldsymbol{J} = \frac{N\, I}{S_a}$ (3-52)

Solid conductor : $\boldsymbol{J} = -\boldsymbol{\sigma}\frac{\partial \boldsymbol{A}}{\partial t} + \boldsymbol{\sigma}(\nabla\, \boldsymbol{U})$ (3-53)

As the rotor current of the induction machine is induced by the stator flux and the existence of parallel paths in the induction machine, a time-stepping simulation is chosen to simulate the dynamic behaviour of the induction machine. This is because the static simulation or time harmonics simulation could not be precisely used to calculate the UMP. Open source software, such as FEMM, is not suitable to acquire the UMP. Therefore, an alternative software, Infolytica MagNet was used for the FEA simulations. The time-stepping simulation can calculate all the steady-state solution, which also includes the non-sinusoidal profile affected by the machine's geometry [123]. As an eccentric rotor causes uneven airgap that causes more harmonic contents of magnetic flux in the airgap, the time-stepping simulation is used in all the simulations to calculate the fundamental and the harmonic field distribution.

The 2D FEA analysis is used in this thesis. It is assumed that the Z-axis, which is the machine axial direction, is constant. The main advantage of using 2D FEA is to reduce the computational time. A longer computational time is needed for simulating a machine with rotor eccentricity because rotor eccentricity could not be analysed by using the symmetrical characteristics, in which a fraction of the whole machine is analysed in the symmetric machine. This is because the asymmetrical airgap causes additional magnetic flux harmonics induced in the rotor.

However, the end winding resistance and reactance are not accounted for the 2D FEA. Therefore, end winding resistance and inductance need to be added to the circuit as a lumped resistance and inductance to improve the accuracy. Other than this, the skewed cage rotor effect cannot be introduced into the 2D FEA. To simulate a skewed cage rotor more accurately, a multi-slice 2D FEA method is used. The rotor angle is different for each slice, but the rotor circuit for every slice is connected.

For the meshing of the FEA, the size of the mesh depends on the geometry and the material complexity. The airgap has the smallest mesh size because of the high energy stored. As the rotor is a moving part and the stator is a stationary part, the continuity of vector potential between the interfaces of the stator and the rotor needs to be created [124]. The airgap needs to be re-meshed at every time step in order to solve the problem.

To reduce the computational time, the moving-band technique is used, in which an additional layer is added in between the stationary part and the rotational part. Therefore, the airgap is divided into 3 sections which is shown in Figure 3-8. The moving band layer is re-meshed for every single position, which prevents the whole airgap re-meshed every time step when the rotor rotates.

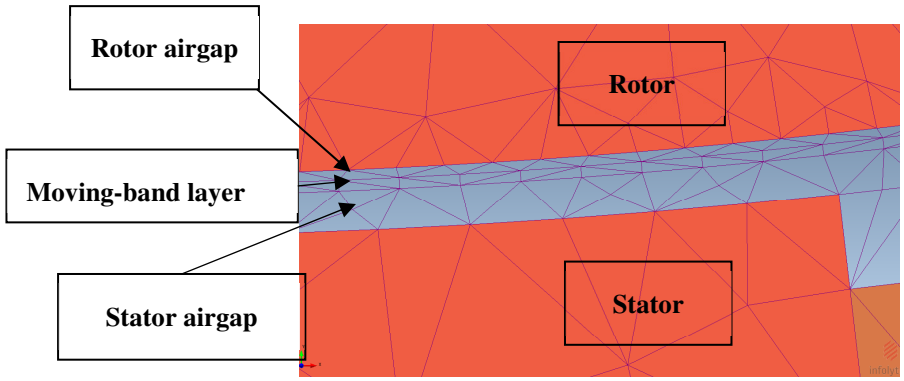

Figure 3-8: Meshing of the airgap in 2D FEA.

The summary of the induction machines used in the thesis is shown in Table 3-4. The rated voltage for all four 3-phase induction machines is 415 V at 50 Hz supply frequency. Machine-2 is modelled based on the induction machine used during the experimental work. The detailed specifications are shown in Appendix A.

No.	Machine Type	Pole Number	Power Rating	Rated Slip	Mean Airgap Length
1	Cage Rotor	4	7kW	0.05	0.5mm
2	Cage Rotor	8	5.5kW	0.05	0.9mm
3	Wound Rotor	4	7kW	0.05	0.5mm
4	Wound Rotor	8	5.5kW	0.05	0.5mm

Table 3-4: Simulated machines.

The reasons of selecting these machines are: 1) Investigations on both the cage and wound rotor induction machine are made in this thesis, which including their UMP characteristic and methods to reduce UMP, 2) the pole number of 4 and 8 is the popular pole number in the industry. Then, the overview of the usage of the four induction machines and the type of analysis are shown in Table 3-7.

3.5.3 Creating rotor eccentricity

For the induction machine with static eccentricity, the rotor rotates at its own centre axis but not at the centre of the stator bore. The static eccentricity can be created by shifting either the stator or rotor to a new position. After shifting the stator or rotor, the stator or rotor airgap layers need to be redrawn because the movement creates an uneven airgap. If the rotor is shifted to create static eccentricity, a new centre of rotation needs to be set at the centre of the rotor. Figure 3-9 shows the machine with rotor eccentricity in 2D FEA, in which the uneven airgap is illustrated.

For the induction machine with dynamic eccentricity, the rotor rotates at the centre of the stator bore axis but not on its own axis. To create the dynamic eccentricity, it is accomplished in the same way as for static eccentricity, in that either the stator or the rotor can be shifted and the stator airgap layer needs to be redrawn. However, the rotor's centre of rotation is set at the centre of the stator bore. In addition, the rotor movement will create a hole in the airgap that causes an error in the simulation because there is no material property assigned to that hole. Hence, an additional layer of air needs to be added that partially overlap the airgap of the rotor region to solve this problem.

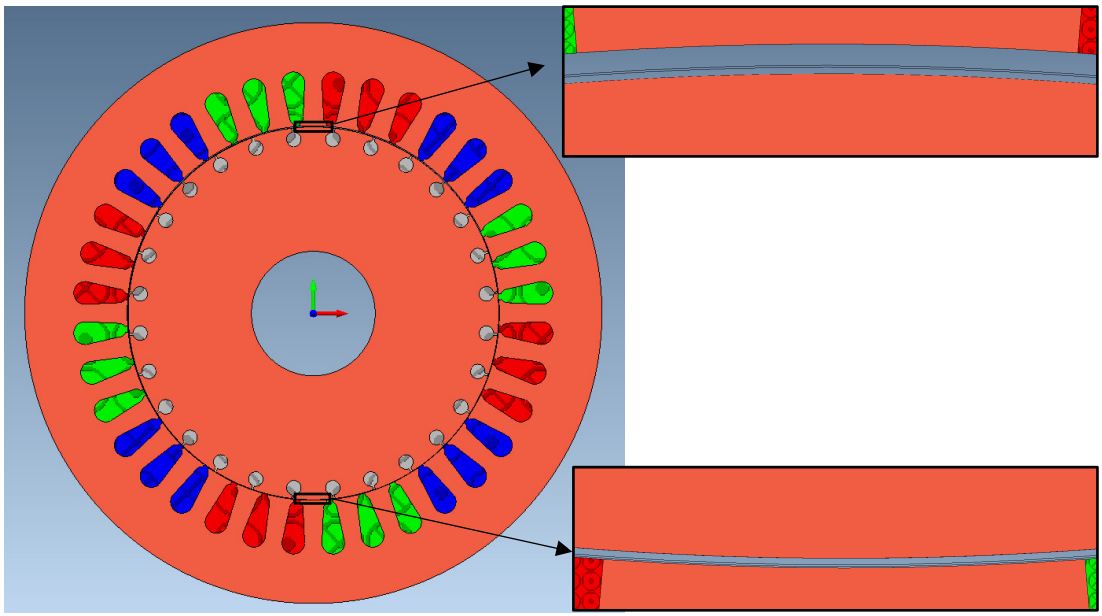

Figure 3-9: Creating 50% eccentricity of static or dynamic in 2D FEA

3.6 Experimental Setup

The experiment was carried out on an 8-pole 5.5 kW cage rotor induction machine (Machine-2). Figure 3-10 illustrates the overview of the experimental setup.

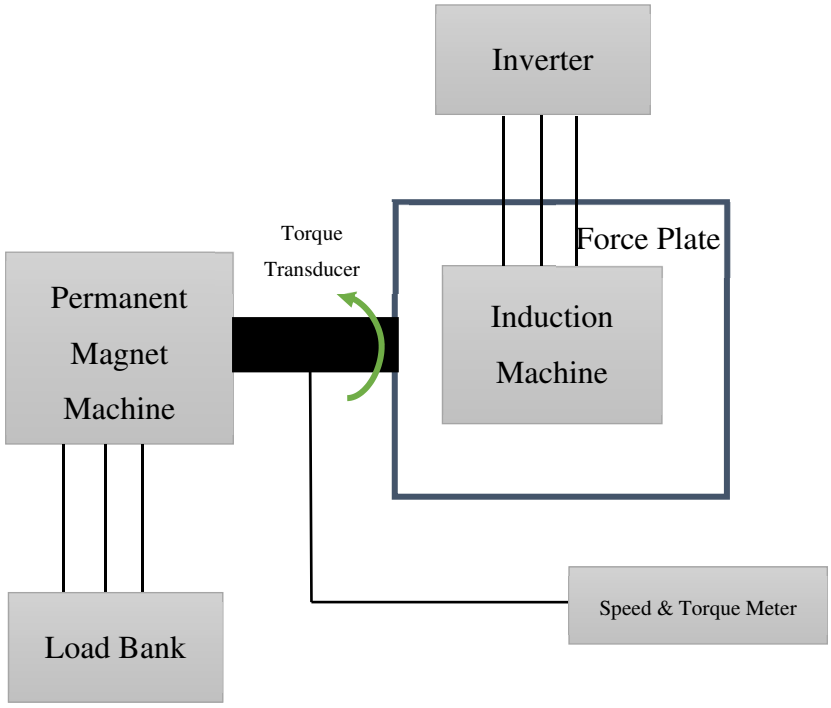

The induction machine is supplied with a three phase inverter. For the experiment, the induction machine was tested as a motor. The permanent magnet machine acts as a mechanical load, which is connected to the rotor via a torque transducer. The benefit of using permanent magnet machine is that the machine is self-excited. The rotational speed of the permanent magnet machine is proportional to the voltage induced in the stator windings. Then, the permanent magnet machine is connected to a load bank to damp the energy generated by the permanent magnet machine.

The stator and rotor need to be separated in order to measure the net attraction force or the UMP between them. The end-cap of the induction machine was removed

to separate the rotor and the stator. The original bearing on the rotor was used without any modification. The rotor was then mounted on a test rig with a new bearing holder. The stator was bolted on top of the force plate to receive the measurement. Then, the force plate under the stator will measure the reaction force on the stator. The results from the force plate were then sent to the charge amplifier and data acquisition system. The received data was sent from the data acquisition system to the computer. The data was recorded and analysed in the computer using, DynoWare, a Graphical User Interface software developed by Kistler.

The overall setup for the experimental work is shown in Figure 3-11. The specification for each apparatus is shown in Appendix B.

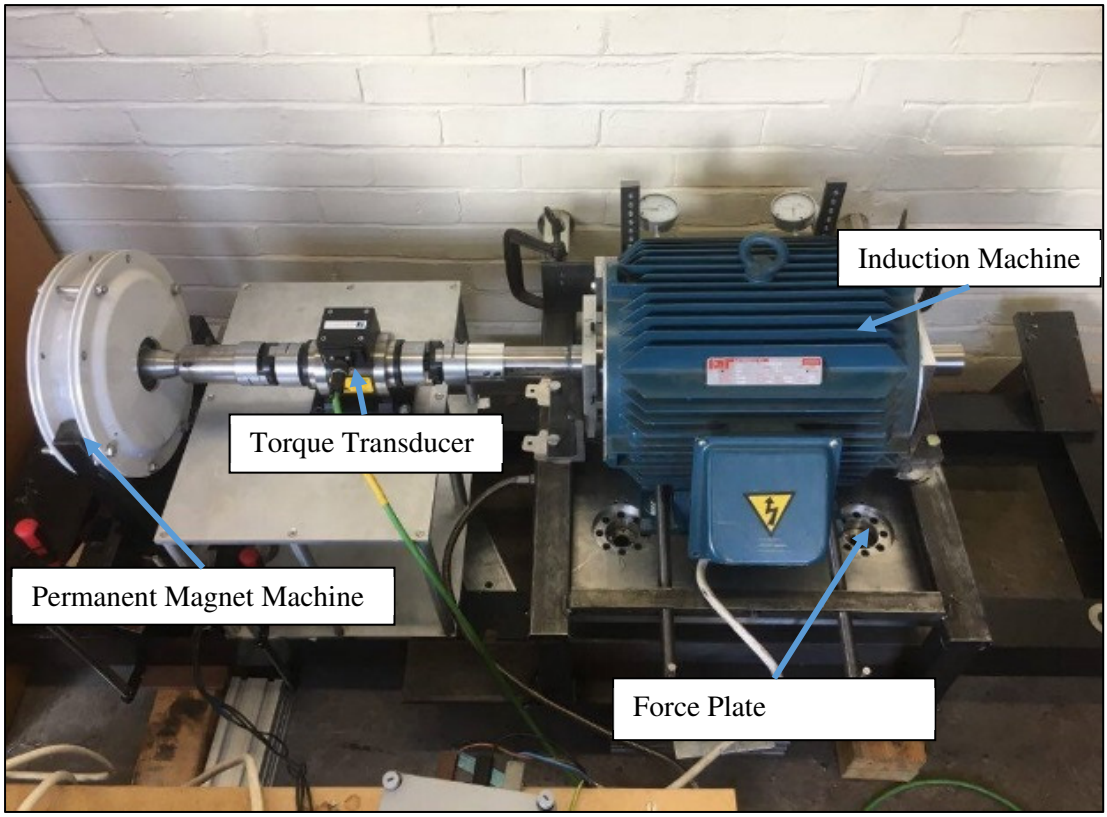

Figure 3-11: Experimental work setup.

Figure 3-12 illustrates the side view of the test rig. The three parts of the test rig were aligned by using shims. However, some misalignment may still be present. Therefore, Oldham couplings were used between the permanent magnet machine, the torque transducer, and the rotor of the induction machine to allow for some flexibility.

The flexible coupling could allow some small misalignment, and could damp the vibration force between each component. In addition, a slight misalignment at the rotor needed to be created by putting shims underneath it in order to produce the static eccentricity. The misalignment created from the static eccentricity should remain under the tolerance of the Oldham coupling.

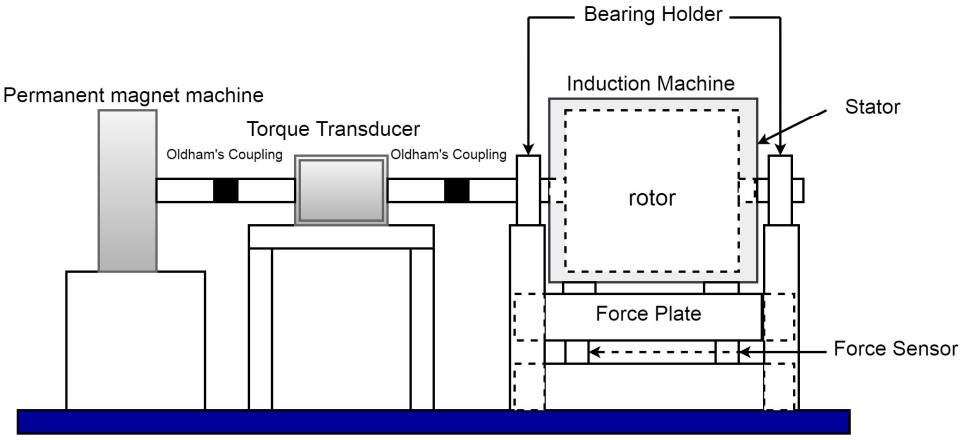

Figure 3-12: Side-view of the test rig.

3.6.1 Static eccentricity

Static axial-constant eccentricity was tested in all of the experiment works in this thesis. The static eccentricity is created by placing the shims under the two bearing holders on each side. This would create a static eccentricity in a vertical direction. The static eccentricity created will depend on the thickness of the shims. Two of the shims used are shown in Figure 3-13. The setup to create a static eccentricity is shown in Figure 3-14.

Figure 3-13: Shims.

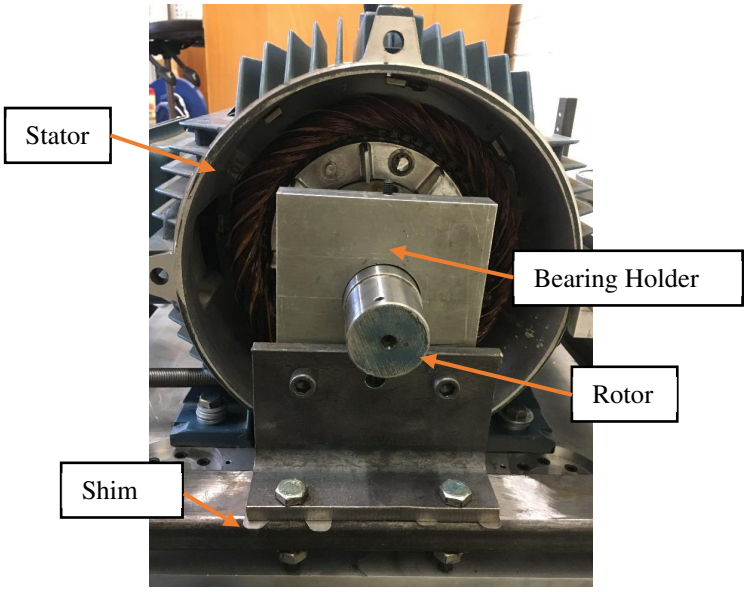

Figure 3-14: Experimental setup with static eccentricity.

After examining the airgap length by using a feeler gauge, the bearing holder of the rotor is bolted down to the test rigs. As four bolts were needed to be bolted after the static eccentricity was set, the alignment will be shifted if the bolts are fully tightened separately. Therefore, the bolts needed to be tightened in a sequence with increasing torque.

The disadvantage of the test rig design is its low stiffness in the horizontal direction, which is sensitive to horizontal forces. If the rotor is slightly misaligned toward the horizontal direction, UMP will cause the eccentricity to be further increased in the horizontal axis direction. This scenario is unavoidable because the structure of the test rig is not specifically made for force measurement. Therefore, special care needed to be taken when running the test.

Clock gauges were installed to measure the horizontal movement. The two clock gauges were attached to the rotor stand, which is shown in Figure 3-15. A small metal plate was mounted on the stator so that the clock gauge has a smooth surface to measure the movement. The clock gauges could measure the relative distance between the stator and rotor. When running the experiment, the clock gauge was used to verify that the horizontal movement of the rotor is within the acceptable range.

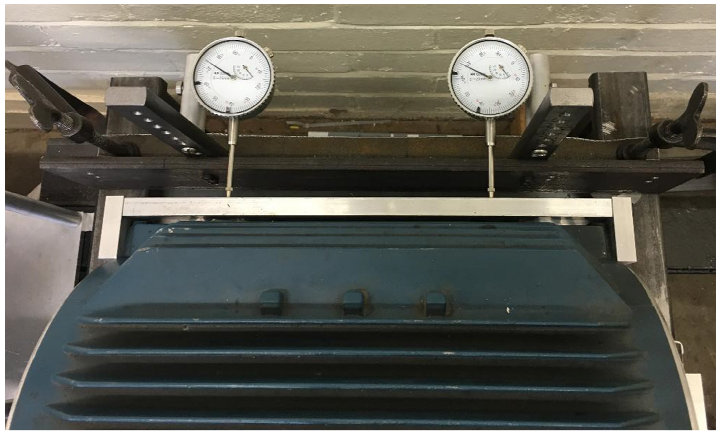

Figure 3-15: Clock gauge setup.

3.6.2 Force measurement

The UMP exerted on the bearing is the force that needs to be measured. As the UMP is the net attraction force between the stator and rotor, the stator and rotor were separated in order to measure the force exerted on the bearing. Therefore, after separating the stator and rotor, they were mounted on a different platform, where the stator was mounted on the force table and the rotor is mounted on an external stand. From Newton's third law, the reaction force from the stator was the same as the rotor. The main reason that the force measurement was taken from the stator is that the rotor was coupled to other moving parts, such as the torque transducer and the permanent magnet machine. The imperfect coupling and the vibration of other moving components may cause more noise in the force measurement.

The force table was made with a thick aluminium plate and four force sensors. The force sensors were mounted on the aluminium plate, which acting as the legs of the force table. The signal from each force sensors was processed to find the force from three different axes and the moment force as well. The dimension of the aluminium top plate was 500 mm x 500 mm x 60 mm. The length and width of the top plate depend on the size of the induction machine. Meanwhile, the thickness of the top plate depends on its material and length. The selection of the dimension of the force plate was based on Figure 3-16, which shows the minimum thickness from the force sensor datasheet. This is to prevent the natural frequency of the table within the measurement frequency.

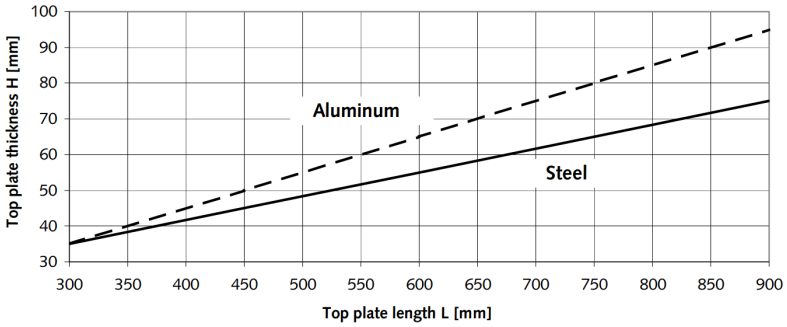

Figure 3-16: Thickness of top plate [125].

The two most widely used sensors were the piezoelectric sensors and the strain gauges force sensors. Piezoelectric sensors rely on a crystal that produces an electrical charge proportional to the acting force. For the strain gauge force sensors, the force was measured by the strain gauge, which extends proportionally to the acting force. The changing of the strain gauge would result in the changing of electrical resistance.

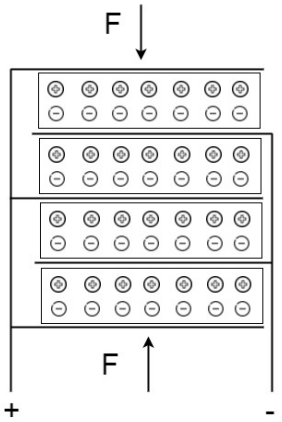

Figure 3-17: Concept of the piezoelectric sensors.

The sensors that were used in the experimental work were the piezoelectric sensors. The model used is Kistler 9366C, which can measure forces up to 25 kN. The piezoelectric materials in the sensors produce positive or negative electrical charges when a force was acting on it. The charge generated was proportional to the force acting on it. The concept for one axis is shown in Figure 3-17. The force sensor also has a high natural frequency that is required for highly dynamic force measurement.

However, the charge produced by the piezoelectric sensor is too small to be measured. The charge amplifier was used to amplify the negative charge from the

piezoelectric sensor into a high positive voltage that is proportional to the charge. Therefore, the sensor has a negative sensitivity. The charge amplifier used in the experiment was the Kistler 5070A model, as shown in Figure 3-18. As UMP measurement from static eccentricity was tested, the charge amplifier's maximum frequency of 45 kHz was more than enough.

Figure 3-18: Kistler 5070 charge amplifier.

The Kistler 9366C is a set of four 3-component force sensors. The three signals from each sensor is sent to Kistler 5070. The three orthogonal forces (F_x, F_y, F_z) and the three moments (M_x, M_y, M_z) were calculated. The moments (M_x, M_y, M_z) are not used in the UMP measurement because torque is not produced by the UMP. Based on the labelling of the force sensor in Figure 3-19, the calculation of the orthogonal forces (F_x, F_y, F_z) can be written as (3-54)-(3-56), where the subscript addend in the formula is for the force signal added before it is sent to the Kistler 5070. For example, in (3-54), the F_{x1+2} is used because the distance between the first and the second sensor is parallel to the X-axis, so, the X-axis force of the both sensors are the same, in which they are added before they were sent to the Kistler 5070.

$$F_x = F_{x1+2} + F_{x3+4} \tag{3-54}$$

$$F_z = F_{z1+3} + F_{z2+4} \tag{3-55}$$

$$F_y = F_{y1} + F_{y2} + F_{y3} + F_{y4} \tag{3-56}$$

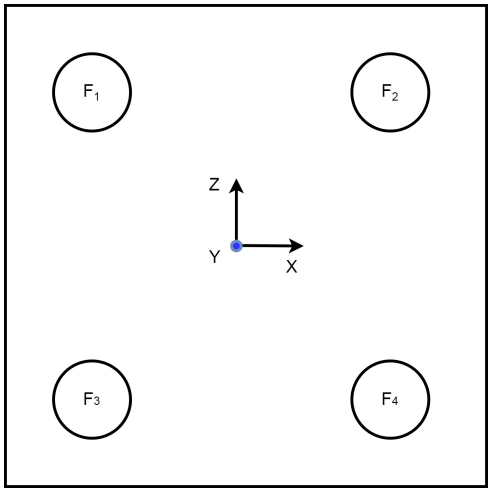

Figure 3-19: Force sensor distribution on the force table.

Figure 3-20 shows the cross-section of the induction machine with an eccentric rotor; the rotor eccentricity is set in the direction of the Y-axis. If the end winding leakage flux that crosses the airgap from the stator frame is neglected, the Z-axis force can be ignored, because all the magnetic flux that crosses the airgap is perpendicular to the Z-axis. In this thesis, F_y is also named as the vertical force, and F_x is named as the horizontal force.

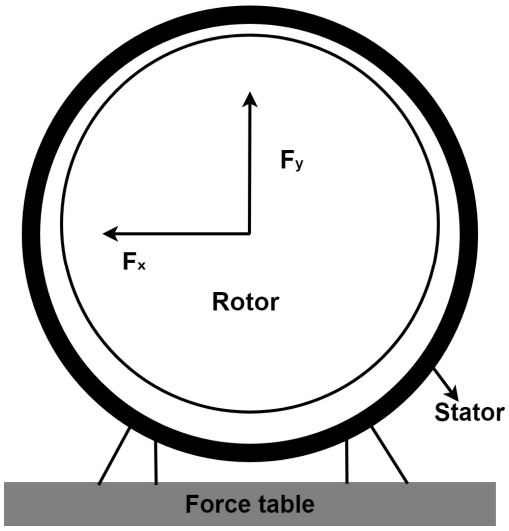

Figure 3-20: Cross-section of the induction machine in test.

3.6.3 Verification of the force measurement

Precise measurement of the UMP from the force plate is important to receive accurate experimental results. Verifications of the force plate had been done on the force plate in this subsection. In the first verification, the weight was placed at different sides of the plate. The weight (Y-axis force) is assumed to be perpendicular to the X-axis and the Z-axis, in which the force of the X-axis and Z-axis are zero. A calibrated 10 kg (98.1 N) weight was used. The 10 kg weight was placed on the 5 position (marked in blue), which is illustrated in Figure 3-21. The measurement results at each position are shown in Table 3-5. The results show that the error of the measurement was less than 0.4%. It can be concluded that the position of the applied weight on the force plate does not affect the measurement results.

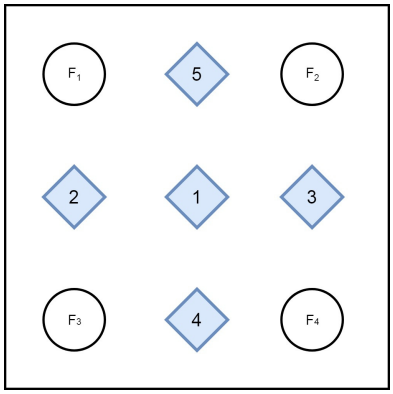

Figure 3-21: Position of the weight placed on the force table.

No.	F_{y1} (N)	F_{y2} (N)	F_{y3} (N)	F_{y4} (N)	Sum of individual forces (N)	**Error (%)**
1	46.87	6.50	-0.380	45.07	98.06	**0.0398**
2	79.95	-24.98	-0.075	43.08	97.97	**0.128**
3	6.35	41.17	0.017	50.86	98.39	**-0.302**
4	49.04	-35.77	0.098	85.09	98.46	**-0.365**
5	52.92	34.92	0.003	10.17	98.01	**0.088**

Table 3-5: Summary of the measurement of each force sensor.

In the second verification, as the UMP caused by static eccentricity, which is a static force, will be measured in this thesis. The European Standard of ISO 7500-1 was used to verify the static uniaxial force in the force measuring system [126]. The five tests conducted in the ISO 7500-1 are:

1) Relative resolution (a), the percentage of the measuring resolutions.

$$a = \frac{resolution}{Indicated\ Force} \times 100 \tag{3-57}$$

2) Relative zero error (f_0), the error when the force plate is not loaded.

$$f_0 = \frac{zero\ force\ measurement}{Maximum\ value\ of\ calibrated\ range} \times 100 \tag{3-58}$$

3) Reversibility error (v), the difference between the values obtained with increasing and decreasing force at the same reference force.

$$v = \frac{increasing\ force - decreasing\ force}{mean\ of\ both\ forces} \times 100 \tag{3-59}$$

4) Relative indication error (q), the error between the measured value and the reference value, where F is the force and sub-script n is the number of tests from 1 to 3.

$$q_n = \frac{F_{measured,n} - F_{reference,1}}{F_{reference,n}} \times 100 \tag{3-60}$$

$$q = \frac{q_1 + q_2 + q_3}{3} \tag{3-61}$$

5) Repeatability error (b), the error between the reading in the same test.

$$b = q_{maximum} - q_{minimum} \tag{3-62}$$

The maximum permissible value for each class under the ISO 7500-1 Standard is shown in Table 3-6. Therefore, from the results taken in the test of the force plate, it falls under the category of Class 0.5. This means that the force plate had been calibrated with the highest standard.

Class of machine range	Maximum permissible value (%)				
	q	b	v	f_0	a
0.5	± 0.5	± 0.5	± 0.75	± 0.05	0.25
1	± 1.0	± 1.0	± 1.5	± 0.1	0.5
2	± 2.0	± 2.0	± 3.0	± 0.2	1.0
3	± 3.0	± 3.0	± 4.5	± 0.3	1.5
	Results of the tested force plate (%)				
0.5	$\mathbf{+0.25}$	$\mathbf{+0.10}$	$\mathbf{-0.34}$	$\mathbf{+0.03}$	$\mathbf{5 \times 10^{-5}}$

Table 3-6: Characteristic values of each class and the results of the tested force plate.

3.6.4 Rotor

High precision in creating a rotor eccentricity is needed to get an accurate result. As the airgap of the machine is small, the measurement error from the feeler gauge has a significant impact on the actual static eccentricity applied. A slight mechanical misalignment due to the tolerance of the feeler gauge will increase the degree of eccentricity.

Therefore, skimming the rotor is essential to minimise the influence of the mechanical tolerance of the feeler gauge. 0.4 mm was skimmed off the rotor surface to increase the mean airgap length from 0.5 mm to 0.9 mm. The 8-pole machine usually has a smaller airgap to reduce the magnetising current. The no-load magnetising current was increased from 3 A to 5.4 A. From Figure 3-22 and Figure 3-23, the rotor slots had been changed from closed rotor slots to open rotor slots. The changes in rotor slots may also affect the characteristic of the higher flux harmonics.

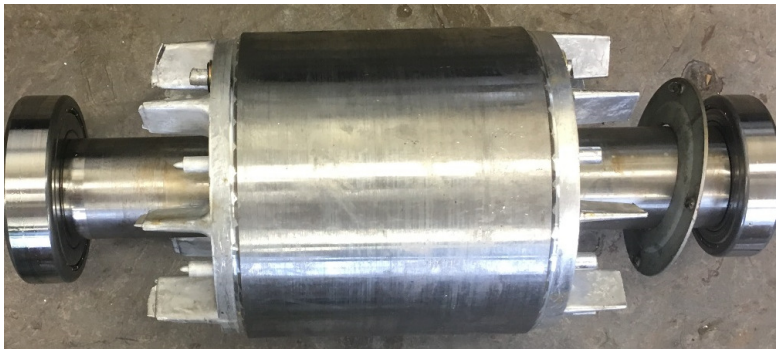

Figure 3-22: Rotor before skimming.

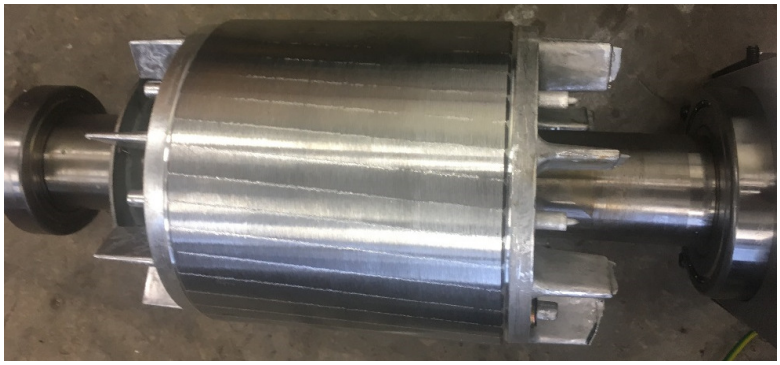

Figure 3-23: Rotor after skimming.

3.6.5 Inverter

A three-phase power supply was connected to the induction machine through an inverter. A Hitachi SJ200 inverter was used in the experiment. The inverter has a power rating of 7.5 kW. The output waveform of the inverter was a Sinusoidal Pulse Width Modulation waveform. Although there is a lot of higher harmonics content in the waveform, electrical machines with a high number of stator turns naturally act as a low pass filter. Therefore, the flux induced by the higher harmonics voltage is negligible.

By using the inverter, the amplitude and frequency of the excitation voltage can be varied. In addition, the inverter could also prevent the inrush current during the induction machine startup. The inverter can run in either scalar control or vector control. Sensorless close loop control is not chosen to be used in the experiment because the excitation frequency needs to be fixed when comparing of the UMP at a different rotor slip.

3.6.6 Harmonics analysis of the measurement results

In the UMP analytical model from (3-40), the UMP consists of 2 different components: the constant component and the 2-times supply frequency component. When taking the UMP results from the experimental work, the force measurement also includes the force from the vibration of the test rig which was caused by the mechanical coupling from the induction machine to the permanent magnet machine. In addition, there was also some minor force from the environment. Therefore, Fast Fourier Transform (FFT) was used to extract the force measurement data to get the UMP caused by the rotor static eccentricity.

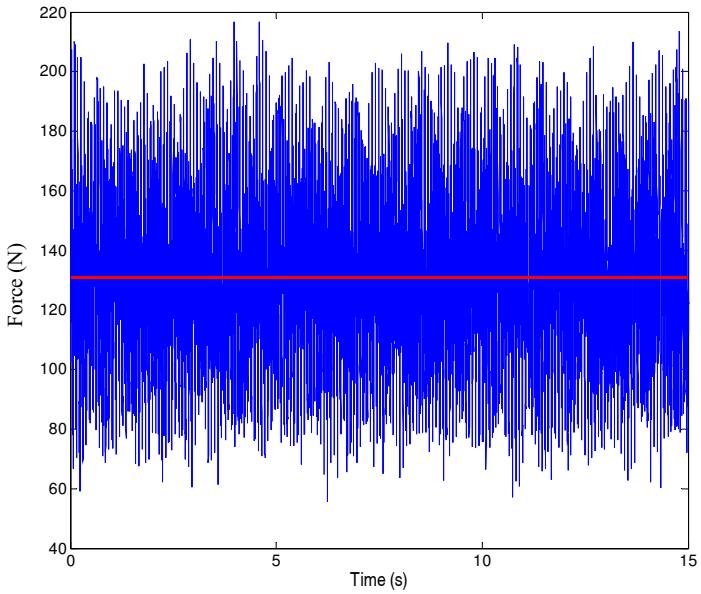

Figure 3-24: UMP of 50% static eccentricity at no-load with 0.5 pu rated voltage.

For the experimental work, the UMP of Machine-2 with 50% static eccentricity at no-load with 0.5 p.u rated voltage and 50 Hz supply frequency is shown in Figure 3-24. Then, the FFT analysis of the results in Figure 3-24 is demonstrated in Figure 3-25. The FFT analysis had shown that the dominant force component is at 0 Hz, which represents the constant component of the UMP. The 99.93 Hz component represents the 2-times supply frequency component. Due to the reason that the induction machine was supplied with an inverter, there was a slight error which caused the supply frequency to be a bit lower than 50 Hz.

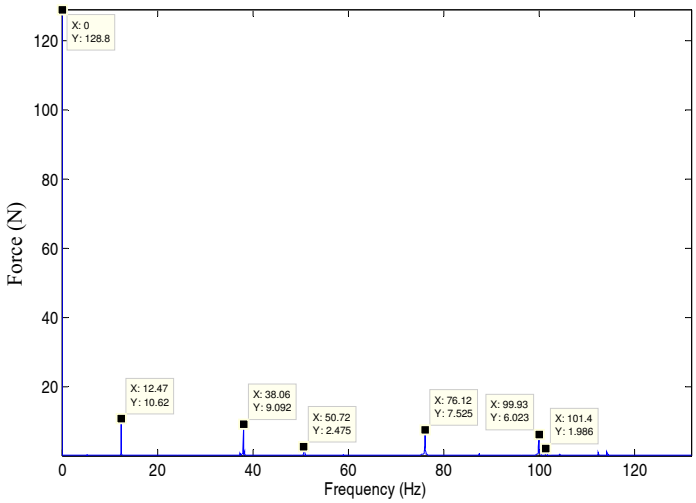

Figure 3-25: FFT for the UMP in Figure 3-24.

From Figure 3-25, the 12.47 Hz is the rotor rotational frequency. It shows that the machine was running close to synchronous speed, in which the synchronous rotating frequency of an 8-pole machine is 12.5 Hz. The other frequencies of 38.06-Hz, 50.72 Hz, 76.12 Hz, and 101.4 Hz are the harmonics of the rotor rotational frequency. From the analytical calculation, the rotor rotational frequency was caused by dynamic eccentricity. However, the result shown is the UMP of a rotor with static eccentricity. There are two reasons that may have caused this scenario:

- Slight dynamic eccentricity in the bearing: the $\boldsymbol{p \pm 1}$ magnetic flux caused by the dynamic eccentricity was not damped at zero slip.
- Mechanical coupling: There are two flexible couplings in the system, where the induction machine was coupled to the torque transducer, and the torque transducer was coupled with the permanent magnet machine.

Figure 3-26 shows the FEA simulation results of the 50% static eccentricity at no-load with 50% rated voltage and 50 Hz supply frequency. The FFT analysis of the results in Figure 3-26 is shown in Figure 3-27.

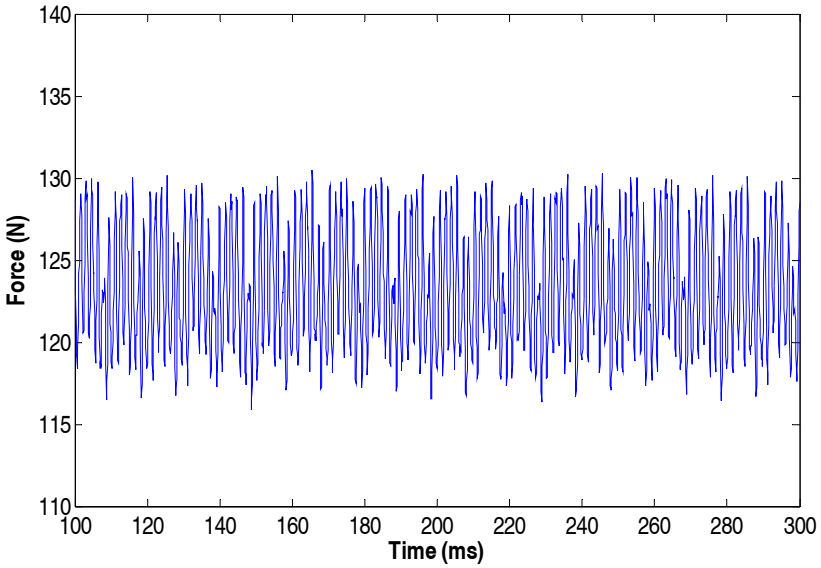

Figure 3-26: FEA of Machine-2 with 50% static eccentricity at no-load.

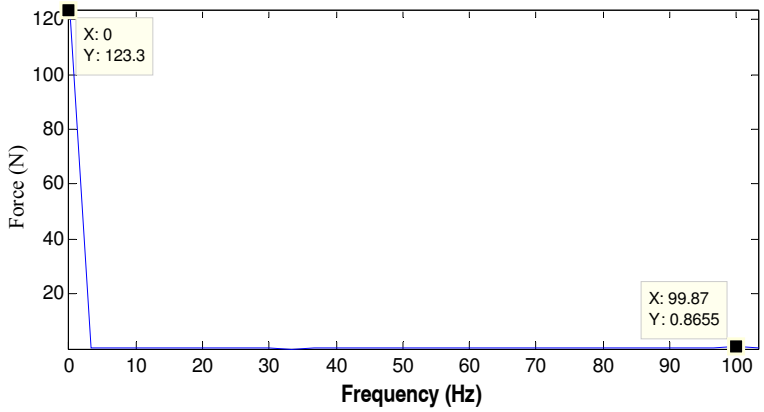

Figure 3-27: FFT analysis for Figure 3-26.

The UMP results from FEA are shown in Figure 3-26. FFT analysis is performed to analyse the harmonic components in the FEA results. From the FFT analysis in Figure 3-27, it shows that the main component of the UMP produced by the static eccentricity is the constant component (0 frequency component).

Comparing Figure 3-25 and Figure 3-27, although the constant component of the experimental results and the FEA results are comparable, the 100 Hz component in the FEA result is much smaller. This is because the 100 Hz component is due to the interaction between the backward rotating flux with the forward rotating flux. Ideally, the backward rotating flux will not occur, when the supplied voltage and the

magnetisation of the machine are balanced. Therefore, the 100 Hz for the experimental result was higher than the FEA.

This section has shown that the UMP with 2-times supply frequency is almost negligible. Therefore, when analysing the UMP for the machine with static eccentricity, only the constant component of the UMP is considered.

3.6.7 UMP measurement

After setting up the test rigs, the UMP with different degrees of eccentricity were tested in this section to validate the reliability of the test rigs; Machine-2 was set to operate at 50% rated voltage and 50 Hz supply frequency. The major frequency component of the static eccentricity UMP is the zero frequency component or the constant force. By using FFT analysis, the zero frequency component of each case was extracted and is presented in Figure 3-28.

Figure 3-28 shows that there was a small amount of UMP when the rotor was set at 0 degree of eccentricity. This scenario is hard to be avoided due to the tolerance of the feeler gauge and the mechanical error during the setup. Overall, the graph shows that the UMP increases as the degree of eccentricity increases, which correlates with the analytical study shown in Section 3.4.

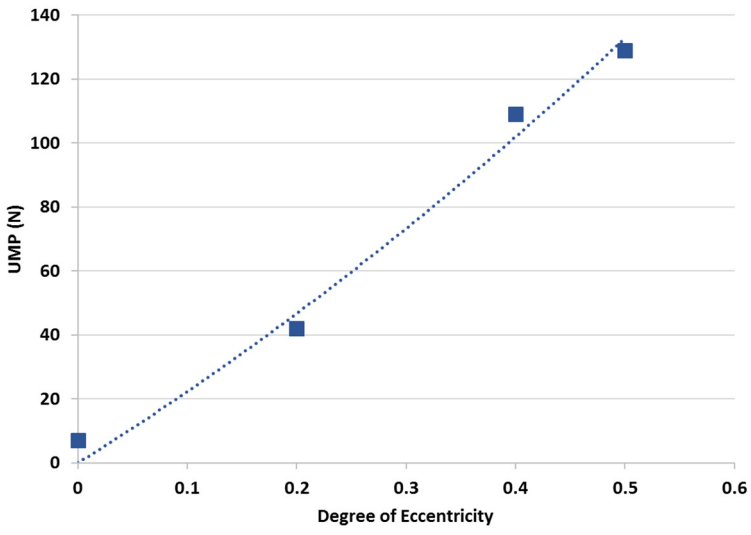

Figure 3-28: UMP at different degree of eccentricity.

3.6.8 Comparison between vertical and horizontal force

As was discussed in Sub-section 3.6.2, the horizontal force (X-axis force) would change the rotor eccentricity in the horizontal direction because the test rig has low stiffness in the horizontal direction. The change in the distance between the stator and the rotor for different horizontal force is shown in Figure 3-29. The relative distance is measured with the clock gauge, which is shown in Figure 3-15.

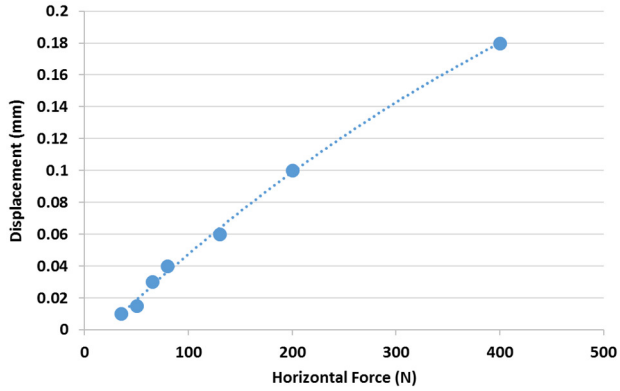

Figure 3-29: Change in the distance between the stator and the rotor.

From the characteristic of the test rigs shown in Figure 3-29, it can be deduced that the UMP caused by the initial rotor eccentricity would further increase the rotor eccentricity. So, another test was done to investigate this issue. The rotor was set at 8% of static eccentricity (predicted) in the X-axis direction and it was run at no-load. Then, a different excitation voltage with 50 Hz supply frequency was used. The estimated results were calculated based on the initial experimental results and the analytical model in (3-41).

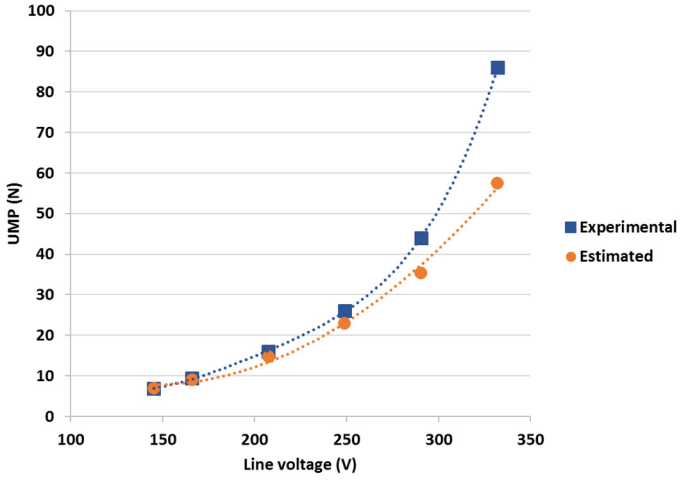

Figure 3-30: UMP of 8% static eccentricity in the X-axis direction.

Figure 3-30 shows that the difference between the estimated value and the experimental results increased when the UMP increased. The estimated UMP is based on the 8% static eccentricity, while a constant eccentricity is not used in getting the experimental results. In the experimental work, the rotor eccentricity would be further increased as the UMP increased, which causes a larger UMP. Hence, for this test rig, measuring the UMP in the X-axis direction may not be accurate when the UMP is larger than 40 N.

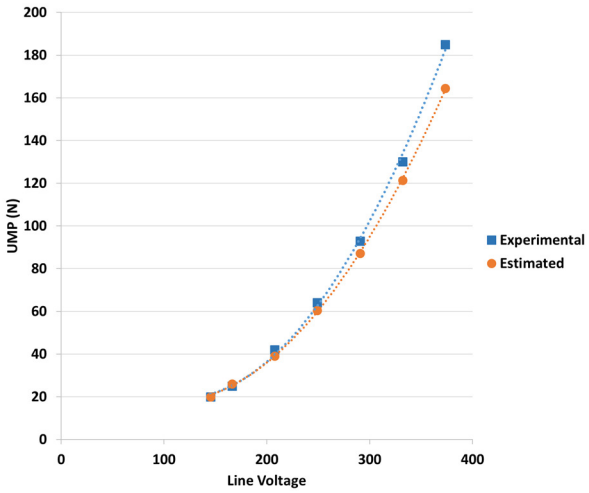

Figure 3-31: UMP of 20% static eccentricity in the Y-axis direction.

Figure 3-31 shows the UMP of Machine-2 with 20% of static eccentricity at the Y-axis direction. When the UMP is below 140 N, it can be deduced that the eccentricity did not increase as the UMP increased because good correlation was shown between the experimental results and estimated results. However, the difference becomes larger when the UMP is larger than 140 N, which means that the eccentricity might be changed when the UMP is larger than 140 N.

Therefore, all the experimental works in the latter part of the thesis would be tested on the rotor with Y-axis static eccentricity and the UMP tested should not be higher than 140 N. However, due to the UMP damping effect from the parallel winding would produce some X-axis UMP when the eccentricity is set toward the Y-axis direction; this issue will be discussed in Section 4.1. Hence, when measuring the Y-axis force, the clock gauge on the experimental test rigs needed to be checked in the test to minimise the error.

3.7 Validation of FEA modelling

The modelling work could represent the behaviour of the induction machine based on theoretical equations. However, modelling work could not entirely represent the problem in a real case scenario because assumptions need to be made in the FEA to simplify the model, such as constant changes in the axial direction, the boundary conditions in electromagnetic problems, and the geometry and dimension of the machine. Therefore, experimental works need to be done to verify the reliability of the FEA model. The validation work was done on Machine-2. The rotor eccentricity was set to 20% of static eccentricity and the 35% of the rated voltage was used. The low rated voltage was used, because of the limitation of the test rigs; the measurement is accurate when the UMP is less than 140 N, which is shown in Sub-section 3.6.8.

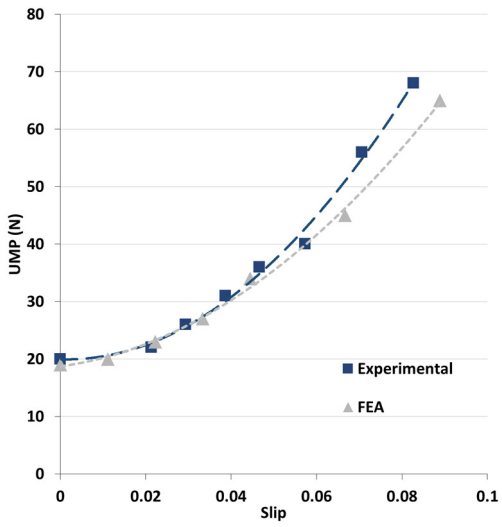

Figure 3-32: UMP of Machine-2 with 20% of rotor eccentricity at 35% rated voltage.

It is shown in Figure 3-32 that the UMP from the FEA and the experimental results increased as the rotor slip increased. When the current increased with rotor slip, the increment of rotor slip led to an increment of leakage flux across the airgap, in which a larger UMP was produced. As the leakage flux caused by the skewed rotor is not considered in the 2D-FEA, the UMP from experimental work is larger than the FEA results when the slip increased, this issue will be discussed in Section 4.5.

In conclusion, a good correlation was shown between the FEA and experimental results when the induction machine runs in the low slip region. FEA has proven to be a reliable method to investigate the UMP caused by an eccentric rotor.

3.8 Summary of the FEA and experimental work in the thesis

Chapter	Objective	Machine-	FEA	Experiment
3.6.6	Investigate the harmonics in the UMP of static eccentricity	2	✓	✓
3.7	Verify the reliability of FEA modelling	2	✓	✓
4.1.2	Study on the proposed UMP Damping Coefficient	2	✓	✓
4.1.4	Investigate on the influence of the excitation frequency on the UMP	2	✓	✓
4.1.5	Investigate on the influence of the rotor resistance on the UMP	2	✓	
4.2	Categorise the magnetic flux across the airgap	1, 2	✓	
4.3.1	Comparison between wound rotor and cage rotor induction machine	1, 2, 3	✓	✓
4.3.4	Examine the dynamic eccentricity	1, 3	✓	
4.5	Study on the effect of the skewed rotor	1	✓	
4.6	Study on the influence of axial-varying eccentricity	1	✓	
4.7	Discussion on the additional power losses caused by rotor eccentricity	1, 3	✓	
5	Verification of the proposed empirical method and UMP/Torque ratio	1, 2, 3	✓	✓
6.2	Investigate on reducing UMP through the slip control method	1, 2, 3	✓	✓
6.3	Investigate on the proposed damper winding configuration to reduce UMP	3, 4	✓	
6.4	Comparison between the slip control method with the damper winding topology	3, 4	✓	

Table 3-7: Overview of the works done in the thesis.

Table 3-7 shows the overview of the works done in the thesis. All the analysis is supported by analytical modelling. The FEA and experimental results will be used to verify the analytical model.

Although experimental work could provide good insights on the UMP in reality, it is susceptible to the surrounding factors and human error. Hence, ways to increase the accuracy have been shown in Section 3.6; such as verifying measurement error (Sub-section 3.6.3), reducing the mechanical tolerance (Sub-section 3.6.4), filtering the noise in the measurement (Sub-section 3.6.6), and preventing changes in rotor eccentricity (Sub-section 3.6.8).

3.9 Blank Rotor Analysis

This subsection is to analyse the magnetic flux harmonics distribution around the airgap through the FEA, which had been previously discussed using an analytical model in Section 3.1. The space harmonics of the airgap flux extracted from the FEA is used to investigate the changes in the magnetic permeance harmonics caused by rotor eccentricity.

The stator of Machine-1 with a 2-pole pair is used in this analysis. Then, the cage rotor is switched to a blank rotor, which is built with an iron core in order to have a clearer understanding of each space harmonics order. If a cage rotor is used, the airgap flux contains a lot of harmonics which is produced by the zigzag leakage flux. The zigzag leakage flux changes with different rotor angles, which is difficult to analyse. The leakage flux harmonics may have merged with the other harmonics and this will influence the analysis of the magnetic flux. The comparison of the magnetic flux space harmonics between cage rotor, wound rotor and blank rotor are shown in Appendix D. Furthermore, in [92], Dorrell pointed out that the blank rotor and the wound rotor gave the similar UMP results. However, this similarity is only applicable when the wound rotor induction machine is not loaded.

In Sub-section 3.9.1, the comparison of the airgap flux has been made between the concentric and eccentric blank rotor. In Sub-section 3.9.2, the comparison between the UMP of different degrees of eccentricity is shown.

3.9.1 Additional pole-pair flux due to rotor eccentricity

The FFT analysis of the magnetic flux distribution around the airgap of Machine-1 with the concentric blank rotor is shown in Figure 3-33. The 2nd harmonic component is the fundamental pole-pair harmonics. The 10^{th}, 14^{th}, 22^{nd}, and 26^{th} are the stator winding harmonics. The 34^{th} and 38^{th} harmonics consist of both the stator winding harmonics and the stator slots harmonics.

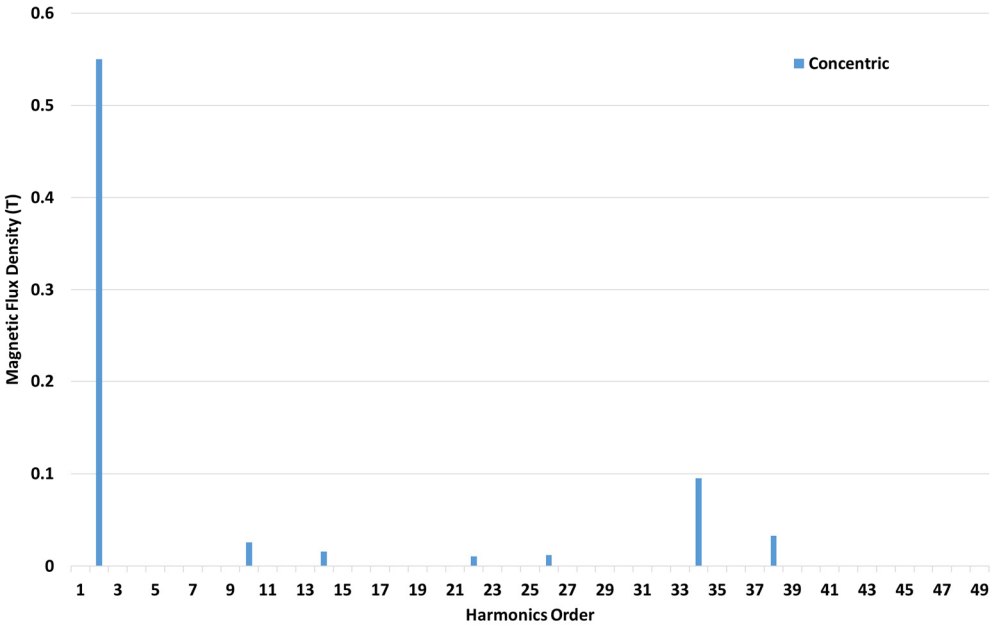

Figure 3-33: Airgap flux space harmonics of a concentric blank rotor.

When referring to Figure 3-34, the fundamental 2^{nd} harmonic is slightly reduced when the eccentricity increases. As the total stator flux is excited with a constant voltage, it means that the total flux produced should be constant. When the degree of eccentricity increases, the stator leakage inductance also increases, which reduces the fundamental flux. By comparing Figure 3-33 and Figure 3-34, all the additional harmonics are produced by the airgap eccentricity. However, only the interaction between the pole-pair ± 1 flux produces UMP.

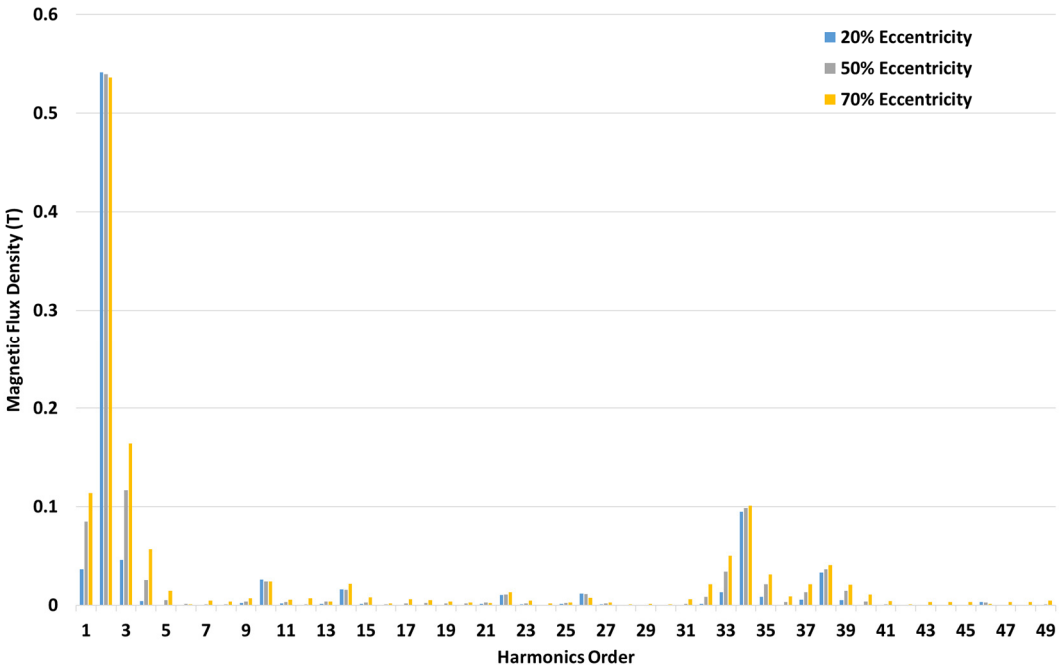

Figure 3-34: Airgap flux space harmonics of an eccentric blank rotor.

In Figure 3-34, it had shown that the increment of the higher space harmonic airgap flux is not linearly proportional to the rotor eccentricity. There is a nonlinear relationship between the magnetic permeance and the degree of eccentricity. To investigate the effect of eccentricity towards the sideband harmonics, the magnitude of the fundamental harmonic flux and the stator slot harmonics flux are shown in Table 3-8. The percentages shown are the percentage of the sideband harmonics with respect to the main harmonics. The unipolar flux is neglected because the magnetic reluctance of the unipolar flux path is very high [127].

Space Harmonics	20% Eccentricity		50% Eccentricity		70% Eccentricity	
	Magnitude	%	Magnitude	%	Magnitude	%
1	0.036	6.706	0.085	15.699	0.114	21.255
2	0.541		0.540		0.536	
3	0.046	8.480	0.117	21.630	0.164	30.594
4	0.004	0.760	0.026	4.737	0.057	10.627
5	0.000	0.087	0.005	0.911	0.015	2.716
31	0.000	0.186	0.002	1.572	0.006	6.142
32	0.001	1.363	0.008	8.444	0.021	21.246
33	0.013	13.819	0.034	34.337	0.050	49.842
34	0.095		0.099		0.101	
35	0.008	8.812	0.021	21.499	0.031	30.870
36	0.001	0.629	0.003	3.069	0.009	8.995
37	0.005	16.448	0.013	36.070	0.021	52.154
38	0.033		0.037		0.041	
39	0.005	15.967	0.014	39.591	0.021	50.718
40	0.000	1.458	0.004	10.794	0.011	26.124

Table 3-8: Magnitude and percentages relative to the magnitude of its main flux for each magnetic flux harmonic with different eccentricity.

In addition, it has been shown that the 2nd harmonic pole pair produces additional 1st and 3rd flux harmonics from the 1st order magnetic permeance harmonic. The 4th and 5th harmonics are caused by the higher magnetic permeance harmonics. For the 20% eccentricity, the 4th and 5th harmonic are very small, which can be neglected in the UMP calculation. This had been pointed out in the assumptions made in Sub-section 3.1.3. Due to the permeance harmonics from the uneven airgap, the magnetic flux from the stator winding harmonics and the stator slot harmonics also produce their own sideband flux.

As shown in (3-18) with the assumptions made in Sub-section 3.1.3, the percentage of the $p \pm 1$ sidebands flux should be half of the percentage of rotor

eccentricity. As a blank rotor is used in the simulation, the fundamental pole-pair flux is the main flux that contributes to UMP. For example, 20% of eccentricity should have 10% of $p \pm 1$ sidebands flux. However, it was shown that the $p \pm 1$ sidebands flux of the fundamental pole-pair harmonic is lower than 10%. This is because the existence of stator slots has increased the effective airgap length, which means that the actual percentage of eccentricity is lower. Meanwhile, the $p \pm 1$ sidebands flux of the stator slot harmonics are around 10% because the magnetic flux always crosses the airgap from the stator teeth.

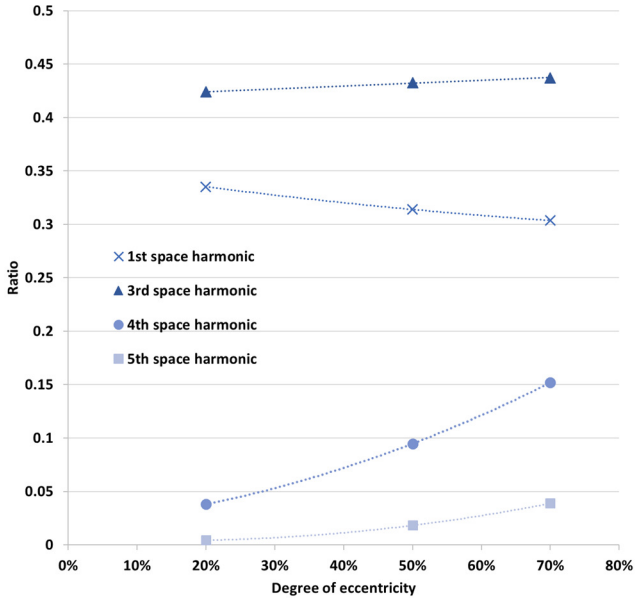

Figure 3-35: Ratio of the fundamental pole pair harmonics sidebands flux with respect to its own eccentricity.

Aside from this, the magnitude of the sideband of each magnetic flux of a concentric rotor is different. This is due to some magnetic flux harmonics component that may have merged or swamped into the other component. This scenario can be proven by the ratio between the fundamental pole pair harmonics sidebands flux with respect to its own percentage of eccentricity which is illustrated in Figure 3-35. For example, the 1st space harmonics flux is lower than the 3rd space harmonic flux. The positive component of the 2nd and 3rd order magnetic permeance harmonics produce 4th and 5th space harmonic flux, in which the magnetic permeance harmonics increases when the degree of eccentricity increases. Therefore, the ratio of 3rd, 4th and 5th sideband flux increase with the percentage of eccentricity. However, the 1st space

harmonic flux is entirely different because the ratio decreases when the percentage of eccentricity increases. This is due to the negative component of the 2nd and 3rd order magnetic permeance harmonic which may have merged with the 1st space harmonics flux.

3.9.2 UMP with different eccentricity

With the magnitude of the sideband flux changing with the percentage of eccentricity, the UMP characteristic is also affected when the percentage of eccentricity is high. The blank rotor is used in this section with the same simulation setup from Table 3-8. The UMP from different eccentricities are compared to different excitation voltage.

From Figure 3-36, it is seen that the UMP increases as the voltage increases. As the voltage is linearly proportional to the magnetic flux, the UMP has a quadratic increment. This section will compare the difference in the UMP analytical calculation if the linear relationship is used in the higher eccentricity percentage, such as 50% and 70%.

Therefore, a linearly normalised UMP is used in the calculation where the UMP is divided by its own eccentricity. In order to compare the 3 different cases, the ratio between the normalised UMP of the 50% and 70% eccentricity with the 20% eccentricity is shown in Figure 3-37. The 20% is used as the base unit of the comparison because the magnetic permeance harmonics almost has a linear relationship with the percentage of eccentricity when the percentage is smaller than 20%, which is shown Sub-section 3.1.3.

From Figure 3-37, the normalised UMP of the 50% and 70% eccentricity have a ratio that is higher than 1. The 70% eccentricity has a higher ratio than the 50% eccentricity. This has proven the UMP increases more than the linear increment. In addition, the ratio drops when the excitation voltage increases. This is caused by the saturation effect that reduces the magnetic inductance, in which the additional sideband flux is also reduced.

The UMP increment is less than the magnetic permeance ratio shown in Sub-section 3.1.2 and is due to:

- Core saturation reduces the difference between the narrowest airgap and the biggest airgap.
- Some of the magnetic harmonics may have merged together or cancelled each other.
- For the no-load case, the magnetising current reduces when the eccentricity becomes bigger. This will reduce the increment of the leakage flux that crosses the airgap.

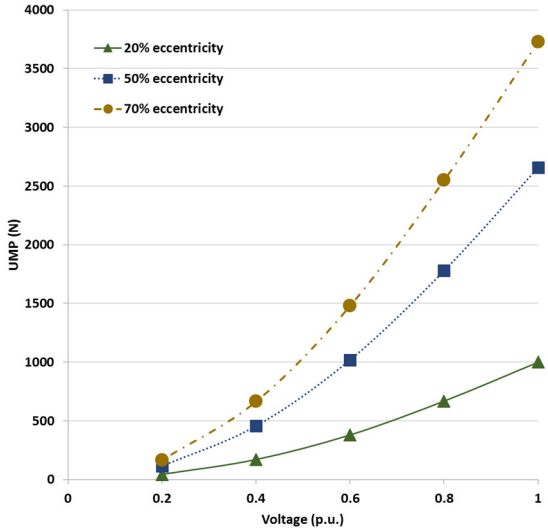

Figure 3-36: UMP with difference percentage of eccentricity vs excitation voltage.

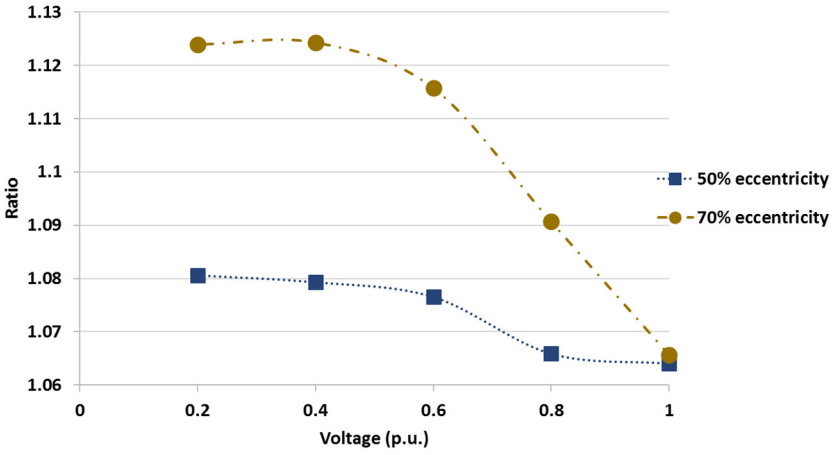

Figure 3-37: Ratio between normalised UMP of the 50% and 70% eccentricity with the 20% eccentricity.

3.10 Chapter Summary

The magnetic flux distribution around the airgap of an eccentric rotor is investigated through the analytical model by using the Permeance Harmonic Analysis. The two assumptions made for the UMP calculation of low degrees of rotor eccentricity are: 1) only the first permeance harmonic component is considered, 2) the normalised magnitude of the first permeance harmonic component is the same as the degree of eccentricity. Then, with the assumptions made, the UMP analytical model derivation is shown. The UMP is caused by the interactions between the magnetic flux harmonics with the order difference of 1.

Furthermore, the setup of the FEA has been presented in this chapter, which include meshing method, creating eccentricity, and choosing the type of winding. Then, the calibration of the force plate and the setup of experimental work were shown. After that, the UMP results taken from the experimental work and the FEA were analysed in FFT analysis. It has shown that the constant component of the UMP for static eccentricity is the dominant UMP component when compared to the 2-times supply frequency UMP component. This is because the 2-times supply frequency component is caused by the interaction between forward and backward rotating flux, in which the backward rotating flux is negligible in a series connected stator winding with balanced supplied voltage. The experimental work was done on Machine-2 to validate the 2D-FEA. The slightly lower UMP from the 2D-FEA is due to the effects of a skewed rotor that was not taken into account.

By using the FEA, a blank rotor was used to investigate the magnetic flux around the airgap, and to study the relationship between the UMP and the degrees of eccentricity. The sidebands flux caused by the rotor eccentricity were shown from the space harmonics breakdown of the magnetic flux in the airgap. Additionally, the analysis has shown that the UMP does not linearly increase for higher degree of eccentricity.

3.10.1 Practical relevance of this chapter

Understanding of the airgap flux caused by the rotor eccentricity is the core to analyze the UMP. The proposed UMP analytical models in the later part of this thesis

are based on the characteristics of the airgap flux, which include the UMP calculation for a skewed cage rotor (mentioned in Section 4.5), the UMP calculation for axial-varying static eccentricity (discussed in Section 4.6), iron and copper losses of induction machines with eccentric rotor calculation (identified in Section 4.7), and the UMP calculation through empirical method (brought out in Chapter 5). Hence, the blank rotor analysis provides insight on the changes of magnetic permeance harmonics caused by the rotor eccentricity, which could be used in the magnetic flux calculation. The reasons of using a blank rotor in the analysis is that the magnetic flux distribution will not be affected by the zigzag leakage flux and the induced current in the rotor; the comparison of the magnetic flux space harmonics between blank, cage and wound rotor is shown in Appendix D.

In addition, both the FEA and experimental work will be used to verify the analytical models described in this thesis. Therefore, the setup of both FEA and experimental work were shown in this chapter. As the results of the experimental work had a higher harmonic content, FFT analysis was shown to extract the useful force information that reflects the UMP caused by rotor eccentricity.

4 Characteristics of UMP

Based on the rotor winding configuration, induction machines can be divided into cage rotor and wound rotor induction machines. Typically, the cage rotor induction machine has a parallel connected rotor bar (see Figure 4-1(a)), in which the current in every rotor bar can be different, while the wound rotor induction machine has a series connected rotor winding (see Figure 4-1(b)), in which the same current flows in the rotor winding of the same pole. The voltage in the parallel connected rotor winding can be induced by all the magnetic flux space harmonics. Meanwhile, the voltage in the series connected rotor winding can only be induced by the magnetic flux with the fundamental pole pair harmonics group.

The parallel circuit in a cage rotor allows the flow of circulating current to produce the counteracting flux to damp the UMP. In order to calculate the damping effect, numerical methods are commonly used, because the analytical method cannot calculate the circulating current in the rotor bar [34]. Hence, UMP Damping Coefficient is proposed in the thesis, so that the damping effect can be included in the steady-state UMP analytical calculation. The proposed Damping Coefficient could reduce the computation time in calculating the UMP. In addition, the UMP Damping Coefficient can also be used to gain a better understanding in UMP damping effect.

Then, the UMP Damping Coefficient is verified by using FEA and experimental work. The airgap flux and UMP of the cage rotor and wound rotor induction machine are compared and are investigated. Also, the UMP Damping Coefficient is further used to calculate the UMP in a skewed cage rotor and axial-varying eccentricity.

Furthermore, as the magnetic circuit changes in the machine with eccentric rotor, this will cause additional power losses in the system. The power losses are calculated and compared between with and without rotor eccentricity for both the cage rotor and wound rotor induction machines.

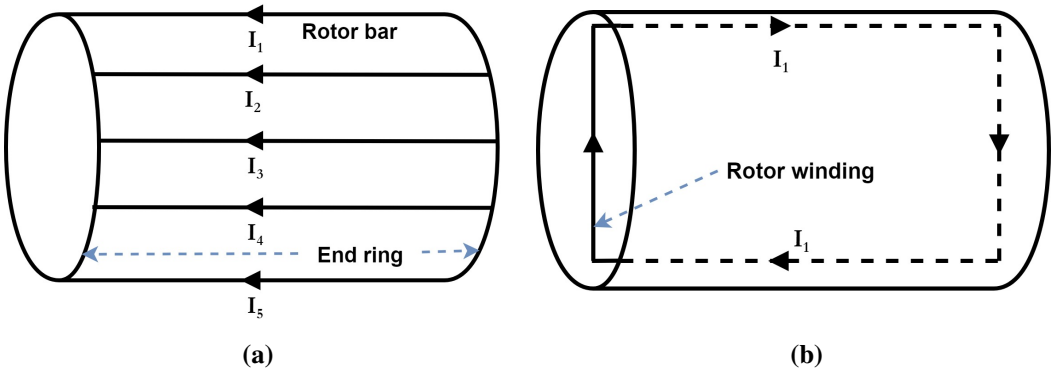

Figure 4-1: Rotor winding configuration: (a) cage rotor (parallel-connected), (b) wound rotor (series-connected).

4.1 UMP Damping Effect

Unlike the wound rotor, the cage rotor bar is not pole specific due to the parallel winding connection. As the parallel circuits in the rotor bars allow the circulating current to flow, the pole-pair ± 1 stator flux, could be induced in the parallel path in the cage rotor. The circulating current produces a counteracting flux to damp the UMP. The damping effect of the cage rotor induction machine is investigated in this section. Investigation of the damping effect is important in order to calculate the UMP of the cage rotor induction machine. The damping of the flux depends on several aspects: L/R ratio, airgap leakage flux and also flux rotational speed. Comparisons are made for these variables in this chapter.

4.1.1 Analytical model for the damping effect

The damping effect is investigated through analysing the counteracting flux produced by the rotor. The superscript "$p \pm 1$" is the sideband flux caused by the rotor eccentricity. As the pole-pair ± 1 stator flux, $\boldsymbol{\lambda}_s{}^{p\pm1}$, induced voltage across the rotor bar, the current flows in the rotor bar and produces $\boldsymbol{\lambda}_r{}^{p\pm1}$, which damps the $\boldsymbol{\lambda}_s{}^{p\pm1}$. This damping is determined by the magnitude and the angle of $\boldsymbol{\lambda}_r{}^{p\pm1}$. As $\boldsymbol{\lambda}_r{}^{p\pm1}$ is induced from the stator flux, the direction of the $\boldsymbol{\lambda}_r{}^{p\pm1}$ is opposing the $\boldsymbol{\lambda}_s{}^{p\pm1}$. For a steady state analysis, the vector diagram of the summation of $\boldsymbol{\lambda}_s{}^{p\pm1}$ and $\boldsymbol{\lambda}_r{}^{p\pm1}$ is shown in Figure 4-2. All the rotor's parameter shown refers to the stator side. The $\boldsymbol{\lambda}_f{}^{p\pm1}$ is the resultant ± 1 flux that interact with its main pole pair flux that produced the UMP. Due to the counteracting flux from the rotor, the magnitude of the $\boldsymbol{\lambda}_f{}^{p\pm1}$ is smaller than the $\boldsymbol{\lambda}_s{}^{p\pm1}$, which means the UMP is damped. Also, the damping effect changes the direction of the UMP.

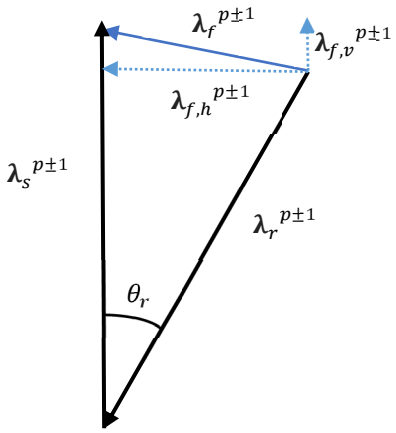

Figure 4-2: Vector diagram of the resultant flux in the airgap.

The angle difference between $\boldsymbol{\lambda}_s{}^{p\pm1}$ and $\boldsymbol{\lambda}_r{}^{p\pm1}$ (θ_r) can be determined by the voltage dropped across the reactance and the resistance, which is shown in (4-1), where R_r is the rotor resistance, L_r is the rotor inductance, and ω_{slip} is the angular frequency difference between the angular frequency of $\boldsymbol{\lambda}_s{}^{p\pm1}$ and the rotor angular frequency.

$$\theta_r = \tan^{-1}\frac{R_r}{\omega_{slip}L_r} \tag{4-1}$$

The magnitude of the ${\lambda_r}^{p\pm1}$ is a function of the rotor current, i_r. The rotor current is:

$$\boldsymbol{i_r} = \frac{\omega_{slip}{\boldsymbol{\lambda}_s}^{p\pm1}}{\sqrt{{R_r}^2 + (\omega_{slip}L_r)^2}} \tag{4-2}$$

The additional pole pair ±1 resultant flux need to be calculated in order to calculate the UMP. By using a vector summation of ${\boldsymbol{\lambda}_s}^{p\pm1}$ and ${\boldsymbol{\lambda}_r}^{p\pm1}$, the resultant magnetic flux, ${\lambda_f}^{p\pm1}$, is shown in (4-3).

$$\begin{aligned} {\lambda_f}^{p\pm1} &= \sqrt{\left({\lambda_s}^{p\pm1}\right)^2 + \left({\lambda_r}^{p\pm1}\right)^2 - 2{\lambda_s}^{p\pm1}{\lambda_r}^{p\pm1}\cos\theta_r} \\ &= {\lambda_s}^{p\pm1}\sqrt{1 + \left(\frac{\omega_{slip}k_\sigma L_r}{\sqrt{{R_r}^2 + (\omega_{slip}L_r)^2}}\right)^2 - 2\frac{\omega_{slip}k_\sigma L_r}{\sqrt{{R_r}^2 + (\omega_{slip}L_r)^2}}\cos\theta_r} \end{aligned} \tag{4-3}$$

The flux coupling factor, k_σ, was introduced and is shown in (4-4).The imperfect flux coupling will cause the ${\boldsymbol{\lambda}_r}^{p\pm1}$ value to become smaller when calculating the resultant flux direction. The value k_σ is between 0 to 1.

$$k_\sigma = \frac{L_r - L_\sigma}{L_r} \tag{4-4}$$

The leakage inductance, L_σ, varies with the slip frequency [128]. A higher rotor slip will cause magnetic saturation due to the higher current in the circuit. The saturation effect and the leakage inductance are neglected in the calculation. It was assumed that the rotor eccentricity acts toward the vertical direction, and the resultant magnetic flux component can be divided into two components:

1) Vertical component:

$$\lambda_{p\pm1}^V = {\lambda_s}^{p\pm1} - L_r\frac{\omega_{slip}{\lambda_s}^{p\pm1}}{\sqrt{{R_r}^2 + (\omega_{slip}L_r)^2}}cos\theta_r \tag{4-5}$$

2) Horizontal component:

$$\lambda_{p\pm1}^{h} = -L_r \frac{\omega_{slip}{\lambda_s}^{p\pm1}}{\sqrt{{R_r}^2 + (\omega_{slip}L_r)^2}} sin\theta_r \tag{4-6}$$

The angular shift of the magnetic flux is:

$$\theta_f = \tan\frac{\boldsymbol{\lambda}_{\boldsymbol{p\pm1}}^{\boldsymbol{V}}}{\boldsymbol{\lambda}_{\boldsymbol{p\pm1}}^{\boldsymbol{p}}} \tag{4-7}$$

Recalling the UMP derivation from (3-40)-(3-43), the α did not influence the total UMP because the $\cos^2(\alpha) + \sin^2(\alpha) = 1$. Therefore, the magnitude of the UMP is proportional to the resultant $p \pm 1$ flux. The UMP Damping Coefficient, β, was introduced to show the percentage of the UMP after damped by the rotor counteracting flux. Hence, the UMP is **lower** when the Damping Coefficient is **smaller**.

$$\beta = \frac{{\boldsymbol{\lambda}_f}^{p\pm1}}{{\boldsymbol{\lambda}_s}^{p\pm1}}$$

$$\beta = \sqrt{1 + \left(\frac{k_\sigma}{\sqrt{1 + (\frac{R_r}{L_r\omega_{slip}})^2}}\right)^2 - 2\frac{k_\sigma}{\sqrt{1 + (\frac{R_r}{L_r\omega_{slip}})^2}}\cos\theta_r} \tag{4-8}$$

$$\beta_v = 1 - L_r \frac{\omega_{slip}}{\sqrt{{R_r}^2 + (\omega_{slip}L_r)^2}} cos\theta_r \tag{4-9}$$

$$\beta_h = -L_r \frac{\omega_{slip}}{\sqrt{{R_r}^2 + (\omega_{slip}L_r)^2}} sin\theta_r \tag{4-10}$$

For the cage rotor induction machine, the UMP Damping Coefficient in (4-8) can be added as a multiplying variable into the UMP formula (3-40)-(3-43) for steady state calculation, in which the Damping Coefficient could reflect the remaining UMP

after the damping from the counteracting flux. Meanwhile, (4-9) and (4-10) can be used to find the direction of the UMP.

4.1.2 Verification of UMP Damping Coefficient

In order to verify the analytical model of the UMP Damping Coefficient, the FEA and experimental work are done. Machine-2 is used in this analysis. The analytical model only considers the fundamental magnetising flux, where the higher magnetic flux space harmonics are ignored because most of the higher space harmonics flux did not induce voltage in the rotor bar.

Therefore, in order to minimise the leakage flux or higher space harmonics flux that crosses the airgap, a low excitation frequency (10 Hz) was chosen to be used in the FEA and experimental work because it is within the rated angular slip frequency. This is because the magnetising flux is the dominant flux when the machine runs below its rated angular slip frequency. The reasons of choosing 10 Hz excitation frequency are: 1) the angular slip frequency of 0.25 slip with 10 Hz excitation frequency is equal to angular slip frequency of 0.05 slip (rated slip) with 50 Hz excitation frequency, 2) In order to verify the damping coefficient of an 8-pole machine, the rotor slip until 0.25 slip needs be investigated because the peak of the damping coefficient shown in Figure 4-3 is around 0.2 slip.

Meanwhile, due to the limitation of the test rigs design, a low magnetising flux (23% of the rated flux) and a low degree of eccentricity (20% static eccentricity toward the Y-axis direction) are selected to prevent large horizontal force that would create additional rotor eccentricity in the X-axis direction. As Voltage-Hertz control is used in the inverter drives to maintain the rated flux of the machine, the gain of the voltage-hertz relationship is set to 23% in the inverter to acquire the 23% rated flux.

Figure 4-3 shows the UMP Damping Coefficient of the 8-pole machine, which was derived from (4-5), (4-6) and (4-8). The UMP Damping Coefficient has a peak of around 0.2 slip, which is the synchronous frequency for the 5-pole pair flux. From (4-8), when the slip frequency of the 5-pole pair flux is 0, the rotor does not produce the counteracting flux to damp the 5-pole pair flux. In addition, the horizontal force

direction is also changed from negative to positive at around 0.2 slip. In (4-6), the horizontal flux formula is a sine function. The direction of the horizontal flux depends on whether the rotor flux is lagging or leading the stator flux. The rotor flux induced by the 3-pole pair flux always lags the stator flux at all the slip. However, the 5-pole pair flux changes from leading to lagging after the 0.2 slip. From here, it could be proven that the UMP caused by the fundamental magnetising flux is not acting toward the shortest airgap. The direction changes with rotating slip. However, the change in direction was negligible at a higher rotor slip when the UMP caused by the airgap leakage flux is taken into account.

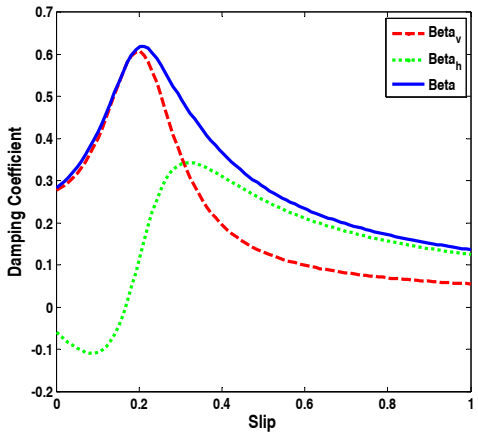

Figure 4-3: UMP Damping Coefficient for an 8-pole machine with 10 Hz excitation frequency.

Figure 4-4 shows the Y-axis UMP acts in the same direction as the eccentric rotor. As the magnetic flux density at the narrowest airgap is higher, the Y-axis UMP points to the narrowest airgap at every rotor slip. When the slip increases, the UMP increases until around 0.2 slip. This is caused by the increment of Damping Coefficient, where the UMP damping effect became least effective. When the rotor slip is larger than 0.2, the UMP Damping Coefficient starts to decrease which causes the UMP to drop because the magnetising flux reduces when the slip increases. As only the fundamental magnetising flux is considered in the analytical model, the UMP calculated from the analytical model is lower than the FEA and experimental results. Meanwhile, the UMP from the FEA results are lower than the experimental results because the skewed rotor is not taken into account in 2D-FEA.

Figure 4-5 shows the horizontal force changes its direction at around 0.2 slip. The zero-crossing point is different in all three cases, because the analytical model only considered the fundamental pole-pair flux, where the FEA and experimental works had included all the higher space harmonics. Then, the difference between the FEA and experimental works mainly come from the mechanical tolerance when creating the rotor eccentricity.

The overall pattern of the graph for Figure 4-4 and Figure 4-5 are correlated with Figure 4-3. This proved that UMP damping exists in a cage rotor induction machine. Also, this can be used to verify the proposed UMP Damping Coefficient formula.

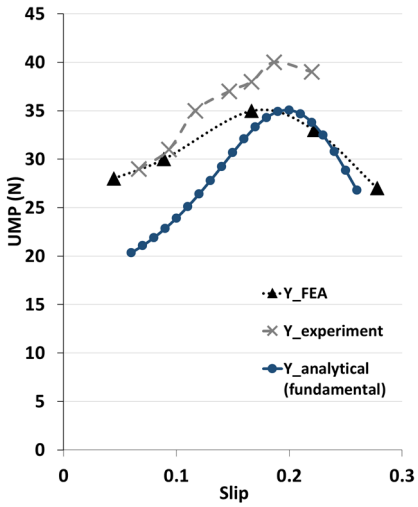

Figure 4-4: Y-axis UMP of 20% static eccentricity in Y-direction.

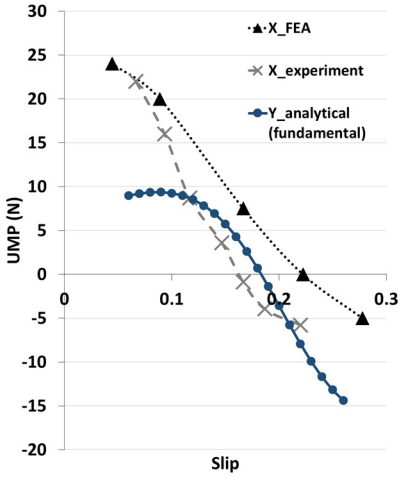

Figure 4-5: X-axis UMP of 20% static eccentricity in Y-direction.

4.1.3 Damping effect in static and dynamic eccentricity

This section discusses only the fundamental magnetising flux of the machine. The magnetising flux is the magnetic flux that couples the stator and the rotor. The fundamental flux in (3-40)-(3-43) showed that the additional ± 1 pole pair flux has a different rotational frequency for the static and dynamic eccentricity. The stator and rotor MMF were needed to calculate the magnetic flux across the airgap for the UMP calculation. Therefore, the rotational frequency of the additional pole pair fluxes needs to be investigated for estimating the rotor induced MMF. The visualisation examples in Figure 4-6 to Figure 4-9 used a 4-pole machine. The discussed magnetising flux damping effect in this section is only applicable for cage rotor induction machine.

For static eccentricity, the UMP is a function of the slip frequency of the pole pair ± 1 flux. As the fundamental magnetic flux and its pole pair ± 1 flux have the same angular frequency, the magnetic flux of a higher pole number has a slower rotation speed than the lower pole number. Figure 4-6 shows the rotating magnetic flux in the airgap, where the length of the thick arrow represents the rotational speed, and the direction of the peak magnetic flux is represented by the thin arrow; the black, purple and yellow colour represent 2, 3 and 1 pole pair respectively.

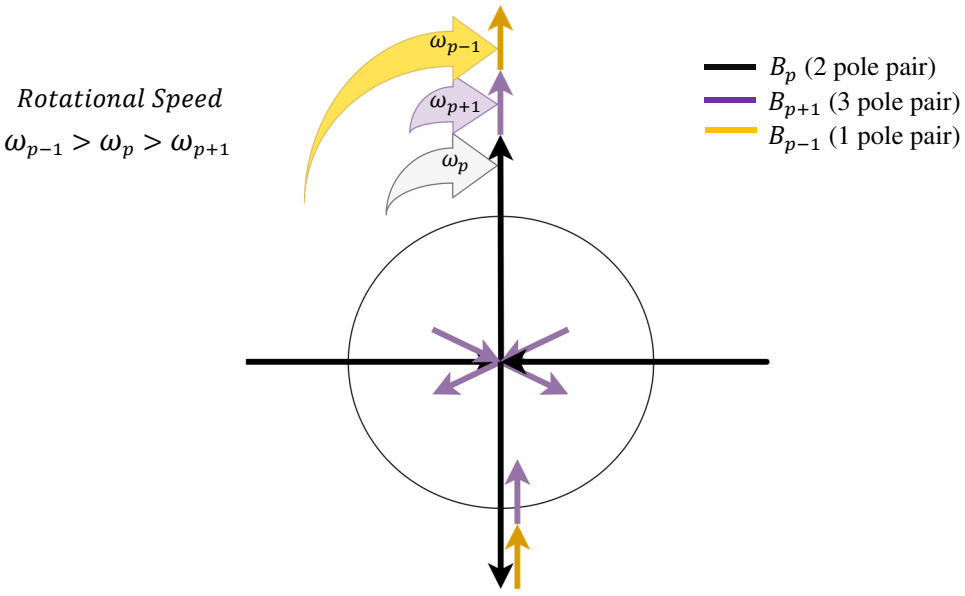

Figure 4-6: Magnetic flux vector and rotational speed with static eccentricity.

The induced rotor MMF could damp the pole pair ± 1 magnetic flux for most of the rotor slip, except at around 0.33 slip because the rotor runs at the synchronous speed of a 3-pole pair magnetic flux. Therefore, the UMP will slightly increase at 0.33 slip. Figure 4-7 shows the UMP Damping Coefficient of a static eccentricity, which was calculated from (4-8)-(4-10). Results demonstrated that the peak Damping Coefficient of the static eccentricity is at 0.333 slip. In Figure 4-7, the peak Damping Coefficient is 0.51, which means that only 49% of the additional magnetic flux can be damped by the cage rotor. Hence, the UMP is **higher** when the UMP Damping Coefficient is **larger**.

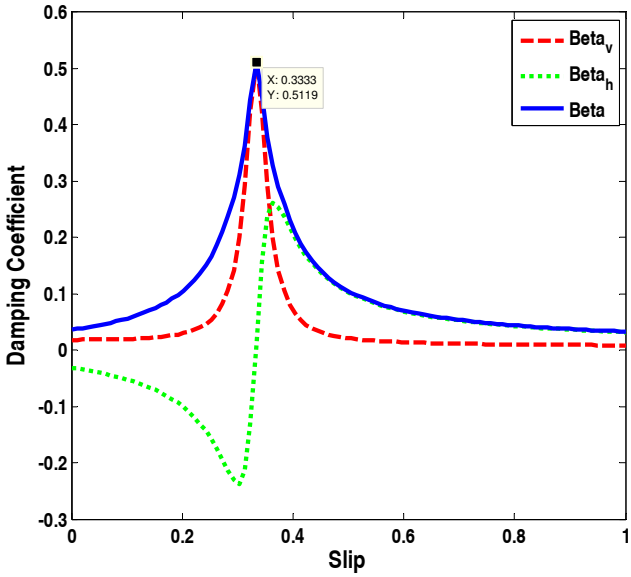

Figure 4-7: UMP Damping Coefficient for 4-pole machine with 50 Hz supply.

From [113], the author has shown that, for the dynamic eccentricity, the rotor rotational frequency is a function of the rotational speed of pole pair ± 1 magnetic flux. So, the direction of the UMP produced by the dynamic eccentricity is a function of time. Figure 4-8(a) showed that when the machine was running at a no load condition, in which the rotor rotated close to synchronous speed, the fundamental and the pole pair ± 1 magnetic flux rotated at the same rotational speed. When the slip increased, in Figure 4-8(b), the rotor rotated slower, which caused the angular frequency of $p + 1$ flux to decrease and caused the rotational speed of $p - 1$ flux to increase.

For the dynamic eccentricity, when the induction machine is running near the synchronous speed the pole pair ± 1 stator magnetic flux does not induce the

counteracting rotor MMF. Then, when the machine is loaded, the counteracting rotor MMF can be produced to damp the pole pair ±1 magnetic flux. Therefore, the UMP caused by dynamic eccentricity will reduce when the machine is loaded from no load.

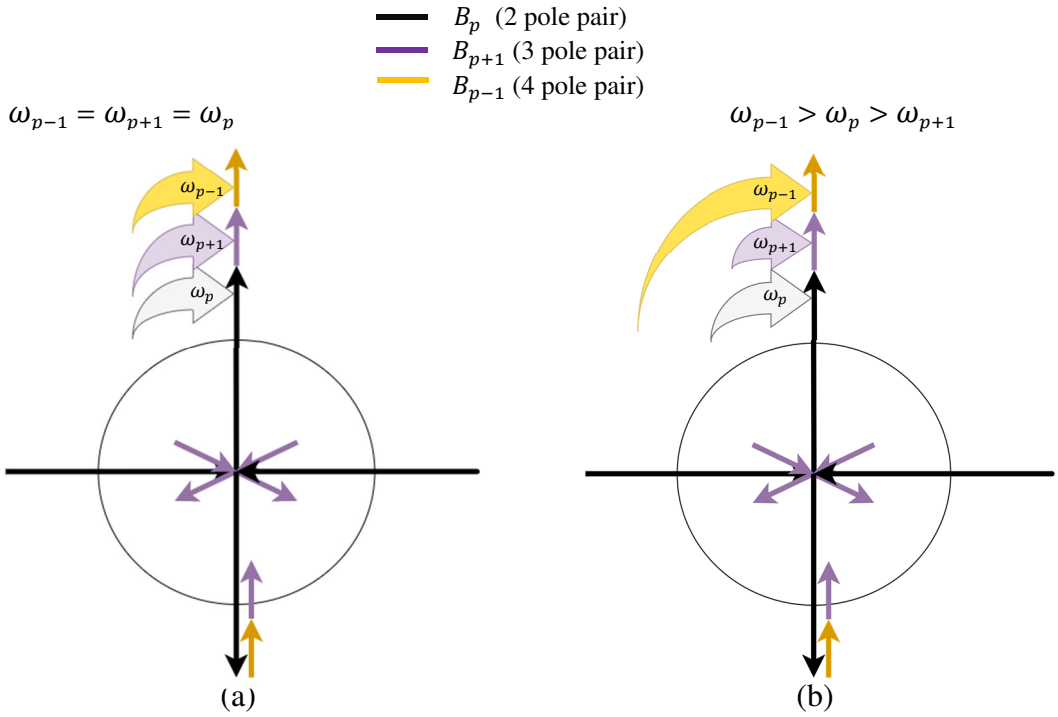

Figure 4-8: Magnetic flux vector and rotational speed of an induction machine with dynamic eccentricity at (a) slip = 0 and (b) at slip > 0

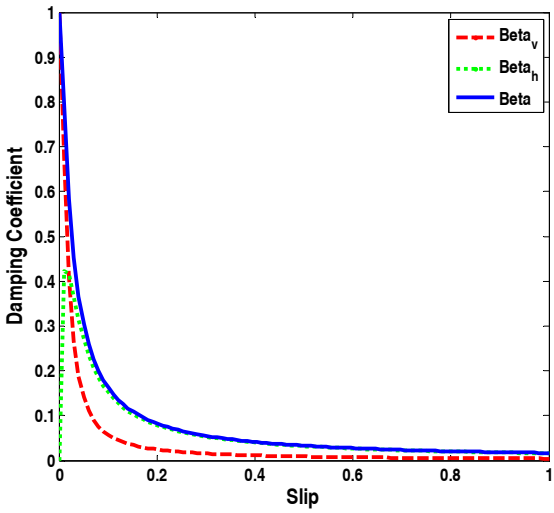

Figure 4-9: UMP Damping Coefficient for dynamic eccentricity with 50 Hz supply frequency

4.1.4 Effect of UMP from different supply frequency

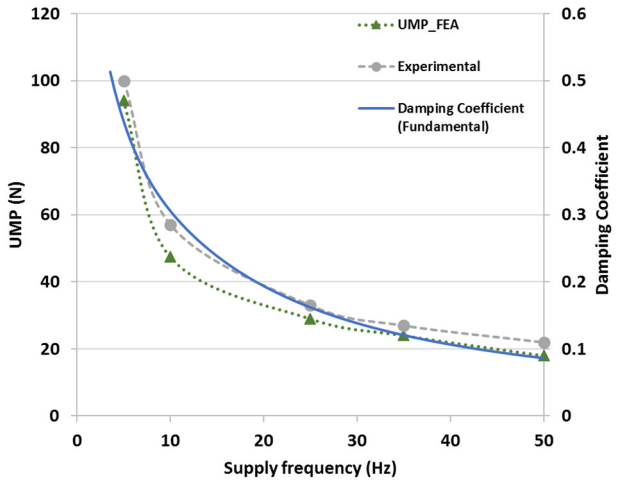

Figure 4-10: UMP and Damping Coefficient at different supply frequency.

Figure 4-10 shows Machine-2 running at no-load with a 35% rated voltage and 20% static eccentricity. To maintain the magnetising flux, the ratio of the magnitude and frequency of the voltage was controlled to be the same at every supply frequency. As the UMP Damping Coefficient is a function of the rotating flux slip frequency where the rotating flux is controlled by the supply frequency, the Damping Coefficient is affected by the supply frequency. When the magnetising flux is maintained to be the same at different supply frequency through voltage-hertz control, and the magnetising flux is the dominant flux at no load, the UMP is directly proportional to the UMP Damping Coefficient. It was demonstrated that the UMP is higher when the supply frequency is lower.

4.1.5 Effect on UMP from different rotor resistance

Different NEMA designs of induction machines have different torque-speed characteristic and also current characteristics. The main difference between the four NEMA designs is the rotor bar resistance. Therefore, it is essential to investigate the influence of the rotor resistance on the UMP damping effect as the Damping Coefficient is a function of the rotor resistance.

Machine-2 was used in the FEA simulations because changing the rotor bar resistance in the experimental work is complicated and the rotor needed would have

to be redesigned and rebuilt. Therefore, only the FEA simulation was used to prove the influence of rotor bar resistance. Let the original rotor bar resistance as 1 p.u., the tested rotor bar resistance are 1 p.u, 2 p.u., and 3 p.u. The UMP of three different rotor bar resistances from the FEA results are shown in Figure 4-11(a).

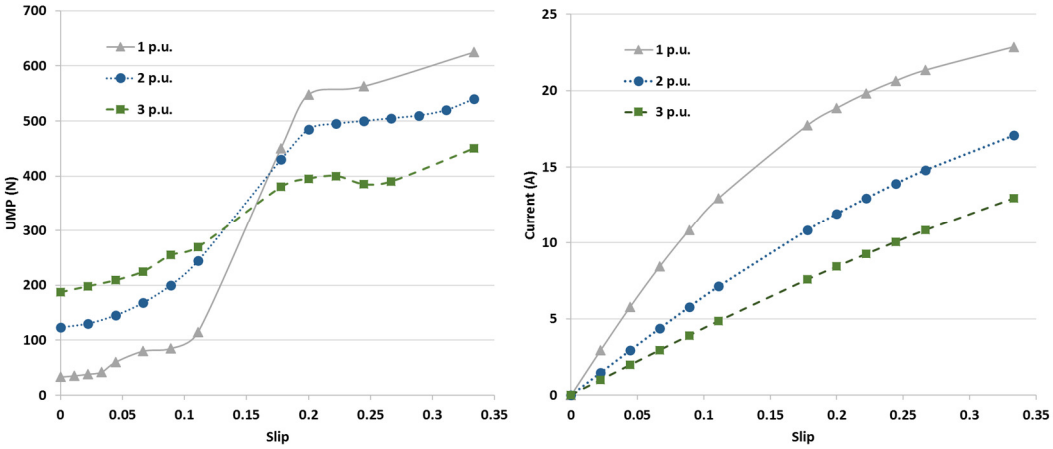

(a) (b)

Figure 4-11: Machine-2 with different rotor bar resistance: (a) UMP (b) rotor phase current.

Referring to Figure 4-11(a), from 0 to 0.1 slip, the machine with 1 p.u. rotor resistance had the lowest UMP, while the machine with 3 p.u. rotor resistance had the highest UMP, because the higher resistance would reduce the damping effect from the rotor bar. As the magnetising flux is the dominant flux at a low rotor slip, the damping effect would significantly influence the UMP. From (4-2), the counteracting current is inversely proportional to the square root of the rotor resistance. In addition, the angle between the counteracting flux and the stator flux is shifted. Both of these scenarios reduce the damping effect.

The reason that the difference of UMP becomes smaller when the slip further increased is because of the contribution of the airgap leakage flux increased as the slip increased and the airgap leakage flux is not affected by the damping effect of the rotor bar. After 0.15 slip, the machine with 1 p.u. rotor resistance had the highest UMP, while the machine with 3 p.u. rotor resistance had the lowest UMP, which is the opposite of the UMP at a low rotor slip. This scenario is due to the lower induced current in the higher rotor bar resistance. The rotor phase current in the machine is

illustrated in Figure 4-11(b). As the current of the machine with 1 p.u. rotor resistance has the highest rate of increment, the UMP of the machine had the highest rate of increment when the slip increased. This is because the contribution of airgap leakage flux increases as the current increases, which the increment of airgap leakage flux causes to a larger UMP.

4.2 Magnetic Flux across the Airgap

The magnetic flux that crosses the airgap would produce an attraction force between the stator and rotor. In a concentric rotor, an evenly distributed flux line will have a net force of zero exerted on the rotor. Therefore, this section investigates the type of flux that crosses the airgap. The magnetic flux in a machine includes, fundamental pole pair flux, slot leakage flux, belt leakage flux, zigzag leakage flux, end winding leakage flux, and skew leakage flux. The leakage flux can be defined as flux that does not couple the stator and rotor winding [118]. All leakage flux can be described as higher space harmonics flux. The skew leakage flux and the end winding leakage flux are not considered in the 2-dimension UMP analysis. The magnetic inductance of the flux that crosses is affected by the airgap permeance which produces the additional pole-pair ± 1. The UMP is produced when the additional pole pair ± 1 flux interacts with their original pole-pair flux harmonics.

The magnetic flux that crosses the airgap is produced by the stator and rotor MMF. UMP can be calculated by receiving the information of the resultant flux across the airgap. A few assumptions were made to simplify the UMP calculation:

1. The damping effect of the magnetic flux from the stator belt harmonics is negligible. The stator belt harmonics flux induces voltage in the rotor that is only 5-10% of the fundamental flux. In addition, the UMP calculation is a square function of the magnetic flux.
2. The stator and rotor airgap leakage inductance and current are assumed to be the same. As the rotor current is induced by the stator flux, it is difficult to

separate the stator and rotor airgap leakage inductance because separately excited stator and rotor would not give the accurate leakage flux information.

3. There is no interaction between the airgap leakage flux produced by the stator and the rotor.
4. Although the end winding leakage flux would also contribute to the total UMP, the end winding leakage flux would rather choose to flow through the rotor casing that has a lower magnetic reluctance than the airgap. Therefore, the end winding leakage flux is neglected for the UMP calculation.

The stator slots and the rotor slots cannot be avoided because windings need to be placed. With the presence of the stator and rotor slots, the magnetic field is distorted. The harmonic contents in the airgap include the winding arrangement harmonic and the slots harmonic [129]. An analytical model can only estimate the fundamental flux, but not the higher space harmonics flux accurately, because the pattern of the airgap leakage flux is different for each machine design and it is difficult to be estimated analytically whether the leakage flux is crossing the airgap. Therefore, the FEA was used in the analysis, because the geometry and the windings of the induction machine were to be included in the analysis. After receiving the results from the FEA, the results can then be used for the UMP calculation through empirical method. This will be shown in Section 5.1.

4.2.1 Categorised airgap magnetic flux

All the harmonics fields induced back EMF in the winding, which is shown in (4-11).

$$E = \sum_{n=-\infty}^{+\infty} E_n \tag{4-11}$$

The magnetic flux that crosses the airgap can be divided into two groups: fundamental pole-pair harmonics and the all higher harmonics flux. The higher harmonics flux can be known as airgap leakage flux. The reason for separating into two groups is that the sideband of the fundamental flux will be damped by the cage rotor, but the airgap leakage flux will not be damped by the cage rotor. So, this categorisation is not as important for the wound rotor induction machine, where there

is no counteracting flux produced by the pole-specific rotor. The inductance of the fundamental harmonics is shown in (4-12).

$$L_1 = L_m \tag{4-12}$$

The inductance for the airgap leakage flux is shown in (4-13).

$$L_\delta = \delta L_m \tag{4-13}$$

where,

$$\delta = \sum_{\substack{n=-\infty \\ n\neq 1}}^{+\infty} \left(\frac{k_{w,n}}{n k_{w,1}}\right)^2 \tag{4-14}$$

The winding harmonics calculation in (4-14) was shown in Section 3.2. When rotor eccentricity exists, the harmonics will not be affected by the degree of eccentricity [130]. Therefore, the harmonics calculation for a concentric rotor can be used in calculating eccentric rotor. The airgap leakage flux mainly involved:

1) The stator belt harmonics: $\boldsymbol{c6 \pm 1}$
2) The stator slots harmonics: $\boldsymbol{cN_s \pm p}$
3) The rotor belt harmonics: all odd harmonics except the fundamental
4) The rotor slots harmonics: $\boldsymbol{cN_s \pm p}$

4.2.2 Fundamental magnetising flux

Both the fundamental magnetising flux and airgap leakage flux change with slip. The airgap leakage flux increases when the slip increases. When the leakage flux increases, the fundamental magnetising flux will drop.

Figure 4-12 shows the fundamental magnetising flux of a machine with 1.5 ohm stator resistance, 0.5 ohm rotor resistance, and 6% stator and rotor leakage reactance. The magnetising flux is reduced with the increment of slip. As the total flux in a machine is constant if the voltage across the stator resistance is neglected, the leakage flux increases with the increment of slip.

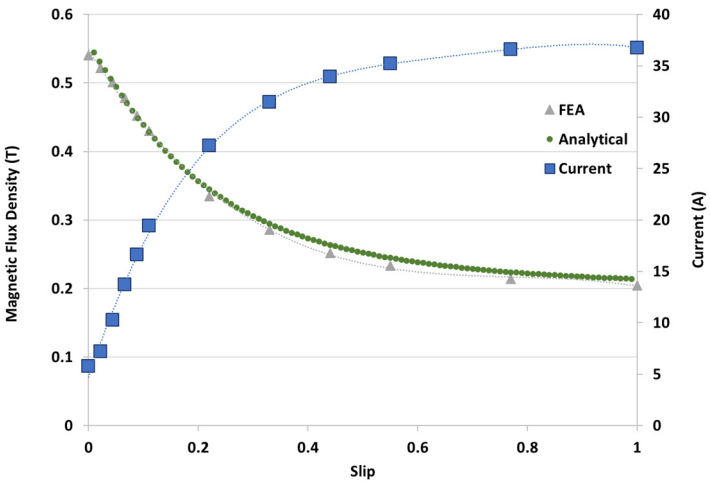

Figure 4-12: Fundamental magnetising flux.

4.2.3 Airgap leakage flux

The assumption was made that the airgap leakage flux is the flux that does not couple between the stator and rotor. The airgap leakage flux is a function of the airgap leakage flux inductance and the current, as shown in (4-15).

$$\Phi_\delta = L_\delta(i)i \qquad (4\text{-}15)$$

The inductance is a function of the current, because the magnetic permeability of the stator and rotor core is not linear. The leakage inductance shown in (4-15) is referred to as flux linkage with the fundamental pole pair winding.

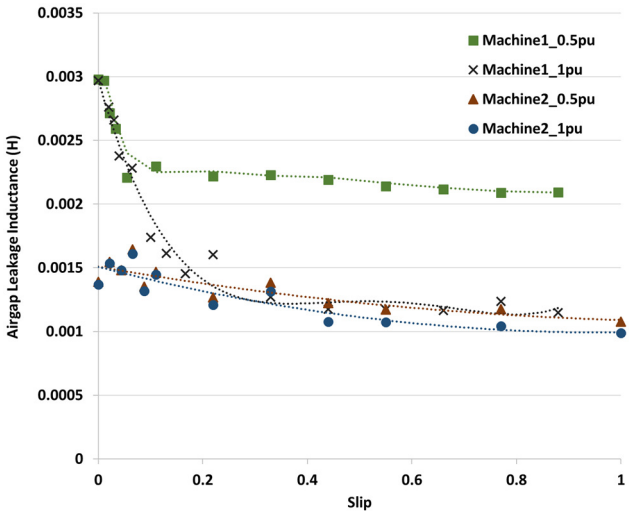

Figure 4-13: Airgap leakage inductance.

It was stated in [49] that the airgap flux is susceptible to continual variation and also affected by the magnetic saturation, so the author extracted the magnetic flux density value in FEA from the centre of the airgap to reduce the error. When coupling between the stator and rotor flux is not considered, static FEA simulation is commonly used to find the leakage inductance of the induction machine by [128], [131], [132]. As the airgap leakage inductance is a subset of the total leakage inductance and the airgap leakage flux is contributed by both the stator and rotor MMF, instead of using the static FEA simulation, the time-stepping FEA simulation is used to find the airgap leakage inductance at different rotor slips. The airgap leakage inductance is found based on (4-15) with the airgap leakage flux taken from FEA. Figure 4-13 shows the airgap leakage inductance for Machine-1 and Machine-2 at their rated voltage and also at half of the rated voltage.

From Figure 4-13, the leakage inductance for all cases initially reduces when the slip increases, because of the increment of current causes magnetic saturation. The changes in the airgap leakage inductance start to stabilise after 0.3 slip, because of the slow current increment. Machine-1 is a 2-pole pair machine with a 0.5 mm airgap, and Machine-2 is a 4-pole pair machine with a 0.9 mm airgap. With a bigger airgap, Machine-2 has a much lower airgap leakage inductance than Machine-1. This is because the magnetic reluctance is higher for a bigger airgap. Analytically, from (4-13), it shows the airgap leakage inductance is a function of the magnetising inductance, where magnetising inductance is a function of the airgap length.

When Machine-1 was running at its rated voltage, the leakage inductance dropped drastically as the slip increased when compared with other cases. The synchronous speed of Machine-1 is twice that of Machine-2, which caused the current to be higher with the same slip when compared to Machine-2. Therefore, when Machine-1 is supplied with the rated voltage, the high current flows in the high slip region caused deep core saturation and caused the airgap leakage inductance to drops drastically.

4.2.4 UMP from the airgap leakage flux

From the assumptions made in Sub-section 3.1.3, the magnitude of the $p \pm 1$ flux is proportional to the degree of eccentricity and the magnitude of p flux. When the degree of eccentricity and the machine parameter are constant, the UMP is proportional to the summation of the square function of all space harmonics magnetic flux in a concentric airgap, which is shown in (4-16). For a concentric rotor, only magnetic flux with space harmonics associated with its pole-pair number exists.

$$UMP \propto \sum_{\substack{p=3 \\ odd}}^{\infty} {B_p}^2 \tag{4-16}$$

Regarding the induced voltage calculation from (3-22), the total induced back EMF from the airgap leakage flux is proportional to the multiplication of the overall airgap leakage inductance with the current. For the leakage inductance calculation, the higher magnetic flux harmonics contribute less to the inductance calculation because it is referred to the flux coupled to the fundamental pole pair windings. However, from (4-24), the magnitude of each harmonic that adds to the UMP calculation only depends on the magnitude of the magnetic field.

Since the current B^2component has a quadratic relationship with the current and the core saturation affects the B squared component, the UMP relationship can be simplified as in (4-17), where the magnitude of each magnetic flux harmonics is assumed to be linearly proportional to the current.

$$UMP \propto I^2 k_{sat}(I) \tag{4-17}$$

4.2.5 Overview

As B^2 is proportional to the UMP, the B^2 of the fundamental harmonics flux and the airgap leakage flux with different rotor slips are analysed in this section. The B^2 of Machine-1 and Machine-2 are shown in Figure 4-14 and Figure 4-15 respectively. Machine-1 is a 2 pole-pair machine with 0.5 mm airgap, and Machine-2 is a 4 pole-

pair cage rotor machine with 0.9 mm airgap. The B^2 calculation in this section does not include the UMP damping effect from the cage rotor.

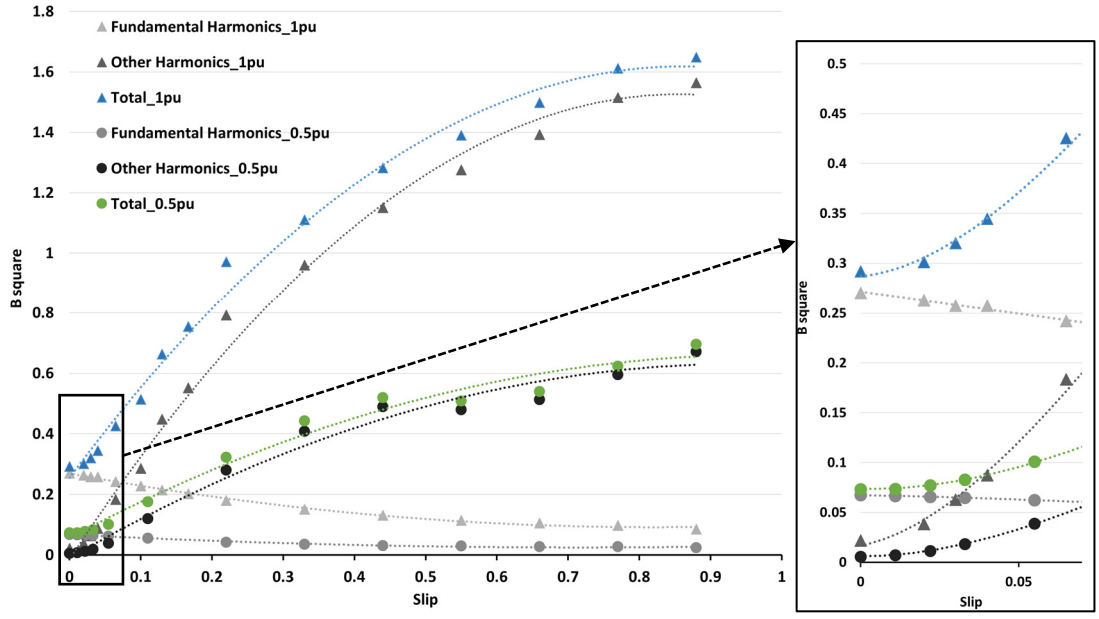

Figure 4-14: B squared graph for Machine-1.

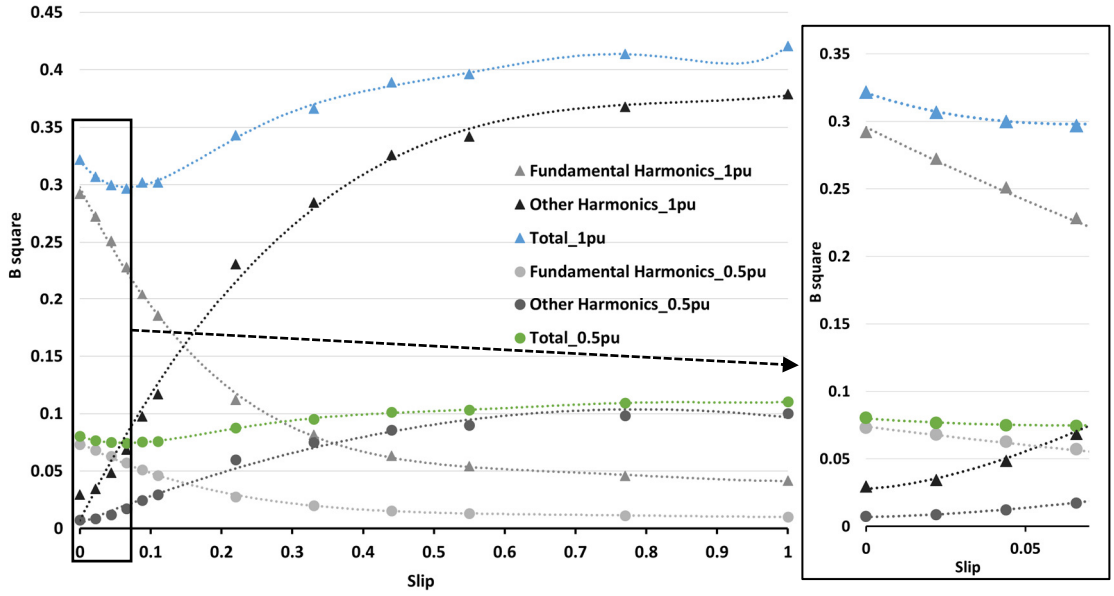

Figure 4-15: B squared graph for Machine-2.

The B^2 value for the fundamental magnetising flux reduced when the slip increased. Due to Machine-2 having a higher leakage factor, the rate of reduction of the fundamental magnetising flux of Machine-2 was larger than Machine-1 as the slip

increased. Other than this comparing Figure 4-14 and Figure 4-15, it clearly shows that the B^2 value for the fundamental magnetising flux at a synchronous speed is the same regardless of the airgap length and the pole pair number because the rated airgap flux is the same for both machines. Then, for both Machine-1 and Machine-2, the B^2 caused by the fundamental flux with the 0.5p.u excitation voltage is four times lower than the 1 p.u. excitation voltage because of the quadratic relationship. The 4-times relationship was almost constant throughout different operating slips.

As the airgap of Machine-1 is smaller than Machine-2, Machine-1 has a much larger B^2 from the airgap leakage flux than Machine-2. This is because the lower reluctance in the smaller airgap of Machine-1 causes the more magnetic flux crosses the airgap. Meanwhile, due to the saturation effect in the high slip region, for Machine-1, the difference of the B^2 from the airgap leakage flux between 0.5 p.u. and 1 p.u. at the rated slip, it got smaller as the slip increased, where the difference became only 2.2 times at a 0.9 slip. At the high slip region, Machine-2 has a lower current than Machine-1 because Machine-1 has a lower pole-pair number than Machine-2. Therefore, the saturation effect of Machine-2 is not as significant as Machine-1. This scenario has been discussed in Sub-section 4.2.4. If we compared Machine-1 with 1 p.u. and Machine-2 with 0.5 p.u., although the current was almost the same, the smaller airgap would cause B^2 from airgap leakage flux to be higher.

The total B^2 is the summation of the B^2 from the fundamental flux and the B^2 from the airgap leakage flux. In Machine-2, the total B^2 reduced when the slip increases from 0 to 0.05 slip. However, the reduction of the total B^2 did not happen in Machine-1. This is because of the increment of airgap leakage flux in Machine-2 is lower than Machine-1.

However, the total B^2 shown in this section did not take into account the damping effect from the cage rotor. So, it could not directly reflect the total UMP in Machine-1 and Machine-2, which are the cage rotor induction machine. In order to get the relationship between the B^2 with the UMP in the cage rotor induction machines,

the B^2 caused by the fundamental flux needs to be multiplied with the Damping Coefficient.

Therefore, if the damping effect is considered, it has been shown in Section 4.1 that 95% of the B^2 can be damped by the cage rotor when it is supplied with a 50 Hz excitation frequency. In this case, the dip of the total B^2 at the rated slip shown in Figure 4-15 will not exist, because the of contribution of the B^2 caused by the fundamental flux had been significantly reduced. Furthermore, when the machine is running in its operating region, the change of UMP is nearly proportional to the B^2 caused by the airgap leakage flux.

4.3 Comparison between Wound Rotor Induction Machine and Cage Rotor Induction Machine

To further investigate the UMP damping effect in the cage rotor induction machine, which had been pointed out in Section 4.1, comparison of the UMP between the wound rotor induction machine and the cage rotor induction machine is presented in this section.

Before analysing the differences, previous experimental work done by other researchers was first investigated, in order to validate the findings in this section. Table 4-1 shows the tabulated summary of the experimental results done by other researchers for both types of induction machines. The results had shown that the UMP increases when the machine with static eccentricity is loaded, in which this is correlated with the results taken in this thesis.

Although the machine used by each researcher had different machine parameters, the table shows the significant UMP difference between the cage rotor and the wound rotor induction machine when static eccentricity occurred. For example, with the same machine parameters used in Case-1 and Case-5, the UMP of Case-1 (wound rotor) with 35% of static eccentricity is 370% larger than the UMP of Case-5 (cage rotor) with 45% of eccentricity.

As the magnetising flux can be damped by the cage rotor, the UMP difference between the cage rotor and the wound rotor induction machine is significant at both

no-load and full-load conditions; the magnetising flux is the dominant flux when the machine operates below the rated slip (See Figure 4-14). The comparison between cage rotor and wound rotor induction machine with static eccentricity will be discussed in Sub-section 4.3.1.

Other than the rotor winding configuration affecting the damping of the UMP, the type of eccentricity at different load will also affect the damping of UMP. There is no previous experimental work done on the dynamic eccentricity of the wound rotor induction machine, because the magnitude of the UMP of dynamic eccentricity is the same as static eccentricity.

For the cage rotor induction machine, there is a minimal UMP damping effect on the UMP of dynamic eccentricity when it is not loaded. The analytical model of this scenario was discussed in Sub-section 4.1.3. Therefore, by comparing Case-9 and Case-10 which used the same cage rotor induction machine, the UMP of the rotor with 20% dynamic eccentricity was 240% higher than the rotor with 20% static eccentricity at no-load. When the machine operated at full load, the difference of UMP between Case-9 and Case-10 was reduced to 70%. This is because of the increment of the effectiveness of the UMP damping effect, which is shown in the UMP Damping Coefficient from Figure 4-9. The UMP caused by the dynamic eccentricity will be further discussed in Sub-section 4.3.4 with the FEA simulations.

No.	Ref.	Rating	r x L	Eccentricity	Type of eccentricity	Airgap Length	Phase Voltage	**No-load UMP**	**Full-load UMP**
Wound Rotor Induction Machine									
1	[90]	10kW	0.017	0.35	Static	0.75mm	240V	**≈3.70kN**	**≈4kN**
2	[133]	7.46kW	0.016	0.30	Static	0.5mm	240V	**≈1.20kN**	**-**
3	[134]	15kW	-	0.25	Static	-	240V	**0.77kN**	**1.10kN**
4	[92]	-	0.03	0.40	Static	1.5mm	240V	**1.45kN**	**-**
Machine-3 (FEA)		7kW	0.016	0.30	Static	0.5mm	240V	**1.28kN**	**1.6kN**
Machine-4 (FEA)		5.5kW	0.016	0.30	Static	0.5mm	240V	**1.05kN**	**1.25kN**
Cage Rotor Induction Machine									
5	[90]	10kW	0.017	0.45	Static	0.75mm	240V	**≈0.80kN**	**≈1.10kN**
6	[15]	-	0.03	0.40	Static	0.5mm	120V	**0.02kN**	**≈0.17kN**
7	[40]	35kW	0.03	0.45	Static	0.5mm	240V	**≈0.2kN**	**-**
8	[135]	15kW	0.014	0.04	Static	0.45mm	240V	**≈0.03kN**	**-**
9	[136]	15kW	0.017	0.20	Static	0.45mm	220V	**0.39kN**	**0.55kN**
10	[136]	15kW	0.017	0.20	Dynamic	0.45mm	220V	**1.33kN**	**0.95kN**
11	[137]	11kW	0.012	0.45	Dynamic	0.56mm	240V	**1.35kN**	**1.00kN**
Machine-1 (FEA)		7kW	0.016	0.50	Static	0.5mm	240V	**0.26kN**	**1.5kN**
Machine-2		5.5kW	0.014	0.20	Static	0.5mm	120V	**0.04kN**	**0.08kN**

Table 4-1: Overview of the experimental results from previous work and the results from this thesis.

4.3.1 Static eccentricity

The comparisons were made between Machine-1 (4-pole cage rotor) and Machine-3 (4-pole wound rotor). Figure 4-16 shows the magnetic field of both induction machines at synchronous speed. The rotors have the same static eccentricity of 50% towards the negative Y-axis direction.

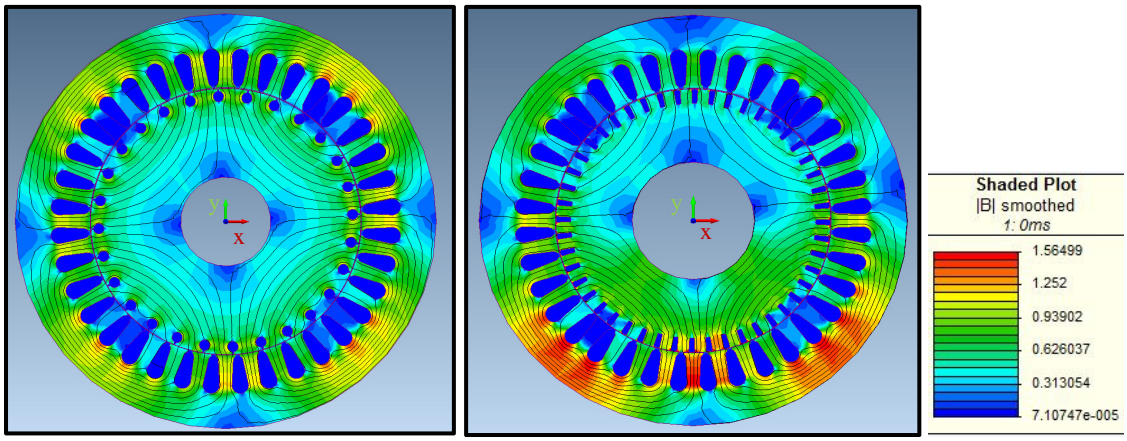

(a) (b)

Figure 4-16: FEA results: (a) Cage rotor (b) Wound rotor induction machine.

From Figure 4-16 (b), the wound rotor induction machine has a higher magnetic flux density at the negative Y-axis direction. For Figure 4-16 (a), even though there is a 50% eccentricity, the magnetic flux is more evenly distributed around the machine. The magnetic flux distribution around the airgap is shown in Figure 4-17.

In Figure 4-17, the dotted line is the magnetic flux density of a concentric rotor, in which only the fundamental flux was considered. By comparing Figure 4-17 (a) and Figure 4-17 (b), the cage rotor has a more evenly distributed magnetic flux than the wound rotor. This is because the additional pole pair ± 1 flux was damped by the parallel windings of the cage rotor bar. Therefore, for the wound rotor in Figure 4-17 (a), in which the rotor does not damp the magnetic flux and the narrowest airgap of the rotor eccentricity is at 270°, the magnetic flux density at 270° was higher than the magnetic flux density at 90°.

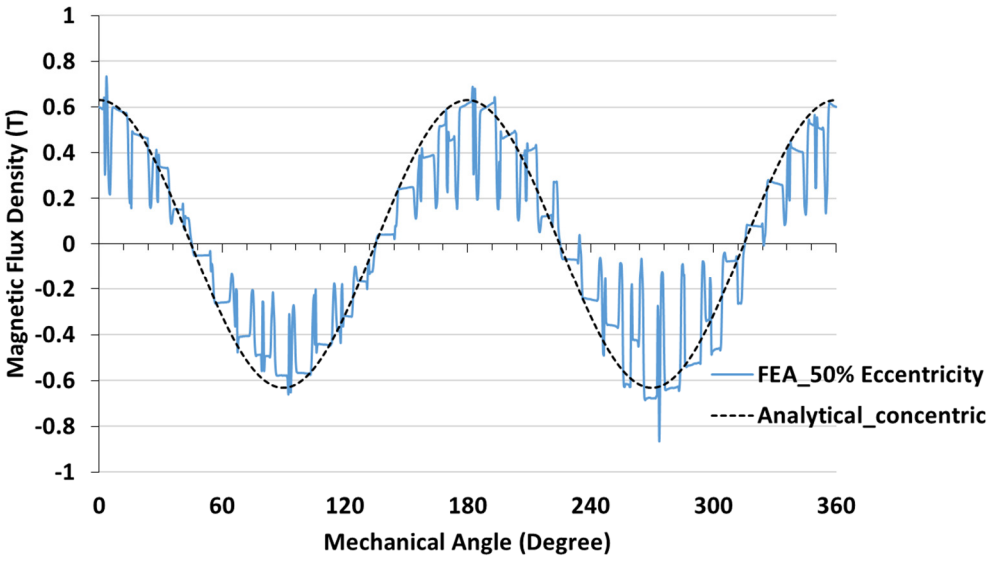

(a)

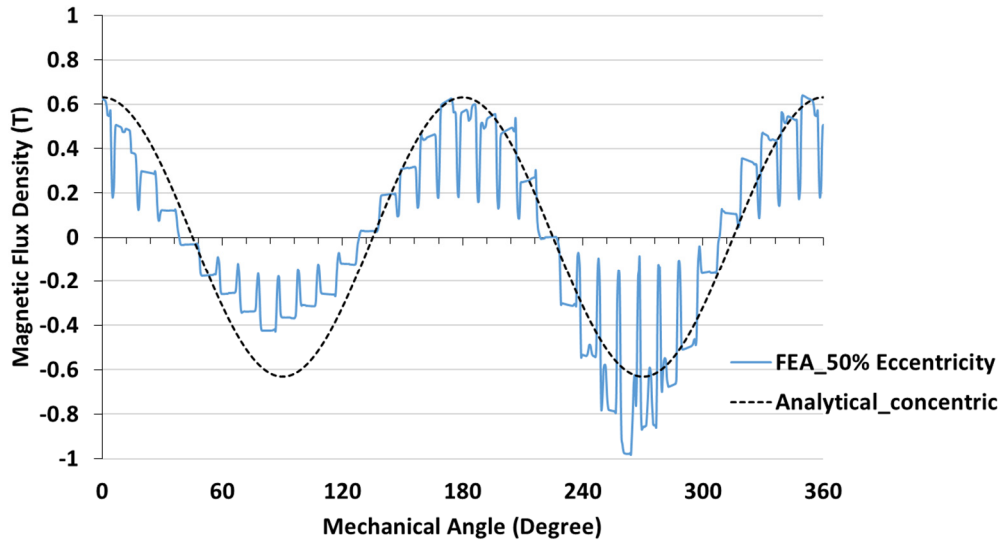

(b)

Figure 4-17: Magnetic flux density distribution (a) Cage rotor (b) Wound rotor.

Further to the magnetic flux density comparison of cage and wound rotor induction machine, the UMP of Machine-1 and Machine-3 from no-load to full-load are illustrated in Figure 4-18. In order to validate the findings, the experimental and FEA results of Machine-2 are added into the comparison in Figure 4-18. 50% of static eccentricity in Y-axis direction was set in the three machines. Both Machine-1 and Machine-3 are excited with rated voltage, while 50% of the rated voltage is used on Machine-2.

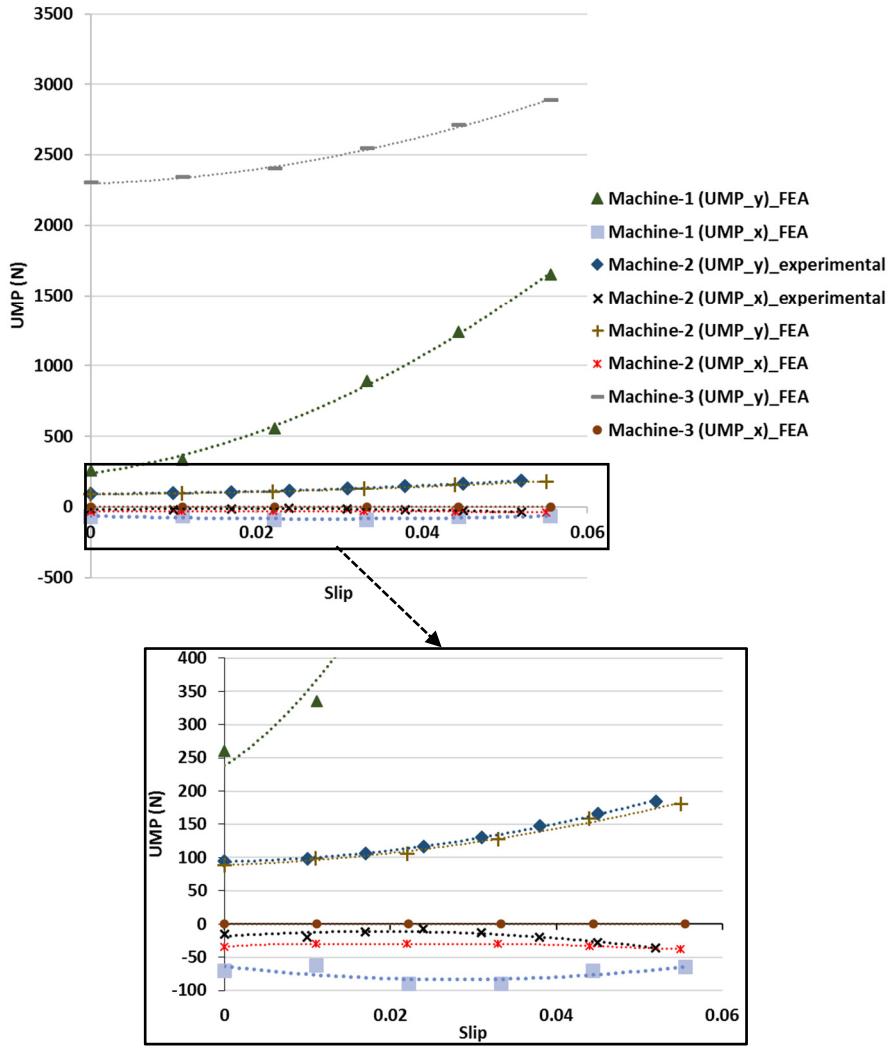

Figure 4-18: UMP of the three machines with 50% of static eccentricity.

In Figure 4-18, the FEA model of Machine-2 is validated with the experimental result. In the Y-axis UMP, the FEA results are correlated with the experimental results. However, there is a difference of UMP in the X-axis direction between the experimental and FEA results. The difference might be caused by the mechanical error when creating the eccentricity in experimental work. For example, 10% error in the experimental work would cause a UMP of around 25 N when the machine is excited with 0.5 p.u. voltage. In [138], the author pointed out that 10% of rotor eccentricity, due to the manufacturing tolerance, might exist even in a newly-manufactured machine.

In Figure 4-18, comparing the forces of the three induction machines, three points can be concluded:

1) The UMP of cage rotor induction machine is generally much lower than the wound rotor induction machine.
2) Cage rotor induction machine has a non-zero X-axis UMP when the static eccentricity is in Y-axis direction.
3) The UMP increases quadratically as the slip increases

Firstly, as shown in Figure 4-18, the Y-axis UMP of the cage rotor is generally much smaller than the wound rotor induction machine. Comparing Machine-1 and Machine-3, when the machine was running at synchronous speed, Machine-3 had a UMP of 2300 N, and Machine-1 had a UMP of 260 N. The difference of around 2000 N mainly came from the damping of the magnetising flux by the cage rotor, in which the magnetising flux was the dominant flux when the machine operated near to synchronous speed.

Secondly, the existence of X-axis UMP in the cage rotor induction machines is due to the damping of UMP caused by the circulating current, which was discussed in Section 4.1. The X-axis UMP of the wound rotor induction machine was zero because the rotor eccentricity was set toward the Y-axis direction and the damping of UMP did not exist

Thirdly, the UMP increases quadratically as the slip increases because of the increment of airgap leakage flux, which is caused by the increment of the current. However, the rate of increment of Machine-2 is much lower than Machine-1. This is because of the larger airgap length would reduce the airgap leakage inductance, which was discussed in Sub-section 4.2.3. Furthermore, due to the fact that Machine-1 and Machine-3 have the same airgap length and machine's dimensions, the UMP caused by the airgap leakage flux should be almost the same. However, the difference of the Y-axis UMP decreased as the slip increased. This was mainly because the effectiveness of UMP damping reduced as slip increased for static eccentricity (See Figure 4-7).

Then, FFT analysis is applied on the airgap flux of Machine-1 and Machine-3 at different load, in which the detailed space harmonics order of the magnetic flux could be used to prove the discussions from Section 4.2. In addition, it can also be used to investigate the difference between cage rotor and wound rotor induction machine. The airgap space harmonics order shown in the latter part of the thesis are the number of the pole pair harmonics, instead of the harmonics order of the fundamental pole pair. The simulation results for a wound rotor induction machine is shown in Figure 4-19, and the simulation results for a cage rotor induction machine is shown in Figure 4-20. In this section, the space harmonics are shown until the 60th pole-pair space harmonics for each analysis.

4.3.2 Airgap flux harmonics in the wound rotor induction machine

Figure 4-19(a) shows that all the odd pole-pair space harmonics do not exist in the airgap. This means that there is no UMP acting on the rotor, because the UMP is produced by the interaction between B_p and $B_{p\pm1}$. For the magnetic flux space harmonics around the airgap, the 34th and 38th harmonics are the stator slot harmonic of Machine-3. Other than this, the wound rotor with 48 rotor slots has the rotor slot harmonics of the 46th and 50th. The belt harmonics are all the even pole pair harmonics, except the fundamental pole pair harmonics. Due to the balanced three-phase connections, the triplen harmonics of the stator belt harmonics and the wound rotor belt harmonics are zero.

The fundamental pole-pair harmonics (2nd harmonic) dropped as the load increased, because of the increment of the rotor leakage flux. Other than the fundamental harmonics, all the space harmonics increased when the load increased.

Figure 4-19 (b) shows that the odd harmonics airgap flux exists because of the rotor eccentricity. The odd harmonics magnitude is a function of the even harmonics that caused by rotor eccentricity, which is shown in (3-19). The interaction between all B_p and $B_{p\pm1}$ produces UMP.

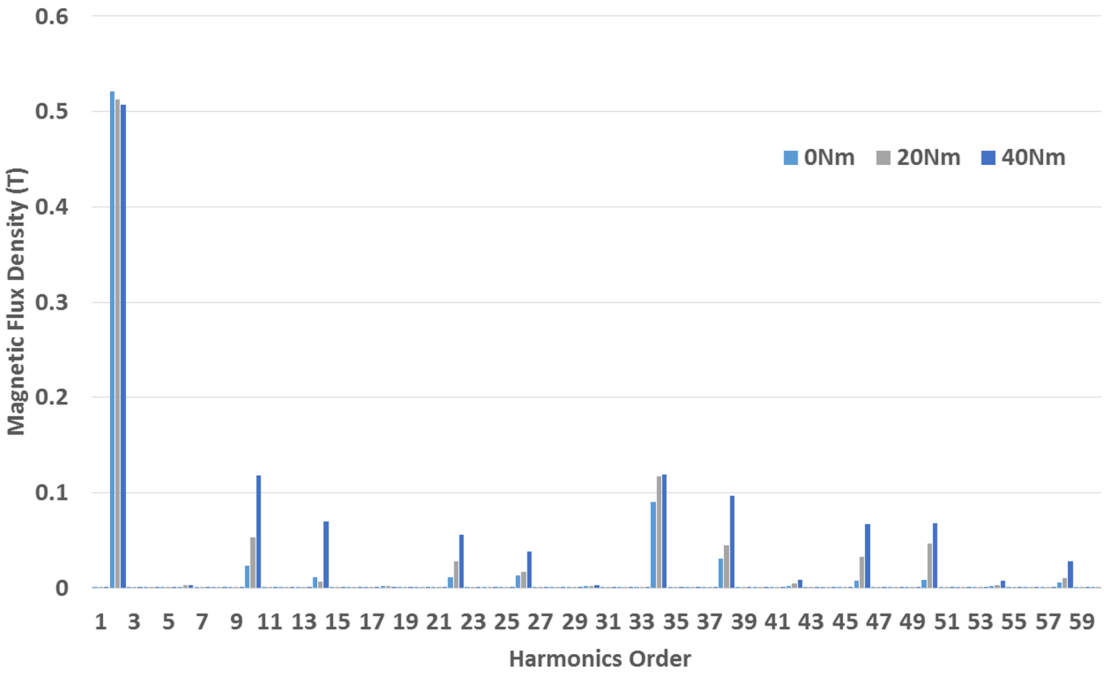

(a)

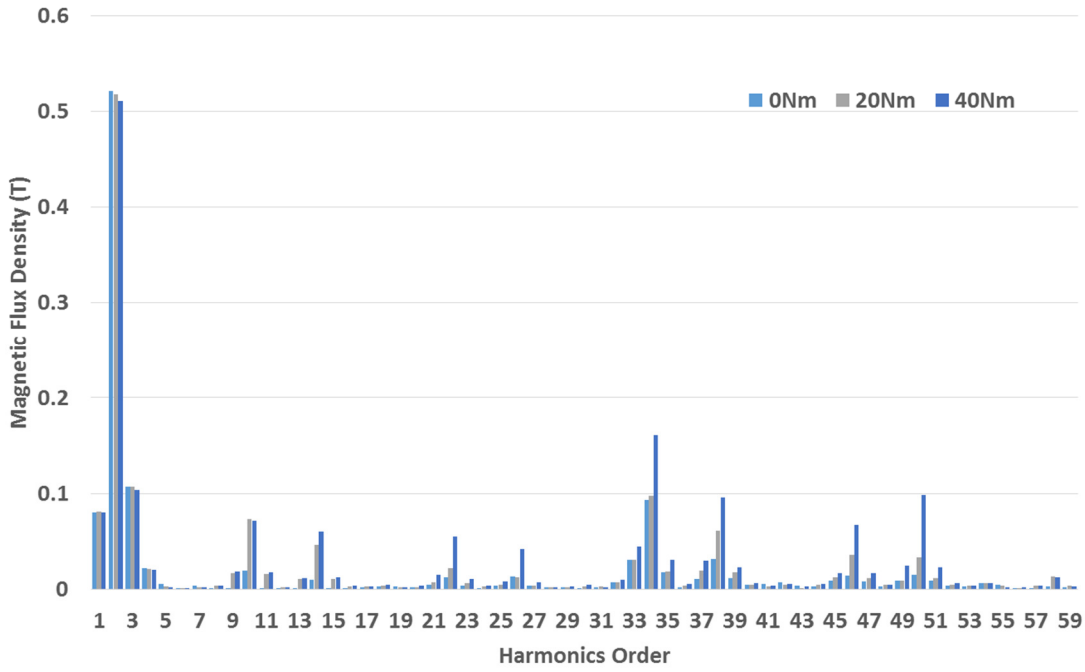

(b)

Figure 4-19: Airgap flux space harmonics in wound rotor induction machine (Machine- 3) of: (a) concentric rotor (b) 50% static eccentricity.

4.3.3 Airgap flux harmonics in the cage rotor induction machine

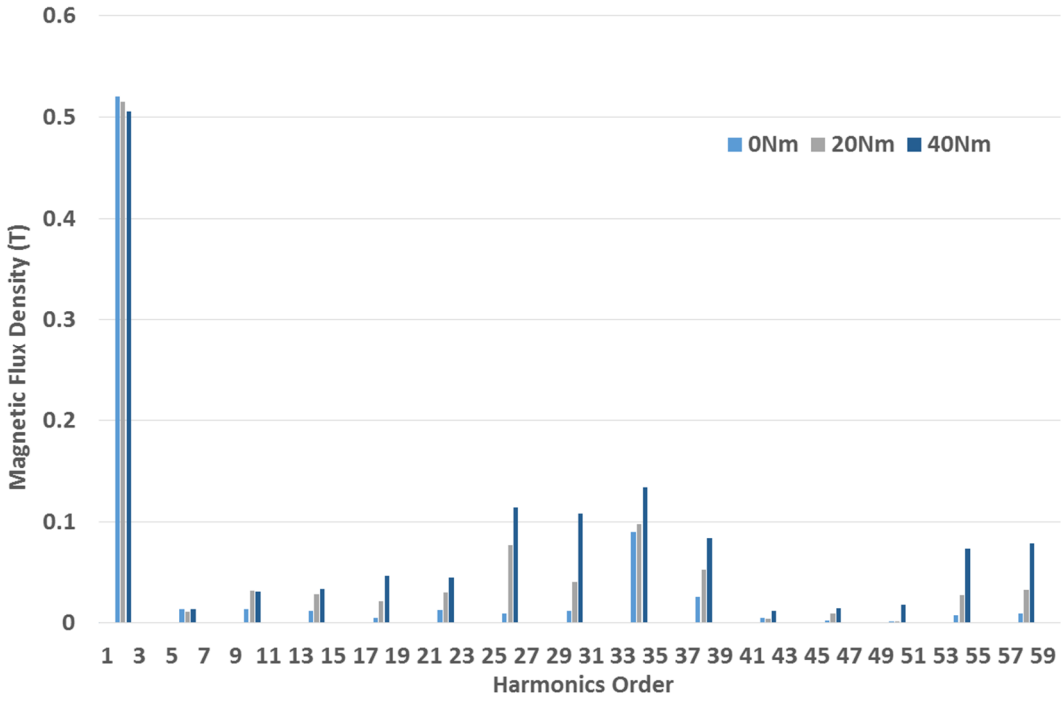

(a)

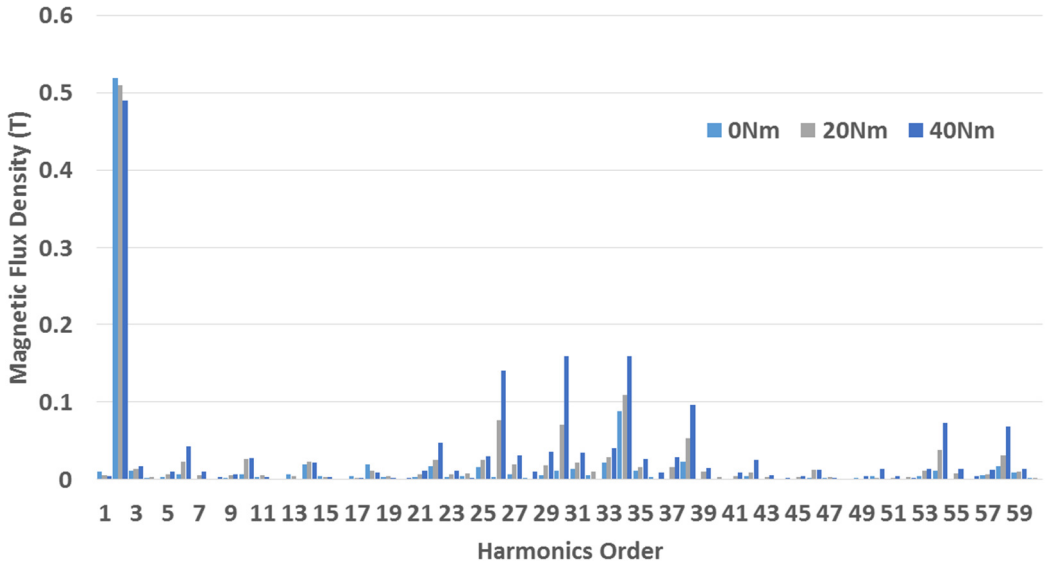

(b)

Figure 4-20: Airgap flux space harmonics cage rotor induction machine (Machine-1) of (a) concentric rotor (b) 50% eccentricity.

From Figure 4-20 (a), unlike the wound rotor which is pole-specific where the triplen harmonic is nullified, the cage rotor produced its own belt harmonics which

include the triplen harmonics (6^{th}, 18^{th}, 30^{th}). Then, the cage rotor with 28 rotor bars had the first rotor slot harmonics of 26^{th} and 30^{th}, and second rotor slot harmonics of 54^{th} and 58^{th}. The second rotor differential harmonics are smaller than the first rotor differential harmonics. This means that the higher harmonics magnitude contributes less to the overall UMP, because the UMP is proportional to the sum of the magnetic flux squared. When comparing Figure 4-19(b) and Figure 4-20(b), it shows that the magnitude of the 1^{st} and 3^{rd} harmonics produced by the fundamental are significantly smaller in the cage rotor than the wound rotor. This is because the counteracting flux produced by the cage rotor could damp the sideband harmonics of the fundamental magnetising flux.

In conclusion, the sideband harmonics of the fundamental magnetising flux can be damped by the rotor bar. Meanwhile, the sideband flux of the rotor belt harmonics, stator slots harmonics and rotor slots harmonics are the higher order space harmonics, which cannot be damped by the cage rotor. These airgap flux characteristics are essential in calculating UMP.

4.3.4 Dynamic eccentricity

Dynamic eccentricity causes the rotor to rotate at the stator axis but not on its own axis. The direction of the narrowest airgap changes with rotational speed. Therefore, the UMP revolves around the machine when the rotor rotates. Machine-3 (wound rotor) revolving UMP from the dynamic eccentricity is shown in Figure 4-21.

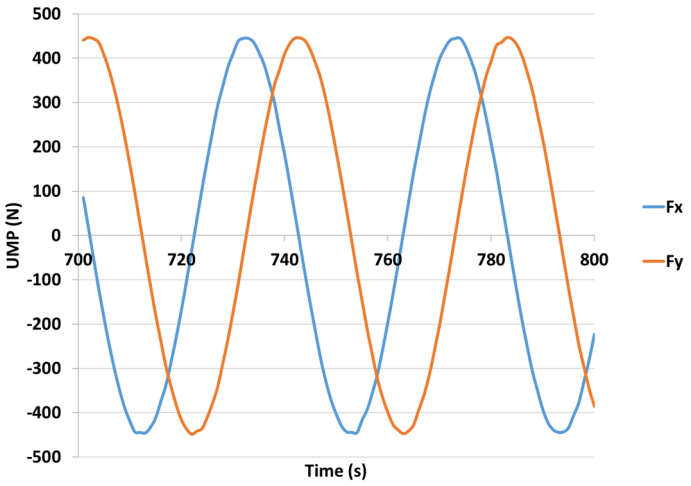

Figure 4-21: UMP from the rotor with dynamic eccentricity.

In Figure 4-21, the Y-axis UMP lagged the X-axis UMP by 90 degrees. Therefore, the resultant UMP of the dynamic eccentricity is constant. Figure 4-22 is the FEA simulation results of Machine-1 and Machine-3 with 10% of dynamic eccentricity. For the wound rotor induction machine, the UMP magnitude was the same for the static and dynamic eccentricity, but the direction of the UMP changed with time which is shown in Figure 4-21.

With the cage rotor induction machine, the static and dynamic eccentricity had different UMP Damping Coefficient, which are shown in Figure 4-7 and Figure 4-9 respectively. The damping effect is negligible when the machine with dynamic eccentricity is running at a synchronous speed. In Figure 4-22, the wound rotor and the cage rotor induction machines have almost the same UMP when running at a synchronous speed. As the slip increased, the damping effect became more and more significant. Therefore, the UMP dropped as the slip increased. However, as the slip further increased, the UMP from the airgap leakage flux increased, which caused the overall UMP increased after around 0.03 slip.

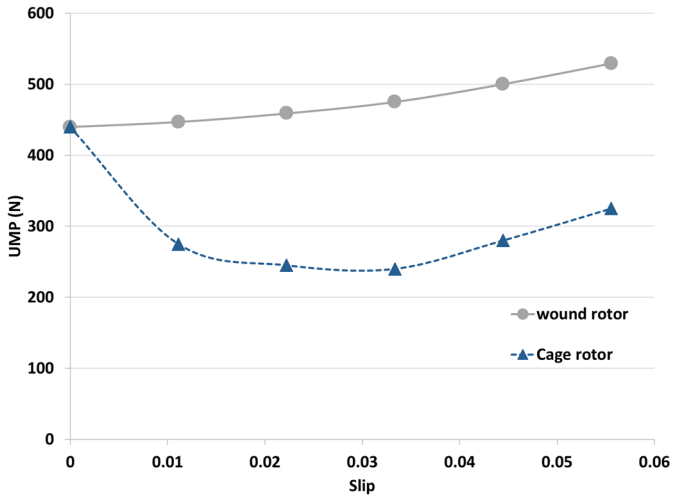

Figure 4-22: UMP of the wound rotor (Machine-3) and cage rotor (Machine-1) induction machine with dynamic eccentricity.

4.4 Multi-slice 2D-FEA

A multi-slice 2D FEA analysis is often used for skewed rotor simulation where the rotor angle is not axially constant. If compared to a 3D FEA simulation, multi-slice 2D FEA could significantly reduce the computational time [139]. For the multi-slice 2D FEA, the cage rotor induction machine is separated into a number of slices. Each slice has the same axial length and the stator and the rotor circuit is connected to each slice. In addition, it is assumed that the changes in each slice are neglected. Each slice has a different geometry, so, the inductance of the circuit is different for each slice. The multi-slice concept is shown in Figure 4-23.

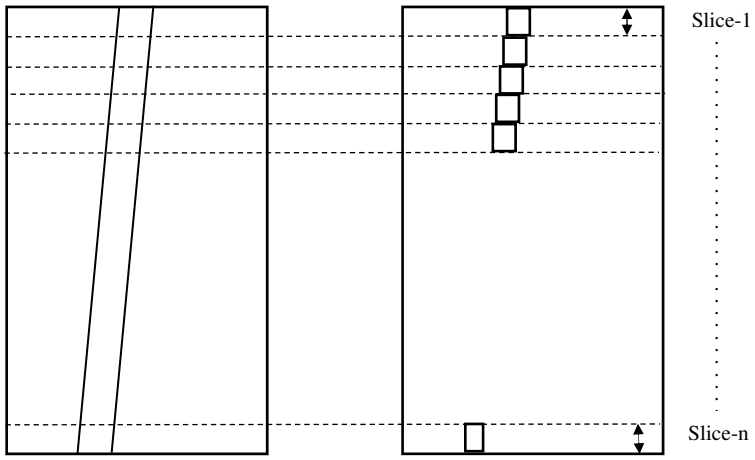

Figure 4-23: Concept of the multi-slice 2D FEA.

To analyse the static eccentricity in a skew rotor by using the multi-slice 2D-FEA, the same degree of static eccentricity was created in each slice but the angle of the rotor was shifted based on the average angle difference between each slice.

For the analysis of the axial-varying static eccentricity, the degree of static eccentricity for each slice was created based on the average eccentricity and the eccentricity gradient in the axial direction, in which the calculation of the eccentricity of each slice is shown in Sub-section 4.6.1.

4.5 Skewed Rotor

Small and medium-sized induction machines are usually constructed with a skew rotor bar to minimise the torque ripple and noise. When the rotor is skewed by one stator slot pitch, the skew rotors can eliminate the unwanted effect from the stator slot harmonics flux [53]. The side-view of the skew rotor is shown in Figure 4-24.

However, Dorrell had pointed out that skewing the cage rotor would increase the UMP in cage rotor induction machines, because the rotor skewing reduces the pole pair ± 1 counteracting flux in induction machines [54]. The reduction of the damping effect would increase the UMP caused by the fundamental flux. In addition, as skewing the rotor bar reduces the coupling between the stator and rotor circuit, it increases the leakage flux which also includes the airgap leakage flux. With the increment of airgap leakage flux, the UMP will also be increased.

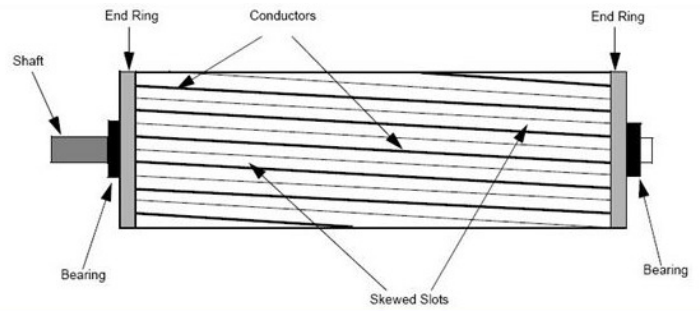

Figure 4-24: Skewed cage rotor [140].

The issue is comprehensively studied in this section, where a new UMP analytical model is also proposed by using the UMP Damping Coefficient. The skew rotor was investigated by using Machine-1. The UMP comparison between with and without rotor skewing is shown in Figure 4-25. The skewing factor of one stator slot pitch is used, in which the rotor is skewed at 10 mechanical degrees. For the multi-slice 2D FEA simulation, as five slices are used, each slice is shifted by 2 mechanical degrees.

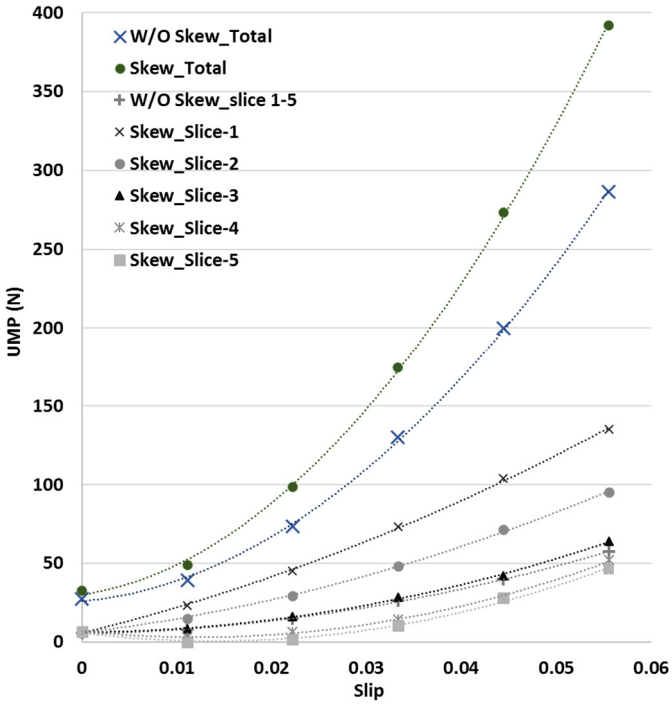

Figure 4-25: UMP with and without rotor skewing.

From Figure 4-25, the total UMP of the skewed rotor is higher than the UMP of the rotor without skew. Figure 4-25 also illustrates that the UMP difference between with and without rotor skewing increases as the rotor slip increases. There are two reasons that contribute to the UMP difference between with and without rotor skewing: 1) the effectiveness of the UMP damping reduces when the rotor is skewed, and 2) the rotor skewing would increase the leakage flux as the leakage flux could not be damped by the rotor bar. The relationship between the UMP from the fundamental flux with and without rotor skewing is shown in (4-18). In (4-18), the UMP_1 is the UMP caused by the fundamental magnetising flux in a machine with an unskewed rotor; $UMP_{sk,1}$ is the UMP caused by the fundamental magnetising flux in a skewed rotor machine; $k_{sk}^{p\pm1}$ is the skewing factor and β is the damping coefficient.

$$UMP_{sk,1} = \beta k_{sk}^{p\pm1} UMP_1 + \left(1 - k_{sk}^{p\pm1}\right) UMP_1 \tag{4-18}$$

$$UMP_{sk,1} = UMP_1 \left(k_{sk}^{p\pm1} \left(\frac{1}{k_{sk}^{p\pm1}} - 1 + \beta \right) \right) \tag{4-19}$$

In (4-19), it is clear that the overall UMP is a function of the skewing factor and the UMP Damping Coefficient. Values of $k_{sk}^{p\pm1}$ and β are always smaller than 1, which means that the UMP will definitely increase, because of the reduction of coupling between the stator and rotor. From (3-26), the skewed rotor harmonics equation has shown that the reduction in the magnitude of the low harmonics order is relatively small, as the numerator and the denominator values are nearly the same.

The UMP Damping Coefficient introduced in Section 4.1 is the ratio between the resultant UMP and the UMP from the fundamental flux. Figure 4-26 shows the UMP ratio after considering rotor skewing, where k_{sk}^{p+1}=0.989 and k_{sk}^{p-1}=0.998.

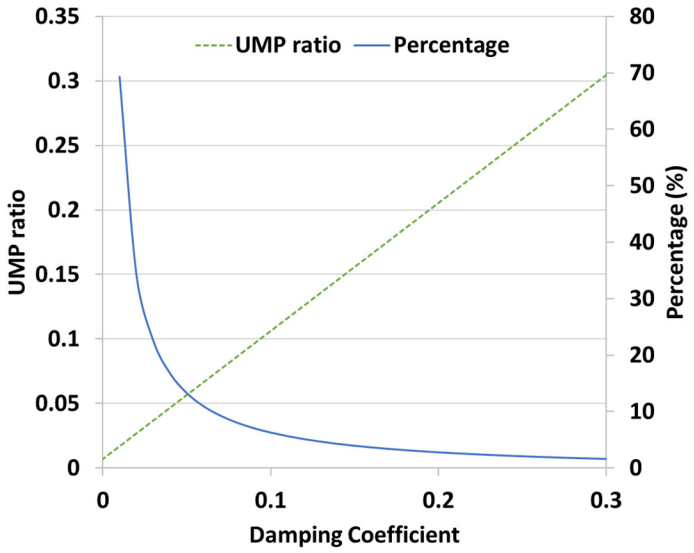

Figure 4-26: Influence of UMP Damping Coefficient on the UMP ratio and percentage of increment.

Figure 4-26 shows that the UMP ratio increased after considering the skewed rotor. The percentage of increment varied with the UMP Damping Coefficient without a skewed rotor. As the UMP Damping Coefficient increased, the increment percentage of the UMP ratio dropped. For example, in Machine-2, the UMP Damping Coefficient was 0.05 when it was running synchronous speed of 50 Hz excitation voltage. Therefore, the increment of UMP should be around 13% at synchronous speed.

Referring to Figure 4-25, the difference in UMP increased with the rotor slip because the skewed rotor caused additional leakage flux that crosses the airgap. This additional leakage flux is skewed leakage flux, which is also a function of current. The skewed leakage inductance can be added on top of the airgap leakage inductance for the UMP calculation. The airgap leakage inductance is constant if the magnetic core saturation is not taken into account.

From Figure 4-27, it shows that the difference between the UMP with and without rotor skewing increased as the slip increased, because a high portion of UMP was caused by the fundamental flux when it was running at a synchronous speed. The FEA results in Figure 4-27 shows a difference of 15% at synchronous speed, which is almost the same as the 13% calculated in Figure 4-26; the analytical calculation is slightly lower, because the additional leakage flux is not taken into account.

As the contribution of the UMP caused by the airgap leakage flux increased when the rotor slip increased, the percentage difference became higher, and the increment "saturated" when the rotor slip was higher than 0.02. The "saturation" of increment was due to UMP caused by the airgap leakage flux being much higher than the UMP caused by the fundamental flux.

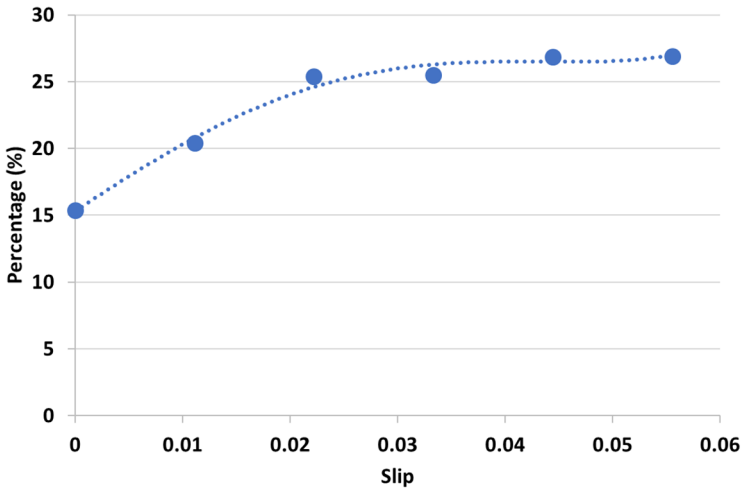

Figure 4-27: Percentage difference between the UMP with and without rotor skewing.

4.6 Axial-varying Eccentricity

The assumption of constant eccentricity across the axial direction of the rotor is not entirely applicable to a real case scenario. Therefore, axial-varying eccentricity needs to be added as an additional factor that influences the damping effect and UMP calculation.

4.6.1 Calculation for axial-varying eccentricity

Figure 4-28 shows the side view of an induction machine with an axial-varying eccentricity. The axial-varying eccentricity has assumed that the rotor does not bend, so the eccentricity changes linearly along the axial direction.

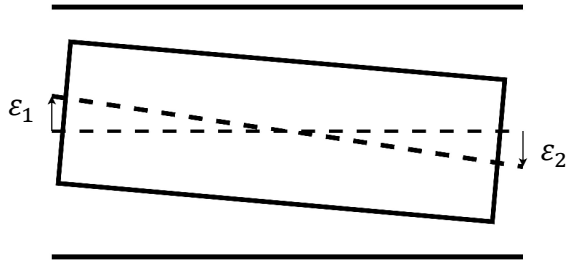

Figure 4-28: Side view of axial-varying eccentricity.

The axial-varying eccentricity is a function of the rotor axial coordinate, which is shown in (4-20).

$$\varepsilon(l) = \varepsilon_1 - \frac{\varepsilon_1 - \varepsilon_2}{L} l \tag{4-20}$$

where l is the local point in the axial direction. For an eccentric rotor, the magnetising inductance is different with different rotor eccentricity, because the magnetic permeance changes with the rotor eccentricity [141]. By considering only the first harmonic, the correction factor for the magnetising inductance due to the rotor eccentricity can be written as:

$$k_{ecc}(l) = \frac{1}{\sqrt{1 - \varepsilon(l)^2}} \tag{4-21}$$

In addition, the magnetising inductance is also affected by the magnetic saturation. The overall correction factor is:

$$k_p = k_{sat} k_{ecc} \tag{4-22}$$

where k_p is the overall correction factor and the k_{sat} is the saturation factor. Although the magnetic permeance is higher in an eccentric rotor, the magnetic saturation caused by the eccentric rotor will reduce the magnetic permeance. Combining the correction factor with the original stator inductance, the stator inductance with an axial-varying eccentricity can be calculated by using:

$$L_S^{mean} = L_S\left(\frac{\int_0^L k_p \, dl}{L}\right) \tag{4-23}$$

Before going into the UMP calculation, the average eccentricity from the axial-varying eccentricity needs to be calculated. After applying the correction factor, k_p, the average eccentricity of the machine is shown in:

$$\varepsilon^{actual} = \frac{1}{L}\int_0^L k_p(l)\varepsilon(l)dl \tag{4-24}$$

To analyse the UMP through the multi-slice 2D FEA, the actual eccentricity for the multi-slice simulation is the discrete integral of (4-24) which is:

$$\varepsilon^{actual} = \frac{1}{n}\sum_{sl=1}^{n} k_p(sl)\varepsilon(sl) \tag{4-25}$$

For an axial-varying rotor, the voltage induced at any point is different because the magnitude of the $p \pm 1$ flux has a different magnetic field strength with different eccentricity. As the rotor bar current is the same for each slice, the counteracting rotor flux remains the same, even when the magnitude of the stator $p \pm 1$ flux changes axially. The assumption is that the θ_r is 0 in the operating region of the induction machine, because the slip frequency for the $p \pm 1$ flux is high, where the reactance is much higher than the resistance. The effective eccentricity is introduced in (4-26).

$$\varepsilon_{eff}(sl) = \varepsilon(sl) - [(1-\beta)\varepsilon^{actual}] \tag{4-26}$$

The ε that was used in the formula is actually the ratio between $p \pm 1$ flux and p flux. Therefore, ε_{eff} was introduced to calculate the resultant $p \pm 1$ in the airgap. For a constant axial eccentricity, ε_{eff} is the multiplication of ε and the UMP Damping Coefficient, β. The equations for the total UMP acting on the rotor is:

$$UMP_i = \sum_{sl=1}^{n} \sum_{p=-\infty}^{\infty} \frac{\pi r l_{sl} \varepsilon_{eff}(sl)}{2\mu_0} B^{p2} \tag{4-27}$$

where l_{sl} is the length of the slice. For the magnetic flux with high space harmonics, the $\varepsilon_{eff}(sl) = \varepsilon(sl)$, because there is no counteracting flux induced in the rotor bar.

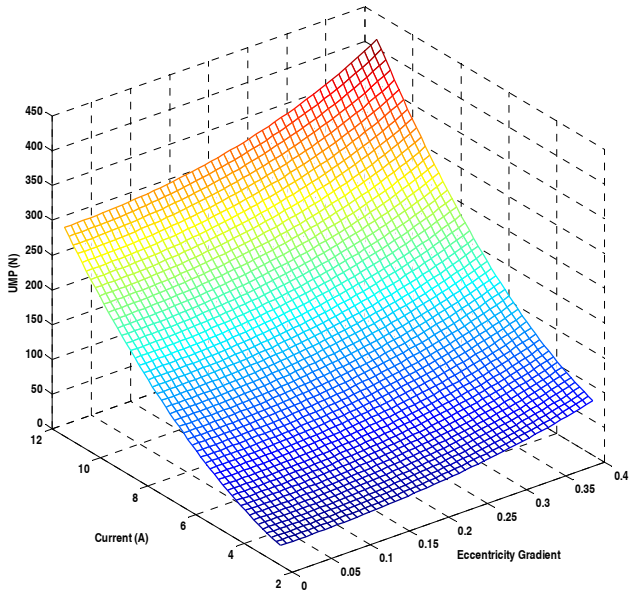

Figure 4-29: Analytical calculation for a 4-pole cage rotor machine with average 20% eccentricity.

Figure 4-29 is simulated by using (4-20)-(4-27). The eccentricity gradient is the steepness of the axial-varying eccentricity. The magnetising flux is assumed constant in this simulation. Therefore, the airgap leakage flux increased when the current increased. Thus, the quadratic relationship is shown between the current and the UMP. For the machine running at a different current, it was proven that the gradient

of the axial-varying eccentricity will increase the UMP. The increment of UMP is not linearly proportional to the axial-eccentricity gradient.

4.6.2 Results for axial eccentricity

Machine-1 (4-pole cage rotor) is simulated by a 2D multi-slice FEA. Five slices were used in the simulation. The four different cases that will be analysed are shown in Table 1.

Case	ε_1	ε_2	ε^{actual}	Gradient
1	0.2	0.2	0.204	0
2	0.3	0.1	0.205	0.1
3	0.4	0.0	0.208	0.2
4	0.6	-0.2	0.225	0.4

Table 4-2: Four different axial-varying eccentricity cases to be analysed in FEA.

The calculated ε^{actual} is different from the average rotor eccentricity. ε^{actual} is the actual eccentricity that experienced in the rotor. These 4 cases have the same average static eccentricity of 20%. However, the ε^{actual} is also a function of the magnetic permeance which causes the increment of ε^{actual} for a steeper axial-varying eccentricity.

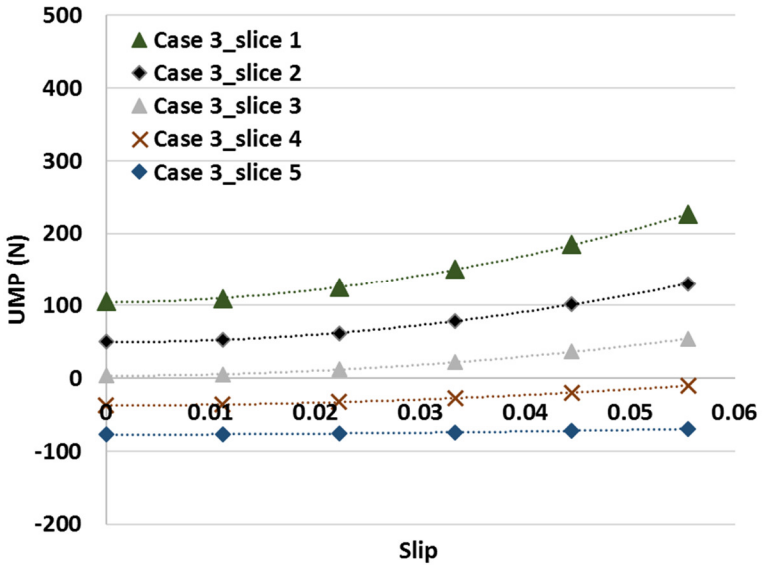

Figure 4-30: UMP for each slice in Case-3.

Case-3 is selected to show the UMP of the five slices in Figure 4-30. When the rotor slip is 0, Slice-1 has the highest positive UMP, and Slice-5 has a negative UMP. The direction of the UMP is related to the difference between the average eccentricity of the whole machine and the eccentricity of each slice. With the increment of the rotor slip, it can be seen that the UMP increment for each slice was related to their local degree of eccentricity (0% eccentricity in Slice-1, 10% eccentricity in Slice-2, 20% eccentricity in Slice-3, 30% eccentricity in Slice-4, 40% eccentricity in Slice-5). The increment of UMP is based on the local eccentricity of each slice because: 1) the increment of UMP when the slip increases is due to the increment of airgap leakage flux, 2) the airgap leakage flux does not induce voltage in the stator and rotor circuit, so the leakage flux of each slice does not affect each other. Therefore, Slice-1 had the largest increment while Slice-5 had zero increment when the rotor slip increased.

It can be concluded that the changes of UMP for each slice is directly proportional to the local degree of eccentricity. Therefore, the UMP of the 1st and 5th slice are enough to reflect the whole situation. The combined view of the 1st and 5th-slice for each case is shown in Figure 4-31, and the total UMP for each case is shown in Figure 4-32. The results from 0 to 0.055 slip are shown, which is within the operating region of the machine.

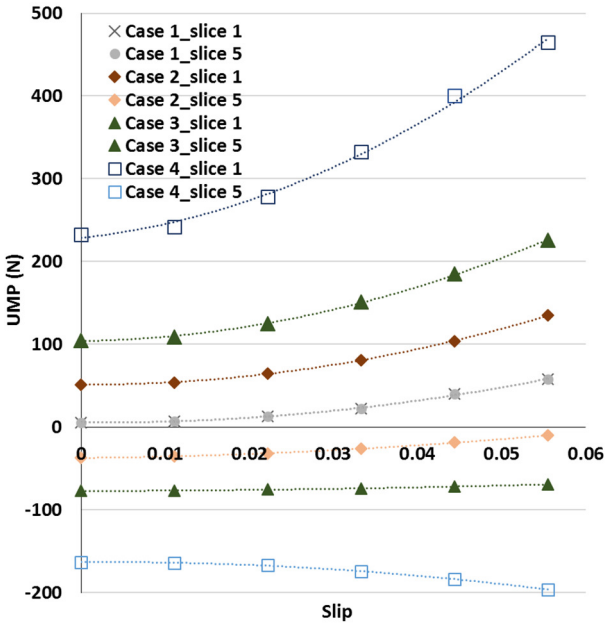

Figure 4-31: UMP for the first and last slice.

Case-4 has the steepest axial-varying eccentricity compared to 3 other cases. From Figure 4-31, the Slice-1 for all cases has a positive UMP because the direction of eccentricity is the same for all cases. When the slip increases, it can be seen that Case-4 has a more significant increment in UMP than the other 3 cases. For high degree of eccentricity, the permeance harmonics from the 2nd and 3rd order cannot be neglected. Therefore, Case-4 shows the sharpest increment in Slice-1.

For the 2nd, 3rd, and 4th case, their Slice-5 had a negative UMP when the machine was running at a synchronous speed. This scenario was due to the damping effect of the rotor because the magnitude of the damping current was determined by ε^{actual}. Due to the fact that the 5th slice of Case-4 had a negative eccentricity, the UMP increased toward the negative direction when the current increased. However, the 5th slice of Case-3, which had a zero eccentricity, the UMP remained the same even when the slip increased. The 5th slice of Case-2 had a positive eccentricity, so the negative UMP was reduced.

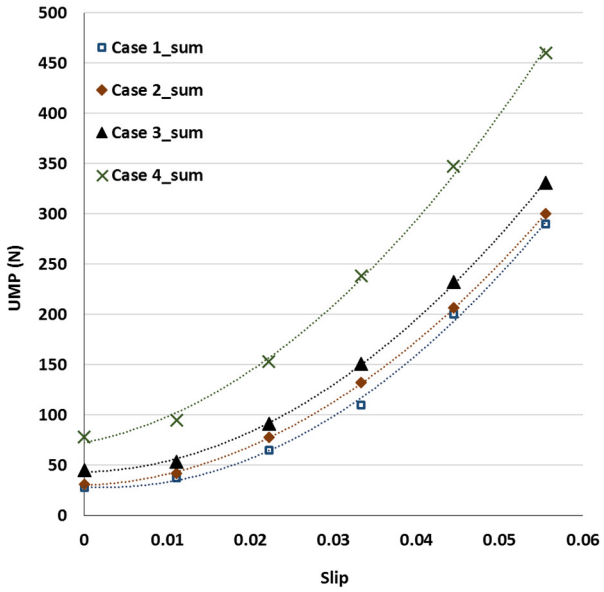

Figure 4-32: Overall UMP for all 4 cases.

The results shown in Figure 4-32 are used to verify the analytical results from Figure 4-29. It shows good correlation between the two graphs. The total UMP increased with the slip because the average eccentricity of all cases was 20% eccentricity in the same direction. In addition, if neglecting the saturation factor, the

overall inductance of the machine also increased when the eccentricity increased. Although the increment of the machine's inductance did not affect the magnetising flux, the increment of the inductance did cause higher leakage flux flows in the machine.

The ε^{actual} is directly related to the UMP from the airgap leakage flux. The difference of ε^{actual} for Case-1 and Case-4 was around 10%. Therefore, it can be shown that the UMP increment does not make a big difference between each case. For the UMP from the fundamental flux, the ε^{actual} is just a part of the UMP calculation, which is shown in (4-26). The UMP Damping Coefficient at a high rotational frequency is usually less than 0.1. In this case, a slight difference in ε^{actual} increased the resultant UMP. Therefore, the UMP at zero slip for Case-1 was 100% higher than Case-4.

4.7 Power Losses due to Rotor Eccentricity

As the eccentric rotor would cause an uneven flux distribution around the airgap, this may have caused additional power losses in the induction machine with rotor eccentricity. This section analyses the changes in the power losses due to rotor eccentricity. The discussion is divided into iron losses, copper losses, and bearing frictional loss.

4.7.1 Iron losses

The two main iron losses are the hysteresis loss and the eddy current loss. Hysteresis loss is caused by the energy dissipating from the domain changes of the ferromagnetic material when the magnetic field has changed in the ferromagnetic material. The anomalous loss is part of the hysteresis loss. Then, eddy current loss is the resistive losses caused by the current conduction in the ferromagnetic material. It is difficult to predict iron losses, because of the magnetic flux around the machine changes in space and time. In addition, it is impossible to isolate the secondary effects from the eddy current.

The Hysteresis loss and the Eddy Current loss formulas are shown in (4-28) and (4-29) [142].

$$P_{loss\_H} = \sigma_H B^{\vartheta} f^{\rho} \tag{4-28}$$

$$P_{loss\_E} = \sigma_E B^2 {l_t}^2 f^2 \tag{4-29}$$

The value of σ_H and σ_E depend on the material properties. Both coefficient values could be varying depending on different conditions. The σ_H varies with the magnitude of the peak magnetic flux density. And, σ_E also varies with both the frequency and the magnitude of the peak magnetic flux density [143]. In both iron losses, increments of magnetic flux and its frequency led to increment of iron losses. ϑ and ρ are determined by a curve-fitting of the loss model from the measured data. When ρ is different from 1, the hysteresis loss also included anomalous loss.

Usually, datasheets of iron cores only show the total losses over a different range of flux density for a specific frequency. The iron losses are not separated into hysteresis loss, anomalous loss and eddy current loss. In [144], the aurthors had shown the separation technique to get the parameters for iron losses calculation. The eddy current loss had a fixed power coefficient of two for all the cases. However, the hysteresis loss power coefficient for the peak magnetic flux density and the frequency were not constant at different frequencies.

Three assumptions were made to simplify the equation:

- The anomalous loss is neglected. Therefore, the frequency power coefficient for the hysteresis loss is 1.
- This section is to analyse the losses caused by the uneven magnetic flux distribution over the machine. Therefore, in order to combine both eddy current and hysteresis loss for an overview of the effect caused by the eccentric rotor, the power coefficient is set to 2 where the R-squared curve fitting is 0.9842.
- The $\boldsymbol{\sigma_H}$ and $\boldsymbol{\sigma_E}$ are assumed to be constant at every frequency and every magnetic flux density. This is because the rated magnetic flux density for an induction machine is low to avoid high magnetising current and most of the

magnetic flux rotates at a low frequency. Therefore, the changes of the coefficients are negligible.

With these three assumptions, the Steinmetz equation for the iron loss model is shown in (4-30).

$$P_{loss\_iron} = B^2\left(\sigma_E {l_t}^2 f^2 + \sigma_H f\right) \tag{4-30}$$

As the B in (4-30) is squared, finding the total harmonic distortion (THD) could find the increment of the iron loss due to an eccentric rotor. The total harmonic distortion is increased in an eccentric machine. (4-32) shows the THD of the magnetic flux harmonics of a concentric rotor.

$$THD = \frac{\sqrt{\left(\frac{1}{2}\varepsilon B\right)_{p+1}{}^2 + \left(\frac{1}{2}\varepsilon B\right)_{p-1}{}^2}}{B} \tag{4-31}$$

$$THD = \sqrt{\frac{1}{2}\varepsilon^2} \tag{4-32}$$

The total iron loss from an eccentric rotor is shown in (4-33). It was demonstrated that the iron loss had an increment of $\frac{1}{2}\varepsilon^2$. For example, 50% eccentricity would increase the iron loss by 12.5%.

$$P_{loss\_iron\_eccentric} = P_{loss\_iron}\left(1 + \frac{1}{2}\varepsilon^2\right) \tag{4-33}$$

The iron losses are not evenly distributed across the induction machine. For example, the tooth tips have a higher flux density than the back iron. However, the stator back iron contributes more than 70% of the total stator iron loss [145]. Therefore, FEA is used because it is suitable to analyse the complex electromagnetic circuits.

In Figure 4-33, the graph shows the predicted iron losses and the simulated iron losses. The prediction is based on (4-33) where the prediction model used the iron losses of a concentric rotor's results from the FEA simulation to estimate the eccentric

rotor iron loss. Then, FEA results for the eccentric rotor were used to compare to the prediction model.

Figure 4-33 proves that the iron loss prediction from (4-33) for both the stator and the rotor iron losses. The rotor iron losses are usually neglected when considering only the fundamental magnetic flux in the low slip region. This is because the iron losses are a function of frequency, where the frequency of the fundamental magnetic flux at low slip is almost zero.

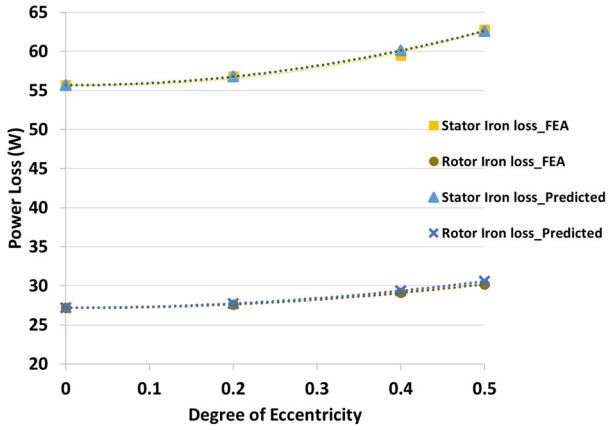

Figure 4-33: Iron losses for Machine-3.

However, the rotor iron losses should not be neglected in the induction machine, because the other space harmonics flux will produce a significant power loss, as shown in Figure 4-33. As discussed in the last few sections, all the space harmonics will generate the additional magnetic flux due to asymmetric airgap. From here, it can be proven that the iron losses prediction model has included all the space harmonics.

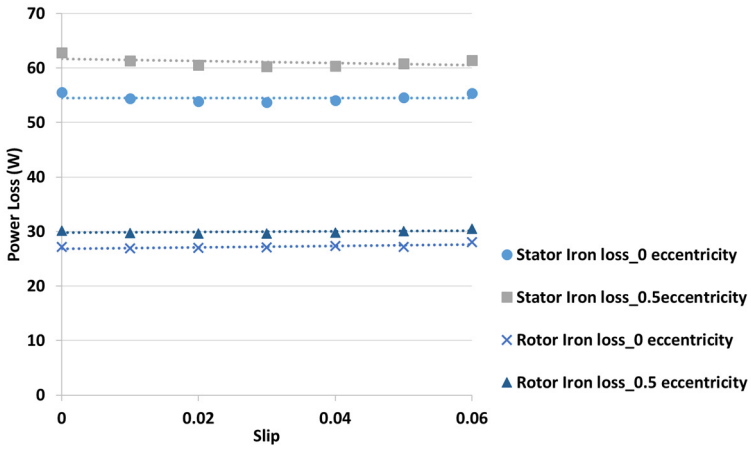

Figure 4-34: Comparison of the iron losses at different rotor slip.

Figure 4-34 shows that iron loss remains constant with varying rotor slip. Therefore, the difference between the eccentric rotor and the concentric rotor remains at different rotor slip. The total iron loss in the wound rotor induction machine will increase by $\frac{1}{2}\varepsilon^2$.

4.7.2 Copper losses

Copper losses are the heat loss in a conductor, which is produced when the electrical current is flowing through the conductor. The conductor's resistance is constant when current is flowing in DC. When a high frequency current flows in the conductor, the skin effect has to be considered. In an induction machine, the copper losses can be separated as stator copper loss and rotor copper loss. When the windings are series connected, the only current with the same pole-pair harmonic could be induced in the circuit. For most of the machine's design, stator windings are series connected. Therefore, an eccentric rotor and a concentric rotor induction machine have almost the same stator copper loss. The basic copper loss formula is shown in (4-34).

$$P_{loss\_copper} = I^2\mathrm{R} \tag{4-34}$$

For the wound rotor induction machine, the rotor copper loss is the same for the eccentric and concentric rotor cases due to the series connection of the rotor where the additional pole pair flux could not be induced in the circuit. Therefore, in this section, only the cage rotor induction machine is discussed.

For cage rotor induction machine, the rotor bar damps the additional pole pair flux. So, higher rotor current total harmonics was induced in the rotor bar. The stator and rotor copper losses were separately analysed. FEA was used to analyse Machine-1. A comparison between the concentric rotor and 50% static eccentricity was made.

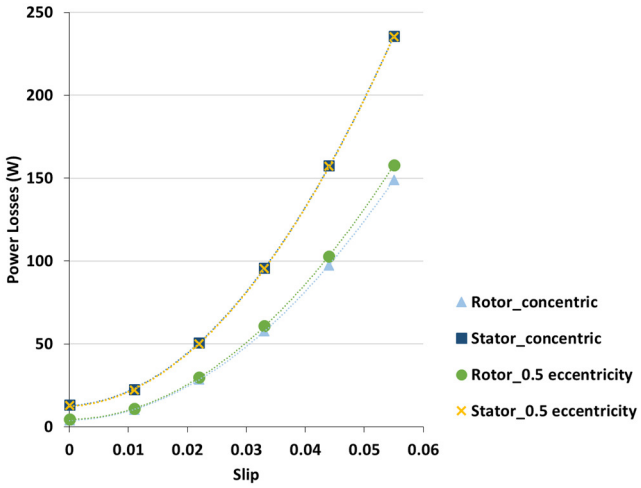

Figure 4-35: Copper Losses in Machine-1.

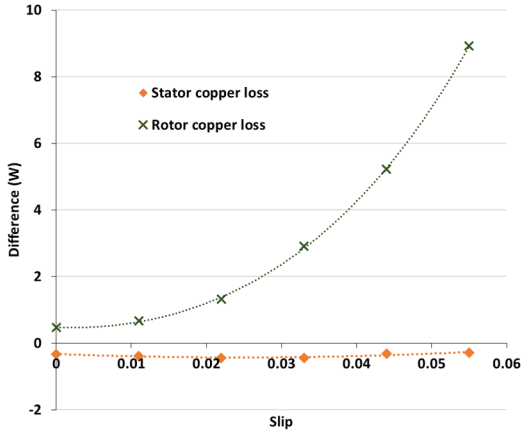

Figure 4-36: Difference in the copper loss between 50% and 0% rotor eccentricity.

The current increased linearly with the rotor slip when the slip was low. Figure 4-35 shows the power loss increases quadratically when the slip increases. Figure 4-36 is used to show the difference in copper losses between a machine with a 50% static eccentricity with 0% static eccentricity.

Figure 4-36 shows that the stator copper loss of 50% eccentricity was slightly lower than the concentric rotor. The small difference was due to the increment of the magnetising inductance due to rotor eccentricity. As rotor eccentricity increases the magnetising inductance, the lesser magnetising current was needed. Therefore, the difference in stator loss is almost constant when rotor slip increases because of the constant magnetising current.

Meanwhile, for the rotor copper loss, the rotor with 50% static eccentricity was higher than the concentric rotor. The difference increased quadratically as the slip increased. This is because there is an additional pole pair ± 1 flux induced in the parallel windings. As discussed earlier, the parallel circuit at the cage rotor bar allows additional circulating current flows. The circulating current causes high copper loss. In [146], the authors showed that the increment of the rotor current was due to the induced current in the eccentric rotor. When the machine was running at a synchronous speed, most additional pole pair ± 1 flux induced in the rotor bar was the fundamental magnetising flux. As the slip increased, there was an increment of pole pair ± 1 flux from the belt harmonics. So, more flux was induced in the rotor bar which caused the difference of rotor copper loss to increase with slip.

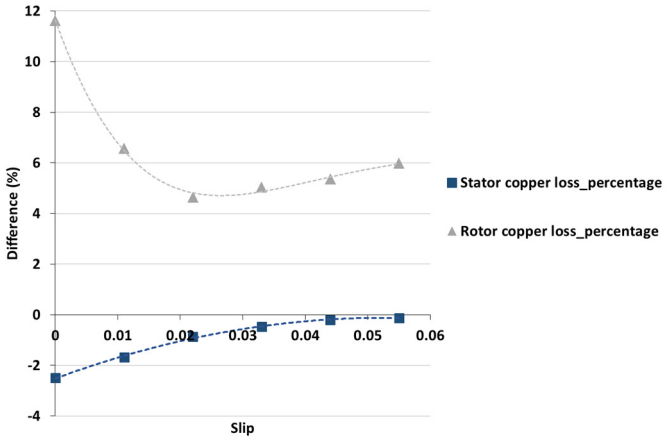

Figure 4-37: Percentage difference of the copper losses between 50% and 0% rotor eccentricity.

Figure 4-37 shows the percentage difference of the results in Figure 4-36, in which the denominator of the percentage calculation is the mean of the copper loss of the 0% and 50% static eccentricity. In Figure 4-37, although there is an increment in the rotor copper loss when the slip increased from 0 slip, the overall percentage difference dropped when the slip increased. This is because the current increment from the load was higher than the induced current by the additional magnetic flux. As the slip further increased from 0.02 slip, the rotor copper loss is slightly increased because the higher belt harmonics flux induces current in the rotor bar. Meanwhile, as the stator copper loss remains is constant at the low slip region, the difference in percentage

decreased as the slip increased. When the machine runs at full-load, the reduction of stator copper loss due to rotor eccentricity can be neglected, while the increment of rotor copper loss is around 5% of the original copper loss.

4.7.3 Bearing frictional loss

The frictional resistance of the object's relative motion creates a frictional loss, which results in heat generation. In a wind turbine generator, 0.6% of energy consumption comes from bearing friction loss [147]. Power dissipated from the frictional loss is transformed into heat which causes the temperature to rise in the machine.

$$P_{loss\_friction} = \mu_{fric} r F_{eq} \omega_m \tag{4-35}$$

The instantaneous power loss due to friction force can be calculated from (4-35). The μ_{fric} of a ball bearing is around 0.0002. The ω_m is in radian per seconds. F_{eq} is the total force acting on the bearing.

$$F_{eq} = k\left(\overrightarrow{W_r} + \overrightarrow{UMP}\right) \tag{4-36}$$

Due to many uncertainties in the mechanical loss, the simulation of Figure 4-38 is based on these assumptions:

- The axial force acting on the bearing is neglected.
- The total radial force is the resultant force of the rotor weight and the UMP from (4-36).
- The rotor weight and the UMP weight are acting in the same direction. The rotor weight of Machine-3 was used, which is 14 kg.
- A ball bearing with a diameter of 40 mm and a friction coefficient of 0.002 was used.
- The constant rotational speed of 1500 RPMs was used.
- k was set to 1. k from (4-36) was the modifier for the different bearing loading. 1 is for a constant loading.
- The radial loading does not increase the degree of eccentricity.

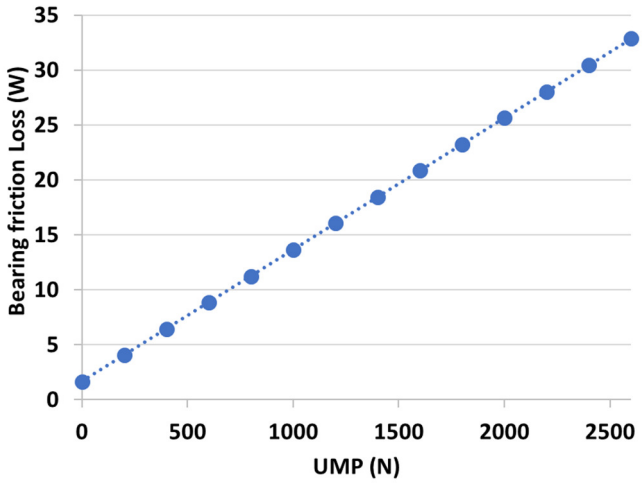

Figure 4-38: Bearing friction loss at different UMP.

Figure 4-38 shows that the power loss increased as the UMP increased. For the wound rotor induction machine (Machine-3) with 50% static eccentricity, the UMP of the machine was 2.5 kN when running at full load. This means that the bearing frictional loss increased from 1.6 W to 32 W. For the cage rotor induction machine (Machine-1) with 50% eccentricity, UMP of the machine was 380 N when running at full load. The bearing friction loss increases from 1.6 W to 6 W.

4.7.4 Summary of machine power losses analysis

With the existence of rotor eccentricity, there are additional power losses in the machine, in which the efficiency of the machine is reduced. Figure 4-39 illustrates the power losses comparison between the concentric rotor and the rotor with 50% static eccentricity in Machine-3 (wound rotor induction machine). It shows that the UMP significantly increased the bearing friction loss. As the UMP remained large when the machine was lightly loaded, the efficiency of the machine was reduced by 3.3% at 0.01 rotor slip (or 9 Nm). When the slip increased, the reduced efficiency of the machine became lower, because of the slow increment of power losses. At a 0.05 slip (full load), the efficiency of the machine was reduced by 0.75%.

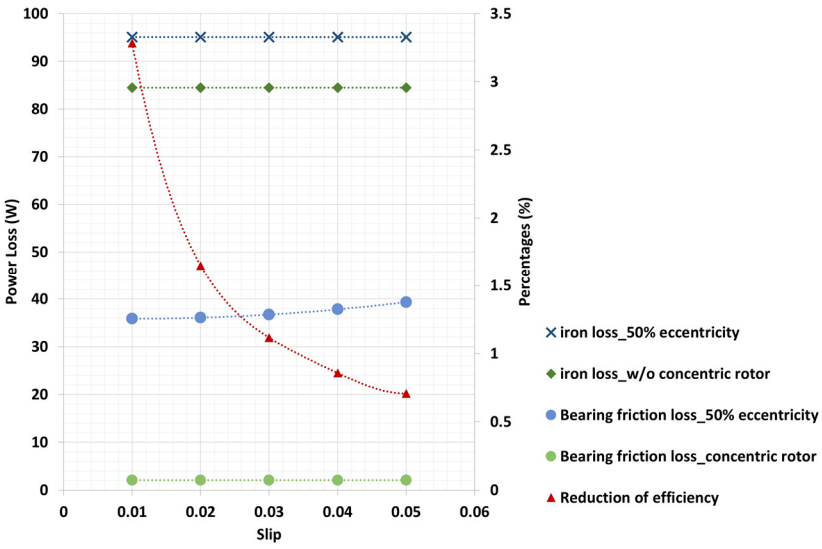

Figure 4-39: Comparison of power losses between 0% and 50% static eccentricity of Machine-3.

Comparing Figure 4-39 and Figure 4-40, the reduction of efficiency in Machine-1 (cage rotor induction machine) was not as significant as the reduction of efficiency in Machine-3, because the UMP of the cage rotor induction machine is lower in the wound rotor induction machine. Also, the difference of copper loss in the cage rotor induction machine was not as significant as the increment of iron loss in the wound rotor induction machine. As the UMP increases quadratically when the slip increases, the contribution of bearing friction loss is least significant when the machine operates close to the synchronous speed. When the slip is larger than 0.03, the increment of bearing friction loss reduces the machine efficiency.

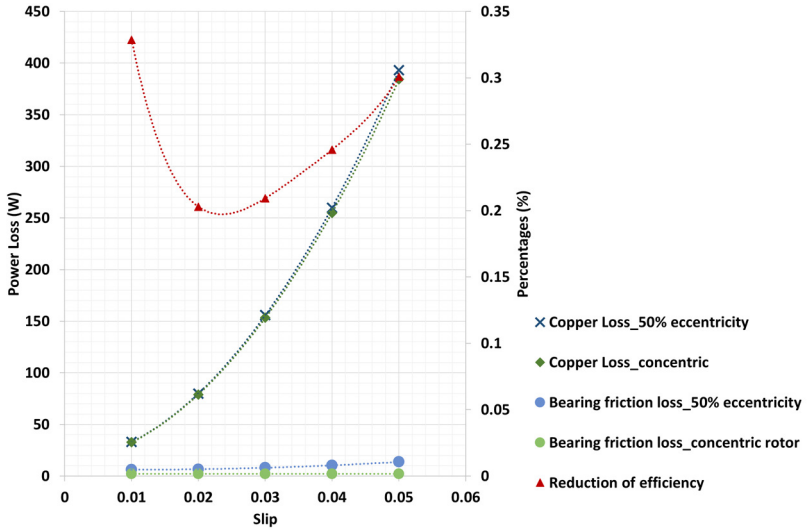

Figure 4-40: Comparison of power losses between 0% and 50% static eccentricity of Machine-1.

The rotor eccentricity should be taken into account when calculating the power losses in order to achieve an accurate power loss estimation. A summary of the power losses of both types of machine at full load and 50% of static eccentricity is shown in Table 4-3.

	Cage Rotor	Wound rotor
Iron Losses	Negligible	12.5% increment of the total iron losses of a concentric machine or 0.15% reduction from the machine efficiency
Copper Loss	4% increment of the copper losses of a concentric machine or 0.12% reduction from the machine efficiency	Negligible
Bearing Friction Loss	652% increment of the bearing friction loss or 0.17% reduction from the machine efficiency	1872% increment of the bearing friction loss or 0.53% reduction from the machine efficiency

Table 4-3: Power losses comparison between Machine-1 and Machine-3 with 50% static eccentricity at full load.

4.8 Chapter Summary

In this chapter, the UMP difference between cage rotor and wound rotor induction machines are investigated. The wound rotor induction machine has a much larger UMP than the cage rotor induction machine because the parallel path in the cage rotor produces a counteracting flux that damps the UMP. The UMP damping effect is only applicable for the magnetising flux, where the pole pair ± 1 flux is cutting through the rotor bar and inducing EMF in the rotor. As the damping effect could only be solved numerically, the UMP Damping Coefficient is introduced for steady-state analysis which can be used in the analytical calculation. The Damping Coefficient is a function of rotor slip, stator excitation frequency and rotor resistance. The influence from the rotor slip, excitation frequency and rotor resistance are verified by using both the FEA and experimental work.

The findings show that the direction of the UMP caused by the magnetising flux did not act toward the narrowest air gap when UMP damping exists. Although the direction of the UMP caused by the magnetising flux changed with slip, the UMP caused by the air gap leakage flux was still acting toward the narrowest air gap. Therefore, as the slip increased, the direction of the UMP was close to the direction of the narrowest air gap, because the air gap leakage flux was the dominant flux when the machine was excited at its rated frequency.

Next, with the Damping Coefficient, UMP calculations for skewed cage rotor and axial-varying eccentricity were further derived. The proposed analytical equations were verified by using multi-slice 2D FEA. For a skewed rotor, the effectiveness of the UMP damping effect from the rotor was slightly reduced, because the skewed rotor had reduced the magnitude of the pole pair ± 1 magnetic flux. In addition, the skewed rotor increased the airgap leakage flux, which caused larger UMP when the slip increased.

Meanwhile, for axial-varying eccentricity, the average rotor eccentricity was not the same as the actual eccentricity. Four different cases with the same average eccentricity, but with different eccentricity gradients, were investigated. The results showed that the axial-varying eccentricity with the higher gradient had a higher UMP, even if the average eccentricity was the same. This was because the higher magnetic permeance harmonics needed to be taken into account for the high degree of eccentricity.

Then, the power losses model for a machine with rotor eccentricity was analysed and compared with a healthy machine. With the existence of rotor eccentricity, the iron loss of the wound rotor induction machine increased, while the rotor copper loss of the cage rotor induction machine increased. As UMP caused additional radial load on the bearing, the bearing friction loss increased. The higher UMP of the wound rotor induction machine significantly increased the bearing friction loss. Lastly, the comparison of the machine efficiency was demonstrated for both types of machines when the rotor eccentricity was taken into consideration.

5 Empirical Method for UMP Estimation

A novel method for UMP calculation is shown in this chapter, which uses an empirical method to estimate the UMP. The proposed empirical method is developed based on the analytical modelling shown in (3-40). The main reason of proposing this empirical method is due to the leakage flux that crosses the airgap, which is machine's geometry dependent and is very difficult to be calculated analytically. The FEA is often used to find the airgap leakage inductance for the conventional analytical UMP calculation. However, the airgap leakage inducatance needs to be recalculated for different loads, rotor eccentricity, and excitation voltage. Therefore, instead of finding the airgap leakage inductance like the conventional UMP analytical calculation in (3-40), the empirical method is a more direct method that uses the available experimental or FEA data to acquire the parameters to calculate UMP; the parameters used in the empirical method are divided into UMP caused by airgap leakage flux and UMP caused by magnetising flux.

In order to use the empirical method to estimate the UMP, knowledge from Chapter 3 and 4 is needed, which includes the UMP Damping Coefficient, the magnetic saturation, the categorisation of airgap flux, the UMP analytical model, and the skewed rotor calculation. The fast computational time of the empirical method is useful when a real-time UMP prediction is needed. Furthermore, a UMP/Torque ratio

is introduced to find the optimum operating slip with the lowest UMP. One of the objectives of the thesis is to reduce the UMP by applying a suitable control strategy. Two reasons that a UMP/torque ratio could be used to find the lowest UMP is: First, torque is linearly proportional to current when the rotor slip is low, and second, UMP is caused by uneven flux distribution, where flux is proportional to current.

5.1 Empirical Method

The UMP model shown in (3-40) is a function of magnetic flux density, which is linearly proportional to the current. Therefore, the UMP can be calculated after acquiring the current of the stator and the rotor. The rotor current characteristic is related to the stator current, because the rotor current is induced from the stator flux.

From the UMP characteristic in Figure 4-18, the UMP is a quadratic function when the induction machine is in its operating region. The constant offset component of the UMP is mainly caused by the magnetising flux and the squared component is caused by the airgap leakage flux. This is because the magnetising flux is almost constant when the induction machine operates below its rated slip. Then, when the slip increases from the no-load condition, the stator and rotor currents have a linear relationship with the slip, so, the airgap leakage flux of the induction machine increases when the slip increases. The airgap leakage flux for each space harmonic also produces their own pole pair ± 1 which produced UMP. Therefore, as the UMP analytical model is a function of the current squared, which is shown in (3-40)-(3-43), the UMP has a quadratic increment as the slip increases.

The leakage flux that crosses the airgap cannot be calculated using an analytical model because of the complex design of an induction machine. The airgap leakage flux is affected by the machine airgap length, the rotor and stator teeth length and also the slot size. The airgap leakage inductance does not change much when the machine is running in its operating region. Therefore, FEA simulation can be used to find the relationship between UMP and current. The constant of the relationship can be found through curve fitting. Then, it can be used empirically to calculate the UMP caused by the fundamental magnetising flux and leakage flux. When the machine is running at a

higher slip, the high current is causing the core saturation, which can affect the empirical calculation. Therefore, the empirical method is only applicable for low slip operation because core saturation is not obvious in low slip operation.

5.1.1 Derivation of the empirical method

Assumptions are made to simplify the UMP model:

- The excitation voltage is equal to the supplied voltage. The stator resistance is negligible at low slip because the current at low slip is much lower than the starting current and the magnetising branch causes most of the voltage drop.
- The total airgap leakage inductance ($\boldsymbol{L_{ag}}$) for the stator and the rotor are assumed to be the same. $\boldsymbol{L_{ag}}$ is assumed to be constant when the induction machine operates at its operating region [148].
- Rotor reactance is negligible at low slip operation because of the low rotor slip frequency. Therefore, the rotor slip is assumed to have a linear relationship with the machine load.
- The product of UMP Damping Coefficient ($\boldsymbol{\beta}$) with the magnetising flux ($\boldsymbol{\Phi_M}$) is assumed to be constant. Figure 5-2 has proven that the multiplication of the $\boldsymbol{\beta}$ with $\boldsymbol{\Phi_M}^{\boldsymbol{2}}$ are almost constant. For static eccentricity, the $\boldsymbol{\beta}$ increases when the slip increases; the magnetising flux decreases when the slip increases, as shown in Figure 5-1. For the wound rotor induction machine where its $\boldsymbol{\beta}$ is equal to 1, the reduction of $\boldsymbol{\Phi_M}$ need to be considered.

As the empirical method is used to estimate the UMP below the rated slip, the rotor leakage reactance can be neglected due to the low rotor slip frequency. Through neglecting the rotor leakage reactance, the magnetising current and the rotor current have a phase angle difference of 90 degrees, so they could be calculated independently. The relationship between the stator and rotor current could be written as (5-1).

$$I_S = \frac{jX_m + R_r}{jX_m} I_R \tag{5-1}$$

Equation (5-2) shows that the magnitude of the stator current is the vector summation of magnetising current and rotor current.

$$I_S = \sqrt{{I_M}^2 + {I_R}^2} \tag{5-2}$$

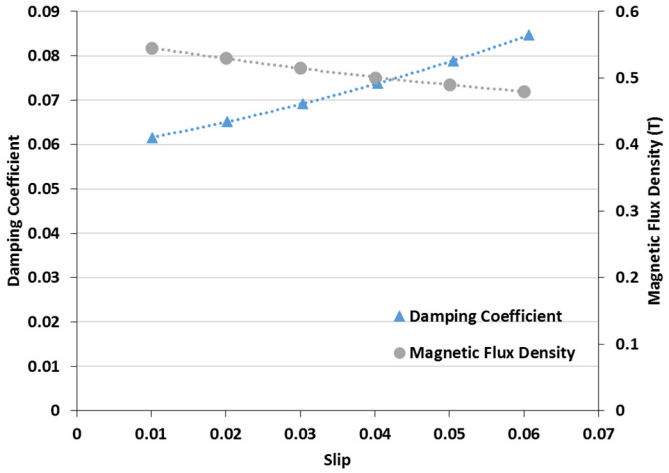

Figure 5-1: UMP Damping Coefficient and magnetic flux density at different slip.

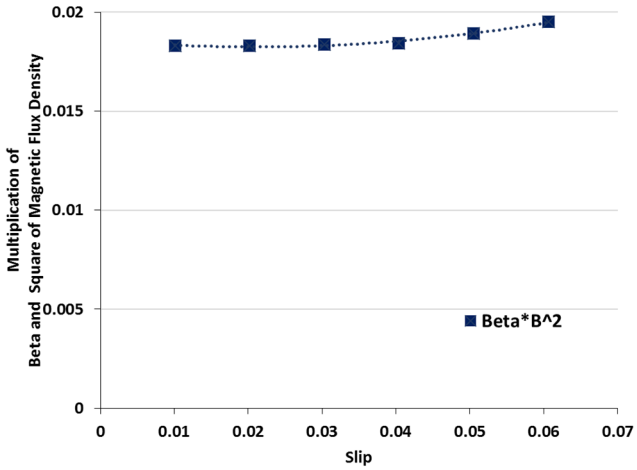

Figure 5-2: UMP ratio of the fundamental magnetising flux at different slip.

Equation (5-3) shows the overall UMP equation at any instant of time. Only the static eccentricity constant component is considered. The magnetic flux can be separated into the magnetising flux and the airgap leakage flux. The rotor's parameters are referred to the stator side.

$$UMP = K\left[\beta(L_M I_M)^2 + (L_{ag} I_M)^2 + (L_{ag} I_S)^2 + (L_{ag} I_R)^2\right] \tag{5-3}$$

The constant $K = \frac{\varepsilon}{8\mu_0 \pi r L}$, which is a function of the degree of static eccentricity and the machine parameters. In (5-3), the 3rd and the 4th components are the same because the stator and rotor airgap leakage flux are assumed to be same. The L_{ag} in (5-3) does not reflect to the flux coupled with fundamental pole pair windings.

$$I_M = \frac{E}{X_M} \tag{5-4}$$

$$I_R = \frac{sE}{R_r} \tag{5-5}$$

Equation (5-5) shows I_R is a function of the rotor slip. Also, I_M is assumed to be constant. E from (5-4) and (5-5) is the machine's rated voltage. The UMP equation from (5-6) could be separated into 2 components: constant component and slip-related components. v^2 is added into (5-6) to normalise for different excitation voltage, where v is voltage in per unit system of the rated excitation voltage (E).

$$UMP = 2Ks^2v^2\left(L_{ag}\frac{E}{R_r}\right)^2 + Kv^2\left[\beta(L_M I_M)^2 + \left(L_{ag}I_M\right)^2\right] \tag{5-6}$$

$$\text{Let,} \quad A = 2K\left(L_{ag}\frac{E}{R_r}\right)^2 \qquad B = K\left[\beta(L_M I_M)^2 + \left(L_{ag}I_M\right)^2\right] \tag{5-7}$$

Equation (5-7) shows the parameterisation of the 2 components in (5-6). From FEA results or experimental results at different slip, 2nd degree polynomial curve fitting is used to find the relationship between the UMP and the slip. The linear component of the 2nd degree polynomial curve fitting is set to zero. Then, the constant component and square component of the curve fitting can be substituted as parameters- A and B.

5.1.2 Limitations

There are a few assumptions made for the proposed empirical method. Therefore, the empirical method is only applicable if it is used for situations within the assumptions. Therefore, the limitations of the empirical method are:

- Curve fitting does not provide the most accurate results, where there is a range of constants that could fit to find the A and B parameters. However, this error will not significantly affect the overall value of the UMP. The average of the parameters can be taken to predict the UMP of the induction machine.
- The empirical method is only applicable below the machine's rated slip, in which the voltage drop across the leakage inductance and the stator resistance are neglected.
- The Damping Coefficient needs to be recalculated for every machine. The characteristic of the multiplication between the Damping Coefficient with the square of magnetising flux may not be assumed constant at low slip region.

5.2 Results for Empirical Method

The 2nd degree polynomial curve fitting is applied to the FEA and the experimental results to find the parameter-A and -B, which is shown in (5-7). The extracted parameters could be used to estimate the UMP at a different degree of rotor eccentricity and different excitation voltage. The empirical method is examined on Machine-1, -2 and -3. The extracted parameters of each machine are compared with each other to study on the characteristic of the UMP.

The extracted parameters from the simulation results of Machine-1 are used to estimate the UMP caused by the different degree of static eccentricity and the UMP caused by dynamic eccentricity, which are shown in Section 5.3 and 5.4 respectively.

5.2.1 Cage rotor induction machine

Both the FEA and experimental works were done on Machine-2 to find the UMP. The rotor with 20% of static eccentricity was created, and the excitation voltage of 0.35 p.u. and 0.5 p.u. were used for this analysis. From Figure 5-3, the FEA results were slightly lower than the experimental results for both 0.35 p.u. and 0.5 p.u. excitation voltage. The difference is mainly because FEA was simulated in a 2D model, where the skewed rotor was not taken into account. The analysis of the skewed rotor was shown in Section 4.5. The larger UMP of the skewed rotor was due to the reduction of the induced pole pair ± 1 magnetic flux in the rotor, so, the damping effect

was reduced. Furthermore, the skewed rotor also increased the airgap leakage flux which also contributed to the larger UMP.

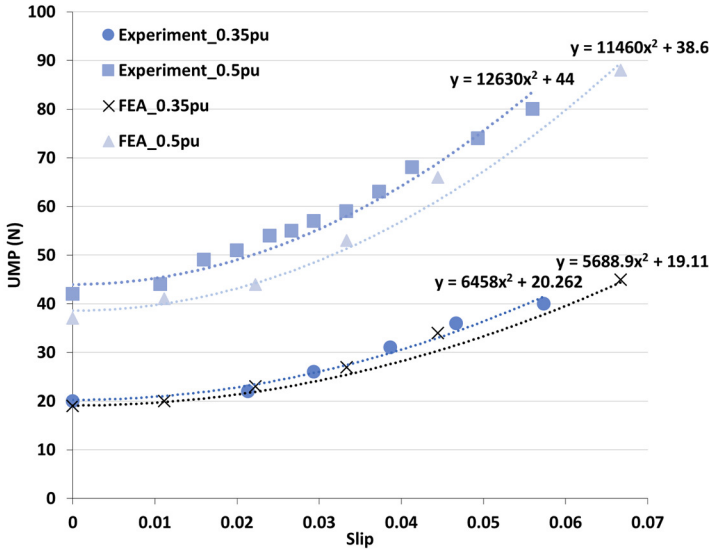

Figure 5-3: UMP vs slip for Machine-2 with 20% eccentricity.

In Table 5-1, the parameter-*B* of the FEA results had a lower value than the experimental results. The smaller parameter-*B* was caused by the reduced damping effect from the cage rotor, because the main UMP in parameter-*B* is from the fundamental magnetising flux. Then, the slightly lower parameter-*A* of the FEA than the experimental result is caused by an increment in airgap leakage flux, which is contributed by the skew leakage flux.

Furthermore, the FEA and experimental results at different supplied voltages are almost the same. This is because the low excitation voltage does not cause magnetic saturation in the iron core.

Voltage (p.u.)	*A*	*B*	R-squared value
0.35 (FEA)	46440	156	0.9910
0.5 (FEA)	45840	154	0.9753
0.35 (Exp)	52718	165	0.9787
0.5 (Exp)	50520	176	0.9665

Table 5-1: Curve-fitting for the results in Figure 5-3.

In Figure 5-3, the FEA was used to find the UMP in Machine-1. The rotor with 20% of static eccentricity was set, and the excitation voltage of 1.0 pu, 0.7 pu and 0.5pu were used for this analysis.

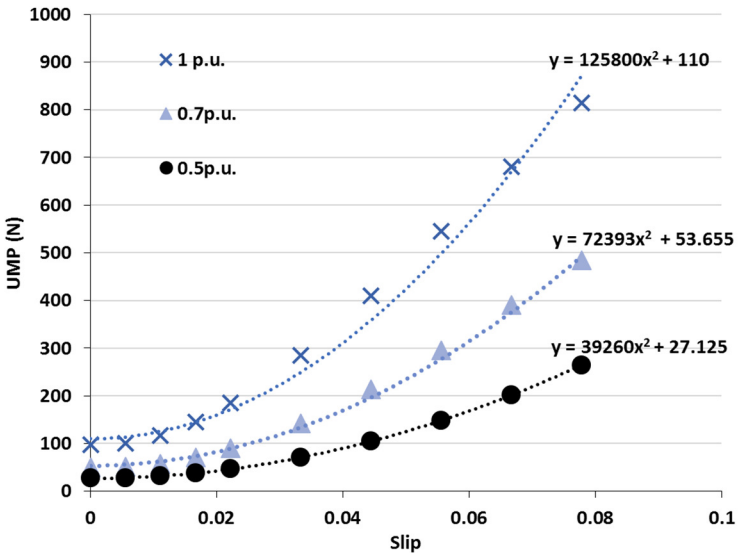

Figure 5-4: UMP vs slip for Machine-1 with 20% eccentricity.

From Table 5-2, the *A* and *B* parameters change as the supplied voltage increases. When the voltage increases, the parameter-*A* decreases, while the parameter-*B* remains almost the same. The reduction of parameter-*A* is due to the magnetic saturation. The 0.5 p.u. and 0.7 p.u. cases have a much closer parameter-*A* than the 1.0 p.u. case. This is because the airgap leakage inductance is affected by the magnetic saturation.

Voltage (p.u.)	*A*	*B*	R-squared value
0.5	157040	108.5	0.9984
0.7	147740	109.5	0.9964
1.0	125800	110	0.9840

Table 5-2: Curve-fitting for the results in Figure 5-4.

Comparing the FEA results of Machine-1 and Machine-2, even though both machines have almost the same volume, peak magnetic flux and eccentricity, the parameter-*B* of Machine-2 was 50% higher than Machine-1. This is because Machine-1 has a lower pole-pair number than Machine-2, where the slip frequency of the additional ± 1 pole-pair fundamental flux is higher. The higher slip frequency would increase the damping of UMP.

However, the parameter-*A* of Machine-1 was 3 times higher than the parameter-*A* of Machine-2. These results were correlated with the results from Figure 4-14 and Figure 4-15. The difference was mainly from the airgap difference between both machines, where Machine-2 has a 0.9 mm airgap and Machine-1 has a 0.5 mm airgap.

5.2.2 Wound rotor induction machine

In Figure 5-3, the UMP in Machine-3 was found by using FEA. The analyses on 20% of static eccentricity and the excitation voltage of 1.0 p.u., 0.7 p.u. and 0.5 p.u. were done.

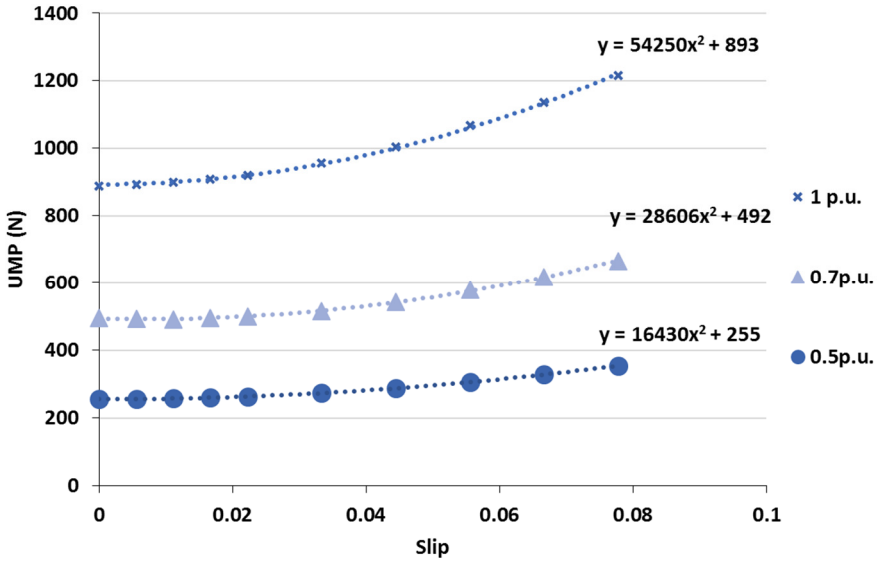

Figure 5-5: UMP vs slip for Machine-3 with 20% eccentricity.

From Table 5-3, the *A* and *B* parameters decreased when the supplied voltage increased due to magnetic saturation. When the machine was experiencing magnetic saturation, the magnetic permeance difference between the narrowest airgap and the

widest airgap will decrease. This will reduce the increment of UMP due to incrthe ement of the excitation voltage. In addition, the parameter-B of Machine-3 was 10 times higher than parameter-B of Machine-1 because the wound rotor could not damp the additional ± 1 pole pair flux.

Voltage (p.u.)	A	B	Standard error
0.5	65720	1020	0.9969
0.7	58380	985	0.9968
1.0	54250	893	0.9984

Table 5-3: Curve-fitting for the results in Figure 5-5.

However, even though the airgap length of Machine-3 is the same as the airgap length of Machine-1, the parameter- A of Machine-3 is much lower than Machine-2. This is because of:

1) Wound rotor does not induce the additional $\pm \mathbf{1}$ pole pair flux, which causes lower induced rotor current and lower rotor leakage flux. In addition, the wound rotor has more rotor slots than the cage rotor. A higher number of slots will reduce the peak magnetic flux.
2) The slight reduction of the fundamental magnetising flux is not taken into account.

In the 2nd reason stated above, the decrement in magnetising flux needs to be considered to find the actual parameter-A. The investigation of the actual parameter-A is to understand the UMP caused by the airgap leakage flux, but it will not be used in the UMP calculation. The magnetising flux can be found either by using a look-up table, or analytical calculation. Parameter-G is introduced as the reduction factor of the UMP caused by magnetising flux, which is a function of the rotor slip. The magnetising flux characteristic at different slip is shown in Figure 5-1. The UMP is proportional to the rotor slip squared with a constant offset, which is shown in (5-8).

$$UMP \propto As^2 + B \tag{5-8}$$

The parameter-B from Table 5-3 is maintained the same but $(1 - Gs^2)$ needs to be added as a multiplier to reflect the UMP from the fundamental magnetising flux. The curve fitting of G is shown in Figure 5-6. As wound rotor does not damp any flux produced by the rotor eccentricity, the airgap leakage flux in B could be neglected because it is relatively small compared to the UMP caused by the fundamental magnetising flux.

$$UMP \propto A_{actual}s^2 + B(1 - Gs^2) \tag{5-9}$$

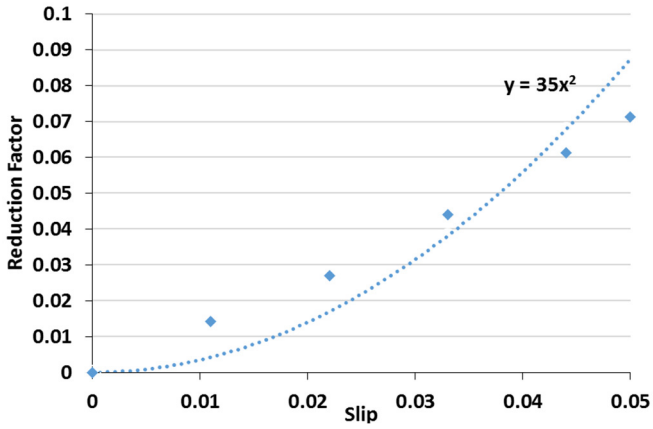

Figure 5-6: Curve fitting for *G*.

Comparing (5-8) and (5-9), the A_{actual} can be found by adding the A with the B with the reduction factor which is shown in (5-10).

$$A_{actual}s^2 = (A + BG)s^2 \tag{5-10}$$

Let $A = 58000$, $B = 1000$, calculation of (5-10) is shown in Figure 5-7. The A_{actual} is 100000. At the rated voltage, the A_{actual} is closer to the A for Machine-1(125800) after considering the reduction factor in the fundamental magnetising flux. As a conclusion, the A_{actual} shown in this section is just to investigate the UMP caused by the airgap leakage flux. However, the reduction factor can be ignored and

the original parameter-A is used, because the purpose of empirical method is to use a simplified method to estimate the final results.

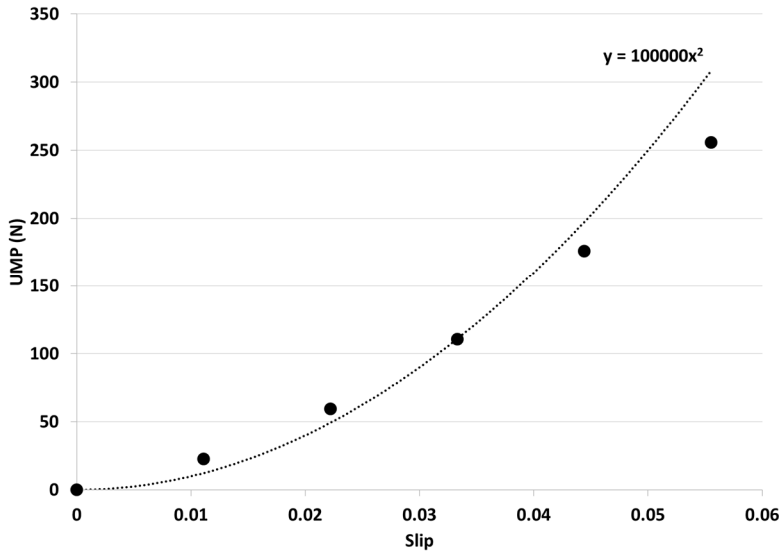

Figure 5-7: Curve fitting to find A_{actual} for Machine-3.

5.2.3 Magnetic saturation

From the curve fitting of the three different machines, we can see that the magnetic saturation affects the A and B parameters. Therefore, saturation factor could be added to increase the accuracy of the empirical method. (5-11) shows the extended empirical method's equation from (5-6) that includes the variable of the UMP Damping Coefficient and also the saturation factor. The saturation factor is a function of rotor slip and excitation voltage.

$$UMP(s) = 2Ks^2v^2\left(k_{sat}L_{ag}\frac{E}{R_r}\right)^2 + Kv^2\left[\beta(s)\left(k_{sat}L_M\frac{E}{X_M}\right)^2 + \left(k_{sat}L_{ag}\frac{E}{X_M}\right)^2\right] \quad (5\text{-}11)$$

In this thesis, the calibration of the magnetic saturation is not done, because the saturation effect would not have much impact on the overall UMP in the machine that is running below its rated slip and voltage. With the refinement in (5-11), the UMP calculation could be used even at a higher rotor slip.

5.3 Implementation of the Empirical Method for the Machines with Static Eccentricity

This section shows the implementation of an empirical method to estimate the UMP of a different scenario. As the magnetic permeance does not change linearly with the degree of eccentricity, the effect of different degree of eccentricity is first investigated by using FEA on Machine-1. Then, the empirical method is compared with the experimental and FEA results of Machine-2 and Machine-3.

5.3.1 Different degree of eccentricity

Figure 5-8 shows the results from FEA and empirical method for different degree of static eccentricity in Machine-1 at rated voltage. To estimate the UMP through the empirical model in (5-6), the value of parameter-A and -B were taken from Table 5-2.

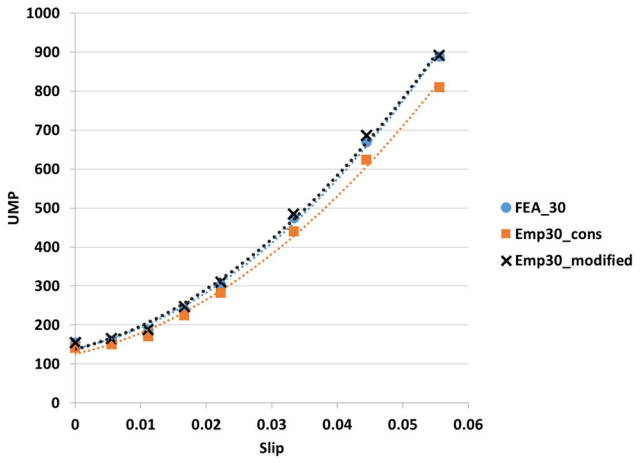

(a)

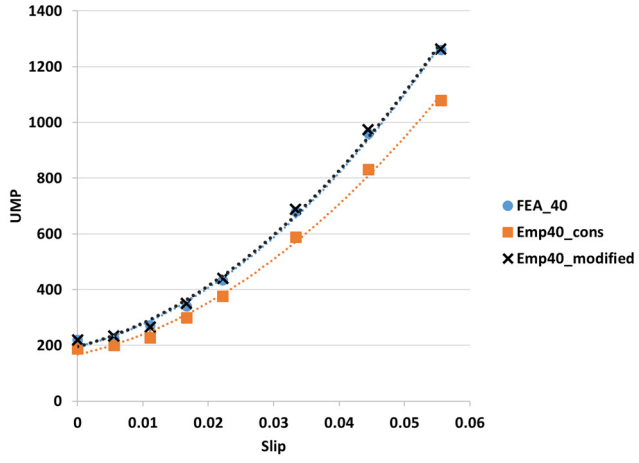

(b)

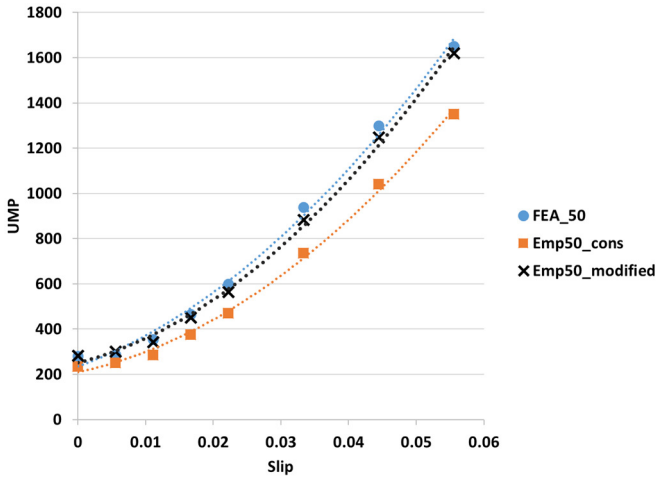

(c)

Figure 5-8: Results of FEA and empirical method for (a) 30% (b) 40% (c) 50% static eccentricity.

Figure 5-8 shows the UMP estimation for a different degree of eccentricity, where the orange line shows the UMP estimation that assumes the magnitude of the pole pair ± 1 sideband flux has a linear relationship with the degree of eccentricity; this assumption made for a low degree of eccentricity is shown in Sub-section 3.1.3. Therefore, as the degree of eccentricity increased, the difference between the empirical method with the FEA results became bigger. To solve this problem, the degree of eccentricity substituted into the variable K in (5-6) needs to be modified. The modification factor is shown in (5-12). The modification factor is machine dependent because it is a function of the saturation factor and the magnitude of the magnetic permeance harmonic.

$$\varepsilon_{mod} = k_{mod}\varepsilon \tag{5-12}$$

5.3.2 Verification of the empirical method

Figure 5-9 (a) shows the UMP of Machine-2 at 30% static eccentricity with 0.5 p.u. voltage. Meanwhile, Figure 5-9 (b) shows the UMP of Machine-3 at 50% eccentricity with 1.0 p.u. voltage. The parameters used in the empirical calculation are extracted from the UMP results of 20% static eccentricity. By comparing the results in both figures, the UMP results estimated by the empirical method are almost similar to the experimental or FEA results. Therefore, the proposed empirical method is verified.

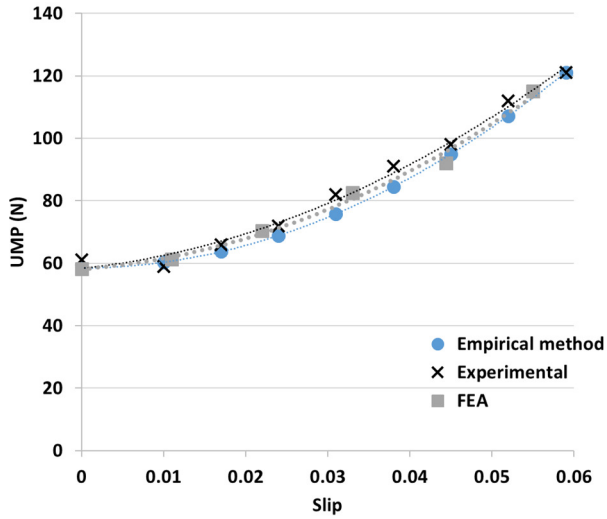

(a)

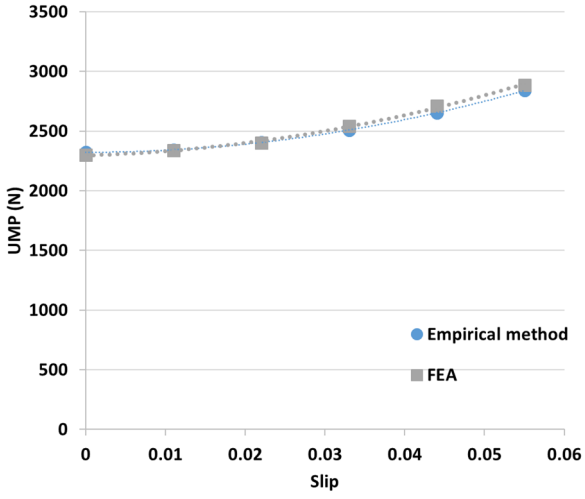

(b)

Figure 5-9: UMP of (a) Machine-2 (30% eccentricity, voltage of 0.5 p.u.), (b) Machine-3 (50% eccentricity, voltage of 1 p.u.)

5.4 Empirical Method for UMP from Dynamic Eccentricity

In this section, the dynamic eccentricity of Machine-1 is calculated by using the parameter-A and -B from the empirical method of static eccentricity. This can also prove the reliability of implementing the empirical method in UMP estimation. The dynamic UMP is then compared with the FEA results. The difference in implementing the empirical method between the dynamic eccentricity and the static eccentricity is the UMP Damping Coefficient at different slip. In the static eccentricity, the Damping Coefficient is assumed to be constant.

As shown in (5-7), B consists of 2 parts: the airgap leakage flux from the magnetising current and the fundamental magnetising flux. The B from Table 5-2 could not be used because it is found for a constant UMP Damping Coefficient. As Machine-1 and Machine-3 have the same stator configuration and airgap length, B can be taken from Machine-3. The A and B parameters should be divided by 2, because 10% eccentricity was tested.

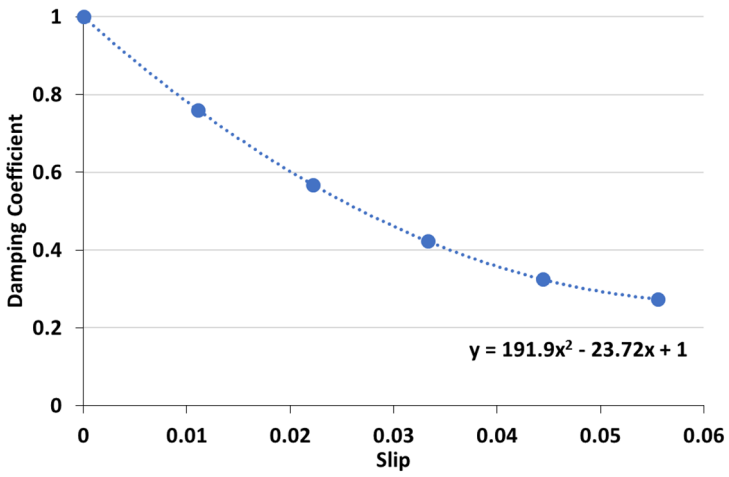

Figure 5-10: UMP Damping Coefficient for Machine-1 with dynamic eccentricity.

Voltage (p.u.)	A	B	β
1.0	67500	447	$191.9s^2 - 23.7s + 1$

Table 5-4: Parameters for Machine-1 with 10% dynamic eccentricity.

For static eccentricity, the damping effect from the cage rotor induction machine is significant even at low slip. Therefore, the airgap leakage flux in B is not negligible. However, for the dynamic eccentricity, the low damping effect at low slip causes the airgap leakage flux in B could be neglected. The Damping Coefficient is shown in Figure 5-10. The parameters of the empirical method is shown in Table 5-4.

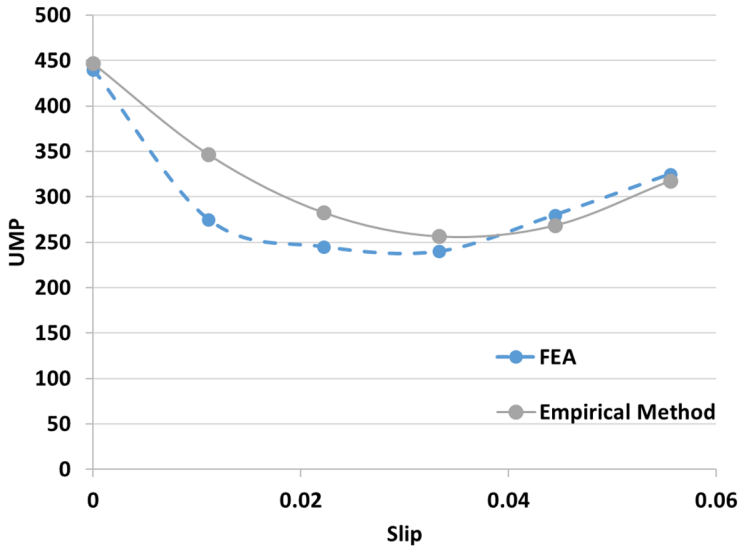

Figure 5-11: UMP comparison between FEA and empirical method for 10% dynamic eccentricity.

Figure 5-11 shows the results of the empirical method and FEA. From 0 slip to 0.033 slip, the UMP reduced because of the increment of damping effect. Then the UMP started to rise back after 0.033 slip because the UMP from the airgap leakage flux began to increase. Both of the results show good correlation between each other. The slight difference of UMP might be coming from the damping of higher space harmonics flux and the magnetic saturation which are difficult to predict.

5.5 Comparison between the empirical method and other methods

The comparison between the proposed empirical method with the conventional analytical method and the 2D-FEA is shown in Table 5-1.

	Empirical Method	Conventional Analytical Method	2D-FEA Method
Required computational time	Prompt **19 μs*	Fast, when circulating current is not taken into account **92 μs (without circulating current)* **≈8 s (with circulating current)*	Time-consuming especially when the airgap is small (0.5mm) ** ≈2 hours*
The effects of circulating current	Can be solved with the proposed Damping Coefficient	Need to be solved numerically which leads to longer computational time	Time-stepping simulation is needed to calculate the rotor MMF harmonics
Accuracy	Higher error may occur when the curve-fitting is wrongly used ***5%*	Higher error may occur in case with larger eccentricity, because higher permeance harmonic is neglected ****5%*	High accuracy when the UMP caused by the end leakage flux is negligible ***3%*
Implementation	A set of UMP results is needed which can be obtained by either FEA or experimental work. Also, the rotor time constant is required	The full space harmonics of stator and rotor winding inductance are needed. Also, the airgap leakage inductance can be calculated by using FEA or empirical method.	Exact drawing of the machine is required
Rotor slip	Only applicable below the rated slip	Can be used to calculate a wide range of slip if the magnetic saturation effect is included in the analytical equation	Can be used for any rotor slip

** Computational time to calculate the UMP for one case, where the processor i7-3770 (Quad Core, 3.40 GHz) is used.*

*** The error is calculated from the results in Figure 5-9(a), where they are compared with the experimental results*

**** The airgap leakage inductance and the Damping Coefficient are extracted from the empirical model based on (5-7). Therefore, the error is the same as the empirical method.*

Table 5-5: Comparison of 3 different methods.

5.6 UMP/Torque Ratio

The UMP characteristic of an induction machine is highly dependent on the airgap leakage flux, fundamental magnetising flux and the UMP Damping Coefficient. Due to the nonlinearity nature of the UMP versus slip that is shown in Figure 5-3 to Figure 5-5, there is a specific operating rotor slip that has the minimum UMP. Therefore, changing the operating slip can reduce the UMP of an induction machine.

In order to find the optimum operating rotor slip, the UMP/torque ratio (γ) is introduced in (5-13). The lowest UMP/torque ratio reflects the operating slip that produced the lowest UMP with the constant amount of torque.

$$\gamma = \frac{UMP}{Torque} \tag{5-13}$$

In this section, the UMP for each machine running at different load and different excitation voltages are presented. Then, the UMP/Torque ratio is calculated to find the optimum operating rotor slip.

5.6.1 Machine-2

Figure 5-12 shows the UMP of both cases does not intersect. Therefore, there is no local minimum in the UMP/Torque ratio in Figure 5-13. The main reason is the results shown for both excitation voltage was only up to 0.06 rotor slip. Therefore, if we take a close look at Figure 5-12, the UMP of 0.35 p.u. will intersect with the UMP of 0.5 p.u. when the torque is further increased to around 10 Nm (FEA). However, the higher slip will cause higher copper loss. Therefore, it is not recommended to run above the rated slip.

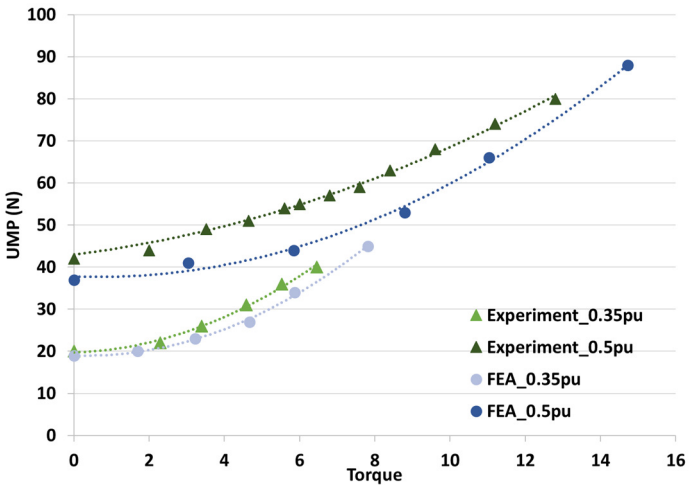

Figure 5-12: UMP vs torque for Machine-2.

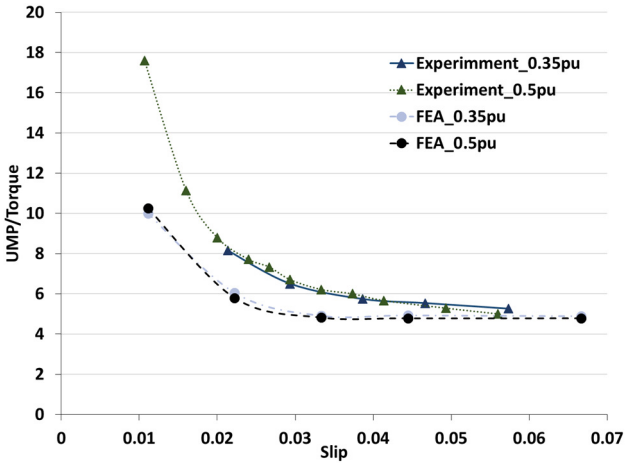

Figure 5-13: UMP/Torque ratio for Machine-2.

5.6.2 Machine-1

Figure 5-14 shows the UMP of all 3 cases intersected at different torques. This means that there is a local minimum in the UMP/Torque ratio. As shown in Figure 5-15, the minimum UMP/torque is around 0.02 rotor slip. The optimum slip may slightly vary with different excitation voltage.

Due to the saturation effect on the airgap leakage flux is not significant at low slip, the three different excitation voltages have around the same minimum UMP/Torque ratio. As the slip further increased, the difference of the UMP/Torque ratio for each case started to increase. However, this does not have an effect on

choosing the best operating slip. For example, 0.02 rotor slip of the 1pu voltage generated a torque of 18 Nm. When the torque is increased to a value that is higher than 18 Nm, the excitation voltage could not be higher than the rated voltage.

Although both Machine-1 and Machine-2 are cage rotor induction machines, the difference in parameter-*A* and -*B* will cause the best operating slip to be different.

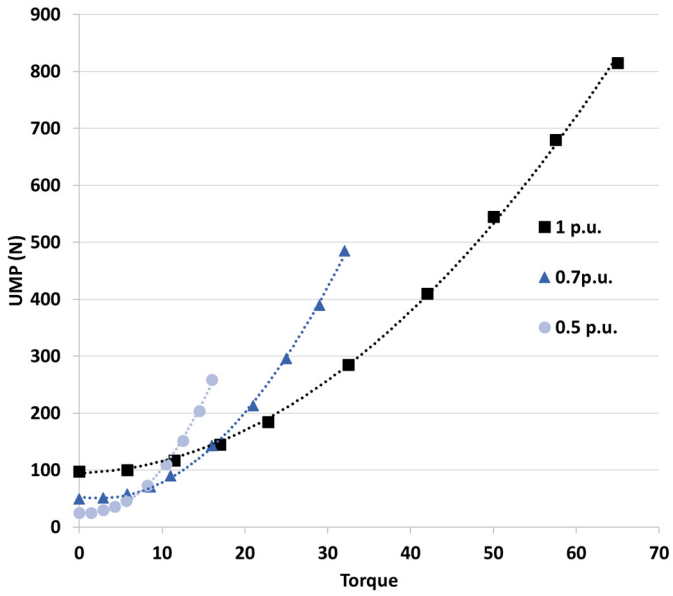

Figure 5-14: UMP vs torque for Machine-1.

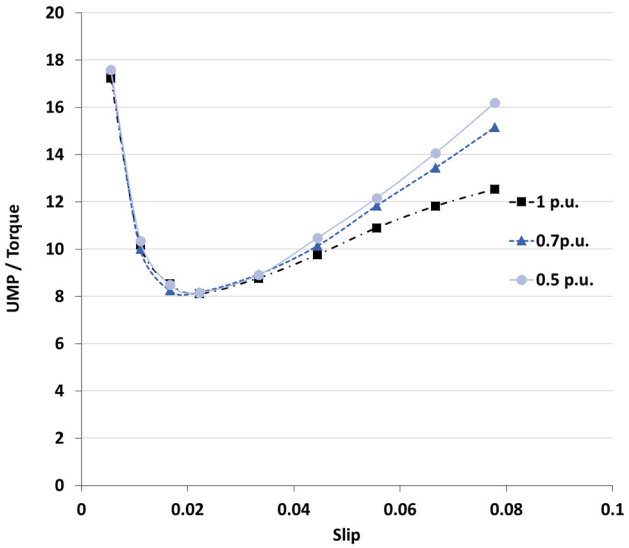

Figure 5-15: UMP/Torque ratio for Machine-1.

5.6.3 Machine-3

From Figure 5-16, it shows that there is also no intersection for the 3 different excitation voltages. Therefore, it can be proven from the UMP/torque curve in Figure 5-17 that the local minimum point does not exist in the graph. For the case with no local minimum in the UMP/torque ratio, the machine can be chosen to run at its rated slip (0.05).

The UMP/torque ratio from Figure 5-17 also shows that the magnetic saturation will slightly affect the UMP/Torque. Comparing Figure 5-15 and Figure 5-17, the effect of magnetic saturation for Machine-3 exists even at 0.01 slip, while the impact of magnetic saturation for Machine-1 only became visible after 0.03 slip. This is because the fundamental magnetising flux is the dominant flux that produced UMP in the wound rotor induction machine. The slight saturation in the fundamental magnetising flux is almost constant at different rotor slips.

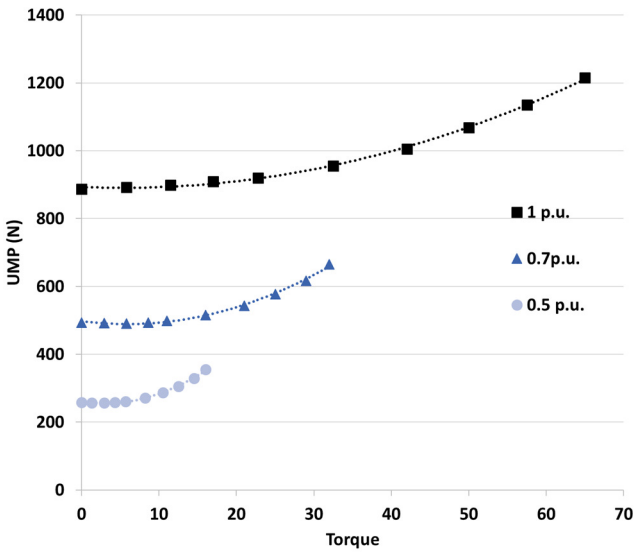

Figure 5-16: UMP vs torque for Machine-3.

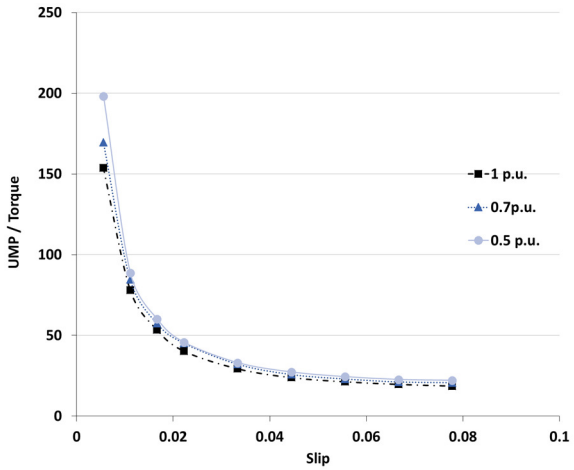

Figure 5-17: UMP/Torque ratio for Machine-3.

5.6.4 UMP/Torque conclusion

The optimum UMP/Torque ratio is machine dependent. For the cases with no local minimum in the UMP/torque ratio (Machine-2 and Machine-3) within 0 to 0.07 slip, the similarity of both machines is that the ratio between the parameter-B and the parameter-A is larger. When the airgap leakage inductance is higher, the increment of the rotor slip will cause a significant increment of UMP because UMP is a function of rotor slip squared. In order to prove this analytically, (5-14) to (5-18) are derived to find the local minimum.

The slip is linearly proportional to the torque, the relationship between torque and slip can be written as (5-14).

$$Torque = k_t s \tag{5-14}$$

Let the supplied voltage of (5-6) be 1 p.u., the UMP/torque ratio can be written as:

$$\gamma = \frac{A}{k_t} s + \frac{B}{k_t s} \tag{5-15}$$

The differentiation of γ with respect to slip gives:

$$\frac{d\gamma}{ds} = \frac{A}{k_t} - \frac{B}{k_t s^2} \tag{5-16}$$

To find the minimum point, the $\frac{d\gamma}{ds}$ in (5-16) is equal to 0, (5-16) becomes:

$$0 = \frac{A}{k_t} - \frac{B}{k_t s^2} \tag{5-17}$$

The optimum operating rotor slip with the lowest UMP is:

$$s = \sqrt{\frac{B}{A}} \tag{5-18}$$

Machine	$\frac{B}{A}$	Slip	Rated Slip
1	0.0006877	0.02622	0.05
2	0.00356	0.058	0.05
3	0.01552	0.1246	0.05

Table 5-6: Calculated optimum operating slip of each machine.

From (5-18), it has shown the optimum slip is a function of the ratio between A and B. Table 5-6 gives the summary $\frac{B}{A}$ ratios and the optimum operating slips of Machine-1, Machine-2 and Machine-3, with 0.5 p.u. excitation voltage and the saturation factor not considered. From Table 5-6, the optimum slip for Machine-2 and Machine-3 is above the rated slip of the machine. Although the calculated optimum slip for these 2 machines are inaccurate due to the neglected saturation effect, the high value of the optimum slip is not important in reducing the UMP. This is because the induction machines are not recommended to operate higher than the rated slip; the higher power losses in the machine, caused by the increment of slip, would be harmful to the machine. Therefore, the induction machines can be set to operate at their rated slip to reduce the UMP.

5.7 Chapter Summary

This chapter analysed how the extraction of parameters from the FEA or experimental results should be used in estimating the UMP through empirical method.

The implementation of the empirical method is investigated because of the difficulty to accurately calculate the airgap leakage inductance. The airgap leakage inductance is affected by airgap length, magnetic saturation, UMP Damping Coefficient, type of rotor and rotor slots number. Instead of acquiring the airgap leakage inductance to calculate the magnetic flux distribution, the empirical method is directly used to find the UMP caused by the airgap flux.

After extracting the parameters in the experimental results of 20% static eccentricity for Machine-2, the empirical method was verified by estimating the UMP of 30% static eccentricity at 0.5 p.u. voltage with 50 Hz supply frequency, in which the results were compared with the results from both FEA and experimental results. Although the verification is done at 50% of the rated voltage and the torque is reduced by 75%, the pattern of the torque-speed curve and the UMP characteristics of Machine-2 remain the same. This is because the inherent changes in both characteristics are mainly more affected by the supply frequency.

Furthermore, the extracted parameters from the results in Machine-1 were used to estimate the UMP caused by the dynamic eccentricity. In addition, as the UMP Damping Coefficient for static and dynamic eccentricity is different, methods to recalculate the UMP Damping Coefficient by using the extracted parameters was presented. Good correlation was shown on the empirical method and the FEA for the calculation of the UMP caused by the dynamic eccentricity.

Then, UMP/Torque ratio is introduced to find the operating slip with the lowest UMP. From the UMP/Torque ratio calculation, Machine-1 (cage rotor) has a local minimum of 0.02 slip in the UMP/Torque ratio. Meanwhile, the slip with the lowest UMP of Machine-2 (cage rotor) and Machine-3 (wound rotor) are much larger than their rated slip. This is because Machine-2 has a bigger airgap than Machine-1, while Machine-3 does not have any parallel path to damp the UMP caused by magnetising flux. Therefore, they can be chosen to operate at their rated slip (0.05) to get the minimum UMP.

6 Methods to Reduce UMP

Due to the non-linearity of UMP-slip characteristic, which was analysed in Chapter 5, the UMP can be reduced if the induction machine is running at its optimum slip, especially when the machine is lightly loaded. Therefore, the slip control method to reduce UMP is proposed. The UMP for the cage rotor and the wound rotor induction machine are simulated by using Matlab/Simulink with the proposed empirical method in Chapter 5. Then, the slip control method is discussed and verified by using experimental work.

Further to this, by using the damper winding idea proposed by Dorrell [96], a new damper windings configuration is introduced to reduce the UMP. The new damper winding configuration has shown great UMP reduction in a wound rotor induction machine. This is because the pole pair ± 1 of the fundamental flux is significantly damped. Although the new set of winding has a simplified design, it can only be used on the induction machine with even pole pair number.

6.1 Slip Control Method

Slip control method is often used to increase the efficiency of a lightly loaded induction machine [149] because induction machines are not efficient when running at close to its synchronous speed. By reducing the magnetising flux, the rated load can be reduced. Reducing flux creates a balance between iron losses and copper losses.

However, changing the magnetising flux is not suitable for situations that need a fast response since changing the rotor flux may take a few hundred milliseconds. The response time depends on the magnitude of the changes and the rotor time constant of the induction machine.

For implementing slip control to reduce the UMP, it would be more effective to reduce the UMP of the induction machine when the machine is lightly loaded. For induction machines in motoring-mode, 50% of the motors in the U.S. operate at less than 60% of their rated load, and 33% of the motors have below 50% load factor [150]. Meanwhile, the average load in the European Union is estimated to be less than 60%; some particular motor may have an average load factor of 25% [151]. For the induction machine running in generating-mode, the wind energy generators do not tend to run at full load continuously. The average load factor for onshore wind turbines is 26.6%, and offshore wind turbines is 37.2% [152]. Meanwhile, the load factor for both tidal current and wave energy is around 35%-40% [153]. Therefore, from this perspective, there is an opportunity to implement slip control to reduce UMP in the induction machine at either motoring or generating mode.

From the last chapter, the UMP/torque ratio has shown that the UMP varies with the rotor slip. The rotor slip can be varied by changing the flux of the induction machine. The magnetising flux of the machine can be changed to obtain the minimum UMP when the machine is not running at full load. The lowest UMP operating point might not have the lowest power losses. Therefore, a new objective can be added to the flux control to find the optimum operating point to reduce both the UMP and the losses. The magnetising flux can be controlled by using either scalar control or vector control.

Different strategies are used in optimising the magnetising flux in the machine. The control algorithm includes slip speed, rotor flux, excitation current or voltage. In [154], the author had categorised the loss minimising control into 3 categories:

1) Single machine parameter control: This is controlled based on a parameter like the power factor or the rotor slip. This method can reduce the input

information where the speed or the load of the machine is not required. This is because power factor or the rotor slip is a function of load and speed.

2) Search control: The power output is kept constant for the whole time, and the machine flux is iteratively adapted to find the minimum input power. This method does not require any information about the parameters of the machine and the control drive. However, the disadvantage is the slow response time, which is usually larger than 7 seconds. In addition, continuous fluctuations of torque might result in the system could not converging into a stable steady-state condition.
3) Loss model control: This is usually used in a vector control. The power loss model can be placed in the existing control topology. This method can be used in either in closed-loop, or open-loop control.

6.1.1 Control system

There are two types of control topology that could be used to implement slip control: vector control and scalar control. The vector control uses the control idea of a DC machine, where the two orthogonal components are controlled individually to receive the desired torque and speed. The increasing popularity of vector control is due to the development of modern power electronics. Two main types of vector controls are the direct torque control (DTC) and the field oriented control (FOC).

The current is separated into two different axes, which are the quadrature axis and the direct axis. The quadrature axis is responsible for producing torque, and the direct axis is responsible for producing flux. The vector control requires the knowledge of the rotor flux position, which can be obtained either by a search coil, or by sensorless estimation. Sensorless topology is a more popular method to estimate the rotor flux position due to its robustness and accuracy. However, the machine's parameters are heavily affected by the machine's temperature.

Although the torque is also a function of the flux, changing the direct component is seldom used, except for specific purposes, like power loss optimisation. This is because of the long response time of changing the direct axis, which might be more than a few hundred milliseconds. This could not be avoided, because the rotor

resistance is usually relatively small, compared to the inductance, where a sudden change of flux creates a high reactance. Therefore, changing the direct axis will create a large amount of rotor leakage flux at the first instant.

Scalar control is a much more stable and straightforward control technique. The scalar control is based on the magnitude of the voltage and the frequency without considering the phase or the magnitude of the current. The response time towards changing the rotational speed is much slower than the vector control. In [155], the author has shown the scalar control is 3 times slower in converging for the energy optimising control for the power factor control. The time may vary depending on the machine parameters. In addition, the scalar control is more vulnerable to sudden load change, or load disturbance, compared to the vector control.

However, the scalar control will be used in the thesis in the experimental evaluation and also in the Matlab/Simulink model. The main reason is that the load and speed changes are not the primary concerns of the control to reduce UMP. If the machine is running at fixed speed and fixed load, changing the rotor flux by using the scalar control, or by using the vector control, have almost the same converging time if the model-based method is used in finding the optimum flux [155]. In terms of the reduction of UMP, scalar or vector control would not have any difference when the machine is running at steady state.

For the scalar control, it controls the ratio between the voltage and frequency. It is also known as Voltage-Hertz control. The relationship between magnetising flux with the supply frequency is shown in (6-1).

$$\Phi \propto \frac{V}{f} \tag{6-1}$$

The linear relationship is based on the assumption that the stator resistance is zero. This assumption is only accurate below the rated condition, because the voltage drop across the magnetising impedance is close to the supply voltage. In this case, the

supplied voltage is assumed to be equal to the excitation voltage. Therefore, with the fixed frequency, changing the supply voltage can change the magnetising flux.

The characteristic of the varying supply frequency is shown in Figure 6-1. It has shown that the torque-speed characteristic changes with frequency. In the constant torque region, the peak torque is constant when the supply frequency increases, because the magnetising flux in the machine is fixed. For the constant power region, the supplied frequency is higher than the machine rated frequency where the magnetising need to be reduced to reduce the back EMF induced in the stator winding because the supplied voltage is capped.

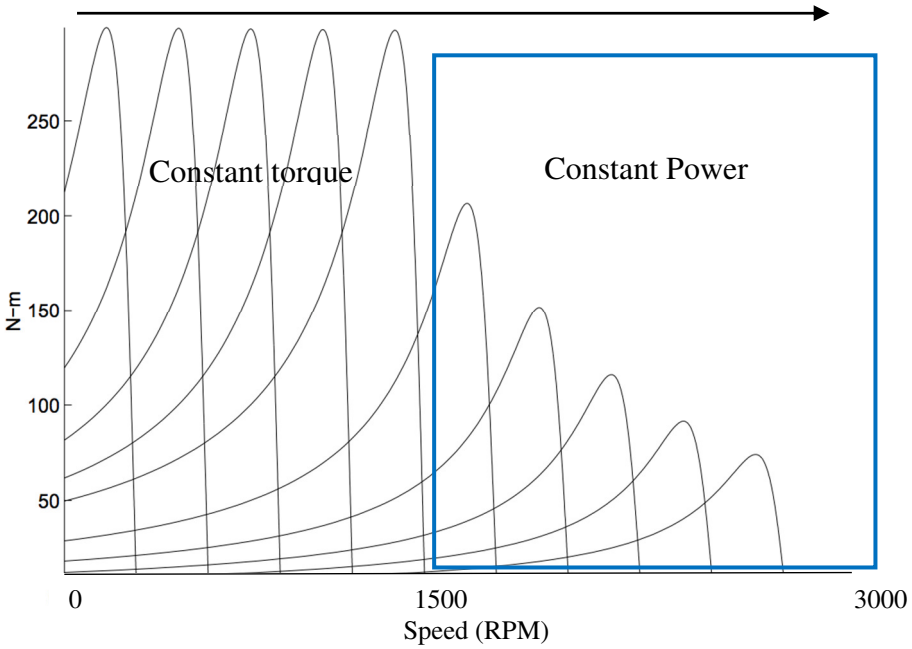

Figure 6-1: Torque speed characteristic with varying frequency [156].

To have a constant magnetising flux at different supply frequency, the voltage drop across the resistance needs to be calculated.

$$V = i_s R + E \tag{6-2}$$

The excitation voltage, E, has a linear relationship with the magnitude of the magnetic flux which is shown in (6-3).

$$E = 4.44 N f \Phi_M \tag{6-3}$$

Assuming that the leakage inductance is small when the rotor rotates close to the synchronous speed, the magnetising flux is the dominant flux. The simplified equivalent circuit is shown in Figure 6-2.

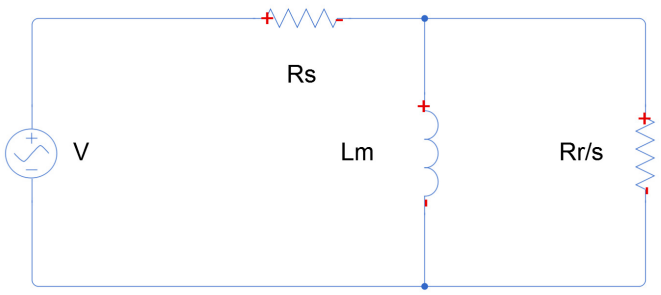

Figure 6-2: Simplified equivalent circuit.

The magnetising current is:

$$i_M = \frac{\Phi_M}{L_M} \tag{6-4}$$

Then, the load current can be written as:

$$i_R = \frac{sE}{\mathrm{R}_r} \tag{6-5}$$

The total current flowing in the stator winding:

$$i_s = \sqrt{{i_R}^2 + {i_M}^2} \tag{6-6}$$

The stator and rotor current information taken from (6-5) and (6-6) are used to calculate the UMP of the induction machine.

6.1.2 Slip control topology

Multiply (6-5) with the excitation voltage and divide it by the rotational speed. The torque of the machine can be written as (6-7).

$$T = \frac{3}{2n_s} \times \frac{sE^2}{(1-s)R_r} \tag{6-7}$$

In the case of constant slip and constant supply frequency, let $K = \frac{3}{2n_s} \times \frac{s}{(1-s)R_r}$, (6-7) can be simplified into (6-8).

$$E = \sqrt{\frac{T}{K}} \tag{6-8}$$

In the scalar control used in the thesis, the model-based control method is applied to maintain the rotor slip. When model-based control is used in loss optimisation in induction machine, the control could provide fast response and does not produce torque ripple [157]. However, the accuracy of the moded-based control is affected by the defined machine's parameter and the inverter loss. In this thesis, as the slip control is used to reduce the UMP, the accuracy issue in the model-based control method can be ignored. Therefore, model-based slip control is used because it can provide fast response to reduce UMP.

In the model-based control, the excitation voltage is calculated so that the machine could maintain at the desired rotor slip. The response of the control depends on input load information. Also, varying the voltage to maintain the rotor slip has a long response time of a few hundred milliseconds, a low-pass filter was used in [158] to prevent load fluctuation when using slip control.

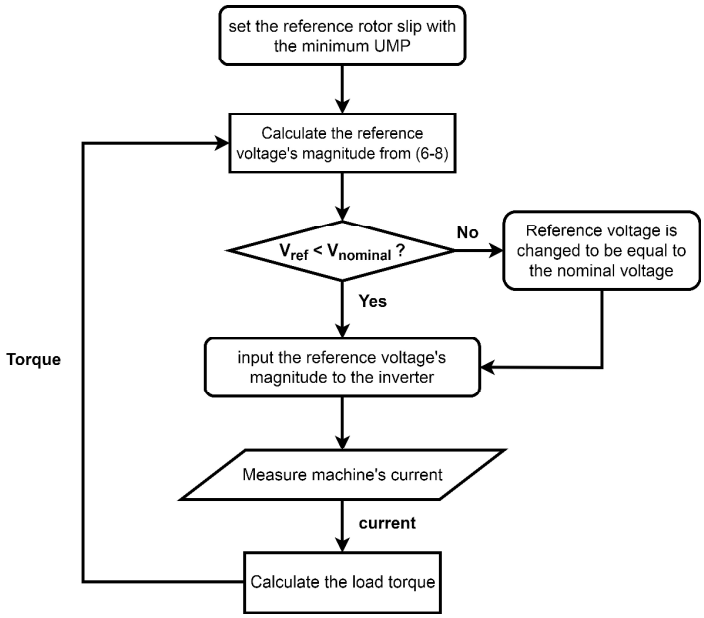

Figure 6-3: Control flow of the slip control method to reduce UMP.

The control flow is shown in Figure 6-3. Firstly, the desired rotor slip to achieve the minimum UMP is set in the control. As pointed out in Section 5.6 that the optimum slip remains at almost the same value at different excitation voltage and different degree of eccentricity, the optimum rotor slip is a constant variable. Then, the excitation voltage is calculated by using (6-8), which is calculated from the K is a constant variable when the slip is fixed, and the machine's torque (at $t = 0$, it can be set to a non-zero value below the rated load). If the calculated reference voltage is higher than the nominal voltage, the reference voltage is set to be equal to the nominal voltage. After that, the reference voltage is set as the input variable of the inverter. From the measured current, the torque of the machine can be calculated. However, the excitation voltage cannot be higher than the bus voltage of the inverter. Due to this reason, the slip control method is only applicable for lightly loaded machines.

As from (6-8), the changing of excitation voltage would change the slip of the machine. This is because the torque-slip characteristic is changed, in which the torque-slip characteristic of Machine-2 from FEA simulation is shown in Figure 6-4. When the voltage is reduced by 50%, the overall torque of the machine is reduced by 75%. Then, the operating point of 10 Nm is pointed out in Figure 6-4 as an example, which shows that UMP can be changed when the slip is changed. In this case, the UMP could be reduced by 63% when the voltage is reduced.

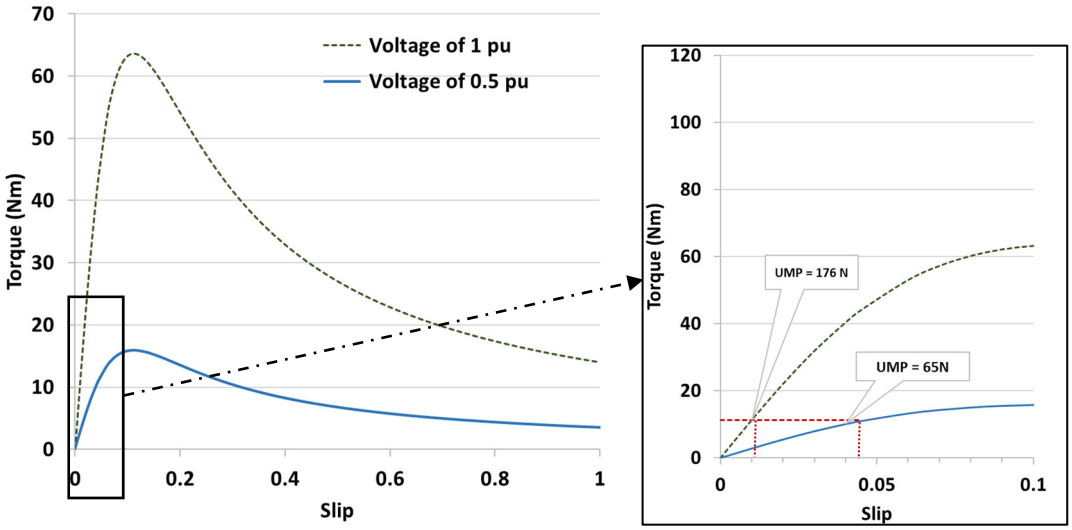

Figure 6-4: Torque-slip characteristic of Machine-2 and the UMP of 20% static eccentricity when the machine is loaded with 10 Nm (FEA)

For Machine-1, the slip control can be used when the load is below 40% of the rated load because the optimum rotor slip is around 0.02, which is 40% of the rated slip. As the reference voltage cannot be higher than the nominal voltage of the inverter, a higher voltage could not be used to maintain the 0.02 slip when the load is over 40%. In addition, higher excitation voltage with the same excitation frequency would cause the magnetic core saturation in the machine. For Machine-2 and -3, this method can be used at all load except at the full load. Figure 6-5 shows the voltage-torque relationship of the model-based slip control for 0.02 slip (Machine-1) and 0.05 slip (Machine-3). The block diagram of the scalar control is shown in Figure 6-6.

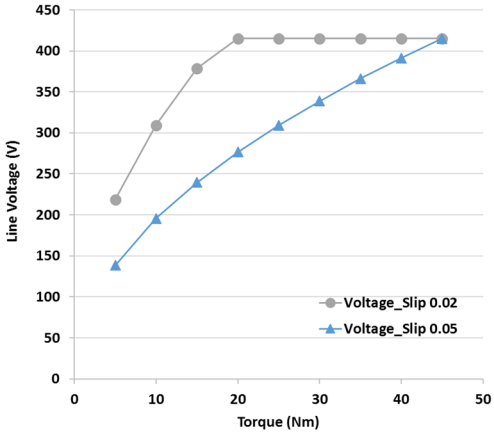

Figure 6-5: Voltage-torque relationship used in the model-based control.

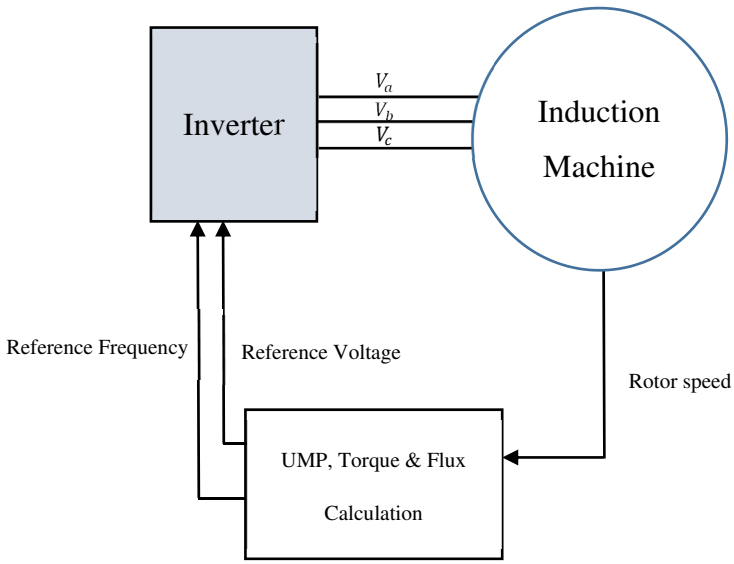

Figure 6-6: Block diagram for scalar control.

6.1.3 Simulation setup

The concept of Voltage-Hertz control uses the relationship that the voltage is proportional to the magnetic flux and inversely proportional to the frequency, as shown in (6-1). The Voltage-Hertz control is often used to maintain the magnetising flux in the induction motor when the induction machine running below its rated speed, or weakening the flux to reduce the back-EMF of the machine when the induction machine running above its rated speed [159], [160].

In this chapter, the Voltage-Hertz control is used to control the rotor slip by varying the magnetising flux of the induction machine, which was used in [107], [161], [162]. As all the simulation in this chapter was done at the rated frequency of 50 Hz, the voltage is linearly proportional to the magnetising flux. Therefore, the voltage is varied based on the input torque to implement the slip control, in which the voltage-torque relationship was shown in Figure 6-5. The flow of the control was shown in Figure 6-3.

All the models were written and simulated in Matlab/Simulink. All the layout of the models is shown in Appendix F.

Then, the UMP of the simulation with ideal sinewave is calculated based on the proposed empirical method in Chapter 5. The parameters for the empirical calculation of Machine-1, Machine-2 and Machine-3 were taken from the Table 5-2, Table 5-1 and Table 5-3 respectively. As the rotor slip and the excitation voltage are the input variable for the parameters, they were measured from the induction machine model to estimate the UMP during the simulation.

Furthermore, the UMP of the simulation with inverter supplied voltage is calculated with the analytical model from (3-40), in which the stator and rotor current is extracted from the induction machine model to fit in the equation. All the magnetic flux, regardless of its time harmonics, is assumed to have the same UMP Damping Coefficient and airgap leakage inductance, which could be found by using the parameter-*B* in the empirical method, while the airgap leakage inductance could be found by using the parameter-*A* in the empirical method.

6.2 Results for the Machine with Slip Control Method

Machine-1, -2 and -3 are used to show the control to reduce UMP. From the last section, the operating slip with the minimum UMP for Machine-1 is 0.02 slip, and Machine-2 and-3 are 0.05 slip respectively. Machine-1 and -3 are tested in motoring and generating mode, while Machine-2 is tested in motoring mode and its results were compared with the experimental results. The positive torque and negative torque represent the motoring mode and generating mode respectively. The simulation results compare the induction motor with and without control. From Sub-section 6.2.1 to 6.2.5, the excitation voltage of the induction machine is supplied through an ideal sinewave, assuming that an ideal filter is used. Then, the inverter supplied excitation voltage are investigated in Sub-section 6.2.8. The UMP of the Machine-1 and -2 with inverter supplied are investigated in Sub-section 6.2.7 and 6.2.8 respectively.

6.2.1 Machine-1 with slip control

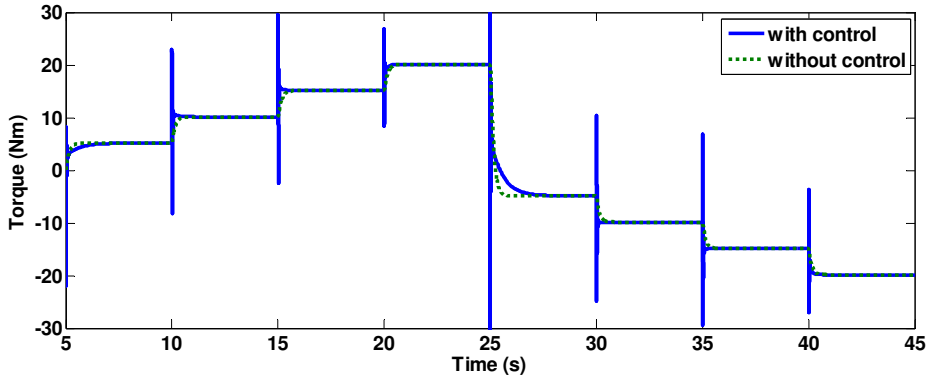

(a)

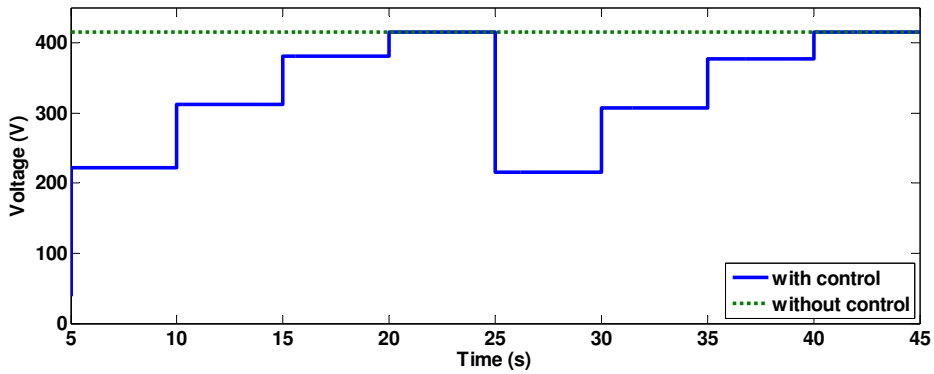

(b)

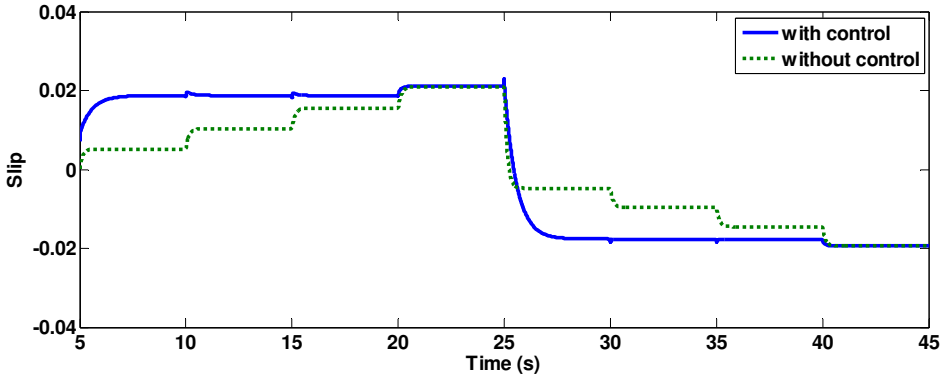

(c)

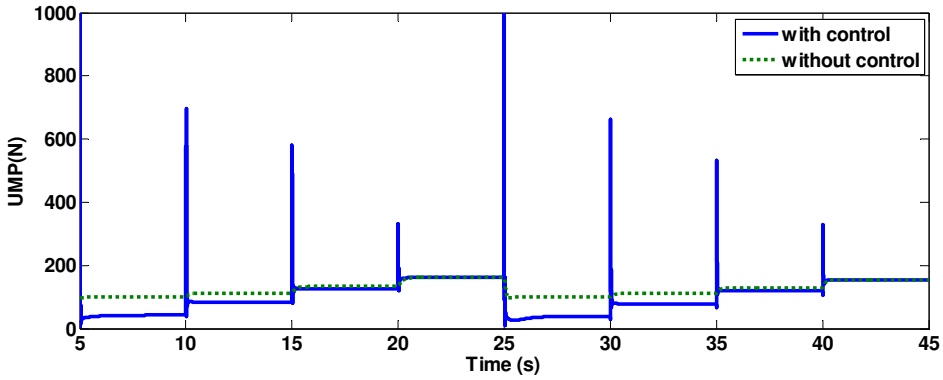

(d)

Figure 6-7: Simulation results for Machine-1 by using slip control (ideal sinewave): (a) torque (b) voltage (c) slip (d) UMP.

From Figure 6-7, the torque is increased from 5 Nm to 20 Nm with a 5 Nm increment step. The motoring mode is from 5 s to 25 s, while the generating mode is from 25 s to 45 s. When the torque is changed at each step, the torque fluctuation had been shown at the beginning of torque change in the machine with slip control. This is because the scalar control could not vary the orientation of the flux at a correct angle to produce torque.

The torque response is not instantaneous for both with and without control. When the reference torque changes, the rotor speed changes. The rotor inertia can be converted into power to delay the changing of machine torque which causes the slow response of the machine's output torque.

With the slip control, the rotor slip is maintained at 0.02. For Machine 2, the rated torque is 45 Nm and the rated slip is 0.05. So, without exceeding the machine

rated flux, the maximum torque to maintain the slip at 0.02 is around 18 Nm with the assumption that the machine slip is linearly proportional to the torque. From the results of slip control, the UMP decreased significantly at 5 Nm. The reduction becomes least significant when the torque increases. When the load reaches 20 Nm, the slip control is switched off because of the voltage reaching nominal value.

The UMP spike was shown at the beginning of every step change. These surges exist on either increment or decrement of the voltage. When a voltage control is applied, the changing of voltage will cause a sudden flux change. This step changes of the flux can be transformed into a series of fluxes with higher harmonic content. The higher harmonic flux would induce a large voltage in the rotor, which produces a current surge. The current surge causes the increment of stator and rotor leakage flux which leads to a larger UMP. This scenario is analysed in the next sub-chapter.

6.2.2 UMP spikes

This section analyses the UMP spikes that occurred when the excitation voltage is changed during the slip control. The experimental and the simulation results on changing the excitation voltage at no load-case for Machine-2 are shown. After creating a 20% of static eccentricity in the machine, the induction machine is excited with 0.3pu voltage, and 50 Hz excitation frequency. Then, maintaining the 50 Hz excitation frequency, the supplied voltage is changed from 0.3 to 0.6 p.u. (Case-1) and 0.6 to 0.3 p.u. (Case-2).

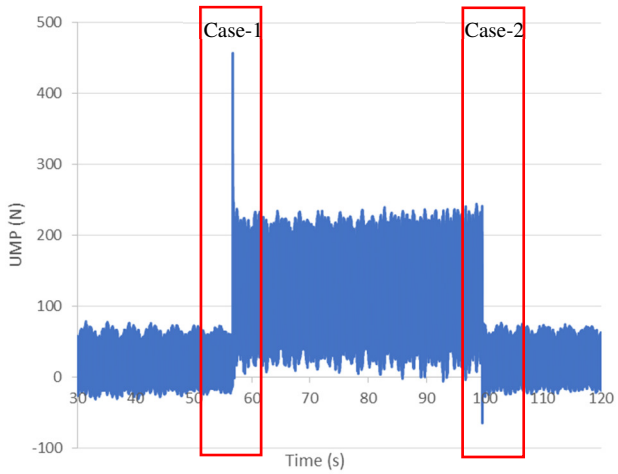

Figure 6-8: Experimental results for UMP with no load.

From Figure 6-8, although the primary component of the UMP caused by the static eccentricity is a constant component, the higher harmonics UMP results could not be filtered out, because the UMP spike from the changing of supplied voltage is going to be investigated. Therefore, other than the UMP spikes, the other higher harmonics content of the UMP is neglected in the analysis. The Case-1 and Case-2 are separated in the following analysis, because the direction of the induced current is different in the increment and decrement of the supplied voltage.

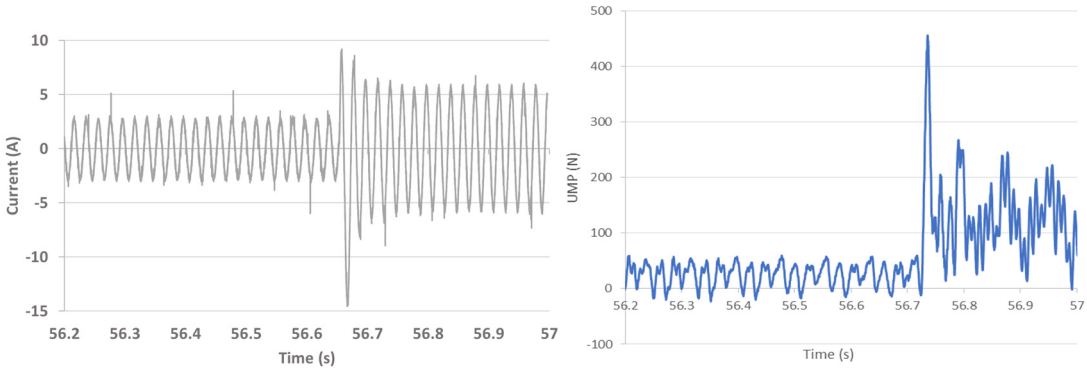

(a) (b)

Figure 6-9: Zoom-in view of Case-1 (a) Current (b) UMP.

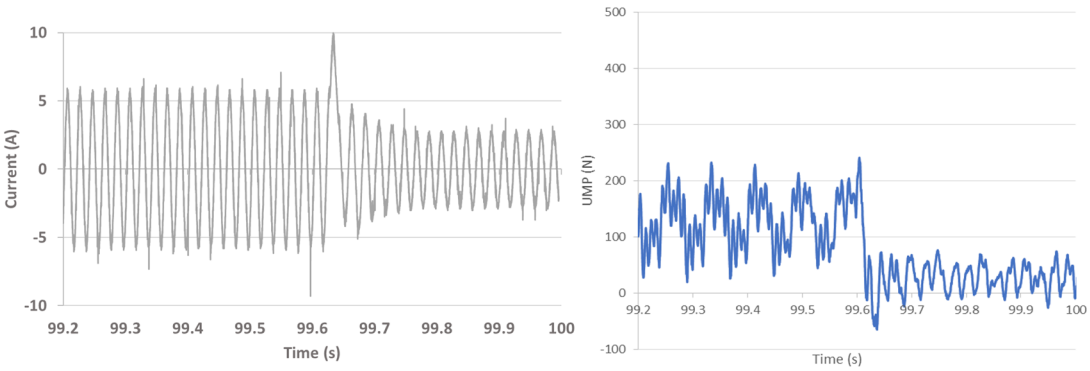

(a) (b)

Figure 6-10: Zoom-in view of Case-2 (a) Current (b) UMP.

The UMP spike is caused by the high airgap leakage flux where the current surges when the voltage changes. In Figure 6-8, there is sizable UMP spike in Case-1. Meanwhile, in Case-2, the UMP spike is least significant. The difference in UMP surge can be seen by comparing Figure 6-9 (b) and Figure 6-10 (b). From Figure 6-9 (a) and

Figure 6-10 (a), the current surged in Case-2 has a peak of 10 A, meanwhile, the current has a peak of 15 A in Case-1.

When the excitation voltage increases or decreases, the step response of the voltage changes can be interpreted as a high rotating frequency flux, which has a high slip when cutting through the rotor bars where the large current is induced. The magnitude of the induced current is the same for the voltage increment and decrement cases. However, the phase angle of the current is opposite. For voltage increment case, the current is added on top of the initial current. Meanwhile, for the voltage decrement case, the current is subtracted from the initial current.

In addition, the UMP spike in Case-2 during the change in voltage is toward the negative direction. This is mainly due to the damping effect. In a transient scenario, the damping flux from the cycle before the changing of the voltage could produce a high counteracting force for the next cycle. This counteracting force is higher than the force from the stator flux. Therefore, a negative UMP is produced. This scenario is not shown in the simulation model from Figure 6-11(b), because the UMP Damping Coefficient used in the analytical model is for steady state operation.

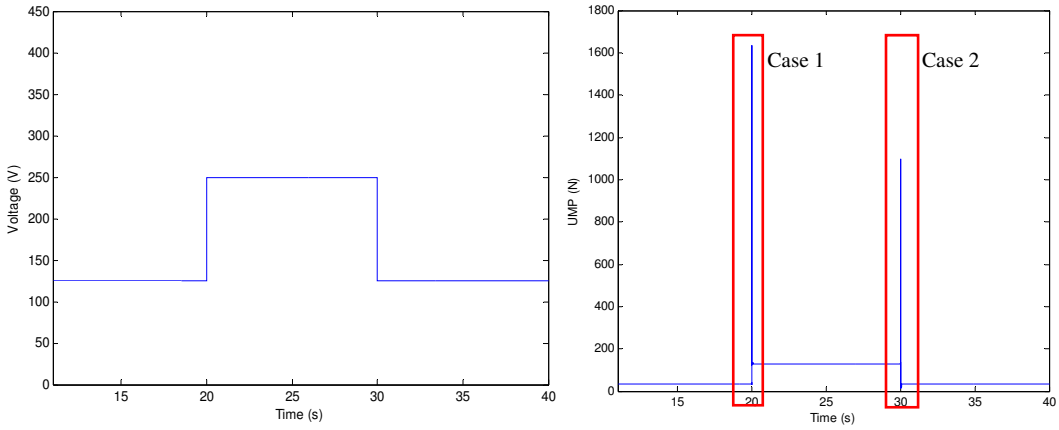

(a) (b)

Figure 6-11: Simulation results (ideal sinewave) with no load: (a) line voltage (b) UMP.

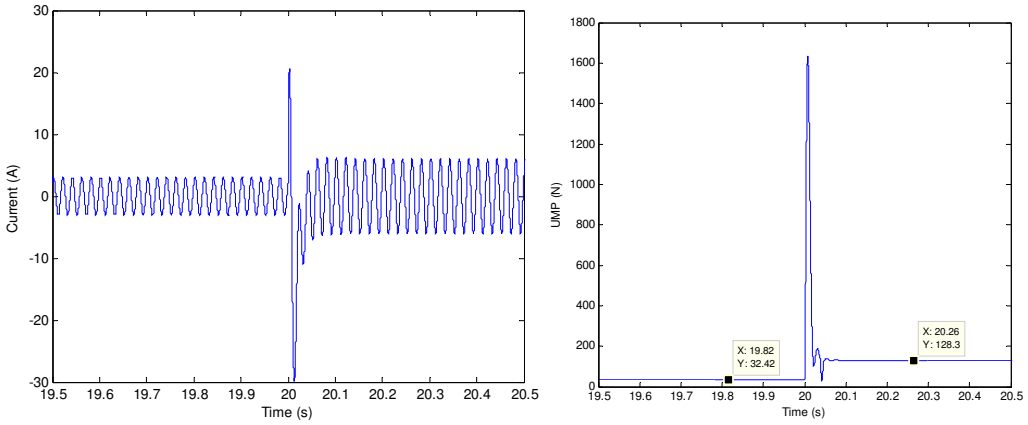

(a) (b)

Figure 6-12: Zoom-in view of simulation results (ideal sinewave) for Case 1: (a) current (b) UMP.

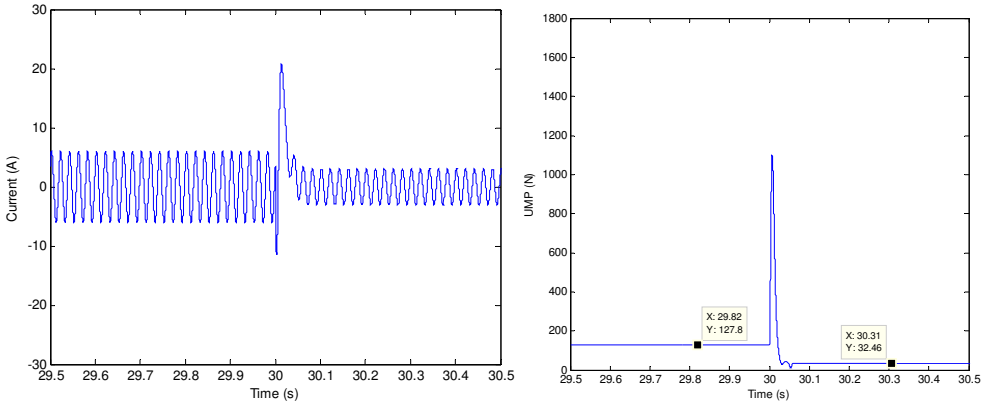

(a) (b)

Figure 6-13: Zoom in view of simulation results (ideal sinewave) for Case-2: (a) current (b) UMP.

From Figure 6-12(a) and Figure 6-13(a), it can be observed that the current spike in the simulation model is much higher than the experimental model. In experimental work, the inverter may have limited the change of output voltage, which could limit the output current. Therefore, the UMP spike in the simulation model is much higher than the experimental model because the UMP is a function of current squared.

6.2.3 Voltage rate of change limiter

The UMP spike from the changing of voltage to maintain the slip is an undesirable scenario because the large UMP spike may reduce the bearing lifetime. To avoid the UMP spike, a rate of change limiter is added to the control of the voltage.

Therefore, the voltage should not be increased instantaneously after receiving the reference voltage command.

Different values of rate of change limiter are used and the simulation results are shown in Figure 6-14. In the voltage increment case, it has shown that the spike is lower when the rate of change limiter is set to a lower value. In the decrement of voltage case, the UMP surge does not exist for all three cases.

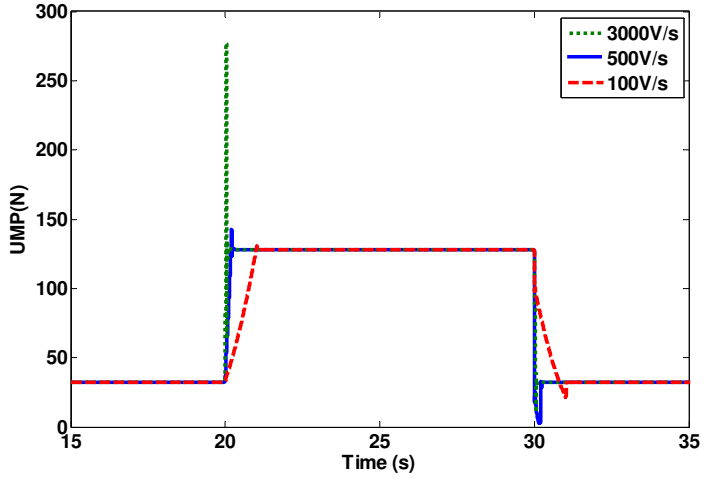

Figure 6-14: Different rate of change limiters for the supplied voltage change.

6.2.4 Machine-1 with slip control and voltage's rate of change limiter

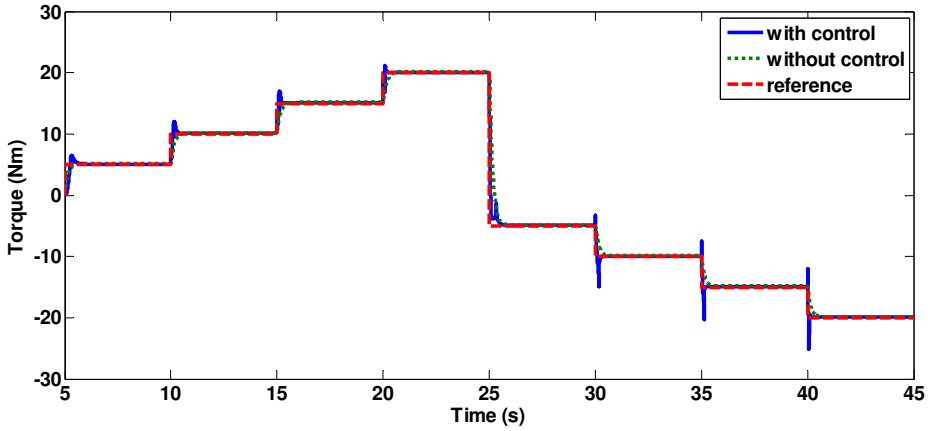

(a)

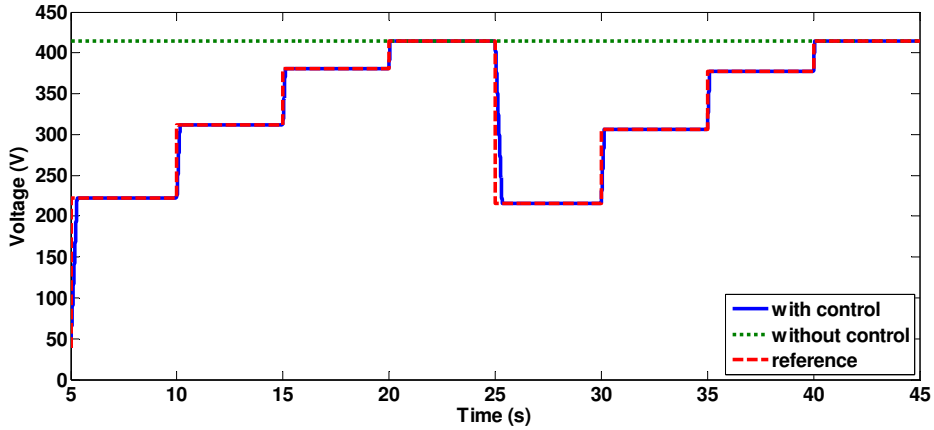

(b)

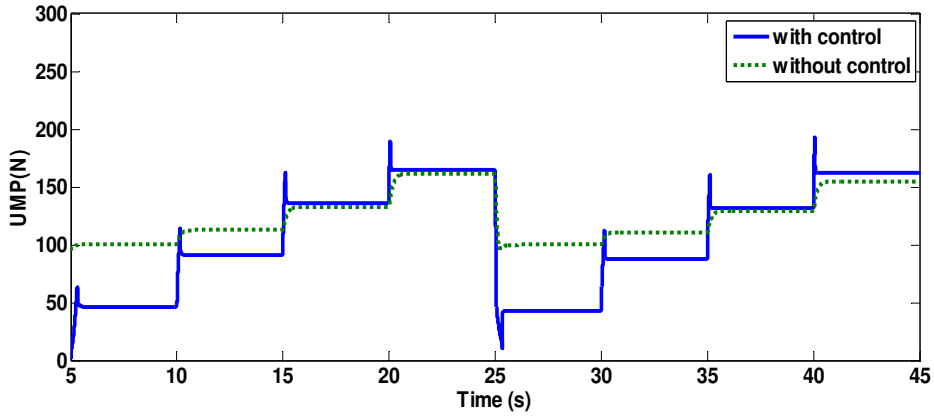

(c)

Figure 6-15: Simulation results for Machine-1 with 500V/s rate of change limiter in the voltage control by using slip control (ideal sinewave): (a) torque (b) voltage (c) UMP.

From Figure 6-15(b), the controlled voltage did not change instantaneously. In addition, it has shown the UMP surge reduced significantly in Figure 6-15(c) if compared to Figure 6-7(d). The spike can be further reduced if the voltage rate of change is further reduced. Therefore, the voltage's rate of change is also one of the design objectives when slip control is applied to reduce UMP.

6.2.5 Machine-3 with slip control method and voltage's rate of change limiter

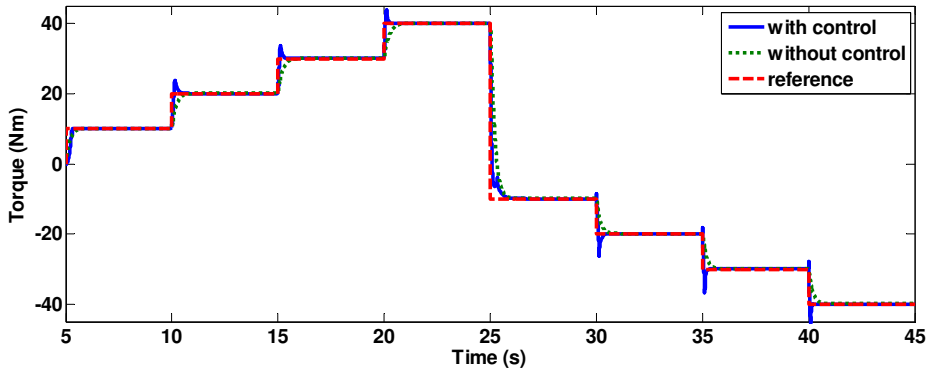

(a)

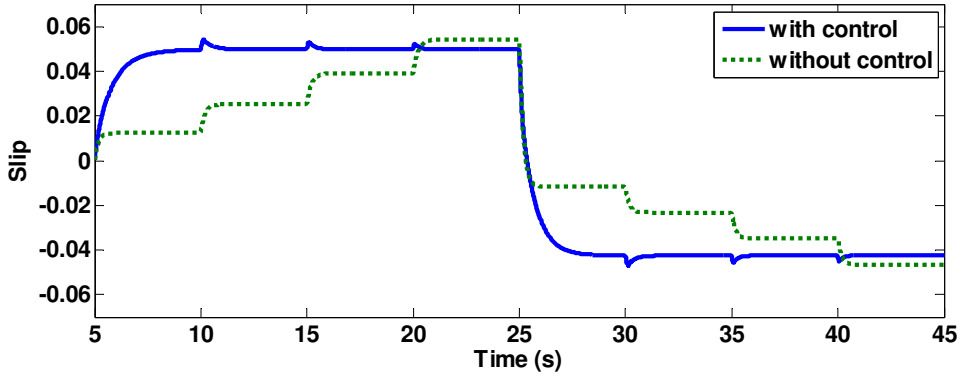

(b)

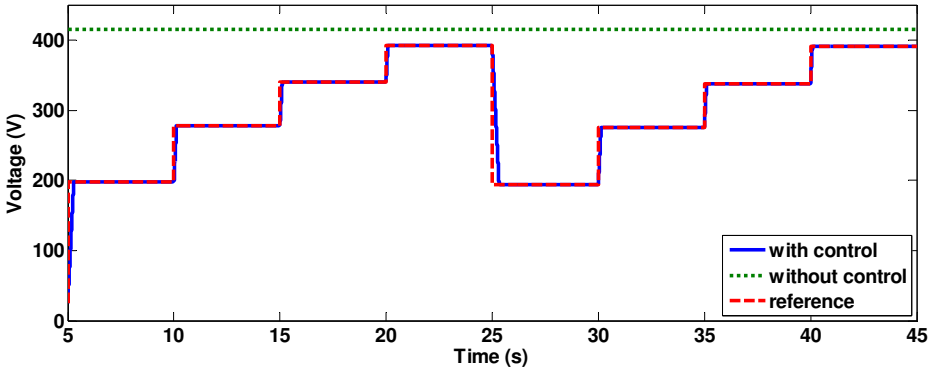

(c)

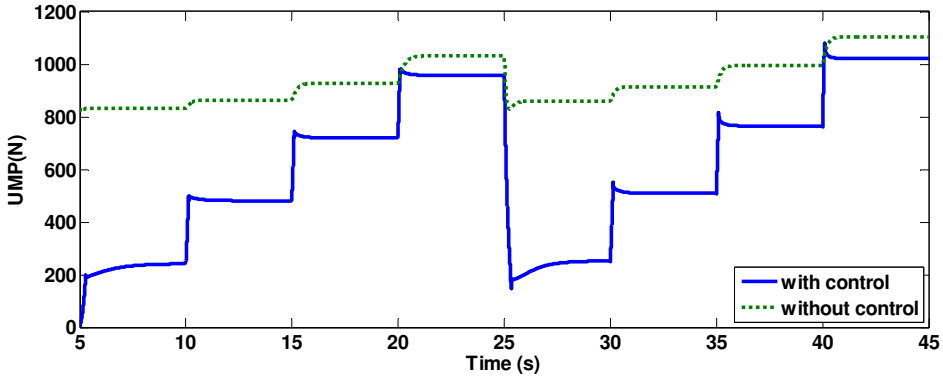

(d)

Figure 6-16: Simulation results with 500 V/s rate of change limiter in the voltage control for Machine-3 by using slip control (ideal sinewave): (a) torque (b) voltage (c) slip (d) UMP.

From Figure 6-16, the torque is increased from 10 Nm to 40 Nm with a 10 Nm increment step. The motoring mode is from 5 s to 25 s, while the generating mode is from 25 s to 45 s. A voltage rate of change limiter is applied in the control.

Machine-3 has an optimum minimum UMP slip of 0.1. However, the machine rated slip is 0.05. Therefore, the slip is controlled to maintain at 0.05 slip. In this case, the machine UMP could be reduced for every operating torque except at the rated torque. Same as Figure 6-7, the UMP reduction becomes least significant when the load increases.

6.2.6 Inverter supplied voltage

An ideal sinusoidal waveform is assumed to be used on the simulation results in the previous subsections. The inverter application without filtering is presented in this subsection.

In the analysis of UMP, the magnetic flux with higher time harmonics, which is produced by the inverter, would cause: 1) current ripple in induction machines [163], in which the current ripple will cause a high frequency UMP because the UMP is proportional to current squared. In this thesis, this issue is discussed without considering the mass and structural design of the machine, 2) increment of total harmonics of magnetic flux in the machine, which would contribute to additional static

UMP in the machine with static eccentricity. The analysis of the influence of the higher voltage harmonics on the UMP of static eccentricity is discussed in this subsection.

The voltage from the experimental work and simulation work are compared in Figure 6-17 and the FFT analysis of the voltage is shown in Figure 6-18.

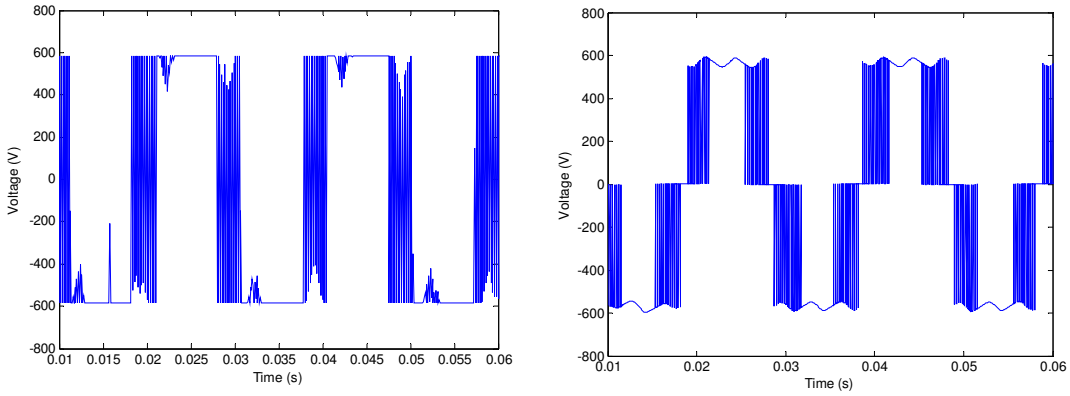

Figure 6-17: Excitation line voltage waveform: (a) experimental (b) simulation

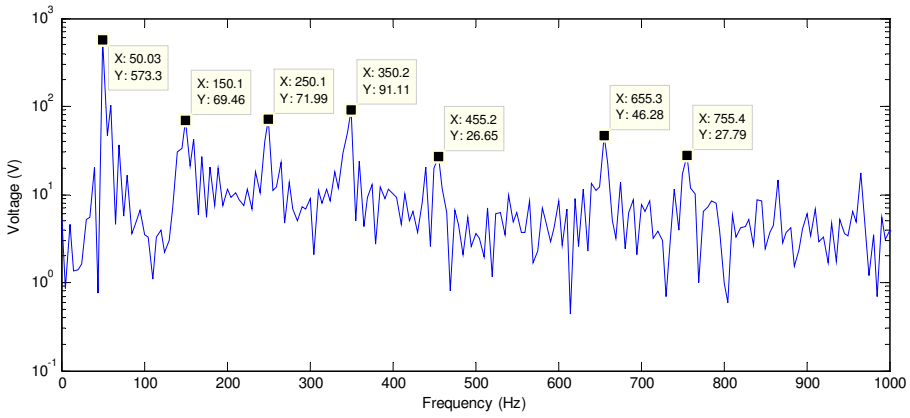

(a)

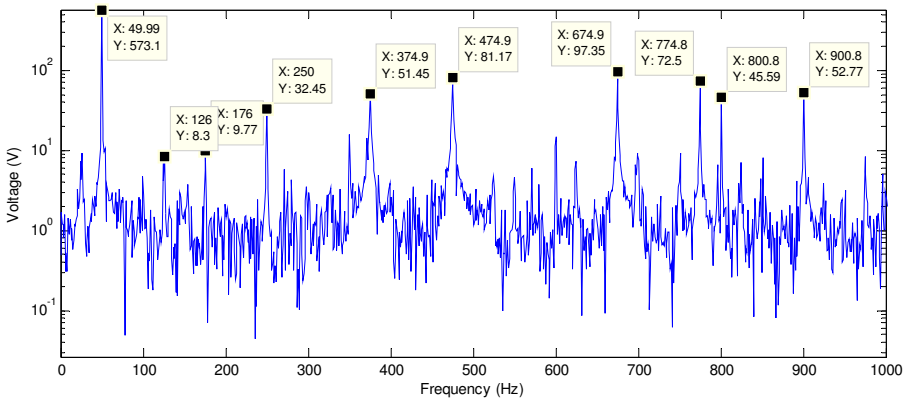

(b)

Figure 6-18: FFT analysis of the line voltage in Figure 6-17: (a) experimental (b) simulation

From Figure 6-18, it has shown that the inverter produces additional higher harmonics voltage. The higher harmonics content of the inverter supplied voltage will increase the magnetic flux with higher time harmonics in the machine. The calculation of the contribution of magnetic flux harmonics on the constant UMP of the machine with static eccentricity is shown in the next 4 paragraphs.

As shown in (6-9), the voltage is linearly proportional to the magnetic flux and inversely proportional to the frequency.

$$\Phi \propto \frac{V}{f} \tag{6-9}$$

Based on the relationship that UMP is proportional to magnetic flux squared the relationship, the relationship of UMP at the constant slip can be written as:

$$UMP \propto \left(\frac{V}{f}\right)^2, (\text{constant slip}) \tag{6-10}$$

For induction machines, the UMP changes with slip. From the analysis of magnetic flux shown in Sub-section 4.2.5, higher rotor slip would induce more current, which increases the airgap leakage flux. Depending on the type of machines, the airgap leakage flux at high rotor slip could be around 10 times larger than the airgap leakage flux at the rated slip. The magnetising flux with higher time harmonics is neglected because the airgap leakage flux is the dominant flux in the high slip region.

As the magnetic flux with higher time harmonics has a much higher rotational frequency than the rotor, which induces more current that causing a higher UMP. So, if the higher voltage harmonics are compared with the voltage at the fundamental frequency, a modifier is added in the equation (6-10), which can be written as (6-11), because fundamental magnetising flux rotates close to the synchronous speed. In addition, the modifier is assumed to be a constant variable, because the speed range of the induction machine in this chapter is below 5% of the synchronous speed.

$$UMP \propto k\left(\frac{V}{f}\right)^2 \tag{6-11}$$

The k in (6-11) is assumed to be 10. With the results from the FFT analysis in Figure 6-18, the influence of the voltage harmonics towards the UMP is shown in Table 6-1 (experimental) and Table 6-2 (simulation).

Frequency	V	$k\left(\frac{V}{f}\right)^2$	Percentage relative to the fundamental component (%)
50	573	131.332	-
Higher voltage harmonics			
150	69.5	2.147	**1.635**
250	72	0.829	**0.632**
350	91	0.676	**0.515**
455	26	0.033	**0.025**
655	46	0.049	**0.038**
755	27	0.013	**0.010**
Total		3.685	**2.853**

Table 6-1: Contribution of voltage harmonics towards the UMP (Experimental).

Frequency	V	$k\left(\frac{V}{f}\right)^2$	Percentage relative to the fundamental component (%)
50	573	131.3316	-
Higher voltage harmonics			
126	8.3	0.043	**0.033**
176	9.77	0.031	**0.023**
250	32.45	0.168	**0.128**
375	51.45	0.188	**0.143**
475	81.17	0.292	**0.222**
675	97.35	0.208	**0.158**
775	72.5	0.088	**0.067**
800	45.59	0.032	**0.025**
900	52.77	0.034	**0.026**
Total		1.085	**0.826**

Table 6-2: Contribution of voltage harmonics towards the UMP (FEA).

From both tables, they show that the voltage harmonics will cause the UMP to be 2.85% higher in the experimental work, and 0.826% higher in the simulation. The contribution of voltage harmonics on the UMP is relatively low. This is because the magnetic flux is inversely proportional to the frequency, and the UMP is proportional to squared of the magnetic flux density. Therefore, this effect is neglected in most of the analysis in this thesis.

Figure 6-19 presents the UMP of Machine-2 with 20% static eccentricity, when the voltage is changed from 0.2 p.u. to 0.8 p.u. with the step of 0.2 p.u. at 50 Hz excitation frequency; the tests were run 2 times with the same setup. Figure 6-19 shows the UMP spikes occurred due to the changing of the excitation voltage. Comparing both the experimental results, the spike is not constant, because the UMP in the transient scenario will be affected by the relative angle between the direction of the fundamental magnetising flux and the narrowest airgap.

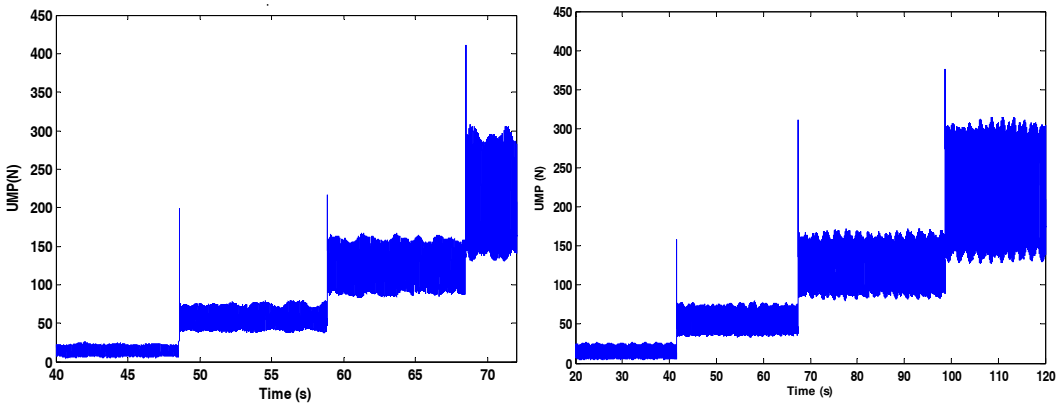

(a) (b)

Figure 6-19: UMP of Machine-2 with 20% static eccentricity, when changing the voltage from 0.2 pu to 0.8 pu at no-load (experimental): (a) first test (b) second test.

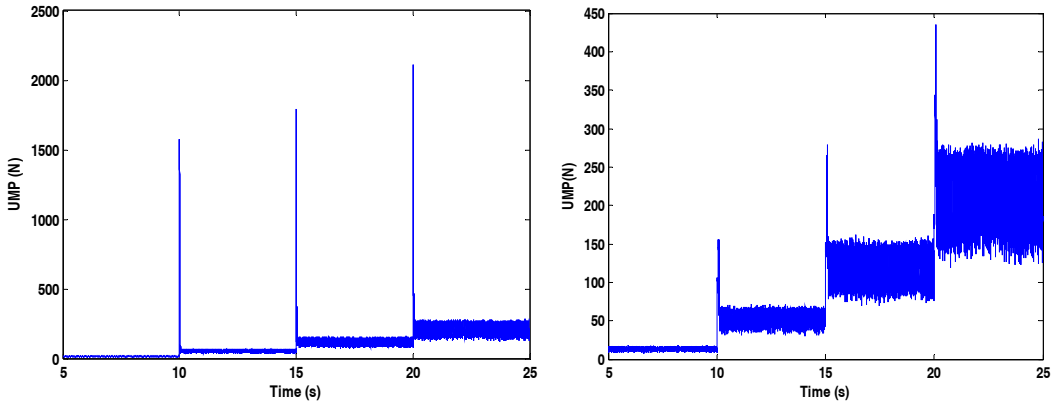

(a) (b)

Figure 6-20: UMP of Machine-2 with 20% static eccentricity, when changing the voltage from 0.2 pu to 0.8 pu at no-load (Simulation): (a) without, (b) with 1000 V/s voltage rate of change limiter.

Figure 6-20(a) illustrates the UMP spikes are larger than the experimental results. In order to model the effect from the experimental work, a voltage limiter of 1000 V/s is added into the simulation, in which the results are shown in Figure 6-20(b).

In Figure 6-20, the UMP ripple of the simulation results is different from the experimental results. The UMP ripple in the experimental results is caused by the mechanical coupling and slight dynamic eccentricity, which was discussed in Sub-section 3.6.6. Meanwhile, the UMP ripple in the simulation results is caused by the current ripple from the high voltage harmonics of the inverter. This can be proven by comparing the UMP harmonics of the experimental and FEA as shown in Figure 6-21, in which the harmonics frequency of the experimental results mainly the harmonics of the rotating frequency (12.5 Hz). Figure 6-21 is the FFT analysis of the results of 0.6 p.u. taken from Figure 6-19(a) and Figure 6-20(b).

Most of the UMP ripple caused by the higher voltage harmonics can be damped by the mass of the machine. However, the UMP ripple will become significant if the UMP ripple runs at the frequency that is near to the natural frequency of the system. In [164], the authors had shown that the noise level at the natural frequency would increase when the eccentricity increases. In order to study the machine vibration, the forces need to be coupled with the stator mechanical response modelling [165]. Therefore, the vibration of the machine is not studied in this thesis, and the presented

UMP ripple does not reflect the actual force exerted on the bearing. It is a guideline of the possible force exerted on bearing.

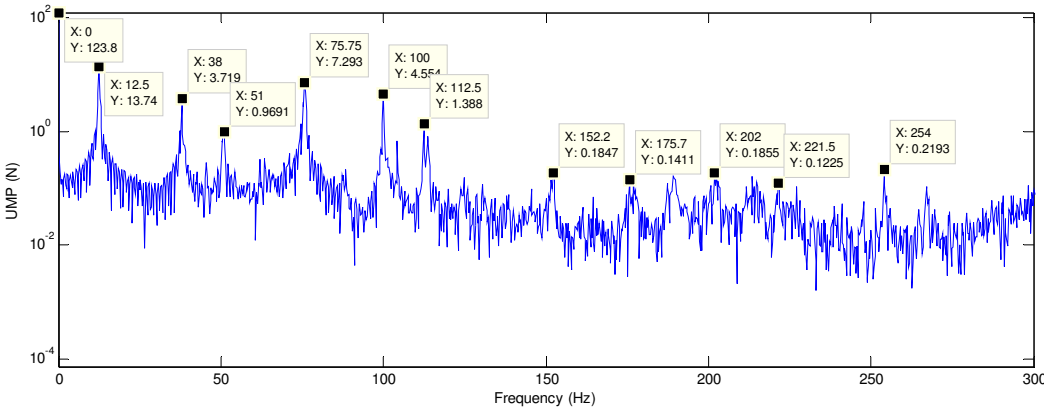

(a)

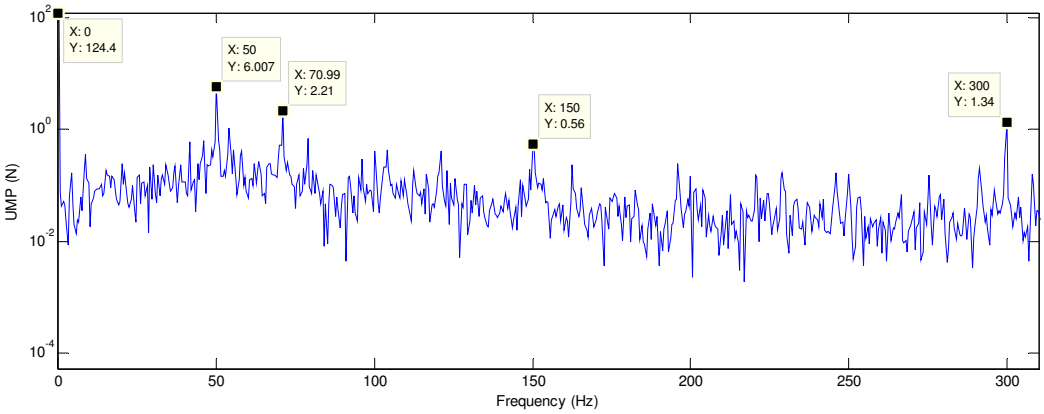

(b)

Figure 6-21: FFT analysis on the Machine-2 with 20% static eccentricity 0.6 p.u. voltage: (a) experimental (b) FEA

6.2.7 Comparison between results from different sources

Machine-2 is used in this subsection to compare the UMP results taken from FEA (ideal sinewave), experimental work, empirical method (ideal sinewave), and analytical model (inverter supplied). Machine-2 is set to run in motoring-mode, and it is loaded with 6 Nm from 5 s to 15 s, and 11 Nm from 15 s to 25 s. Due to the limitation of the test rig, the experimental work without slip control is not done.

When slip control is implemented, the line voltage of 142 V is used for the 6 Nm load, while the line voltage of 205 V is used for the 11 Nm load. The optimum operating slip of Machine-2 is 0.05 slip.

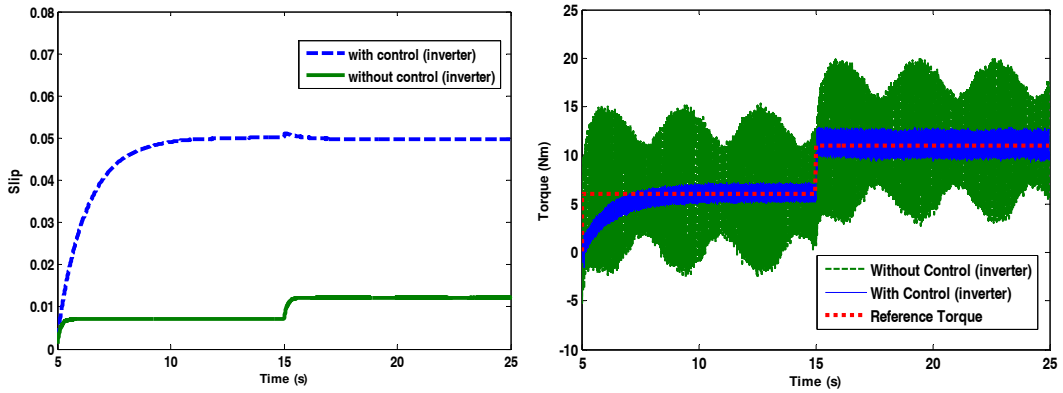

Figure 6-22: Simulation results for Machine-2 with inverter supplied voltage: (a) Slip (b) Torque

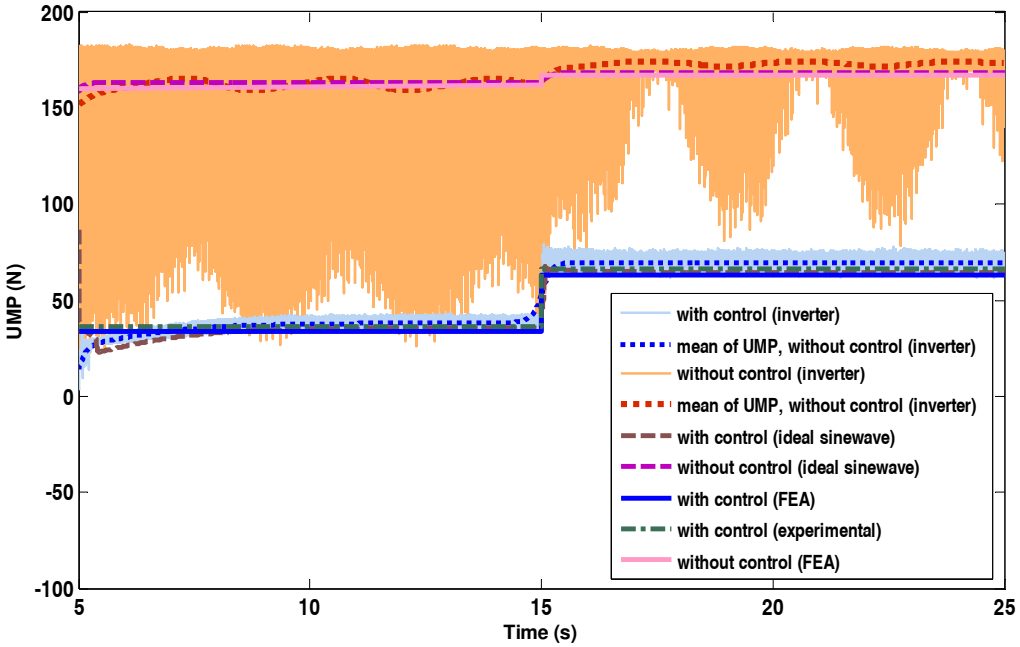

Figure 6-23: Overview of the UMP with and without slip control

Figure 6-22 (b) shows the torque ripple of Machine-2 with inverter supplied voltage. The voltage harmonics from the inverter causes the resultant voltage vector supplied to change with time [166], which resulting the torque to change with time. Although the torque fluctuates, the average torque is equal to the reference torque. This can be proven in Figure 6-22 (a), in which the rotor slip could reach steady-state when the machine is loaded. Meanwhile, the reason that the torque ripple is not shown in the rotor slip is because of the torque ripple is damped by the rotor inertia of the machine.

From Figure 6-22, the machine operates at 0.05 slip when the slip control is used. As both tested loads are below 25% of the machine rated load, great reduction of UMP was shown in Figure 6-23, where the UMP is reduced by around 60% for the 11 Nm load, and around 77% for the 6 Nm load. As discussed earlier, the proposed slip control method is to balance the UMP caused by the magnetising flux and the UMP caused by the airgap leakage flux. When the machine is lightly loaded and is excited with rated voltage, this means that the UMP caused by the airgap leakage flux is low, while the UMP caused by magnetising flux is high. Therefore, by reducing the excitation voltage, the UMP caused by magnetising flux can be reduced, while the UMP caused by airgap leakage flux can be increased. This would reduce the UMP because the UMP is a function of current squared.

Comparing the four methods used in Figure 6-23, a good correlation was shown between each result. The UMP of the machine with an inverter supplied voltage, which is simulated by using the analytical model, is slightly higher than the other results. This is mainly due to the existence of higher voltage harmonics.

From Figure 6-23, there is a fluctuation of UMP in the machine with an inverter supplied voltage; the dotted line in the figure shows the mean of the UMP ripple. Similar to the torque ripple, the UMP ripple is due to the existence of current ripple. Other than the magnetic force exerted on the machine, the vibration of the machine is affected by the mechanical structure, in which the structural mode shapes of the machine needs to be investigated [167]. Further works need to be done to validate the effect of UMP ripple.

6.2.8 Simulation of Machine-1 with inverter supplied voltage

In this Sub-section, the simulation of Machine-1 is done with the same setup as Section 6.2.4 except that the excitation voltage is supplied with an inverter. The UMP results from the simulation are then compared with the UMP of the machine when excited with an ideal sinusoidal waveform.

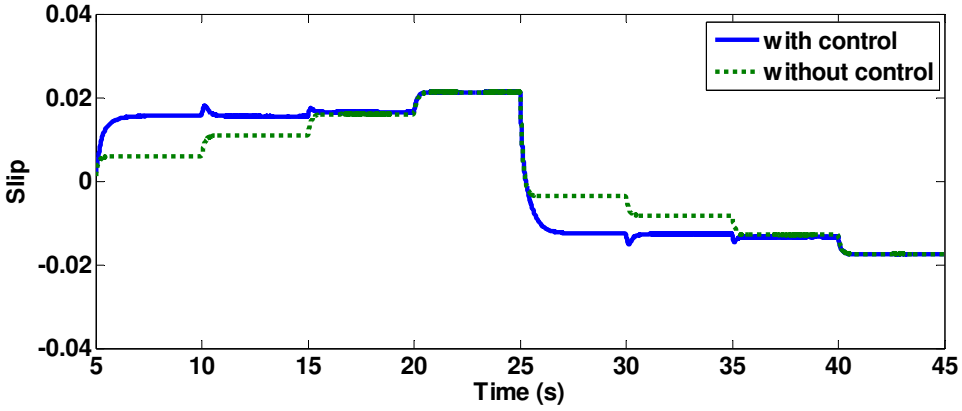
with control
without control
Slip
Time (s)
0.04
0.02
0
-0.02
-0.04
5
10
15
20
25
30
35
40
45

(a)

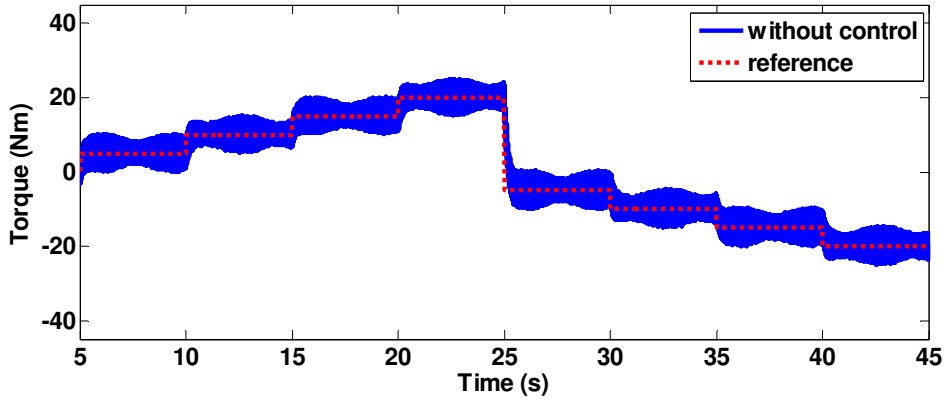
without control
reference
Torque (Nm)
Time (s)
40
20
0
-20
-40
5
10
15
20
25
30
35
40
45

(b)

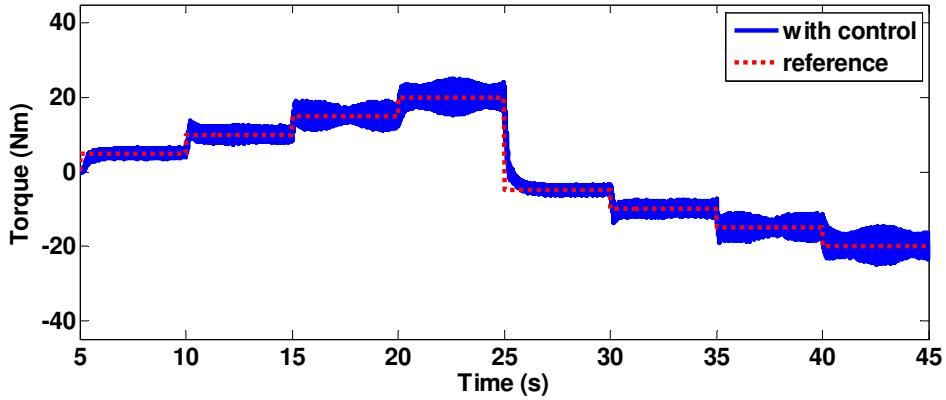
with control
reference
Torque (Nm)
Time (s)
40
20
0
-20
-40
5
10
15
20
25
30
35
40
45

(c)

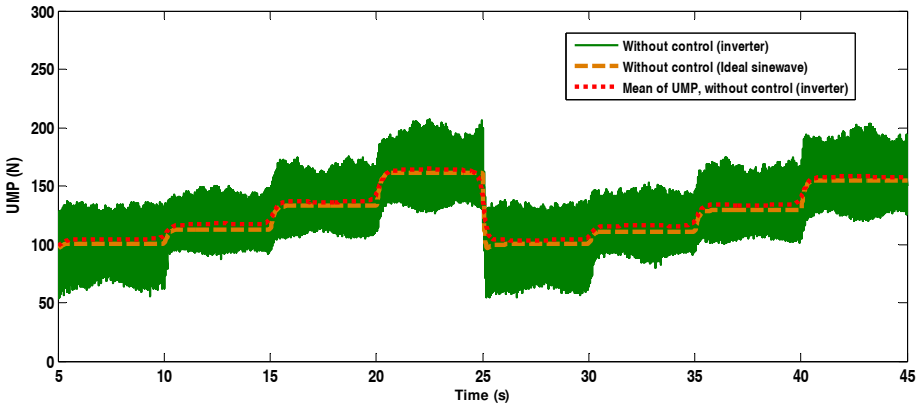

(d)

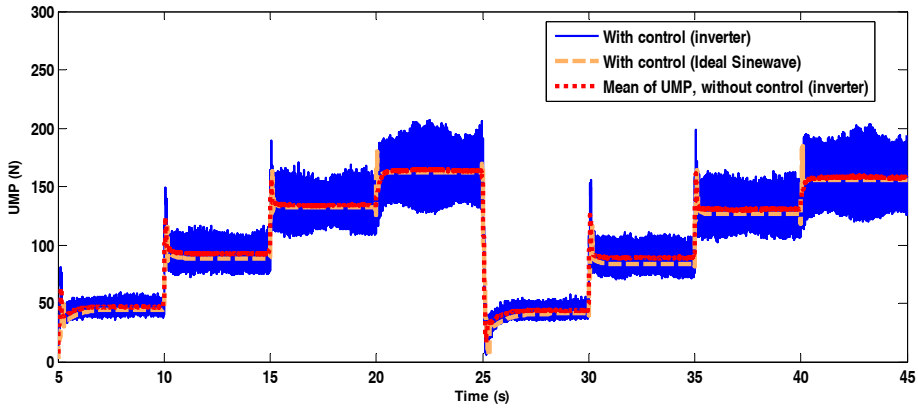

(e)

Figure 6-24: Simulation results for Machine-1 with inverter supplied voltage: (a) slip (b) torque without control (c) torque with control (d) UMP without control (e) UMP with control.

From Figure 6-24, similar to Machine-2 with inverter supplied voltage, the UMP of the machine with inverter supplied voltage is slightly higher than the ideal sinewave supplied voltage. Meanwhile, the reduction of UMP by using slip control method is also shown in the Figure 6-24(d) and (e).

Furthermore, the torque and UMP ripple exist in the analytical modelling. Both the torque and the UMP is smaller when the excitation voltage is lower. This is because the error of the resultant voltage vector is percentage-based. In addition, the machine torque ripple is a high frequency torque, so the rotor inertia, which acting as a low-pass filter, would damp the torque ripple. For the UMP ripple, the machine's mass and structure are not studied in this thesis. Therefore, the UMP ripple is just a guideline for the future work.

6.2.9 Experimental verification

In the experiment, Machine-2 with 20% static eccentricity is loaded with 11Nm. Then, the voltage is varied from 0.35 p.u. to 0.65 p.u. The permanent magnet generator acts as a load for Machine-2. When the rotor slip changes, the induced voltage in the generator will also be different. Therefore, in order to maintain the 11Nm-load, the resistance connected to the generator needs to be changed when the voltage changes. The relationship of the supplied voltage with the rotor slip and the UMP are shown in Figure 6-25.

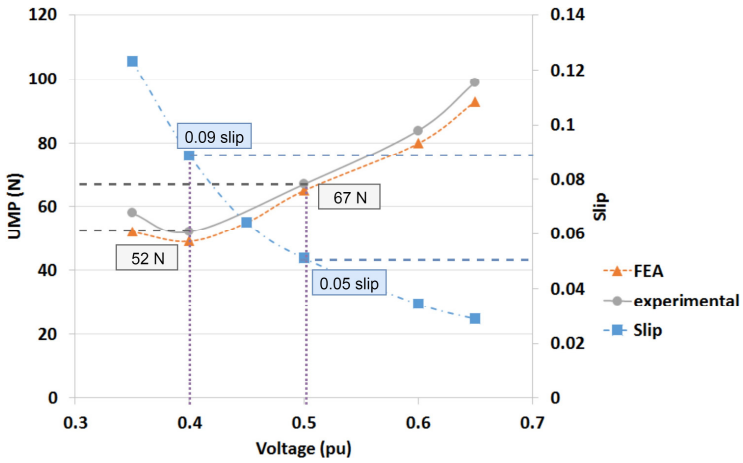

Figure 6-25: UMP and rotor slip at different voltages.

The lowest UMP for the constant 11 Nm load when the machine is supplied with 0.4 p.u. voltage. The minimum rotor slip is at 0.09. As the voltage increases, the slip started to drop because torque is a function of voltage and slip. The UMP/torque ratio of Machine-2 in Section 5.6 shows the minimum UMP is at a rotor slip that is higher than the rated slip (0.05). It is not recommended to run the machine at high slip because of its efficiency issue. Therefore, controlling the slip at 0.05 would give a reduction in UMP. In this case, the control system should supply a 0.5 p.u. voltage when the machine has an 11 Nm load.

6.2.10 Summary for slip control

This chapter has shown that reduction of UMP can be achieved through reducing the magnetising flux in the induction machine. Figure 6-26 and Figure 6-27

are the summary for the percentage of UMP reduction through controlling the rotor slip.

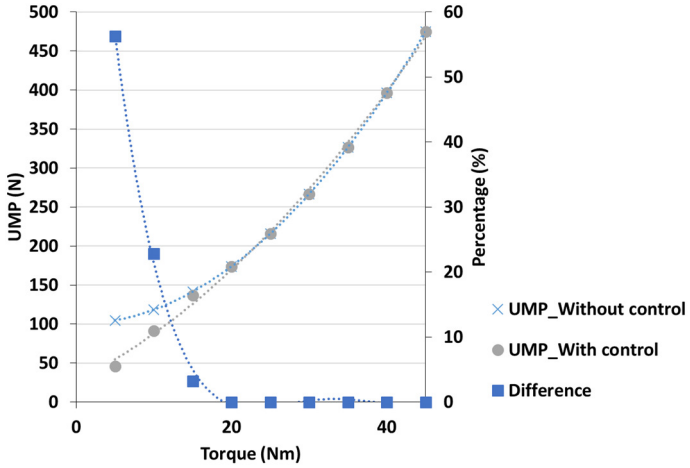

Figure 6-26: UMP comparison between with and without control for Machine-1 (cage rotor).

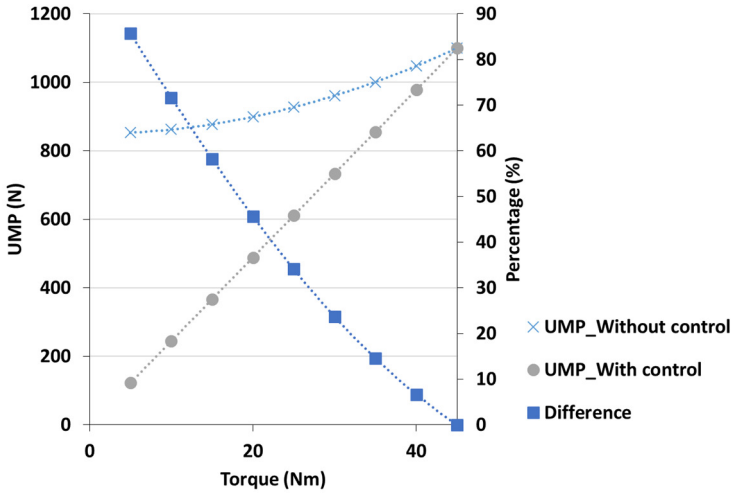

Figure 6-27: UMP comparison between with and without control for Machine-3 (wound rotor).

Cage rotor induction machine has shown a reduction of UMP in light load (5-Nm). However, the percentage of UMP reduction decreases exponentially when the load increases. When the optimum excitation voltage is higher than the rated voltage of the induction machine, the slip control is switched off because of the voltage limit of the inverter. Also, the magnetic core will be saturated when the machine is excited with a voltage that is higher than the rated voltage.

For the wound rotor induction machine, a reduction in UMP had been shown for every operating load except at the rated load. The percentage of reduction can go up to 86% at 5 Nm. Similar to the cage rotor induction machine, the effectiveness of UMP reduction reduces as the load increases.

As a conclusion, the slip control could effectively reduce the UMP if the optimum operating slip is higher than the rated slip. Hence, the slip control would have a significant impact on reducing the UMP of Machine-2 and -3. Through implementing the slip control method, it can not only reduce the UMP, but it could also reduce the bearing friction loss.

6.3 Damper Windings

Other than using the slip control method, a new damper winding configuration is proposed in the thesis to reduce UMP. From Sub-section 4.3, a significant amount of UMP can be reduced when the counteracting flux is generated by the parallel windings in the cage rotor induction machine to damp the UMP. With the similar functionality, the damper windings allow the flow of the counteracting current which damp the uneven magnetic flux distribution. Unlike the parallel windings of cage rotor is located at the rotor, the proposed damper windings are installed at the stator. The main reason of installing the damper winding in the stator is the UMP damping effect would not be affected by the changes of rotor slip.

Damper windings are often used in synchronous machines to reduce the torque ripple and increase the starting torque. The usage of damper windings has been proposed to reduce the UMP of a salient pole synchronous generator in [168]. In addition to that, Dorrell has shown that the installation of damper windings at the stator with the pole pair ± 1 of the main windings will damp the UMP in the wound rotor induction machine [96].

The damper winding configuration proposed in the thesis is wound from one slot to the opposite slot 180° apart. This winding configuration repeats for all the remaining slots. All damper windings are individually wound and they are individually

connected. So, if there are 48 stator slots, there are 24 individual damper circuits. The winding configuration is shown in Figure 6-28.

The proposed damper winding configuration can only be used in the machine with even pole pair numbers. (6-12) shows the induced voltage formula.

$$U = N\frac{\Delta BA\cos\theta}{\Delta t} \tag{6-12}$$

As the magnitude of the B and machine surface area is a constant,

$$U = N\lambda\frac{\Delta\cos\theta}{\Delta t} \tag{6-13}$$

where $\frac{\Delta\cos\theta}{\Delta t}$ is angular rotational speed. The voltage induced by each pole pair can be represented by (6-14).

$$U_i = \sum_{\substack{p=1 \\ odd}}^{i} N\lambda_p\omega_{slip,p} \tag{6-14}$$

The current in each damper winding can be found by using (6-14) in (6-15).

$$\begin{bmatrix} U_1 \\ \vdots \\ \vdots \\ U_i \end{bmatrix} = \begin{bmatrix} L_{11} & M_{12} & \dots & M_{ji} \\ M_{21} & L_{22} & \cdots & \vdots \\ \vdots & \vdots & \ddots & \vdots \\ M_{ij} & \cdots & \cdots & L_{ii} \end{bmatrix} \begin{bmatrix} I_1 \\ \vdots \\ \vdots \\ I_i \end{bmatrix} \tag{6-15}$$

where L_{ii} is the self-inductance of the winding and M_{ij} is the mutual inductance between the damper windings. The mutual inductance between the damper winding and the main winding is neglected, because the main winding consists of even number of pole pair winding harmonics and the damper winding consists of odd number of pole pair winding harmonics. Then, the resultant magnetic flux in the airgap can be calculated by using the current value extracted from (6-15).

6.3.1 Results and simulation for the damper windings

FEA simulation is done to calculate the UMP exerted on the rotor. The analysis on Machine-4 (8 pole wound rotor) with damper windings is shown. Then, Machine-3 (4-pole wound rotor) will be used for verification. 50% static eccentricity towards the +y direction is set for the first case and 20% static eccentricity towards the +y direction is set for the second case. The damper windings properties are: 5 turns per phase; 0.001 ohm resistance. Machine-4 has 48 stator slots.

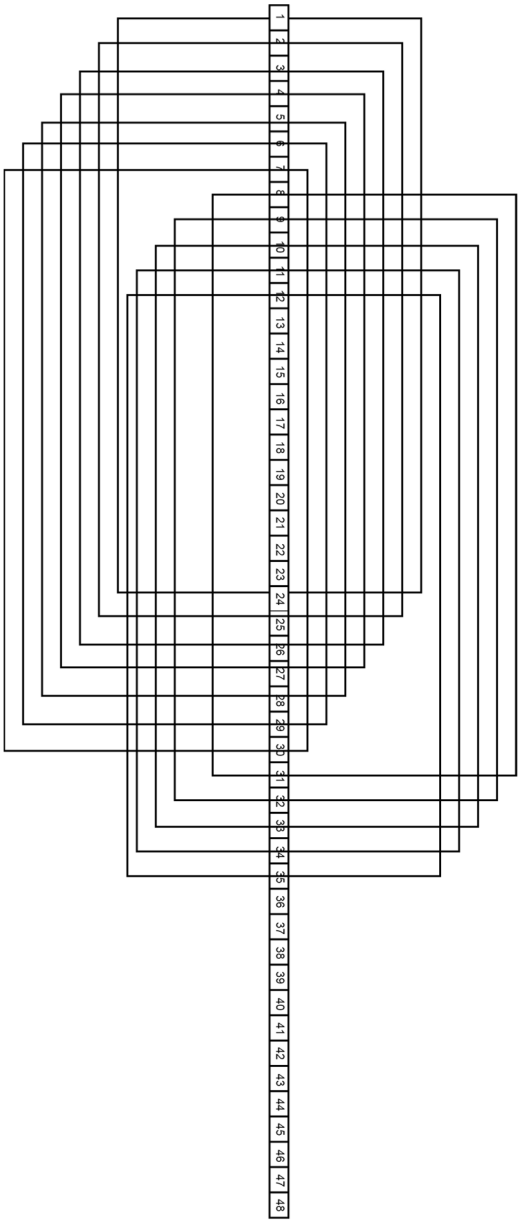

Figure 6-28: Damper windings configuration.

6.3.2 Current

Figure 6-29 shows the current waveform for half of the 24 damper windings. The coil number is labelled in Figure 6-28. The current waveform in each coil has different amplitude and phase shift. The phase shift of the current is shifted with the positioning of the coil. The mechanical angle is 90 degree between coil-1 to coil-12. As this is a 4 pole pair machine, the electrical degree has a 360 degrees difference between coil-1 and coil-12.

Furthermore, the magnitude of the current is getting smaller from coil-1 to coil-12. Due to the airgap at the direction of coil-1 is the narrowest and the damper winding is wound 180 mechanical degree, the higher magnetic flux difference caused by the airgap length difference will induce a higher current. In addition, we can see that although the current from coil-1 to coil-12 is getting smaller, there is fluctuation in the peak current from coil-1 to coil-12. This is caused by the counteracting current of the higher harmonics magnetic flux.

From the current produced by the damper windings, odd pole pair magnetic flux is produced and the counteracting magnetic flux will damp the additional magnetic flux harmonics caused by the rotor eccentricity.

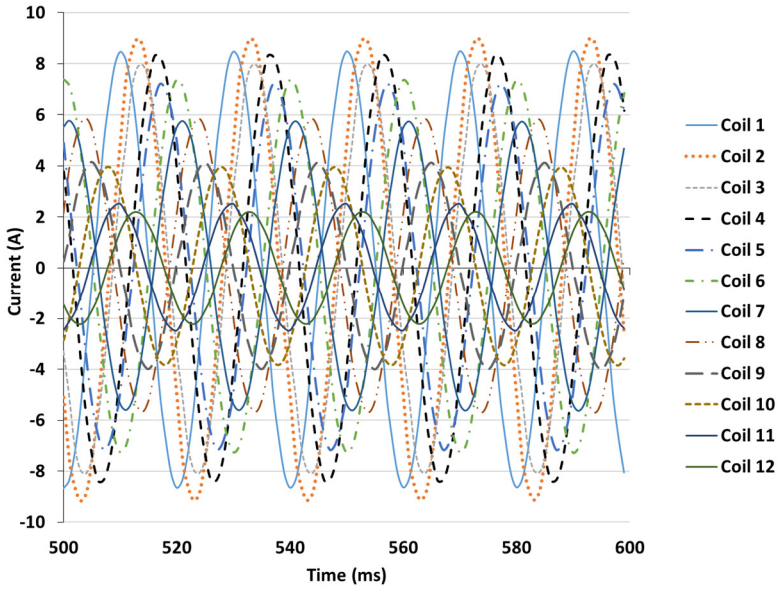

Figure 6-29: Current for each damper winding.

6.3.3 Space harmonic analysis

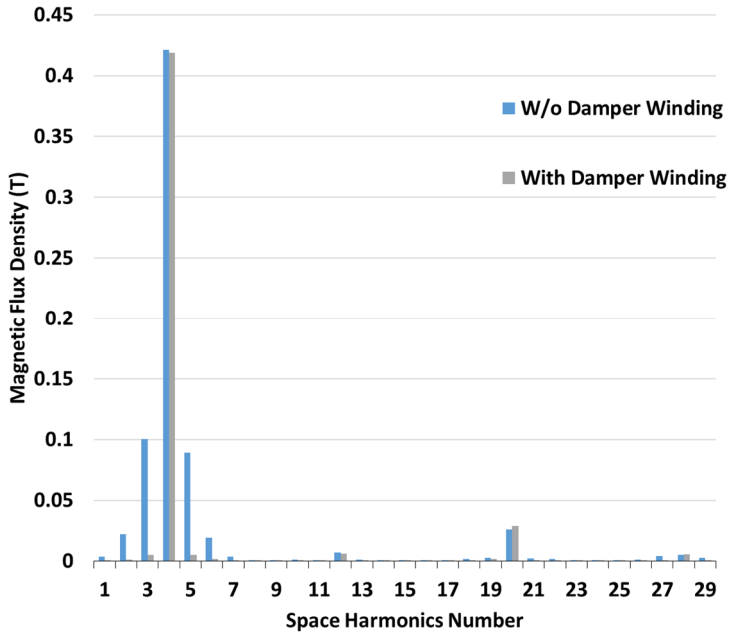

Figure 6-30: Space harmonics of the magnetic flux when Machine-4 is running at no load.

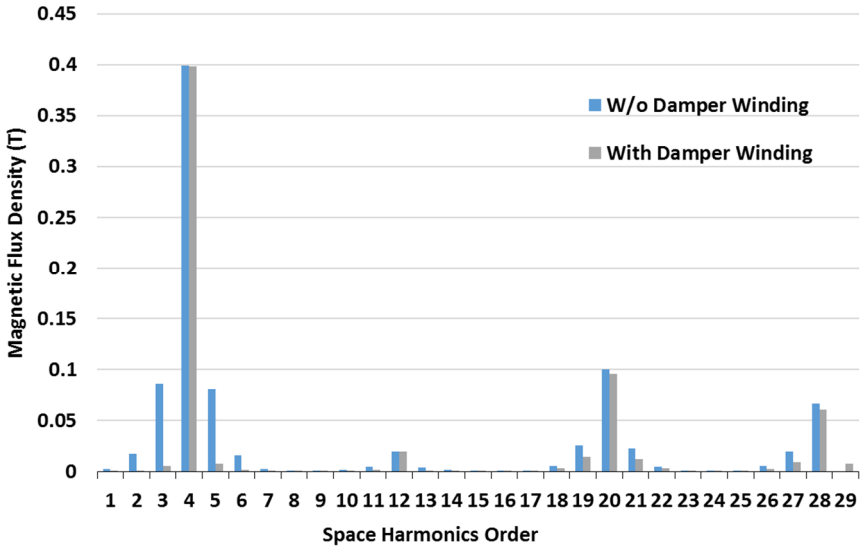

Figure 6-31: Space harmonics of the magnetic flux when Machine-4 is running at rated slip.

Figure 6-30 and Figure 6-31 show the magnetic flux space harmonics around the airgap for no load case and full load case. The similarity between them is the 3rd and 5th harmonic were greatly reduced with the introduction of damper winding. However, most of the higher harmonics flux could not be damped by the damper

windings, because the position of the damper windings are at deep stator slots. This means that the higher harmonics flux is unlikely to induce current in the damper winding. Although the sideband of the higher harmonics flux could not be significantly reduced, the fundamental flux is the dominant flux when the machine runs below its rated slip. When the sideband of the fundamental pole pair flux was damped, the UMP caused by the fundamental flux can be reduced significantly from no-load to full-load.

6.3.4 UMP comparison

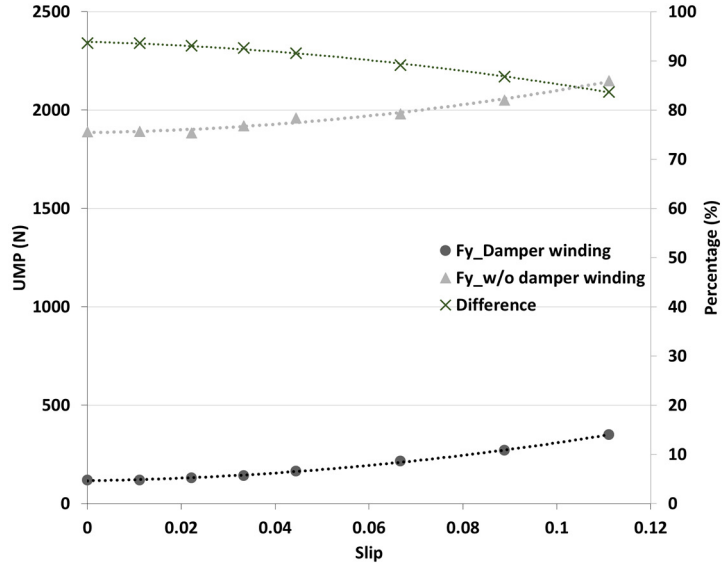

Figure 6-32: Machine-4's UMP with 50% rotor eccentricity, comparison of results between with and without damper windings.

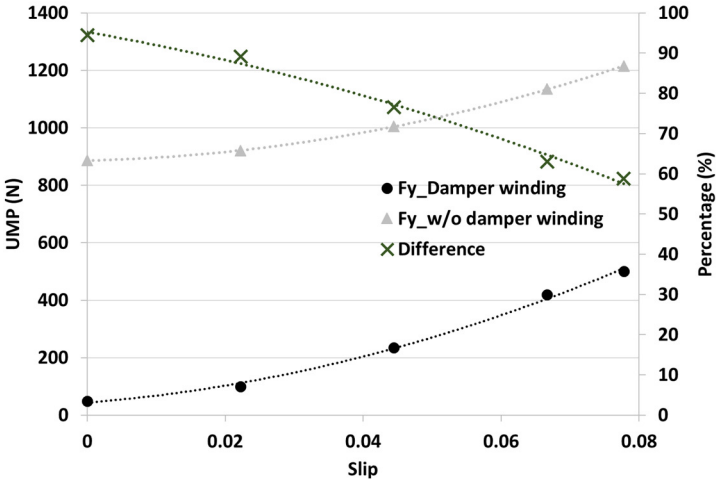

Figure 6-33: Machine-3's UMP with 20% rotor eccentricity, comparison of results between with and without damper windings.

The UMP at the low slip region is shown in Figure 6-32 and Figure 6-33. Both machines have an even pole-pair number, therefore, the odd harmonics created by the rotor eccentricity could be damped by the damper windings. The UMP is greatly reduced because the UMP at the low slip region is caused by the fundamental magnetising flux. When the slip increased, the increment of the airgap leakage flux which could not be damped by the damper winding produced higher UMP. Therefore, the UMP of the wound rotor induction machine with and without damper winding increased as the slip increased.

6.3.5 Losses from the damper windings

As there is current flowing in the damper windings, additional losses need to be considered. Figure 6-34 shows the copper loss over different slip. There is slight decrement from 0 slip to 0.04 slip because of the slight reduction in the magnetising flux. Therefore, lesser current will be induced.

Then, the power loss increases from 0.06 to 0.11 slip because of the increment of the leakage flux. Although the majority of the leakage flux is not induced in the damper winding, the leakage flux pattern is hard to be predicted.

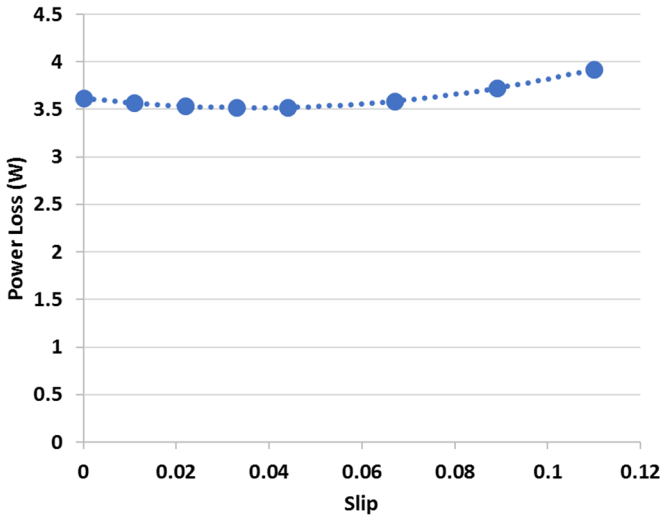

Figure 6-34: Copper loss of the damper windings in Machine-4.

In overall, the power loss for the damper windings is almost constant. The power loss for the damper windings is also relatively small for a 5.5 kW wound rotor

induction machine. In addition, the iron losses can be reduced, because the additional magnetic flux is damped by the damper windings. In this case, the increment of copper loss can be compensated with the decrement of iron losses, which makes the installation of the damper winding in a wound rotor induction machine attractive. Furthermore, the additional bearing friction loss due to UMP can be minimised.

The downside of installing the damper winding is it occupies space in the stator. With the reduction of stator iron core, this would reduce the rating of the induction machine to prevent core saturation. Therefore, if there is space available in the machine, it is worth to install the damper winding because the damper winding could be used with another purpose, like the condition monitoring could be implemented in the system.

6.3.6 Comparison between damper windings with different winding configuration

The proposed winding configuration is to wind the damper windings in each stator slot to its opposite stator slot. With the same idea of damper winding, the spacing between the damper winding is used in Machine-4 with 50% of static eccentricity. The spacing of one and two stator slots is made to compare with the original set of damper winding. Therefore, 24 slots are wound in the one-spacing configuration and 16 slots are wound in the two-spacing configuration.

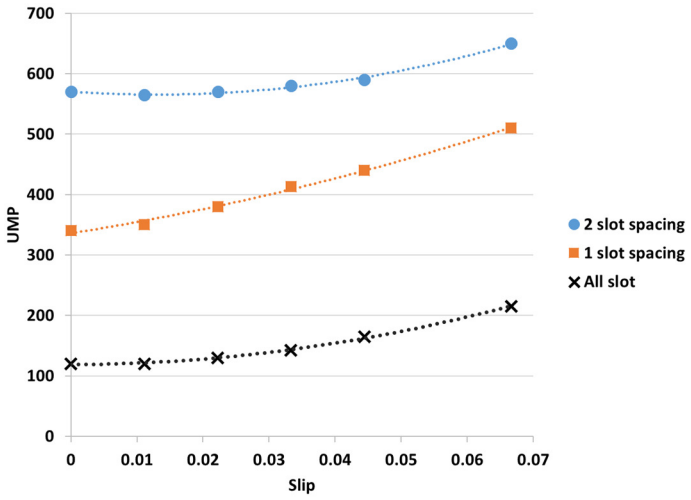

Figure 6-35: Comparison of UMP between different damper winding configuration.

From Figure 6-35, although the UMP can still be reduced if compared to Figure 6-32, the UMP is larger when the spacing of the damper winding increases. When spacing increases, the higher space harmonic of the damper winding's MMF increases. Hence, the effectiveness of the UMP damping decreases.

6.4 Comparison between Damper windings and Slip Control Method for Wound Rotor Induction Machines

In this section, the slip control method and damper windings topology were compared for reducing the UMP of induction machines. Each method has its own advantages and disadvantages. Hence, the comparison table for these two methods is shown in Table 6-3. Then, the UMP comparison between the two methods on Machine-3 is shown in Figure 6-36.

	Damper Winding	Slip Control
Reduction of UMP	UMP can be significantly reduced for any rotor slip. Even at full load, 75% of UMP can be reduced.	The reduction of UMP becomes less effective as the load increases.
Control System	Not needed.	Control system is needed.
Power Density	Power density is reduced because installing damper winding will reduce the active magnetic material.	Remains the same.
Power Loss	Additional copper loss in the damper winding. Figure 6-34 shows the copper loss of 3.5W occurs in a 5.5kW induction machine.	Additional switching power loss of the inverter needs to be included.
Machine Design	New machine design is needed.	Can be used on any type of machine.

Table 6-3: Difference between damper winding method and slip control method.

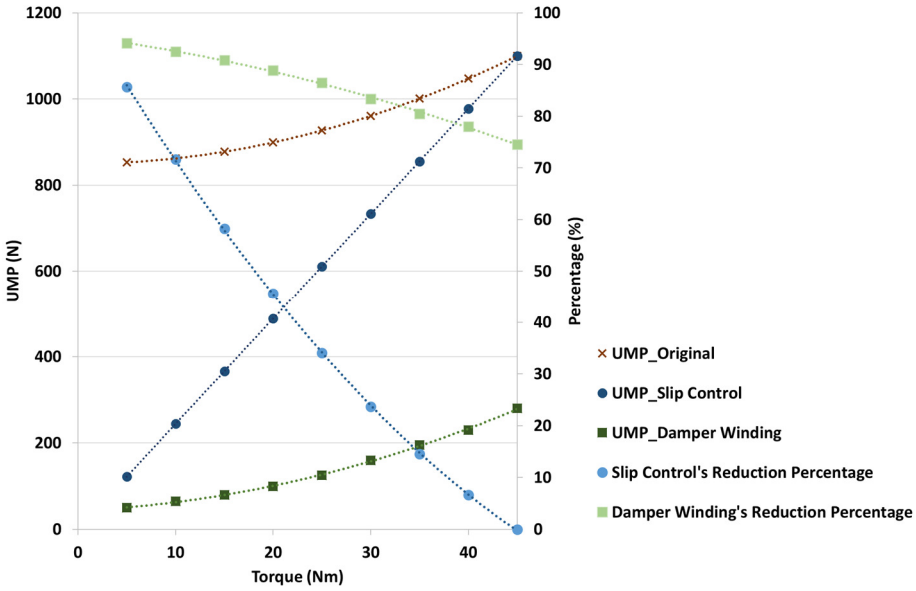

Figure 6-36: UMP comparison between installing damper windings and applying slip control method on Machine-3 with 20% static eccentricity.

6.4.1 Magnetic flux space harmonics

Figure 6-37 shows the magnetic flux space harmonics comparison between the slip control method and the damper winding topology, in which Machine-3 with 20% static eccentricity and with 20% of rated load is tested. The machine with the damper windings topology operates at the rated voltage, meanwhile, the machine with slip control method operates at 44.7% of the rated voltage.

From Figure 6-37, as the slip control method reduces the excitation voltage at light load to get the desired rotor slip, the fundamental magnetising flux after implementing slip control is lower if compared to the damper windings. The reduction of fundamental flux leads to the reduction of the magnitude of the pole pair ± 1 sideband flux. However, the higher space harmonics flux of the slip control method is higher than the damper windings topology because higher rotor slip causes more leakage flux. As the rate of decrement of the UMP caused by the magnetising flux is larger than the rate of increment of the UMP caused by the airgap leakage flux, the overall UMP can be reduced.

As a conclusion, unlike the damper winding topology which reduces the sideband flux of the fundamental magnetising flux, the slip control method is meant to

optimise the UMP caused by the fundamental magnetising flux and the airgap leakage flux. Therefore, slip control method can only be used when the UMP caused by the airgap leakage is smaller when the machine is lightly loaded.

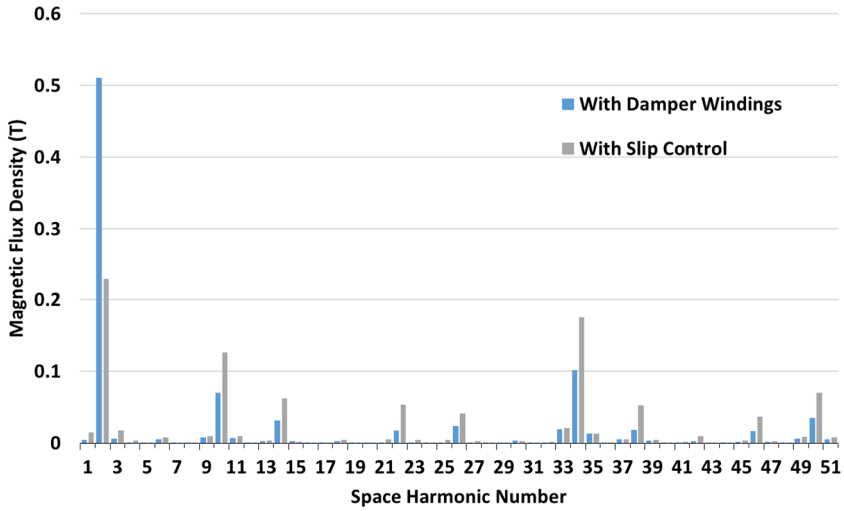

Figure 6-37: Space harmonics of the magnetic flux of Machine-3 with 20% of static eccentricity and with 20% load.

6.4.2 Power losses

The power losses of Machine-3 before and after using the UMP reduction techniques are shown in this subsection. The UMP of Machine-3 with 20% of static eccentricity is illustrated in Figure 6-36. By using the proposed power losses calculation in Section 4.7, the comparison between with and without slip control is shown in Figure 6-38, meanwhile, and the comparison between with and without installation of damper windings is shown in Figure 6-39.

For the slip control method, controlling the slip at 0.05 had increased the power losses. Therefore, the efficiency of the machine is another aspect that needs to be taken into consideration when implementing slip control to reduce the UMP. For the machine with damper windings, which is shown in Figure 6-39, the power losses had been reduced at every operating torque. Unlike the slip control, the damper windings does not change the current and the excitation voltage of the induction machine. Also, the power losses from the damper winding is negligible. Hence, the significant reduction of the UMP from the damper windings had reduced the power losses of the induction machine.

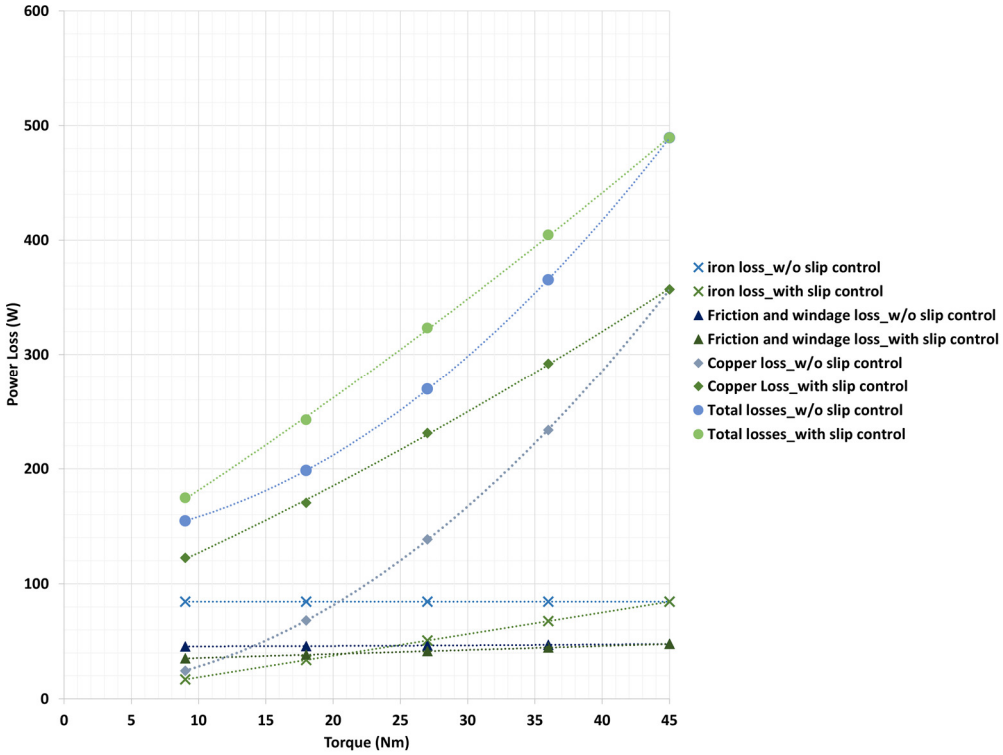

Figure 6-38: Power losses comparison between with and without slip control for Machine-3 with 20% static eccentricity.

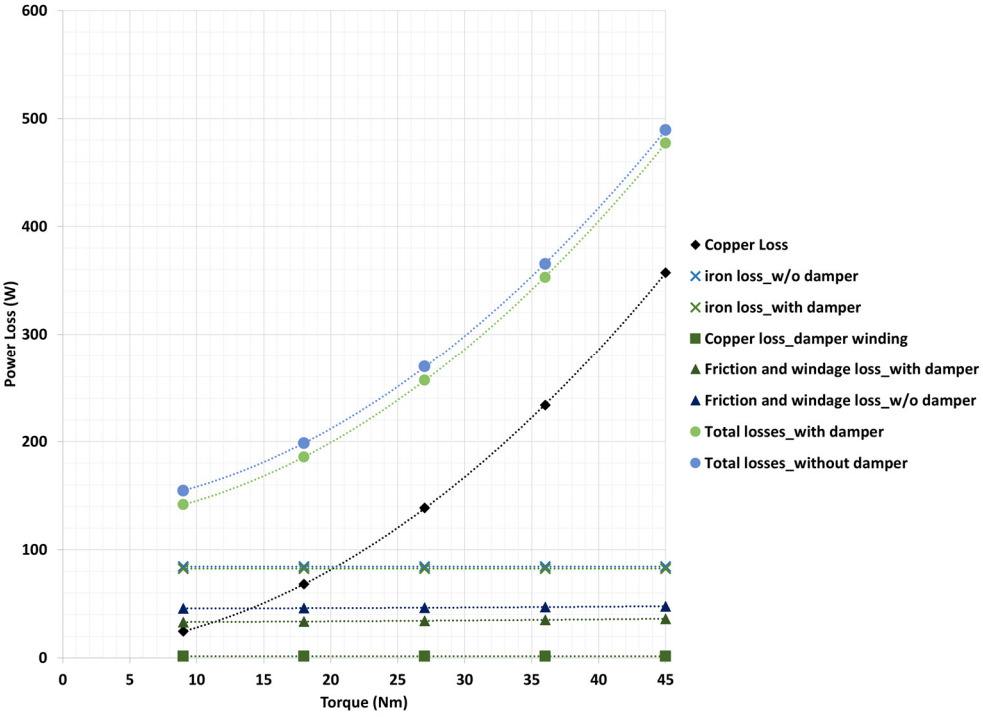

Figure 6-39: Power losses comparison between with and without damper windings for Machine-3 with 20% static eccentricity.

6.5 Bearing Lifetime

It is common for the bearing to fail before the predicted lifetime because many non-fatigue failure causes are not included in the lifetime prediction [169]. From the possible undesirable force exerted on the bearing, the reduction of bearing life can be caused by additional loading, vibration force, unbalance bearing loading, bearing misalignment forces, V-belt tension forces, and bearing looseness forces [170]. As the UMP (can also be known as net radial force in the machine) would produce additional radial load on the bearing, the impact of additional loading is investigated in this chapter. When the bearing is overloaded, the cyclic stress exerted on the bearing would cause a bearing fatigue failure [171].

The analysis of impact of UMP on the bearing lifetime was done through using Basic Bearing Life (L_{10}), as shown in [172]. L_{10} of a bearing indicates the lifetime of 90% of the bearing can be expected to survive [173]. The formula for the L_{10} is shown in (6-16). C_D is the dynamic load capacity which varies with bearing type and manufacturer. Bearing with a better quality or a bigger diameter will have a higher C_D. The bearing lifetime calculation is based on the assumptions in Sub-section 4.7.3.

$$L_{10} = \left(\frac{C_D}{F_{eq}}\right)^3 \tag{6-16}$$

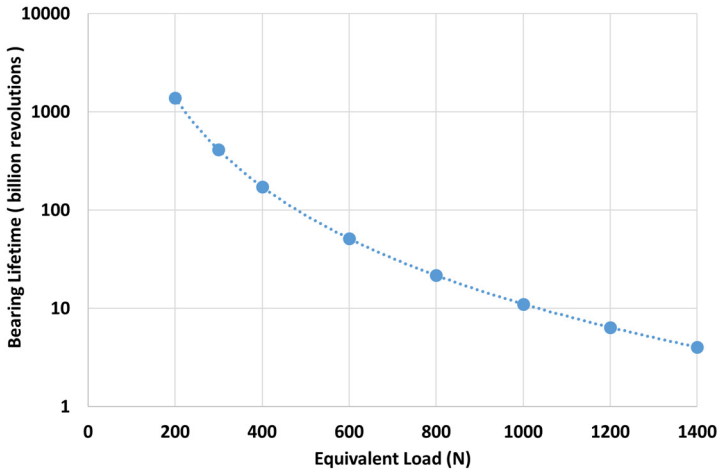

Figure 6-40: Bearing lifetime (revolutions) vs equivalent load.

Figure 6-40 shows the bearing lifetime for a ball bearing with a C_D of 10kN. The UMP and the rotor weight are assumed to act towards the same direction with a constant force. Figure 6-40 shows that the bearing lifetime reduces exponentially when the equivalent load increases.

The analysis of the bearing lifetime only investigates the impact of static UMP; it does not show the exact bearing lifetime, because the axial bearing loading and the working environment of the bearing are not taken into account. In addition, the degree of eccentricity is assumed to remain the same, in which the rotor eccentricity does not get worsen over time. Although a most realistic bearing model is not shown, this section could show the impact of UMP on the bearing lifetime and also highlight the importance of reducing UMP.

6.5.1 Different degree of eccentricity

In Figure 6-41, the bearing lifetime is calculated by using (6-16), in which the UMP values are taken from experimental results in Sub-section 3.6.7. As the slip increased, the bearing lifetime reduced because UMP produces additional loading on the bearing; the bearing lifetime reduction for 0.2, 0.4, 0.5 degree of eccentricity are 48%, 79%, 84% respectively. From here, it can be seen that the UMP could significantly reduce the bearing lifetime. Also, the UMP may also cause additional eccentricity when the rotor shaft is not sufficiently stiff [35], which would further reduce the bearing lifetime.

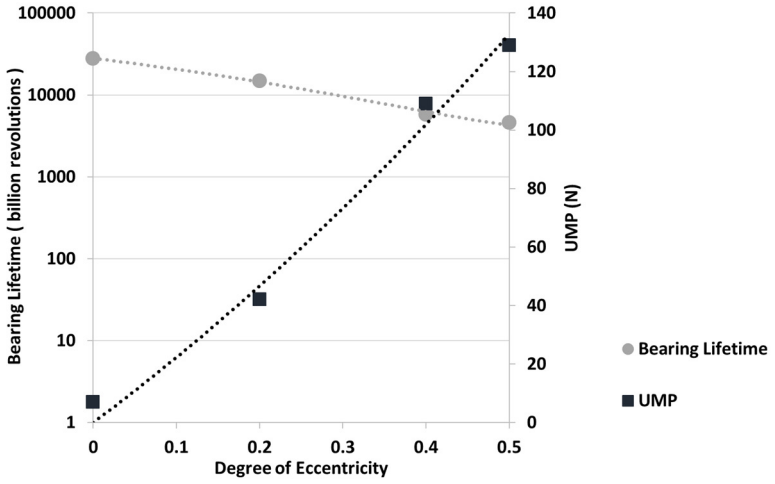

Figure 6-41: UMP and bearing lifetime of Machine-2 with 50% rated voltage at no-load.

6.5.2 Constant load with different rotor slip

Sub-section 6.2.9 shows the impact of varying the rotor slip when a constant load of 11 Nm is applied. This chapter is to further show the impact of the UMP on the bearing lifetime by using the experimental results taken from Sub-section 6.2.9. When the rotor has a weight of 140 N and acts towards the same direction as the UMP, Figure 6-42 shows that if the UMP could reduce from 99 N to 52 N, the bearing lifetime could be increased by around 100%. As the bearing lifetime calculation in (6-16) is a cube function, the bearing lifetime could be significantly increased when the UMP is reduced.

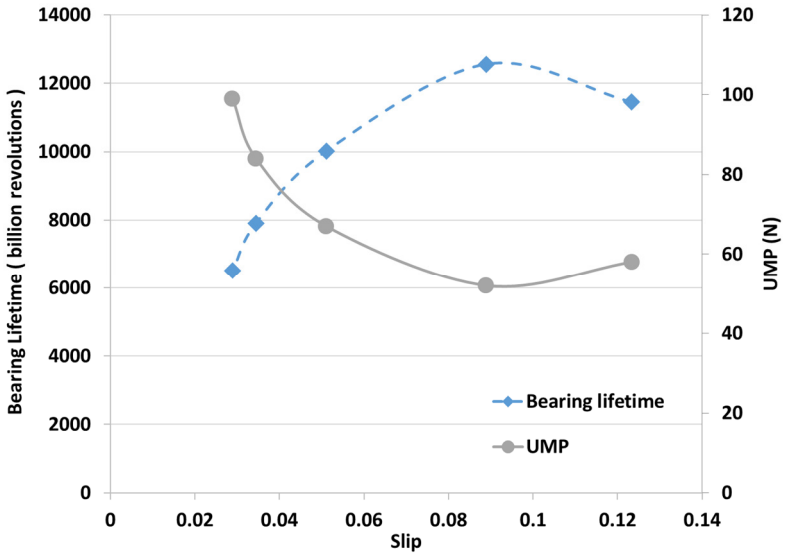

Figure 6-42: Bearing lifetime and UMP of Machine-2 at a constant load of 11 Nm.

6.5.3 Comparison between slip control method and damper windings topology in Machine-3

For different degree of eccentricity, the bearing lifetime of Machine-3 with 40% load is illustrated in Figure 6-44, which is based on the UMP results in Figure 6-43. The UMP increases when the degree of eccentricity increases, in which reduces the bearing lifetime.

Through implementing the UMP reduction techniques, the bearing lifetime could be increased. For example, at 0.5 degree of eccentricity, the bearing lifetime is

increased by 5.5 times when slip control method is used. Meanwhile, as the machine with damper winding can significantly reduce the UMP, the bearing lifetime of the machine with damper winding is significantly higher than the slip control method.

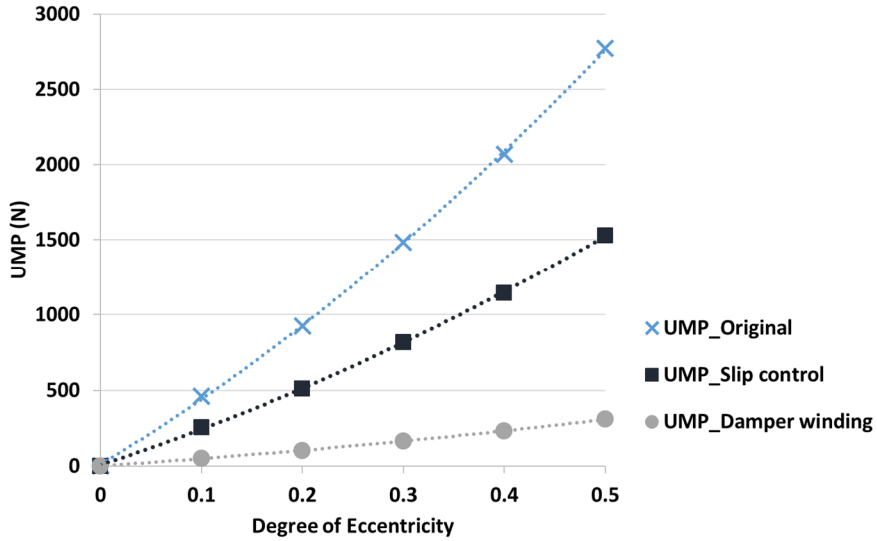

Figure 6-43: UMP at different degree of eccentricity.

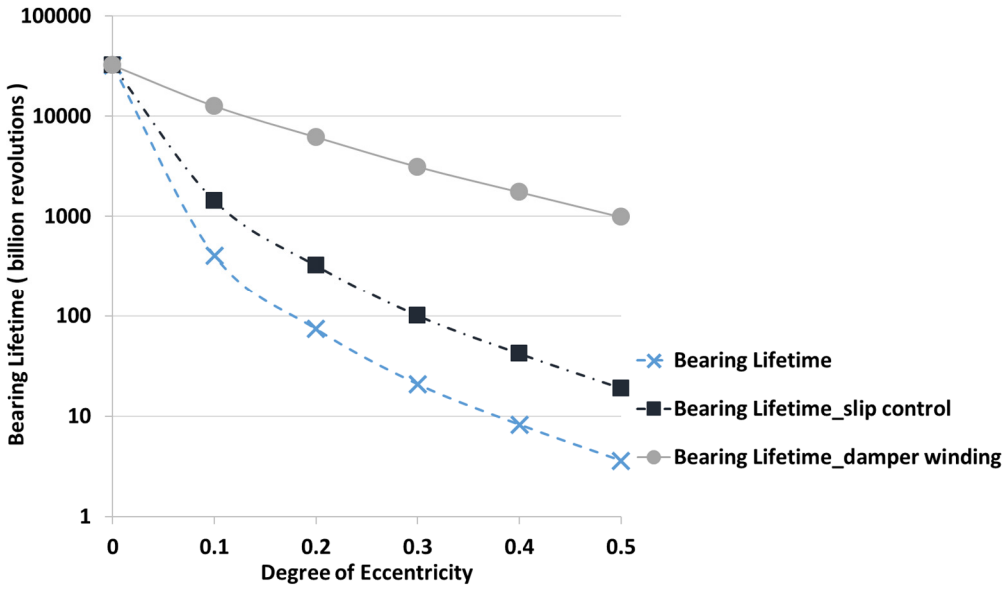

Figure 6-44: Bearing lifetime in revolutions at different degree of eccentricity.

6.6 Chapter Summary

The slip control method had shown promising UMP reduction results on both wound rotor and cage rotor induction machine. However, due to most of the UMP of the cage rotor induction machine had already been damped by the parallel rotor bar, the UMP reduction for the cage rotor induction machine is not as significant as the wound rotor induction machine. Furthermore, rate of change limiter for the reference voltage is needed when controlling the rotor flux. This is because a sudden change in voltage will cause a UMP spike that is harmful to the bearing. Also, the effect from the inverter supplied voltage was also investigated, which has shown that the higher voltage harmonics would increase the UMP of the machine.

Furthermore, the damper windings topology is proposed for the wound rotor induction machine to damp the UMP caused by fundamental magnetising flux. By using the proposed damper windings, more than 75% of UMP can be damped when the machine is running at its operating region.

In addition, the power losses of the slip control method and damper windings topology in a wound rotor induction machine were compared. As the best efficiency of Machine-3 is not at 0.05 slip, the power losses were increased when using slip control to reduce the UMP. Meanwhile, the machine's efficiency can be increased when using damper windings, because it does not change the operating condition of the machine. However, damper windings topology requires additional winding that may reduce the power density of the machine. Therefore, these issues need to be investigated when choosing the method to reduce UMP.

Although bearing L_{10} lifetime calculation shown in this chapter does not reflect the exact bearing lifetime, because only the UMP and rotor weight are considered, it can be used to investigate the impact of UMP on the bearings. From the comparisons made in the L_{10} lifetime, the bearing fatigue lifetime can be significantly increased when using either type of UMP reduction methods, because the reduction of UMP reduces the radial loading of the bearing.

7 Conclusions and Future Work

7.1 Conclusions

Given the high bearing failure rate of induction machines, the importance of reducing the UMP was highlighted in this thesis. Before identifying the methods to reduce UMP, the UMP characteristics were comprehensively discussed. Analytical modelling, FEA, and experimental works were used to study the characteristics of the UMP. Then, two methods were proposed in order to reduce the UMP, which were the slip control method and the damper winding topology.

In Chapter 3, the analytical modelling for UMP calculation was presented. After discussing the magnetic permeance harmonics caused by rotor eccentricity, a few assumptions about the low degree of eccentricity were made to simplify the UMP calculation. The dynamic and static eccentricity were separated in the UMP analysis. The UMP analytical model showed that the UMP is proportional to the multiplication of the degree of eccentricity with the magnitude of the magnetic flux of each pole-pair in the airgap. Meanwhile, the setup of the experimental work and the FEA is shown in this chapter. Prevention works to reduce the error in setting up the experimental test rig were shown. Then, the experimental results were used to validate the reliability of the FEA analysis. Results had shown good correlation when the machine operates

below its rated slip. However, the error increases when the rotor slip is high, because skewed rotor is not taken into account in a 2D-FEA.

Further to this, the UMP during the FEA and experimental results were analysed by using FFT analysis. The constant component and 2-times supply frequency components from the static eccentricity were shown in both cases and matched with the UMP analytical model. When compared to the constant component, the 2-times supply frequency component is negligible, because the backward rotating flux is minimal in a series connected stator winding induction machine. Then, UMP was analysed by using a blank rotor. The analysis of blank rotor could show a clearer space harmonics distribution of the airgap flux because the rotor winding causes zigzag leakage flux and the additional current induced in the rotor would have influenced the results. The FFT analysis of the airgap leakage flux illustrated that pole pair ± 1 magnetic flux exists when rotor eccentricity occurred.

From the significant difference of UMP between the wound rotor and cage rotor induction machine that had been pointed out by many previous researchers, in Chapter 4, the damping effect from the cage rotor bar was comprehensively discussed. The UMP Damping Coefficient was introduced to explain the damping scenario. Also, the Damping Coefficient can be used in the analytical model for steady state analysis. Moreover, only the Damping Coefficient of the fundamental magnetising flux is investigated in this thesis. Both the experimental work and FEA are also used to verify the proposed Damping Coefficient. The Damping Coefficient is a function of the angular slip frequency, rotor inductance and rotor resistance. This results show that the direction of the UMP caused by the magnetising flux is not acting toward the narrowest airgap when there is damping of the UMP. The UMP direction is also a function of the angular slip frequency.

Furthermore, different excitation frequency and rotor bar resistance have been investigated. The findings illustrated that an induction machine with lower excitation frequency had a higher UMP because of the reduction of the effectiveness of UMP damping. This is similar to the rotor bar resistance, where the UMP was higher when

the rotor bar resistance was larger. After that, the difference between the Damping Coefficient of the static and dynamic eccentricity was demonstrated. The flux could not be totally damped by the cage rotor bar, so the airgap magnetic flux was divided into two categories: fundamental magnetising flux and airgap leakage flux. The UMP for both the wound rotor and cage rotor induction machine are shown to conclude the entire analysis on the damping of UMP.

Then, the skewed rotor and axial-varying eccentricity of the cage rotor induction machine was further discussed by using the proposed UMP Damping Coefficient. For a skewed rotor, the imperfect coupling of magnetic flux reduced the effectiveness of the UMP damping, and the increment of the skew leakage flux also caused a larger UMP when the slip increased. Due to the uneven distribution of the magnetic flux around the airgap, additional power losses would occur due to rotor eccentricity. The calculation of iron losses for a wound rotor induction machine with eccentricity was shown, in which the power losses were higher when the degree of eccentricity was bigger. For the cage rotor induction machine, the rotor copper loss showed a 5% increment due to 50% of static eccentricity. Furthermore, the UMP is considered an additional radial load, which caused the bearing frictional loss that increased with the UMP.

In Chapter 5, the empirical method was proposed to calculate the UMP. The empirical method was introduced to simplify the UMP calculation, which could solve the problem of calculating the UMP caused by the airgap leakage flux. Instead of finding the airgap leakage inductance, the empirical method was used directly to estimate the UMP caused by the airgap leakage flux. Also, the UMP caused by the fundamental magnetising flux was included in the UMP estimation. The empirical method was tested on three different machines. The empirical method was then used to estimate the UMP for different static eccentricity and dynamic eccentricity. The estimated results were compared and verified with the FEA. However, the empirical method can only be used below the rated slip, where the rotor reactance can be neglected. Then, a UMP/torque ratio was introduced in order to find the operating slip of the machine with the lowest UMP. It was proven that the minimum UMP rotor slip

did not change with the supplied voltage. The saturation effect was clearly shown in the UMP/torque ratio, but it did not have much effect on the selection of the optimum operating slip. The equation to find the operating slip with the lowest UMP was developed.

In Chapter 6, two methods were proposed to reduce the UMP of induction machines: slip control method and damper winding method. For slip control method, the model-based control method is used to control the rotor slip so that the machine can operate at its optimum operating slip. The occurrence of UMP spike when switching the excitation voltage was discovered. Therefore, the rate of change limit needs to be set in the model to reduce the UMP spike. The UMP reduction in the wound rotor and cage rotor induction machine are shown by using Matlab/Simulink. The results show that the slip control is only effective when the machine is lightly loaded because the concept of slip control is to change the magnetising flux to balance the UMP caused by the airgap leakage flux and the UMP caused by the magnetising flux. Then, an ideal sinusoidal excitation voltage and also an inverter supplied voltage are also compared in this chapter. Finally, the experimental work on a constant load at different voltage levels is shown in this chapter.

The damper windings method uses the characteristic of the circulating current in the parallel winding which could create a counteracting flux to damp the UMP. The proposed damper windings configuration is only suitable for the even pole-pair machine. UMP with and without damper windings are compared on a 4-pole and 8-pole wound rotor induction machine. This showed a significant UMP reduction with the damper windings which is higher than 90% in the machine running at no-load. However, the installation of damper winding will reduce the active part of the induction machine, which needs to be considered in designing an induction machine. Furthermore, the copper loss from the damper winding is shown. It has been proven than the additional copper loss from the damper winding is much lower than the frictional loss from the UMP which makes the installation of the damper winding to be worthy. Finally, basic bearing lifetime calculation was shown to prove the importance of reducing the UMP of the machine.

Overall, the work presented in the thesis can be separated into two parts which is the discussion on the UMP characteristic and the investigation on the methods to reduce the UMP. The discussion of the UMP characteristic had been undertaken by using analytical models, in which a few analytical models are also proposed. The proposed analytical models include calculation of the UMP Damping Coefficient, UMP calculation in a skewed rotor, UMP calculation in axial-varying eccentricity, additional power losses caused by an eccentric rotor, UMP calculation through empirical methods for both static and dynamic eccentricity. The key points that can be highlighted in the first part of the thesis:

1) UMP could be damped by the parallel path in the machine. The damping of UMP will shift the direction of the UMP away from the narrowest airgap. The changing of direction is significant only when the rotor is running at around synchronous speed, because the magnetising flux is the dominant flux in the airgap.
2) A skewed rotor would increase the UMP in cage rotor induction machines because the UMP damping effect is reduced and the increment of the airgap leakage flux.
3) Rotor eccentricity would increase the power losses in the machine. For wound rotor induction machines, additional iron losses are caused by the additional magnetic flux harmonics in the machine. Meanwhile, circulating current in the cage rotor induction machines would increase the copper loss. In addition, the UMP would increase the bearing friction loss in both types of induction machines.

In the second part of the thesis, the investigation of the methods to reduce the UMP had been shown. The two methods shown in the thesis are the slip control method and the damper windings topology. In order to implement the slip control method, an UMP/Torque ratio is introduced to find the operating slip with the lowest UMP. Furthermore, a new damper windings configuration is proposed to reduce the sideband flux caused by the rotor eccentricity. The key points that can be highlighted in the second part of the thesis are:

1) The rotor slip with the lowest UMP is highly dependent on the type of induction machines and the machine parameters.
2) The slip control method is more effective when the induction machines are lightly loaded. Meanwhile, the damper windings topology can effectively reduce the UMP when the machine is running below its rated slip.

7.2 Future Work

There are many ways in which the work undertaken in this thesis could be extended. There are also many applications that could greatly benefit from the idea proposed in the thesis.

From a modelling perspective, the analytical model to calculate the UMP had already been commonly shown. The main problem with using it for accurate calculation is that the leakage flux that crosses the airgap is difficult to be calculated. This thesis uses the FEA method to find the UMP caused by the airgap leakage flux. An improvement could be made if an analytical method could be used to predict the airgap leakage flux. The analytical method probably needs to include a few aspects such as stator and rotor teeth length, stator and rotor slots design, the airgap length and the ratio between the stator and rotor. If this could transform into the analytical model, this would help in designing a machine with a lower UMP when rotor eccentricity occurred. For example, modification of the airgap length had shown a significant difference in the airgap leakage flux. If this information could be standardised by using the analytical method, this would add an additional objective when designing a machine.

As changing the magnetising flux in the machine could affect the power losses, the calculation of the additional power losses due to rotor eccentricity is only briefly described in this thesis. The power losses model could be further extended by including the skin effect of the rotor bar, then, the stray load loss could be added to the calculation. Future work could be extended through optimising between the power loss and the UMP. As the control of magnetising flux is based on the power losses and the UMP, fast computational time is needed to process these information, in which the

proposed analytical calculation for the power losses and the proposed empirical method for UMP calculation can be used.

Optimisation techniques could be used to get a balance between power loss and UMP of the induction machines. The objective function can be set by considering the load pattern, degree of eccentricity, temperature, type of bearing and failure rate. With the fast UMP calculation, predicting the bearing failure can further be done. Then, the objective function in the optimisation could be changed to decrease the bearing failure. However, load fluctuation would affect the selection of the magnetising flux in the machine because of small rotor time constant. Therefore, research can be conducted on the optimum flux selection in a fluctuation load condition.

The installation of damper windings in the wound rotor induction machine had shown to be a promising method to reduce UMP. Therefore, further research can be done to study the side effect of installing the proposed damper winding, in which the thermal performance, power density and torque performance can be included. In addition, research on utilising the damper winding topology to detect the fault in induction machines can also be done. Condition monitoring through the damper winding is feasible, because the proposed damper windings could detect all the odd pole pair harmonics in the machine.

Furthermore, the slots permeance causes noise and vibration, which had already been discussed by many researchers. The existence of rotor eccentricity would amplify the vibration caused by the slot permeance, which causes the deterioration of bearing lifetime. As the noise and vibration of machine are difficult to be calculated, further works can be done to simplify the noise and vibration estimation by using the proposed empirical method, which uses the experimental or FEA data to estimate the UMP.

In addition, given the different control strategy, such as DTC or FOC, could produce different voltage harmonics, the different magnetic flux harmonics in the machine could have contributed differently to the vibration. The influence of the other kind of control strategies can be further investigated. The vibration factor caused by

different control strategy needs to be investigated with the natural frequency of the system. Then, choosing the control topology could also be combined with selecting the stator and rotor slots. Other than reducing the noise level, which is suggested by many researchers, this also could reduce the vibration force exerted on the bearing.

Lastly, machine-learning could also be implemented to simplify the design stage, failure prediction, machine load prediction and control strategy. In the designing stage, the machine design can be differentiated with features. Then, using this data with UMP would help in deciding the best design. Furthermore, the failure prediction could be used by collecting the data before the bearing malfunction, this information can then be processed to estimate when the next failure will occur. After having this prediction, the bearing could be changed before it breaks down or the objective function could be changed to prolong the lifetime. The machine load prediction is essential for a fluctuating load like in a renewable energy generation. For wind energy generation, if the wind power for the next minute or the next 10 minutes could be predicted, the optimum flux can be adjusted to suit the conditions.

Appendix A: Machine Parameters

Machine-1 Parameter	
Power (kW)	7.5kW
Poles	4
Axial Length	178.6mm
Stator Radius	140mm
Rotor Radius	89.75mm
Airgap Length	0.5mm
Stator slots number	36
Stator turns per coil	22
Stator resistance (phase)	1.08 ohm
Rotor Slots number	28
Rotor turns per coil	1
Rotor resistance (phase)	1.105ohm
Magnetising inductance (phase)	0.282H
Leakage Factor	0.11
Rotor Inertia	0.1296 kg/m^3

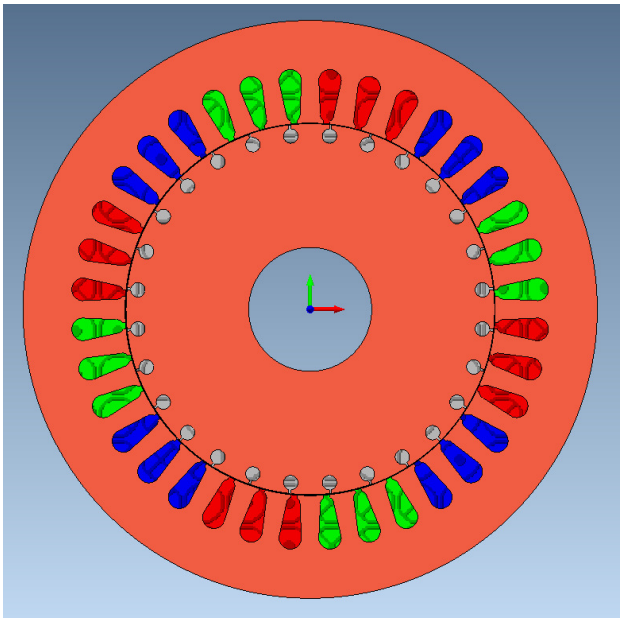

Figure A-1: Geometry of Machine-1 in 2D FEA.

	Machine-2 Parameter	
	FEA	**Experiment**
Power (kW)	5.5kW	
Poles	8	
Axial Length	180mm	
Stator Radius	120mm	
Rotor Radius	78mm	
Airgap Length	0.9mm	
Stator slots number	52	
Stator turns per coil	13	-
Stator resistance (phase)	1.579ohm	1.7ohm
Rotor Slots number	42	
Rotor turns per coil	1	
Rotor resistance (phase)	0.846ohm	0.9ohm
Stator inductance (phase)	0.1795H	0.19H
Leakage Factor	0.18	0.2
Rotor Inertia	0.0804 kg/m^3	

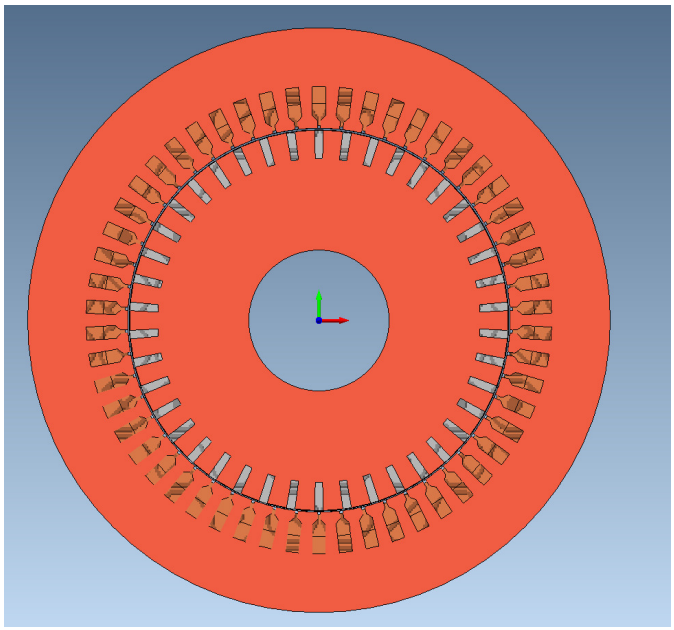

Figure A-2: Geometry of Machine-2 in 2D FEA.

Machine-3 Parameter	
Power (kW)	7.5kW
Poles	4
Axial Length	178.6mm
Stator Radius	140mm
Rotor Radius	89.75mm
Airgap Length	0.5mm
Stator slots number	36
Stator turns per coil	22
Stator resistance (phase)	1.08 ohm
Rotor Slots number	48
Rotor turns per coil	6
Rotor resistance (phase)	1.339ohm
Magnetising inductance (phase)	0.286H
Leakage Factor	0.12
Rotor Inertia	0.1296 kg/m^3

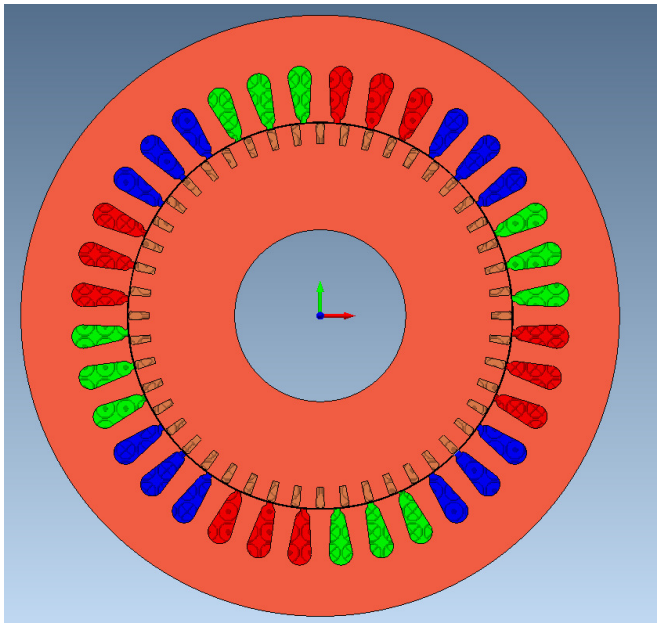

Figure A-3: Geometry of Machine-3 in 2D FEA.

Machine-4 Parameter	
Power (kW)	5.5kW
Poles	8
Axial Length	178.6mm
Stator Radius	140mm
Rotor Radius	89.75mm
Airgap Length	0.5mm
Stator slots number	48
Stator turns per coil	22
Stator resistance (phase)	1.5 ohm
Rotor Slots number	48
Rotor turns per coil	6
Rotor resistance (phase)	1.105ohm
Magnetising inductance (phase)	0.282H
Leakage Factor	0.11
Rotor Inertia	0.1296 kg/m^3

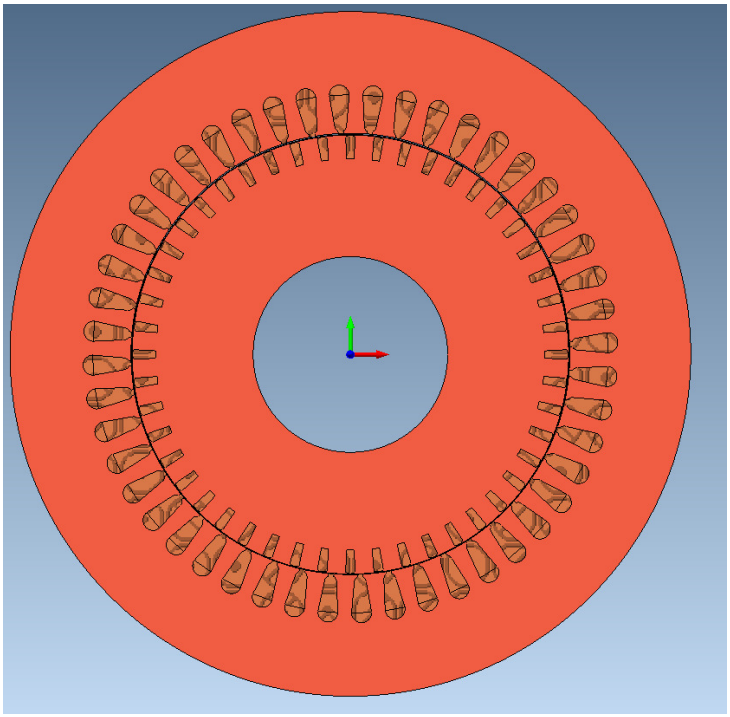

Figure A-4: Geometry of Machine-4 in 2D FEA.

Appendix B: Experimental Apparatus Specifications

Model SJ200			075HFEF
Output Rating	Applicable motor size		7.5 kW
	Rated Capacity	400V	11 kW
		480V	13.3 kW
	Rated output current		16 A
	Overload Capacity		150% for 6 seconds
	Rated output voltage		3-phase, 380V to 480V (corresponding to input voltage)
	Carrier frequency		2 kHz to 14 kHz
Input Rating	Rated input voltage		380 V to 480 V ±10%, 50/60 Hz±5%
Enclosure			IP20 (NEMA 1)
Cooling method			Force ventilation
Weight			3.8 kg

Table B-1: Inverter specification.

Model	Electrodrives BS5000-99
Power	5.5 kW
Speed	710
Frequency	50/60 Hz
Rated voltage	415V
Rated current	13.4
Poles	8
Slip	0.053
Size	D160H

Table B-2: Nameplate details for induction machines (Machine-2).

Model	Magtrol TMB210/432
Nominal Rated Torque	50 Nm
Sensitivity	100 mV/Nm
Maximum speed	4000 RPM
Pulse wheel	60pulses/rev

Table B-3: Torque transducer specification.

Model		Kistler 9366CC
Max allowed measuring range	F_x and F_y	-25…25 kN
	F_z	-25…60 kN
Sensitivity	F_x and F_y	-7.8 pC
	F_z	- 3.8 pC
Difference in sensitivity with various top plates size	F_x ,$F_y$and F_y	$\pm 2\%$
Operating temperature		-20…70 °C
Connection type		Fischer flange 9-pin neg,
Max top plate size		750mm x 750mm

Table B-4: Multicomponent force link set specification.

Model	Dynoware Type5697
Number of channels	28
Resolution (per channel)	16 Bit
Input voltage	± 20 V
Sampling frequency (1 channel)	1000 kS/s
Sampling frequency (14 channels)	71 kS/s

Table B-5: Data acquisition specification.

Model	Kistler 5070A
Number of channel	4/8
Connector type	BNC/ Fischer 8-pole
Measuring range	±200…200 000pC
Measurement uncertainty	<±0.3%
Drift, measuring mode	<±0.05 pC/s
Frequency range (20Vpp)	0-45 kHz
Group delay	<0 µS
Output voltage	±10
Output current	±2 mA
Output resistance	10 ohm
Zero point error	< ±10 mV
Output interference signal	<10 mVpp

Table B-6: Charge amplifier specification.

Appendix C: Eccentric Rotor

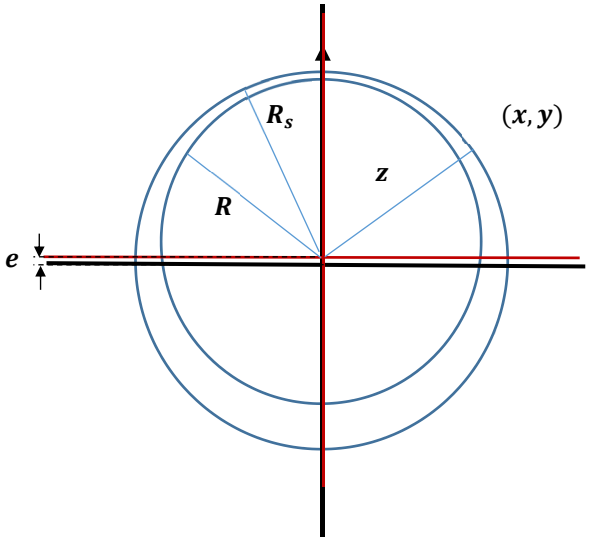

Figure C-1: Eccentric rotor.

The assumption has been made that the airgap perpendicular to the eccentric rotor is the same as the airgap length of an ideally positioned concentric rotor. To prove the assumptions, referring to Figure C-1, let the rotor has an eccentricity towards the positive Y-axis direction, the rotor coordinate can be written as (C-1) [15].

$$(e + y)^2 + x^2 = R^2 \tag{C-1}$$

After expanding,

$$y^2 + x^2 = R^2 - 2ey - 2e^2 \tag{C-2}$$

By using the trigonometry characteristic

$$y^2 + x^2 = z^2 \tag{C-3}$$

(C-2) becomes:

$$z^2 + 2ez\cos\theta + e^2\cos^2\theta = R^2 - e^2(1 - \cos^2\theta) \tag{C-4}$$

After simplification,

$$z + e\cos\theta = R\sqrt{1 + \frac{e^2}{R^2}(1 + \cos^2\theta)} \tag{C-5}$$

As the airgap of an induction machine is much smaller than the radius of the rotor, $e \ll R$, the right hand side of (C-5) equals to R. Therefore,

$$z = R - e\cos\theta \tag{C-6}$$

The airgap length is the distance between the rotor and the stator which can be written as:

$$g = z - R \tag{C-7}$$

Therefore, the airgap length around the airgap is:

$$g' = g(1 - e\cos\theta) \tag{C-8}$$

Appendix D: Magnetic flux space harmonics of blank, wound and cage rotor

Figure D-1 shows the magnetic flux space harmonics of five different time instants in the no-load operation for each type of rotor configuration, in which each machine has the same stator configuration. By comparing Figure D-1 (a), (b) and (c), it shows that the magnitude of each magnetic flux space harmonic in the blank rotor remains almost constant at any instant of time, however, the magnitude of each magnetic flux space harmonic of cage and wound rotor change with time even in a no-load operation. This is because of the induced flux in the rotor bar and the existence of the zigzag leakage flux. Therefore, a more precise analysis on the magnetic permeance harmonics can be done through the blank rotor setup.

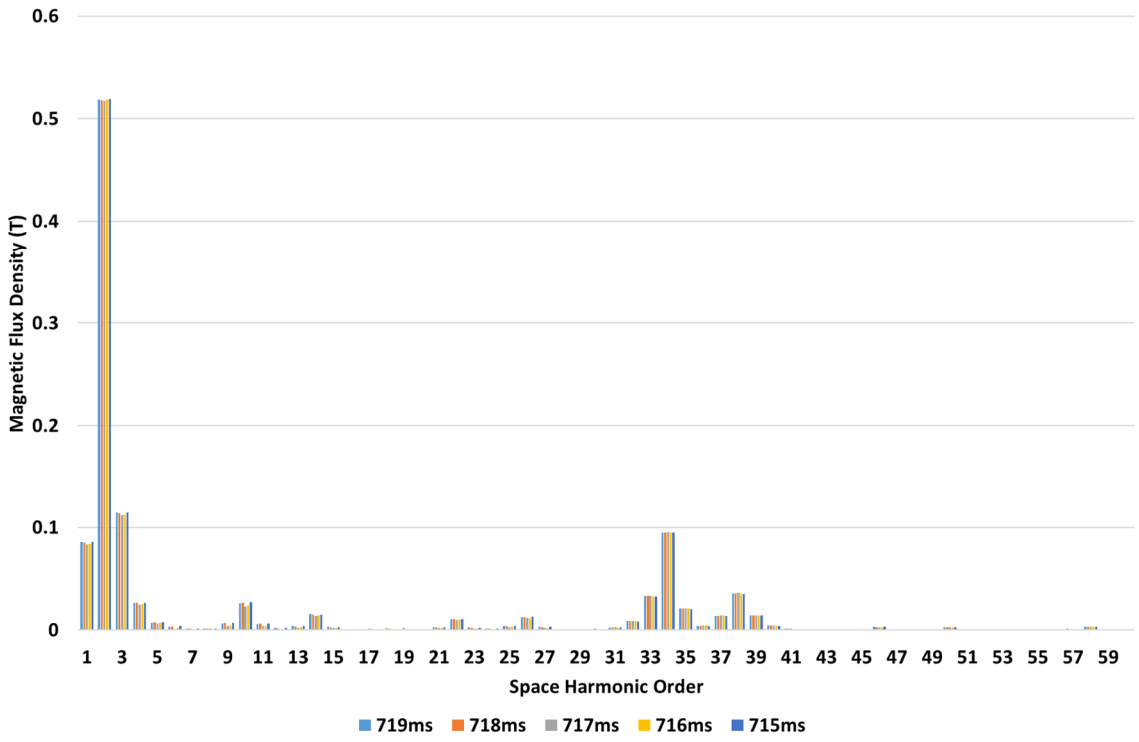

(a)

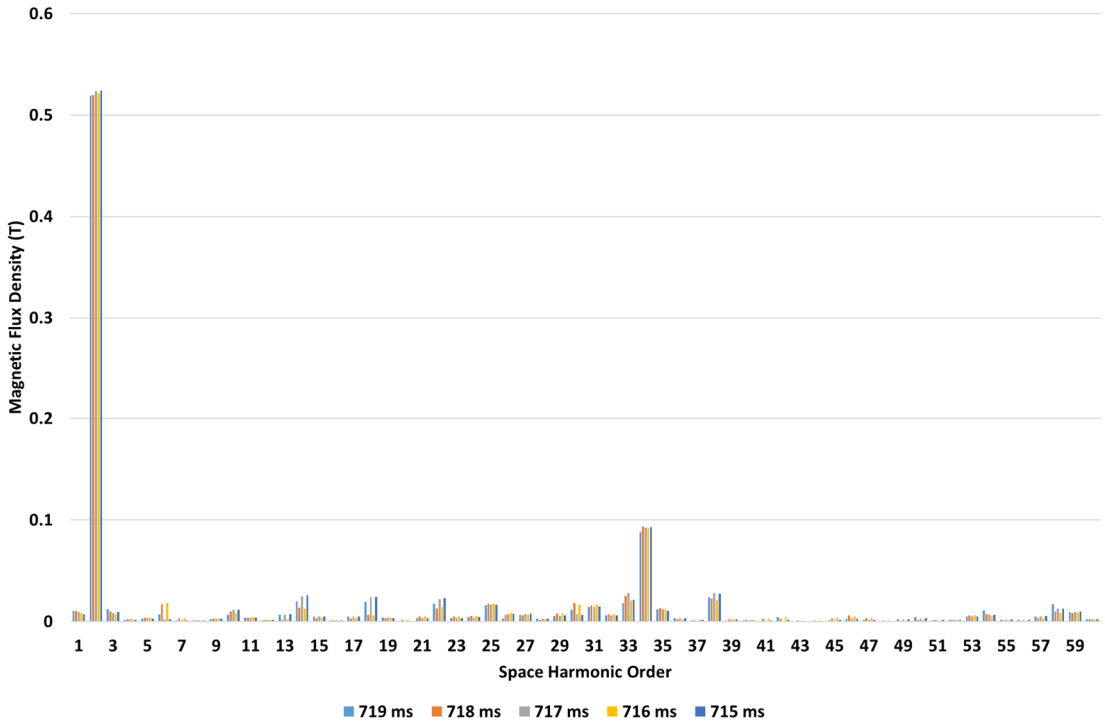

(b)

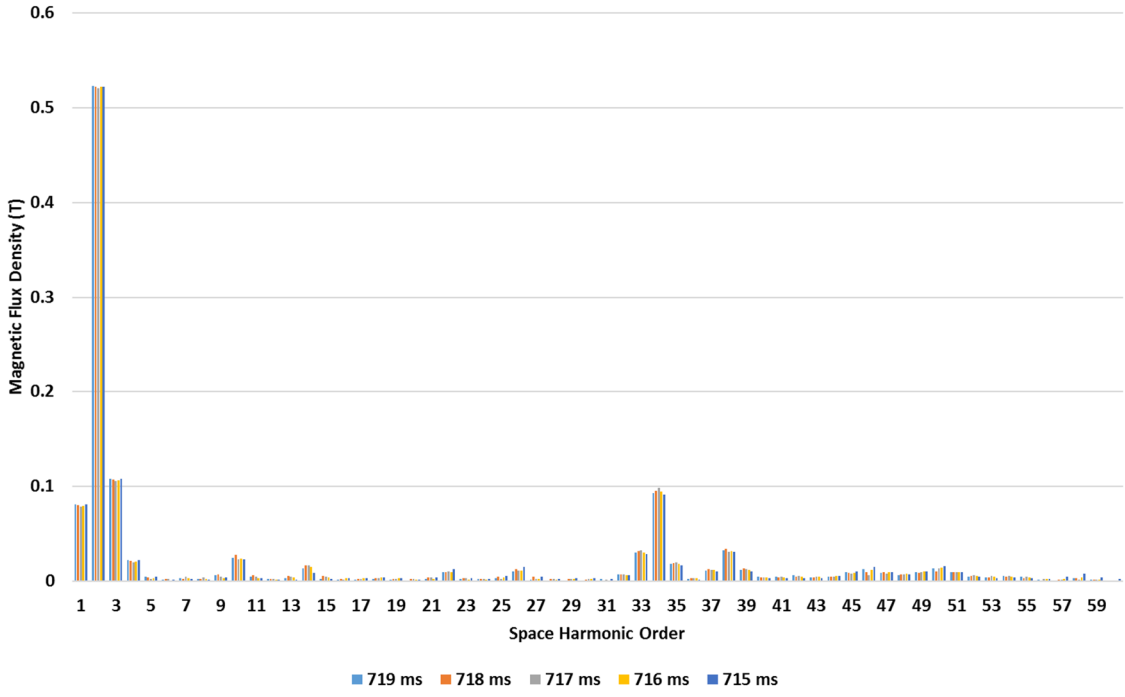

(c)

Figure D-1: Space harmonics of the magnetic flux distribution of (a) blank rotor (b) cage rotor (c) wound rotor induction machine.

Appendix E: Experimental Results

The experimental results is shown in Appendix E. The UMP is filtered in order to find the constant component of the UMP. Figure E-1 shows the experimental results for the Damping Coefficient verification.

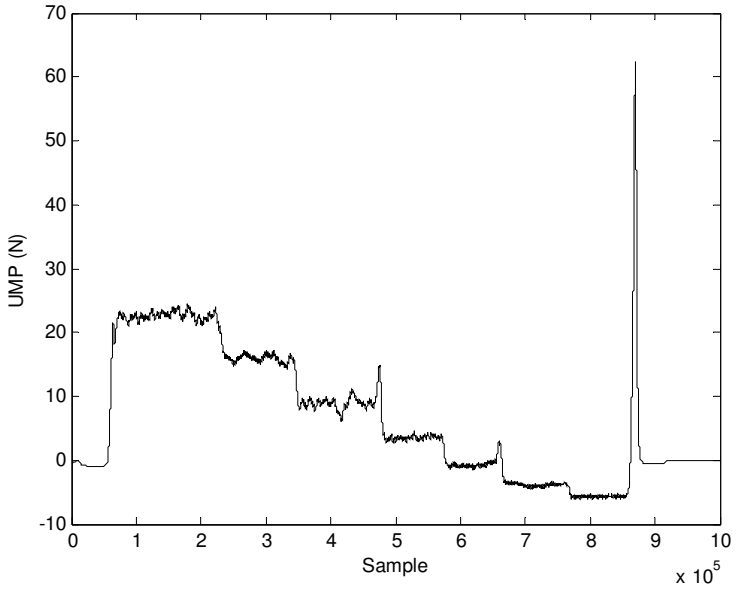

(a)

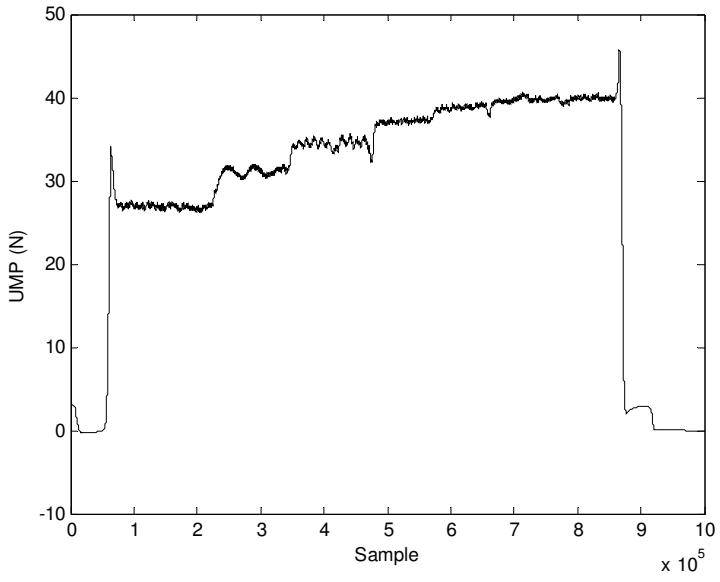

(b)

Figure E-1: UMP for (a) Figure 4-4 (b) Figure 4-5.

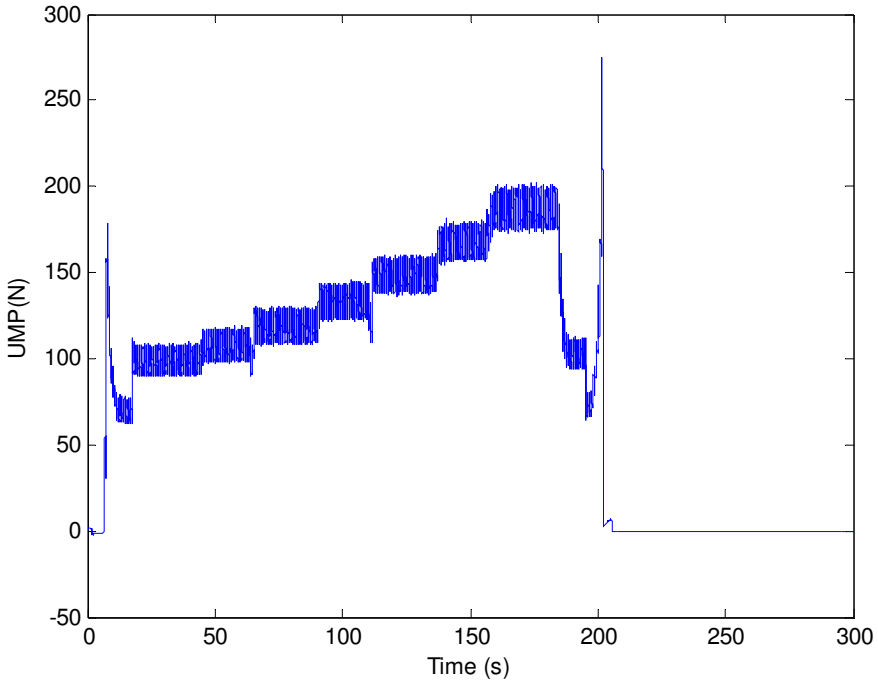

Figure E-2: Experimental results for Figure 4-18 .

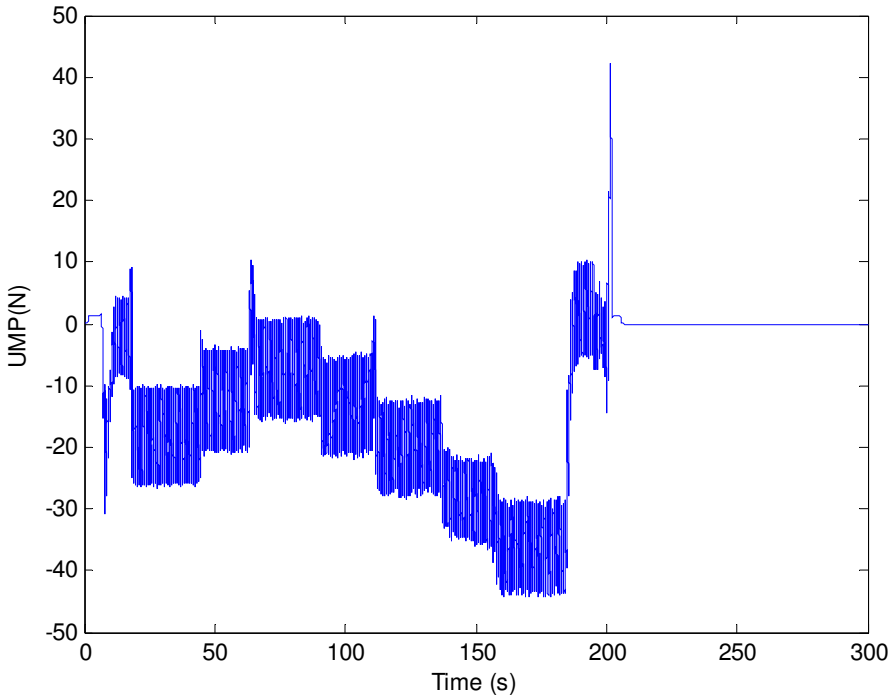

Figure E-3: Experimental results for Figure 4-18.

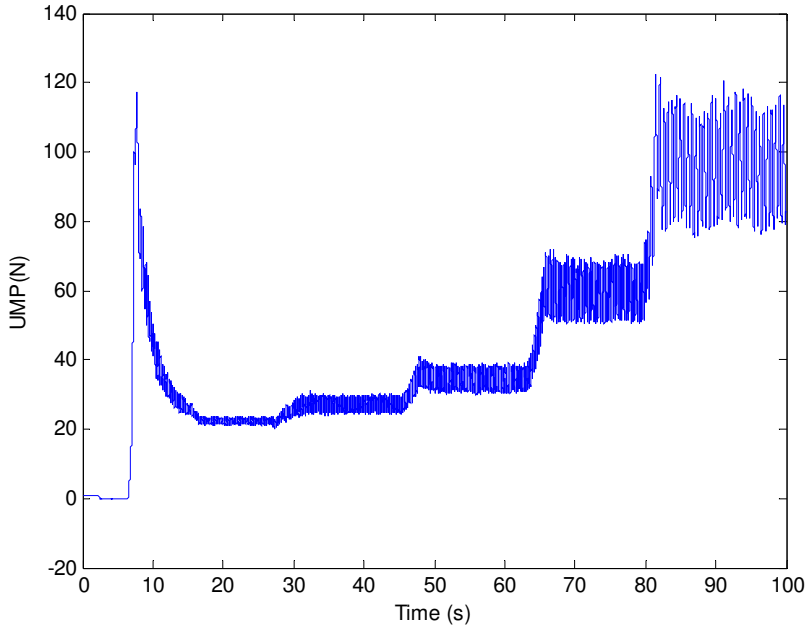

Figure E-4: Experimental results for Figure 4-10.

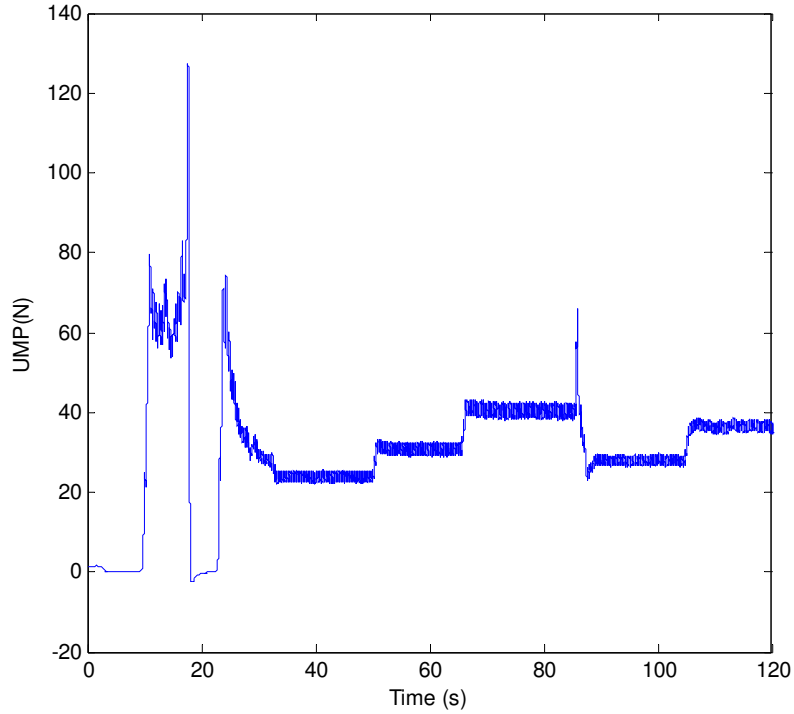

Figure E-5: Experimental results for Figure 5-3 (0.35pu).

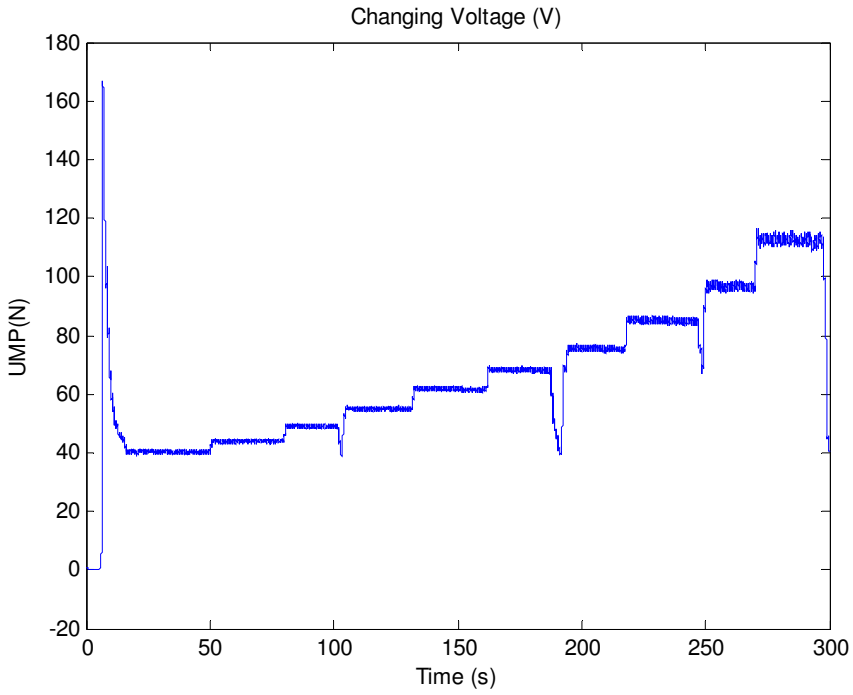

Figure E-6: Experimental results for Figure 5-3 (0.5pu).

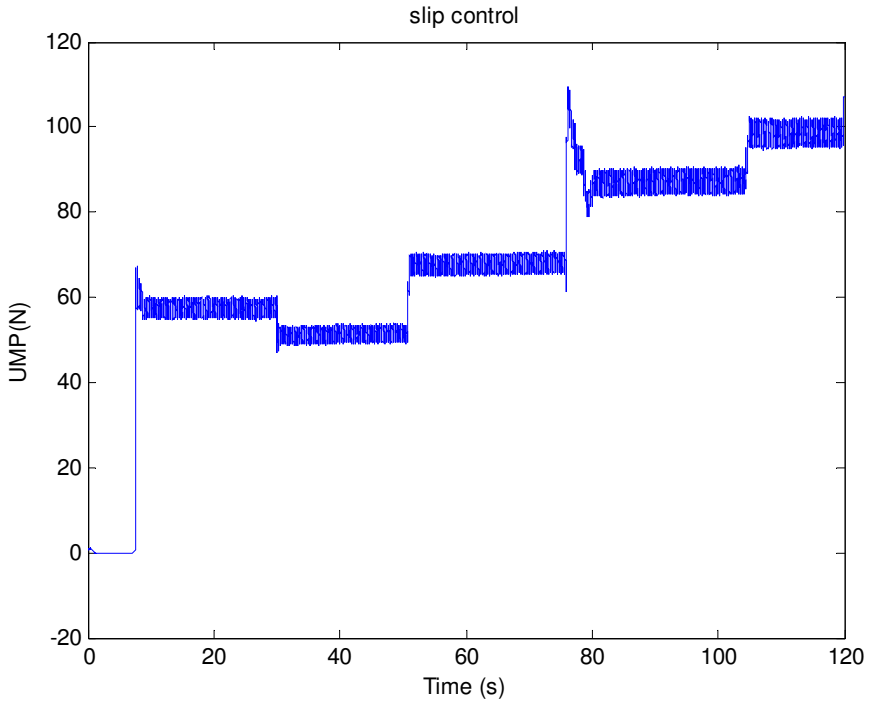

Figure E-7: Experimental results for Figure 6-25.

Appendix F: Matlab/Simulink Setup

The Simulink model for the results shown in Chapter 6 are shown in Appendix F. Figure F-1 shows the Simulink model for both with and without applying slip control. The load torque of the machine is connected to both machines. For the one with slip control, the load torque information is fed in to the supply control block to change the magnetising flux.

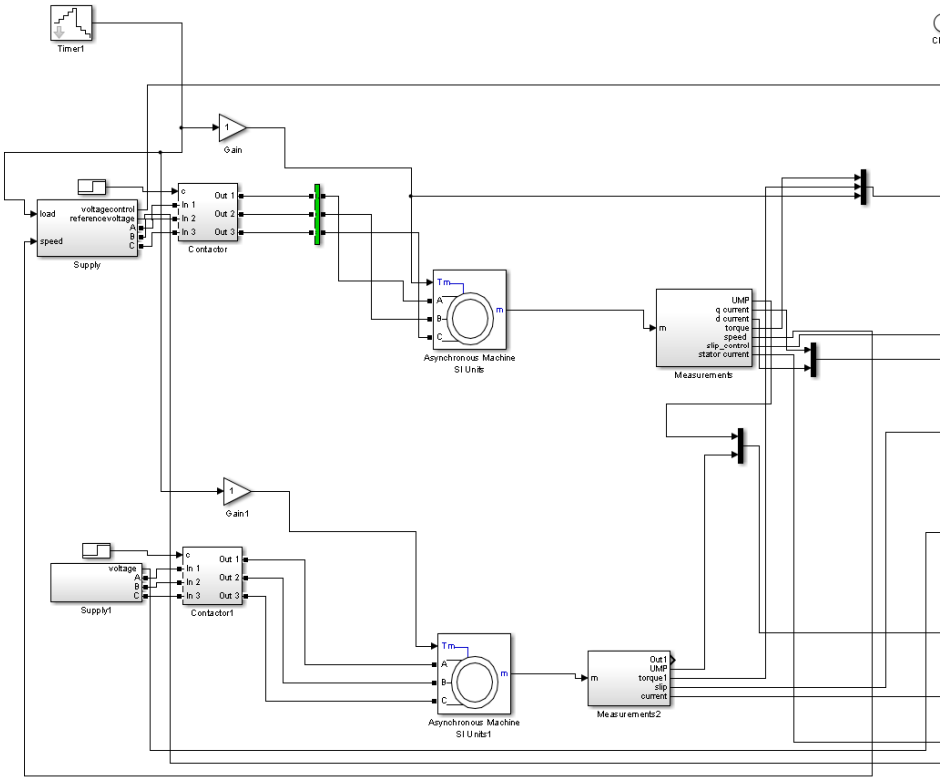

Figure F-1: Overview of the Simulink model.

The asynchronous machine supplied by a pure sinusoidal voltage can be shown in Figure F-2. Then, the inverter supplied is shown in Figure F-3. The reference voltage is precalculated by using the relationship shown in (6-8).

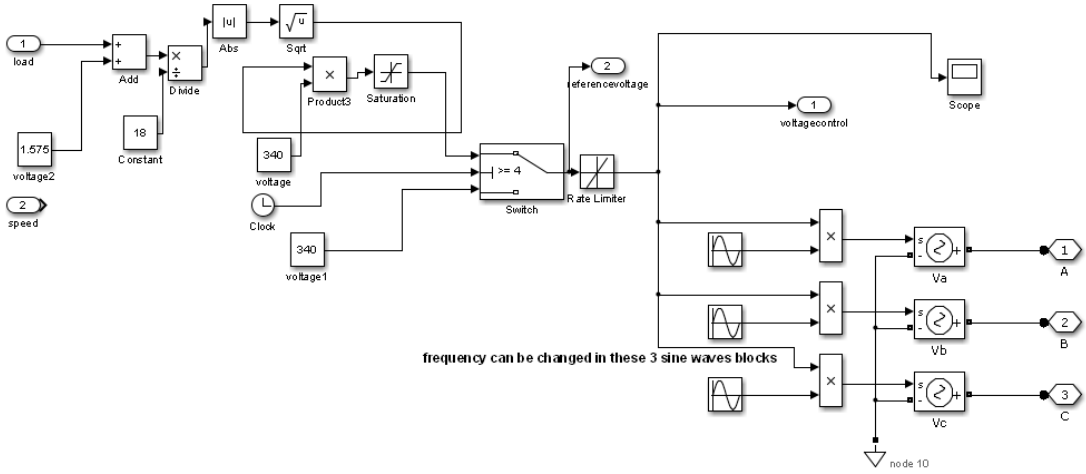

Figure F-3: Pure sinusoidal voltage supplied.

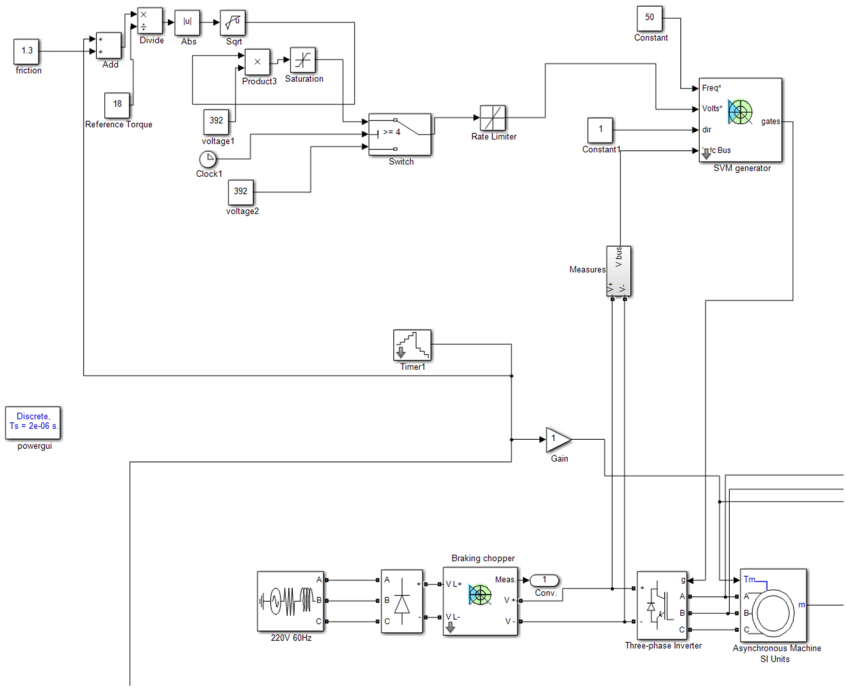

Figure F-3: Inverter voltage supplied.

Then, the current information is taken from the asynchronous machine block for UMP calculation. The angle between the stator and rotor current is calculated. This angle is used for the magnetising flux calculation. For cage rotor, damping coefficient is added to calculate the damping effect. Then, the summation of the UMP from the

magnetising flux, stator's airgap leakage flux and rotor's airgap leakage flux is made. Figure F-4 shows the UMP calculation block.

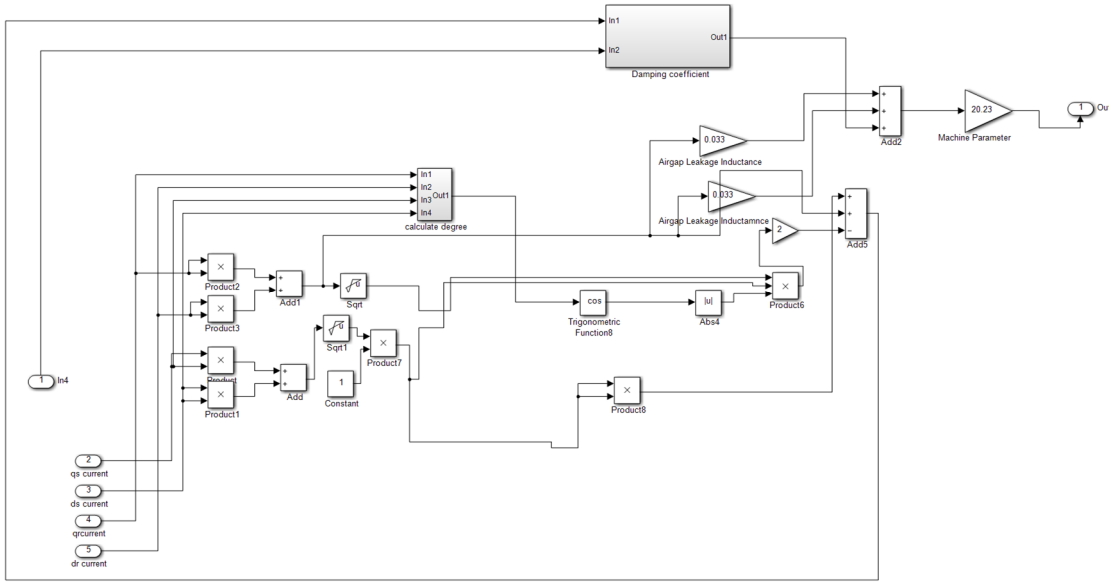

Figure F-4: UMP calculation block.

References

[1] A. T. de Almeida, F. J. T. E. Ferreira and G. Baoming, "Beyond Induction Motors—Technology Trends to Move Up Efficiency," *IEEE Transactions on Industry Applications*, vol. 50, no. 3, pp. 2103-2114, May-Jun. 2014.

[2] F. J. T. E. Ferreira and A. T. de Almeida, "Method for in-field evaluation of the stator winding connection of three-phase induction motors to maximize efficiency and power factor," *IEEE Transactions on Energy Conversion*, vol. 21, no. 2, pp. 370-379, Jun. 2006.

[3] E. H. E. Bouchikhi, V. Choqueuse and M. E. H. Benbouzid, "Current Frequency Spectral Subtraction and Its Contribution to Induction Machines' Bearings Condition Monitoring," *IEEE Transactions on Energy Conversion*, vol. 28, no. 1, pp. 135-144, Mar. 2013.

[4] W. T. Thomson and R. J. Gilmore, "Motor Current Signature Analysis to Detect Faults in Induction Motor Drives – Fundamentals, Data Interpretation, and Industrial Case Histories", *Proc. of 32nd Turbomachinery Symposium*, Texas, 2003, pp.176-182

[5] "Report of Large Motor Reliability Survey of Industrial and Commercial Installations, Part I," *IEEE Transactions on Industry Applications*, vol. IA-21,

no. 4, pp. 853-864, Jul.1985.

[6] O. V. Thorsen and M. Dalva, "Failure identification and analysis for high-voltage induction motors in the petrochemical industry," *IEEE Transactions on Industry Applications*, vol. 35, no. 4, pp. 810-818, Jul.-Aug. 1999.

[7] M. Whittle, “Wind Turbine Generator Reliability: An Exploration of the Root Causes of Generator Bearing Failures,” Ph. D. Dissertation, University of Durham, U.K., 2013.

[8] W. Cao, Y. Xie and Z. Tan, “Wind Turbine Generator Technologies”, Croatia, *IntechOpen*, 2012.

[9] P. J. Tavner and J. P. Hasson, "Predicting the design life of high integrity rotating electrical machines," *Ninth International Conference on Electrical Machines and Drives (Conf. Publ. No. 468)*, Canterbury, 1999, pp. 286-290.

[10] C. Radu, “The Most Common Causes of Bearing Failure and the Importance of Bearing Lubrication”, *RKB Technical Review*, pp. 1-7, Feb. 2010.

[11] J. Modh, S. Bhatiya and H. Joshi, “Review of Different Types of Bearing Failure”, *Journal of Advance Research and Innovative Ideas*, vol. 2, no. 3, 2016.

[12] A. Vencl, V. Gasic, B. Stojanovic, “Fault Tree Analysis of Most Common Rolling Bearing Tribological Failures”, *IOP Conference Series*, vol. 174, no. 1, 2007.

[13] J. Faiz, B. M. Ebrahimi and M. B. B. Sharifian, “Different Faults and Their Diagnosis Techniques in Three-Phase Squirrel-Cage Induction Motors—A Review”, *Electromagnetics*, 2006, pp. 543-569

[14] J. Faiz, M. Ojaghi, “Different indexes for eccentricity faults diagnosis in three-phase squirrel-cage induction motors: A review”, *Mechatronics*, vol. 19, Issue 1, 2009, pp. 2-13.

[15] D. G. Dorrell, “Calculation of unbalanced magnetic pull in cage inductlon machines,” Ph. D. Dissertation, University of Cambridge, U.K., 1993.

[16] A. Belahcen and A. Arkkio, "Computation of additional losses due to rotor eccentricity in electrical machines," *IET Electric Power Applications*, vol. 4, no. 4, pp. 259-266, Apr. 2010.

[17] M. Michon, “Electro-Mechanical Interactions”, 2016. [Online]. Retrieve from https://romaxtech.com/media/95901/romax-electromechanical-interactions-in-hev-design-process.pdf.

[18] M. Michon, R. C. Holehouse, K. Atallah and G. Johnstone, "Effect of Rotor Eccentricity in Large Synchronous Machines," *IEEE Transactions on Magnetics*, vol. 50, no. 11, pp. 1-4, Nov. 2014.

[19] M. M. Hodowanec, "Satisfactory motor bearing service life: a review of often overlooked design considerations," *Conference Record of 1995 Annual Pulp and Paper Industry Technical Conference*, Vancouver BC, 1995, pp. 170-177.

[20] X. P. Xu, Q. K. Han, F. L. Chu, “Nonlinear vibration of a generator rotor with unbalanced magnetic pull considering both the dynamic and static eccentricities”, *Architecture Application Mechanical*, 2016, pp. 1521-1536.

[21] R. L. Nailen P.E., "Converting wound-rotor motors to squirrel-cage," *Electrical Apparatus,* vol. 64, no. 3, pp. 19-24, 2011.

[22] F. Kolonić, A. Poljugan, T. Idžotić, “Development of AC Slip-Ring Motor Based Advanced Crane Industrial Controller”, *Automatika*, vol. 3, no. 4, pp. 165-172, 2005.

[23] A. D. Hansen, F. Iov, F. Blaabjerg, and L. H. Hansen, “Review of contemporary wind turbine concepts and their market penetration,” *Wind Engineering*, vol. 28, no. 3, pp. 247–263, 2004.

[24] Z. Zhang, A. Chen, A. Matveev and R. Nilssen, “High-power Generators for

Offshore Wind Turbines," *Energy Procedia*, Vol. 35, 2013, pp. 52-61.

[25] H. Polinder, J. A. Ferreira, B. B. Jensen, A. B. Abrahamsen, K. Atallah and R. A. McMahon, "Trends in Wind Turbine Generator Systems," *IEEE Journal of Emerging and Selected Topics in Power Electronics*, vol. 1, no. 3, pp. 174-185, Sep. 2013.

[26] J. W. Ringsberg and A. Bergkvist, "On Propagation of Short Rolling Contact Fatigue Cracks," *Fatigue and Fracture of Engineering Materials and Struct*ure, vol. 26, pp. 969–983, 2003.

[27] M. A. Mueller *et al*., "Experimental tests of an air-cored PM tubular generator for direct drive wave energy converters.," *2008 4th IET Conference on Power Electronics, Machines and Drives*, York, 2008, pp. 747-751.

[28] A. S. McDonald, R. Crozier, S. Caraher, M. A. Mueller and J. P. Chick, "Integrated design of direct-drive linear generators for wave energy converters," *2009 International Conference on Sustainable Power Generation and Supply*, Nanjing, 2009, pp. 1-7.

[29] J. K. H. Shek, D. G. Dorrell, M. Hsieh, D. E. Macpherson and M. A. Mueller, "Reducing bearing wear in induction generators for wave and tidal current energy devices," *IET Conference on Renewable Power Generation (RPG 2011)*, Edinburgh, 2011, pp. 1-6.

[30] J. Wu, A. Butler, M. A. Mueller and K. Mostafa, "Combining fatigue analysis information into reliability analysis using Bayesian hierarchical modelling method," *2017 Annual Reliability and Maintainability Symposium (RAMS)*, Orlando, FL, 2017, pp. 1-7.

[31] K. Mostafa, M. A. Mueller and Q. Jiang, "Bearing wear detection and rotor eccentricity calculation in radial flux air-gap winding permanent magnet machines," *7th IET International Conference on Power Electronics, Machines and Drives (PEMD 2014)*, Manchester, 2014, pp. 1-6.

[32] O. Keysan, M. Mueller, A. Mcdonald, N. Hodgins and J. Shek, "Designing the c-gen lightweight direct drive generator for wave and tidal energy," *IET Renewable Power Generation*, vol. 6, no. 3, pp. 161-170, May 2012.

[33] N. Hodgins, O. Keysan, A. McDonald and M. Mueller, "Linear generator for direct drive wave energy applications," *The XIX International Conference on Electrical Machines - ICEM 2010*, Rome, 2010, pp. 1-6.

[34] A. Salah, Y. Guo and D. Dorrell, "Monitoring and damping unbalanced magnetic pull due to eccentricity fault in induction machines: A review," *2017 20th International Conference on Electrical Machines and Systems (ICEMS)*, Sydney, 2017, pp. 1-6.

[35] J. R. Cameron, W. T. Thomson and A. B. Dow, "Vibration and current monitoring for detecting airgap eccentricity in large induction motors," *IEE Proceedings B - Electric Power Applications*, vol. 133, no. 3, pp. 155-163, May 1986.

[36] S. Nandi, H. A. Toliyat and X. Li, "Condition monitoring and fault diagnosis of electrical motors-a review," *IEEE Transactions on Energy Conversion*, vol. 20, no. 4, pp. 719-729, Dec. 2005.

[37] S. Nandi, T. C. Ilamparithi, S. B. Lee and D. Hyun, "Detection of Eccentricity Faults in Induction Machines Based on Nameplate Parameters," *IEEE Transactions on Industrial Electronics*, vol. 58, no. 5, pp. 1673-1683, May 2011.

[38] X. Li, Q. Wu and S. Nandi, "Performance Analysis of a Three-Phase Induction Machine With Inclined Static Eccentricity," *IEEE Transactions on Industry Applications*, vol. 43, no. 2, pp. 531-541, Mar. 2007.

[39] D. G. Dorrell, "Modelling rotor eccentricity in cage induction motors with axial variation of eccentricity", *Proceeding 30th Universities Power Engineering Confeference*, vol. 1, 1995, pp. 1-4.

[40] D. G. Dorrell, "Sources and Characteristics of Unbalanced Magnetic Pull in Three-Phase Cage Induction Motors with Axial-Varying Rotor Eccentricity," *IEEE Transactions on Industry Applications*, vol. 47, no. 1, pp. 12-24, Jan.-Feb. 2011.

[41] C. Di, X. Bao, H. Wang, Q. Lv and Y. He, "Modeling and Analysis of Unbalanced Magnetic Pull in Cage Induction Motors with Curved Dynamic Eccentricity," *IEEE Transactions on Magnetics*, vol. 51, no. 8, pp. 1-7, Aug. 2015.

[42] G. R. Bossio, et al., "Effects of voltage unbalance on IM power, torque and vibrations." *Diagnostics for Electric Machines, Power Electronics and Drives, Cargeses, 2009, pp. 1-6*

[43] US department of energy, “Eliminate voltage Unbalanced”, 2012. [Online]. Available: http://www.nrel.gov/docs/fy13osti/56005.pdf. [Accessed: 25 June 2014]

[44] M. Y. Kaikaa, F. Babaa, A. Khezzar, and M. Boucherma, “Analytical analysis of rotor slot harmonics in the line current of squirrel cage induction motors,” *J. Elect. Eng.*, vol. 57, no. 1, pp. 12–19, 2006.

[45] S. Nandi, "Modeling of induction machines including stator and rotor slot effects," *38th IAS Annual Meeting on Conference Record of the Industry Applications Conference*, Salt Lake City, 2003, pp. 1082-1089.

[46] J. Le Besnerais, V. Lanfranchi, M. Hecquet, G. Friedrich, P. Brochet, "Characterisation of radial vibration force and vibration behaviour of a pulse-width modulation-fed fractional-slot induction machine," *IET Electric Power Applications*, vol.3, no.3, pp.197-208, May 2009.

[47] R. S. Curiac, S. Singhal, "Magnetic noise in induction motors," *Proceedings of Noisecon/ASME NCAD*, 2008, Dearborn, 2008.

[48] H. Chuan, J. Shek, “Calculation of unbalanced magnetic pull in induction

machines through empirical method," *IET Electric Power Application*, 2018.

[49] D. G. Dorrell and M. F. Hsieh, "Calculation of Radial Forces in Cage Induction Motors at Start—The Effect of Rotor Differential," *IEEE Transactions on Magnetics*, vol. 46, no. 8, pp. 3029-3032, Aug. 2010.

[50] A. Di Gerlando, G. M. Foglia and R. Perini, "Analytical modelling of unbalanced magnetic pull in isotropic electrical machines," *18th International Conference on Electrical Machines*, Vilamoura, 2008, pp. 1-6.

[51] P. Frauman, A. Burakov and A. Arkkio, "Effects of the Slot Harmonics on the Unbalanced Magnetic Pull in an Induction Motor With an Eccentric Rotor," *IEEE Transactions on Magnetics*, vol. 43, no. 8, pp. 3441-3444, Aug. 2007.

[52] A. Sinervo, "Effects of slotting and unipolar flux on magnetic pull in a two-pole induction motor with an extra four-pole stator winding.", Ph.D. dissertation, Aalto University, Finland, 2013.

[53] S. L. Nau, "The influence of the skewed rotor slots on the magnetic noise of three-phase induction motors," *Electrical Machines and Drives Eighth International Conference*, vol. 1, no. 3, pp.396-399, Sep. 1997.

[54] D. G. Dorrell, "Calculation of unbalanced magnetic pull in small cage induction motors with skewed rotors and dynamic rotor eccentricity," *IEEE Transactions Energy Conversion*, vol. 11, no. 3, pp. 483-488, Sep. 1996.

[55] E. Rosenberg, "Magnetic Pull in Electric Machines," *Transactions of the American Institute of Electrical Engineers*, vol. 37, no. 2, pp. 1425-1469, Jul. 1918.

[56] R. C. Robinson, " The calculation of unbalanced magnetic pull in synchronous and induction motors," *Transactions of the American Institute of Electrical Engineers*, vol. *62*, no. 10, pp. 620-624, 1943.

[57] E. W. Summers, "Vibration in 2-pole induction motors," *Electrical*

Engineering, vol. 74, no. 5, pp. 424-424, May 1955.

[58] R. C. Robinson, "Line-Frequency Magnetic Vibration of A-C Machines," *Transactions of the American Institute of Electrical Engineers. Part III: Power Apparatus and Systems*, vol. 81, no. 3, pp. 675-679, Apr. 1962.

[59] H. Jordan, G. Roder, and H. Weis, "Under what circumstances may mechanical vibrations of the stator core be expected at supply frequency in 4-pole, 3-phase asynchronous machines". *ERA Translation IB2578*, vol. 21, no. 3, pp. 91-95, 1967.

[60] G. Rai, "Airgap eccentricity in induction motors," *ERA Technology Limited*, Surrey, 1974

[61] W. Schuisky, "Magnetic pull in electrical machines due to the eccentricity of the rotor," *Transaction of Electrical Res. Association*, 295, pp. 391-399, 1972.

[62] R. Belmans, W. Geysen, H. Jordan, and A. Vandenput, "Unbalanced magnetic pull in three phase two pole induction motors with eccentric rotor," *Proceedings of IEE-International Conference on Electrical Machines-Design and Applications, 1982,* pp. 65-69.

[63] S. Williamson, and K. Mirzoian, "Analysis of cage induction motors with stator winding faults," *IEEE Transactions on Power Apparatus and Systems*, vol. 7, pp.1838-1842, 1985.

[64] S. A. Swann, "Effect of rotor eccentricity on the magnetic field in the air-gap of a non-salient-pole machine," *Proceedings of the Institution of Electrical Engineers*, vol. 110, no. 5, pp. 903-915, May 1963.

[65] D. G. Dorrell and A. C. Smith, "Calculation of UMP in induction motors with series or parallel winding connections," *IEEE Power Engineering Review*, vol. 14, no. 6, pp. 56-62, Jun. 1994

[66] N. A. Al-Nuaim and H. Toliyat, "A novel method for modeling dynamic air-

gap eccentricity in synchronous machines based on modified winding function theory," *IEEE Transactions on Energy Conversion*, vol. 13, no. 2, pp. 156-162, Jun. 1998

[67] S. Nandi, R. M. Bharadwaj and H. A. Toliyat, "Performance analysis of a three-phase induction motor under mixed eccentricity condition," *IEEE Transactions on Energy Conversion*, vol. 17, no. 3, pp. 392-399, Sep. 2002.

[68] G. Bossio, C. De Angelo, J. Solsona, G. Garcia and M. I. Valla, "A 2-D model of the induction machine: an extension of the modified winding function approach," *IEEE Transactions on Energy Conversion*, vol. 19, no. 1, pp. 144-150, Mar. 2004

[69] A. Ghoggal, S. E. Zouzou, M. Sahraoui, H. Derghal and A. Hadri-Hamida, "A winding function-based model of air-gap eccentricity in saturated induction Marseille, 2012, pp. 2739-2745 motors," *20th International Conference on Electrical Machines*, Marseille, 2012, pp. 2739-2745.

[70] D. G. Dorrell and D. Ionel, "Radial forces and vibrations in permanent magnet and induction machines," *IEEE Power and Energy Society General Meeting*, San Diego, 2012, pp. 1-6.

[71] M. J. DeBortoli, S. J. Salon, D. W. Burow and C. J. Slavik, "Effects of rotor eccentricity and parallel windings on induction machine behavior: a study using finite element analysis," *IEEE Transactions on Magnetics*, vol. 29, no. 2, pp. 1676-1682, Mar. 1993.

[72] A. Tenhunen and A. Arkkio, "Modelling of induction machines with skewed rotor slots," *IEE Proceedings - Electric Power Applications*, vol. 148, no. 1, pp. 45-50, Jan. 2001.

[73] A. Arkkio, M. Antila, K. Pokki, A. Simon and E. Lantto, "Electromagnetic force on a whirling cage rotor," *IEE Proceedings - Electric Power Applications*, vol. 147, no. 5, pp. 353-360, Sep. 2000.

[74] A. Tenhunen, T. P. Holopainen and A. Arkkio, "Impulse method to calculate the frequency response of the electromagnetic forces on whirling cage rotors," in *IEE Proceedings - Electric Power Applications*, vol. 150, no. 6, pp. 752-756, Nov. 2003.

[75] W. G. Crawford, "Unbalanced magnetic pull as a cause of vibrations in two-pole induction motors'." *Proceedings of Conference on Electrical Machines in the Seventies,* Dundee, 1970.

[76] K. P. Kovacs, "Two-Pole induction-motor vibrations caused by homopolar alternating fluxes," *IEEE Transactions on Power Apparatus and Systems*, vol. 96, no. 4, pp. 1105-1108, Jul. 1977.

[77] R. Belmans, A. Vandenput, and W. Geysen. "Calculation of the flux density and the unbalanced pull in two pole induction machines." *Electrical Engineering,* vol. 70, no. 3, 151-161, 1987.

[78] Barden Precision Bearing, "Bearing Failure: cause and cures", 2008. [Online]. Available:https://www.schaeffler.com/remotemedien/media/_shared_media/08_media_library/01_publications/barden/brochure_2/downloads_24/barden_bearing_failures_us_en.pdf [Accessed: 2 May 2018]

[79] O. Magdun, Y. Gemeinder, A. Binder and K. Reis, "Calculation of bearing and common-mode voltages for the prediction of bearing failures caused by EDM currents," *8th IEEE Symposium on Diagnostics for Electrical Machines, Power Electronics & Drives*, Bologna, 2011, pp. 462-467.

[80] A. Binder and A. Muetze, "Scaling Effects of Inverter-Induced Bearing Currents in AC Machines," *IEEE Transactions on Industry Applications*, vol. 44, no. 3, pp. 769-776, May-Jun. 2008.

[81] J. R. Stack, T. G. Habetler "Fault classification and fault signature production for rolling element bearings in electric machines," *IEEE Transactions on Industry Applications*, vol. 40, no. 3, pp. 735-739, May-Jun. 2004.

[82] T. Bruce, H. Long and R. S. Dwyer-Joyce, "Dynamic modelling of wind turbine gearbox bearing loading during transient events," *IET Renewable Power Generation*, vol. 9, no. 7, pp. 821-830, Sep. 2015.

[83] D. G. Dorrell, A. M. Knight and R. E. Betz, "Improvements in Brushless Doubly Fed Reluctance Generators Using High-Flux-Density Steels and Selection of the Correct Pole Numbers," *IEEE Transactions on Magnetics*, vol. 47, no. 10, pp. 4092-4095, Oct. 2011.

[84] J. Faiz, M. Ojaghi, "Different indexes for eccentricity faults diagnosis in three-phase squirrel-cage induction motors: A review," *Mechatronics*, vol. 19, no. 1, 2009, pp. 2-13.

[85] S. Nandi and H. A. Toliyat, "Condition monitoring and fault diagnosis of electrical machines-a review," *Conference Record of the 1999 IEEE Industry Applications Conference. Thirty-Forth IAS Annual Meeting*, Phoenix, AZ, 1999, pp. 197-204.

[86] F. Sadeghi, B. Jalalahmadi, T.S. Slack, N. Raje, N.K. Arakere, "A Review of Rolling Contact Fatigue," *ASME Journal of Tribology,* vol. 131, no. 4, *Sep.* 2009.

[87] N. Weinzapfel, F. Sadeghi, V. Bakolas, A. Liebel, "A 3D Finite Element Study of Fatigue Life Dispersion in Rolling Line Contacts," *ASME Journal of Tribology,* vol. 133, no. 4, Oct. 2011.

[88] M. N. Kotzalas, T. A. Harris, " Fatigue Failure Progression in Ball Bearings," *ASME Journal of Tribology,* vol. 123, no. 2, pp. 238-242. Mar. 2000.

[89] G. Morales-spejel, A. Gabelli, " The Progression of Surface Rolling Contact Fatigue Damage," *Tribology Transaction,* vol. 58, no. 3, pp. 418-431. Nov. 2014.

[90] M. Bradford, "Unbalanced Magnetic pull in a 6-pole induction motor," *Proceedings of Institution of Engineers*, vol. 115, no. 11, Nov. 1968.

[91] A. Arkkio, M. Antila, K. Pokki, A. Simon, and E. Lantto, “Electromagnetic force on a whirling cage rotor,” *IEE Proceedings-Electric Power Applications*, vol. 147, no. 5, pp. 353-360, 2000.

[92] D. G. Dorrell and A. C. Smith, “The calculation and measurement of unbalanced magnetic pull in cage induction motors with eccentric rotors. Part 2: Experimental investigation,” *IEE Proceedings-Electric Power Applications*, vol. 143, no. 3, pp. 202–210, 1996.

[93] D. G. Dorrell and A. C. Smith, "Calculation of UMP in induction motors with series or parallel winding connections," *IEEE Transactions on Energy Conversion*, vol. 9, no. 2, pp. 304-310, Jun. 1994.

[94] A. Burakov, A. Arkkio, "Comparison of the Unbalanced Magnetic Pull Mitigation by the Parallel Paths in the Stator and Rotor Windings," *IEEE Transactions on Magnetics*, vol. 43, no. 12, pp.4083-4088, Dec. 2007.

[95] H. W. Beaty and J. L. Kirtley, “Electric Motor Handbook,” McGraw-Hill, 1998.

[96] D. G. Dorrell, J. K. H. Shek, M. A. Mueller and M. Hsieh, "Damper Windings in Induction Machines for Reduction of Unbalanced Magnetic Pull and Bearing Wear," *IEEE Transactions on Industry Application*s, vol. 49, no. 5, pp. 2206-2216, Sept.-Oct. 2013

[97] A. Sinervo, A. Arkkio, "Eccentricity Related Forces in Two-Pole Induction Motor With Four-Pole Stator Damper Winding Analyzed Using Measured Rotor Orbits," *IEEE Transactions on Magnetics*, vol. 49, no. 6, pp. 3029-3037, Jun. 2013.

[98] W. Amrhein, S. Silber and K. Nenninger, "Levitation forces in bearingless permanent magnet motors," *IEEE Transactions on Magnetics*, vol. 35, no. 5, pp. 4052-4054, Sep. 1999.

[99] Y. He and H. Nian, "Analytical model and feedback control of the levitation

force for an induction-type bearingless motor," *The Fifth International Conference on Power Electronics and Drive Systems*, 2003, pp. 242-246.

[100] A. Chiba, T. Deido, T. Fukao, and M. A. Rahman, "An analysis of bearingless AC motors," *IEEE Transactions on Energy Conversion*, vol. *9*, no. 1, pp. 61-68, 1994.

[101] A. Sinervo, A. Laiho, and A. Arkkio, "Low-frequency oscillation in rotor vibration of a two-pole induction machine with extra four-pole stator winding," *IEEE Transaction on Magnetics*, vol. 47, no. 9, pp. 2292–2302, Sep. 2011.

[102] H. Chuan, J. Shek, "Minimising Unbalanced Magnetic Pull in Doubly Fed Induction Generators," *IET conference on Power Electronics, Machines and Drives*, Liverpool, 2018, pp. 1-6.

[103] A. Sinervo and A. Arkkio, "Rotor Radial Position Control and its Effect on the Total Efficiency of a Bearingless Induction Motor with a Cage Rotor," *IEEE Transactions on Magnetics*, vol. 50, no. 4, pp. 1-9, Apr. 2014.

[104] H. Chuan and J. K. H. Shek, "Reducing Unbalanced Magnetic Pull of an induction machine through active control," *8th IET International Conference on Power Electronics, Machines and Drives*, Glasgow, 2016, pp. 1-6.

[105] H. Gavrila, V. Manescu, G. Paltanea, G. Scutaru, L. Peter, "New Trends in Energy Efficient Electrical Machines," *Procedia Engineering*, vol. 181, 2017, pp. 568-574.

[106] F. J. T. E. Ferreira and A. T. de Almeida, "Overview on energy saving opportunities in electric motor driven systems - Part 1: System efficiency improvement," *IEEE/IAS 52nd Industrial and Commercial Power Systems Technical Conference (I&CPS)*, Detroit, 2016, pp. 1-8.

[107] M. Cacciato, A. Consoli, G. Scarcella, G. Scelba and A. Testa, "Efficiency optimization techniques via constant optimal slip control of induction motor drives," *International Symposium on Power Electronics, Electrical Drives,*

Automation and Motion, 2006. SPEEDAM 2006., Taormina, 2006, pp. 33-38.

[108] S. Mohammad, B. Farhad, J. Asghar, A. Mohammed., "Power factor Improvement of Combined Input Voltage and Slip Power Control of low power Wound Rotor Induction Generators," *International Journal of Engineering Research and Applications,* vol. 1, pp. 963-968, Oct. 2011.

[109] Cholette, E. Michael, et al. "Monitoring of complex systems of interacting dynamic systems." *Applied Intelligence*, vol. 37 no.1, pp. 60-7, Jul. 2012.

[110] O. Keysan and H. Bulent Ertan, "Higher order rotor slot harmonics for rotor speed & position estimation," *12th International Conference on Optimization of Electrical and Electronic Equipment*, Basov, 2010, pp. 416-421.

[111] M. J. Kim, B. K. Kim, J. W. Moon, Y. H. Cho, D. H. Hwang and D. S. Kang, "Analysis of Inverter-Fed Squirrel-Cage Induction Motor During Eccentric Rotor Motion Using FEM," *IEEE Transactions on Magnetics*, vol. 44, no. 6, pp. 1538-1541, Jun. 2008.

[112] M. Rigoni, N. Sadowski, N. J. Batistela, J.P.A. Bastos, S. L. Nau, and A. Kost, "Detection and analysis of rotor faults in induction motors by the measurement of the stray magnetic flux," *Journal of Microwaves, Optoelectronics and Electromagnetic Applications*, vol. 11, no. 1, pp. 68-80, 2012.

[113] D. G. Dorrell, W. T. Thomson and S. Roach, "Analysis of airgap flux, current, and vibration signals as a function of the combination of static and dynamic airgap eccentricity in 3-phase induction motors," *IEEE Transactions on Industry Applications*, vol. 33, no. 1, pp. 24-34, Jan.-Feb. 1997.

[114] S. Nandi, S. Ahmed and H. A. Toliyat, "Detection of rotor slot and other eccentricity related harmonics in a three phase induction motor with different rotor cages," *IEEE Transactions on Energy Conversion*, vol. 16, no. 3, pp. 253-260, Sep. 2001.

[115] J. Hong, D. Hyun, S. B. Lee and C. Kral, "Offline Monitoring of Airgap

Eccentricity for Inverter-Fed Induction Motors Based on the Differential Inductance," *IEEE Transactions on Industry Applications*, vol. 49, no. 6, pp. 2533-2542, Nov.-Dec. 2013.

[116] D. G. Dorrell, W. T. Thomson and S. Roach, "Combined effects of static and dynamic eccentricity on airgap flux waves and the application of current monitoring to detect dynamic eccentricity in 3-phase induction motors," *Seventh International Conference on Electrical Machines and Drives*, Durham, 1995, pp. 151-155.

[117] A. Tenhunen, T.P. Holopainen, A. Arkkio, "Spatial linearity of an unbalanced magnetic pull in induction motors during eccentric rotor motions", *The international journal for computation and mathematics in electrical and electronic engineering*, vol. 22, no. 4, pp. 862-876, 2003.

[118] Pyrhonen, Juha, T. Jokinen, and V. Hrabovcova, "*Design of rotating electrical machines*," John Wiley & Sons, 2009.

[119] Emetor, 'Winding Factor', [Online]. Available: http://www.emetor.org/glossary/winding-factor/ [Accessed: 12 March 2017].

[120] F. W. Carter, "Air-gap induction", *Electrical World*, New York, 1901, vol. 38, pp. 884-888.

[121] P. P. Silvester and R. L. Ferrari, "*Finite Elements for Electrical Engineers"*, 3rd edition Cambridge University Press, 1996.

[122] W. N. Fu, P. Zhou, D. Lin, S. Stanton and Z. J. Cendes, "Modeling of solid conductors in two-dimensional transient finite-element analysis and its application to electric machines," *IEEE Transactions on Magnetics*, vol. 40, no. 2, pp. 426-434, Mar. 2004.

[123] F. Bangura, F. N. Isaac, N. A. Demerdash and A. A. Arkadan, "A time-stepping coupled finite element-state space model for induction motor drives. II. Machine performance computation and verification," *IEEE International*

Electric Machines and Drives Conference Record, Milwaukee, WI, 1997, pp. WB3/4.1-WB3/4.3.

[124] D. Marcsa, “Rotational Motion Modelling for Numerical Analysis of Electric Machines”, *Acta Technica Jaurinensis*, vol. 10, no. 2, pp. 124-136, Jun. 2017.

[125] Kistler, “Datasheet for Kistler 9366C”, [Online], Available: https://www.kistler.com/?type=669&fid=44721 [Accessed: 1 Nov 2017].

[126] Metallic materials-Calibration and verification of static uniaxial testing machins, ISO 7500-1, 2018.

[127] A. Sinervo, T. Jokela and A. Arkkio, "Unipolar flux in bearingless two-pole machine," *2012 XXth International Conference on Electrical Machines*, Marseille, 2012, pp. 3022-3026.

[128] Z. Ling, L. Zhou, S. Guo and Y. Zhang, "Equivalent Circuit Parameters Calculation of Induction Motor by Finite Element Analysis," *IEEE Transactions on Magnetics*, vol. 50, no. 2, pp. 833-836, Feb. 2014.

[129] S. A. Prashanth, S. Nekkalapu, A. Dalal and P. Kumar, "Analytical determination of slot harmonics content of air-gap magnetic field for an induction machine," *IEEE Power & Energy Society General Meeting*, Denver, CO, 2015, pp. 1-5.

[130] V. Kindl, K. Hruska, J. Sobra and M. Byrtus, "Effect of induction machine's load and rotor eccentricity on space harmonics in the air gap magnetic flux density," *Proceedings of the 16th International Conference on Mechatronics – Mechatronika,* Brno, 2014, pp. 463-468.

[131] A. Tessarolo, "Leakage Field Analytical Computation in Semiclosed Slots of Unsaturated Electric Machines," in *IEEE Transactions on Energy Conversion*, vol. 30, no. 2, pp. 431-440, June 2015.

[132] M. Bortolozzi, L. Branz, A. Tessarolo and C. Bruzzese, "Improved analytical

computation of rotor rectangular slot leakage inductance in squirrel-cage induction motors," *2015 International Conference on Sustainable Mobility Applications, Renewables and Technology (SMART)*, Kuwait City, 2015, pp. 1-5.

[133] D. G. Dorrell and O. Kayani, "Measurement and Calculation of Unbalanced Magnetic Pull in Wound Rotor Induction Machine," *IEEE Transactions on Magnetics*, vol. 50, no. 11, pp. 1-4, Nov. 2014.

[134] G. B. Rai, “Airgap eccentricity in induction motors”, 1974, The Electrical Research Association, Report No. 74-1188

[135] A. Tenhunen, T. Benedetti, T. P. Holopainen and A. Arkkio, "Electromagnetic forces of the cage rotor in conical whirling motion," *IEE Proceedings - Electric Power Applications*, vol. 150, no. 5, pp. 563-568, Sept. 2003.

[136] A. Arkkio, "Unbalanced magnetic pull in cage induction motors with asymmetry in rotor structures," *1997 Eighth International Conference on Electrical Machines and Drives (Conf. Publ. No. 444)*, Cambridge, 1997, pp. 36-40.

[137] D. G. Dorrell, "Experimental behaviour of unbalanced magnetic pull in 3-phase induction motors with eccentric rotors and the relationship with tooth saturation," in *IEEE Transactions on Energy Conversion*, vol. 14, no. 3, pp. 304-309, Sep 1999.

[138] W. T. Thomson and A. Barbour, "On-line current monitoring and application of a finite element method to predict the level of static airgap eccentricity in three-phase induction motors," *IEEE Transactions on Energy Conversion*, vol. 13, no. 4, pp. 347-357, Dec. 1998.

[139] D. R. Griffiths, and J. K. Sykulski. "Automation of Finite Element Aided Design of Induction Motors Using Multi-Slice 2D Models." *COMPEL - The international journal for computation and mathematics in electrical and*

electronic engineering, vol. 25, no. 2, pp. 309-319.

[140] BrightEngineering, “How are Squirrel Cage Induction Motor Constructed”, [Online]. Available: https://www.brighthubengineering.com/diy-electronics-devices/43723-how-are-squirrel-cage-induction-motors-constructed/#imgn_1 [Accessed: 1 June 2018].

[141] D. Guo, F. Chu, D. Chen, “The unbalanced magnetic pull and its effects on vibration in a three phase generator with eccentric,” *Journal of Sound and Vibration*, vol. 254, no. 2, 2002, pp. 297-312.

[142] C. Mi, G. R. Slemon and R. Bonert, "Modeling of iron losses of permanent-magnet synchronous motors," *IEEE Transactions on Industry Applications*, vol. 39, no. 3, pp. 734-742, May-Jun. 2003.

[143] E. Dlala, M. Solveson, S. Stanton and A. Arkkio, "Improved model for the prediction of core loss in finite element analysis of electric machines," *IEEE International Electric Machines & Drives Conference,* Coeur d'Alene, ID, 2015, pp. 340-344.

[144] J. C. Akiror and P. Pillay, "On the coefficients of core loss formulas for electrical machines," *38th Annual Conference on IEEE Industrial Electronics Society*, Montreal, QC, 2012, pp. 1927-1933.

[145] D. M. Ionel, M. Popescu, S. J. Dellinger, T. J. E. Miller, R. J. Heideman and M. I. McGilp, "On the variation with flux and frequency of the core loss coefficients in electrical machines," *IEEE Transactions on Industry Applications*, vol. 42, no. 3, pp. 658-667, May-Jun. 2006.

[146] H. A. Toliyat, M. S. Arefeen and A. G. Parlos, "A method for dynamic simulation of air-gap eccentricity in induction machines," *IEEE Transactions on Industry Applications*, vol. 32, no. 4, pp. 910-918, Jul.-Aug. 1996.

[147] J. Marc, and S. K. F. France. "SKF Energy Efficient deep groove ball bearings for higher driveline efficiency." *Proceedings of the 6th International*

Conference EEMODS, Vol. 9, 2009.

[148] M. Akbaba et al. “Improved estimation of induction machine parameters,” *Electric Power Systems Research*, vol. 34, pp. 65-73, Jul. 1995.

[149] A. G. Abo-Khalil, “Model-based optimal efficiency control of induction generators for wind power systems,” *IEEE International Conference on Industrial Technology*, Auburn, AL, 2011, pp. 191-197.

[150] W. Cao and K. J. Bradley, "Assessing the Impacts of Rewind and Repeated Rewinds on Induction Motors: Is an Opportunity for Re-Designing the Machine Being Wasted?" *IEEE International Conference on Electric Machines and Drives, 2005*, San Antonio, TX, 2005, pp. 278-285.

[151] F. J. T. E. Ferreira, A. T. Almeida, “Induction motor downsizing as a low-cost strategy to save energy”, *Journal of Cleaner Production*, vol. 24, pp. 117-131, 2012.

[152] Department of Business Energy and Industrial Strategy, Digest of United Kingdom energy statistics 2017, [Online]. Available: https://www.gov.uk/government/uploads/system/uploads/attachment_data/file/643414/DUKES_2017.pdf [Accessed: 30/10/2017].

[153] World Energy Resources Marine Energy 2016, [Online]. Available:https://www.worldenergy.org/wpcontent/uploads/2017/03/WEResources_Marine_2016.pdf [Accessed: 28/03/2018].

[154] F. Abrahamsen, F. Blaabjerg, J. K. Pedersen and P. B. Thoegersen, "Efficiency-optimized control of medium-size induction motor drives," *IEEE Transactions on Industry Applications*, vol. 37, no. 6, pp. 1761-1767, Nov.-Dec. 2001.

[155] F. Abrahamsen, F. Blaabjerg, J. K. Pedersen, P. Z. Grabowski and P. Thogersen, "On the energy optimized control of standard and high-efficiency induction motors in CT and HVAC applications," *IEEE Transactions on*

Industry Applications, vol. 34, no. 4, pp. 822-831, Jul.-Aug. 1998.

[156] J. Kirtley, “Induction Machine Control and Simulation”, Massachusetts Institute of Technology, 2003.

[157] M. N. Uddin and S. W. Nam, "New Online Loss-Minimization-Based Control of an Induction Motor Drive," *IEEE Transactions on Power Electronics*, vol. 23, no. 2, pp. 926-933, Mar. 2008.

[158] C. Ta, C. Chakraborty and Y. Hori, "Efficiency maximization of induction motor drives for electric vehicles based on actual measurement of input power," *The 27th Annual Conference of the IEEE*, Denver, 2001, pp. 1692-1697.

[159] R. Mahmood, T. Shah and H. Rehman, "High speed control of induction machines," *2013 7th IEEE GCC Conference and Exhibition (GCC)*, Doha, 2013, pp. 263-267.

[160] S. Hegde, S. Angadi and A. B. Raju, "Speed control of 3-phase induction motor using volt/hertz control for automotive application," *2016 International Conference on Circuits, Controls, Communications and Computing (I4C)*, Bangalore, 2016, pp. 1-5.

[161] X. Feng, B. Chen, "Constant slip control of induction motor at light load," *IECEC 96. Proceedings of the 31st Intersociety Energy Conversion Engineering Conference*, Washington DC, 1996, pp. 1828-1833 vol.3.

[162] Z. Yang, X. Li, C. Zhang and S. Chi, "A new slip compensation method for induction motors based on current vector decoupling," *2017 20th International Conference on Electrical Machines and Systems (ICEMS)*, Sydney, NSW, 2017, pp. 1-6.

[163] M. N. Uddin and S. W. Nam, "New Online Loss-Minimization-Based Control of an Induction Motor Drive," *IEEE Transactions on Power Electronics*, vol. 23, no. 2, pp. 926-933, Mar. 2008.

[164] D. J. Kim, H. J. Kim, J. P. Hong and C. J. Park, “Estimation of Acoustic Noise and Vibration in an Induction Machine Considering Rotor Eccentricity,” *IEEE Transactions on Magnetics*, vol. 50, no. 2, pp. 857-860, Feb. 2014.

[165] E. Leleu, C. Espanet, A. Miraoui and S. Siala, "Analytical modelling of electromagnetic origin vibrations in an induction machine supplied by high power PWM inverter," *IECON 2006 - 32nd Annual Conference on IEEE Industrial Electronics*, Paris, 2006, pp. 836-843.

[166] S. Sharma, M. Aware and A. Bhowate, "Direct torque control of symmetrical six-phase induction machine using nine switch inverter," *2017 IEEE Transportation Electrification Conference (ITEC-India)*, Pune, 2017, pp. 1-6.

[167] P. Kotter, W. Bischof, R. Kennel, O. Zirn and K. Wegener, "Noise-vibration-harshness-modeling and analysis of induction drives in E-mobility applications," *2017 IEEE International Electric Machines and Drives Conference (IEMDC)*, Miami, 2017, pp. 1-8.

[168] M. Wallin, J. Bladh and U. Lundin, "Damper Winding Influence on Unbalanced Magnetic Pull in Salient Pole Generators with Rotor Eccentricity," *IEEE Transactions on Magnetics*, vol. 49, no. 9, pp. 5158-5165, Sep. 2013.

[169] Romax Technology, “When is 20 year gearbox life not 20 years”, 2017. [Online].Available: http://www.romaxtech.com/blog/posts/2017/march/when-is-20-year-gearbox-life-not-20-years/. [Accessed: 27 June 2018].

[170] L. Douglas Berry, “Vibration versus Bearing Life”, *Reliability Magazine*, vol. 12, no. 95, 1995.

[171] H. Bhadeshia, “Steels for bearings”, *Prog. Mater. Sci*. 57, 2012, pp 268–435.

[172] M. Michon, K. Atallah and G. Johnstone, "Effects of unbalanced magnetic pull in large permanent magnet machines," *2014 IEEE Energy Conversion Congress and Exposition (ECCE)*, Pittsburgh, PA, 2014, pp. 4815-4820.

[173] SKF, “SKF energy efficient bearing”, 2007. [Online]. Available: http://www.acornbearings.co.uk/downloads/catalogues/industries/renewable-energy/skf-energy-efficient-bearings.pdf. [Accessed: 22 July 2017].